Dissertation zur Erlangung des Doktorgrades

der Fakultät für Chemie und Pharmazie

der Ludwig-Maximilians-Universität München

Tailoring Properties of Multifunctional Mesoporous Silica Nanoparticles for Controlled Drug Delivery Applications

Christian Argyo

aus

München, Deutschland

2014

Erklärung

Diese Dissertation wurde im Sinne von § 7 der Promotionsordnung vom 28. November 2011 von Herrn Prof. Dr. Thomas Bein betreut.

Eidesstattliche Versicherung

Diese Dissertation wurde eigenständig und ohne unerlaubte Hilfe bearbeitet.

München,

Christian Argyo

Dissertation eingereicht am 07.04.2014

1. Gutachter: Prof. Dr. Thomas Bein
2. Gutachter: Prof. Dr. Christoph Bräuchle

Mündliche Prüfung am 15.05.2014

Abstract

The evolution of mesoporous silica particles at the nanoscale in the past two decades has directed them towards several fields of application including catalysis, sensing and biomedicine. Exceptional interest has been attracted by mesoporous silica nanoparticles (MSNs) as bioimaging devices and drug delivery systems for targeted cancer treatment. This class of porous materials has been established as multifunctional drug delivery nanocarriers since it offers advantageous properties compared to other drug delivery systems such as polyplexes, liposomes, and dense metal or metal oxide nanoparticles. MSNs with high colloidal stability feature a well-defined and tunable porosity at the nanometer scale, high loading capacity, and versatile functional groups for post-synthetic modification such as the attachment of targeting ligands to specifically enter different types of cells. Nevertheless, researchers still face several challenges to improve the biological performance of the drug delivery vehicles based of mesoporous silica. Control over the cargo release from the porous host material, prevention of fast degradation in biological fluids, avoidance of cytotoxic effects, specific cell targeting, and escape from endosomal entrapment are highly desirable features in view of successful applications. These requirements for efficient drug delivery are part of recent research.

In this work, the effective tailoring of mesoporous silica nanoparticle (MSN) design is described to further develop their great potential as multifunctional drug delivery nanocarriers. The requirements for an efficient stimuli-responsive and thus controllable release of cargo molecules into cancer cells and the design principles for smart and autonomous nanocarrier systems are discussed. The *in vitro* and *in vivo* performance of the silica host material can be improved by further modification such as the incorporation of functional groups or magnetic cores and through a stabilization of the silica framework. For an efficient and specific disease treatment on the cellular level, different strategies were employed to achieve control over the endosomal escape of endocytosed MSNs. The coating of the nanoparticles with different organic shells improves their biocompatibility, it can be utilized for the effective encapsulation of cancer therapeutics, and it facilitates attachment of targeting ligands for specific cellular recognition. Several of these key prerequisites for efficient drug delivery nanocarriers based on MSNs are discussed in the present work.

The first part of this work focuses on a novel high temperature liquid phase “calcination” method with high boiling solvents including trioctylphosphine oxide (TOPO), tri-n-

octylamine (TOA), and squalene for template removal and strengthening of the silica network in colloidal MSNs. The standard calcination procedure in air is not suitable for these nano-sized silica particles as it results in strong agglomeration, thus preventing their use in colloidal suspensions. The highest efficiency of this novel approach was obtained by thermal treatment in TOPO at 275 °C. Here, an increasing degree of silica condensation and the retention of the high colloidal stability of the MSNs could be observed. The ability to remove the template and thus saving a preparation step represents an additional advantage of the present calcination method. The resulting MSNs retained the ordered mesostructure, its high porosity, and the large surface area of the original mesoporous nanoparticles, while showing a much greater degree of silica condensation and improved stability than before the treatment. The concept of "liquid calcination" represents a powerful and general approach for the preparation of stable colloidal porous nanoparticles.

The combination of spatially controlled drug delivery and magnetic resonance imaging (MRI) can be achieved by magnetic nanocomposites based on MSNs. The incorporation of a superparamagnetic core into mesoporous silica provided improved properties regarding targeted drug delivery and bioimaging applications. Thus, manganese ferrite nanoparticles (~10 nm) doped with Zn^{2+} were synthesized via thermal decomposition of the iron precursor [$Fe(acac)_3$] in the presence of manganese chloride and zinc chloride in octylether. Oleic acid and oleylamine served as structure directing agents to result in single nanometer-sized crystals. These nanocrystals exhibited an extremely high magnetization (~200 emu/g). Different functionalized mesoporous silica onion-like shells were generated around the magnetic cores via a delayed co-condensation approach. This new synthetic strategy was based on a sol-gel approach in the presence of the template cetyltrimethylammonium chloride (CTAC) in basic milieu (triethanolamine, TEA). The magnetic nanocomposites enabled physically directed movement by applying an external magnetic field. Moreover, the functional silica shells offer multiple modification sites for tailor-made properties of a smart drug delivery system.

In a joint project with Prof. G. Bein, Prof. Rädler and coworkers, a novel nanoscale, injectable drug-delivery system was designed. These nanocarriers combined heparin, which prevents blood clotting, with multifunctional core-shell colloidal mesoporous silica nanoparticles. An EDC amidation reaction resulted in covalent binding of the highly negatively charged polysaccharide exclusively to the external surface of amino-functionalized MSNs The

anticoagulant and biocompatible properties of heparin together with the highly porous features of the nanoparticles may lead to an efficient multifunctional drug-delivery system that can itself act as an anticoagulant and allows for incorporation of biologically active molecules as deliverable cargo.

Stimuli-responsive drug release from MSNs may result in a more targeted release of the drugs, and can be achieved by a change in biological environment, such as altered levels of disease-specific enzymes. Specifically, matrix metalloproteinase 9 (MMP-9) is known to be overexpressed during advanced stages of cancer, while minimally expressed in healthy tissue. Additionally, increased MMP-9 expression has been associated with a poor survival rate of lung cancer patients. Here, a novel synthesis of MSNs containing MMP-9 cleavable peptide linkers in combination with avidin caps was successfully established in cooperation with members of the Comprehensive Pneumology Center (CPC, Helmholtz Institute). The bulky avidin allowed for efficient sealing of the mesopores. These multifunctional MSNs showed no release of the diverse cargo molecules when MMP-9 was absent, but stimuli-responsive drug release in the presence of MMP-9 enzyme could be observed. Dose-dependent release was shown for model cargo, calcein-AM, as well as for the chemotherapeutic drug cisplatin. Functionalized MSNs were found to be non-toxic up to high concentrations, with avidin functionalization having a protective effect regarding toxicity of these particles. Notably, MSNs that contained non-toxic doses of cisplatin together with the proteasome inhibitor bortezomib resulted in an increased cell death, indicating that these particles can also be used for combination treatments, thus indicating another possible advantage of this nanoparticle platform.

Another strategy for internal cellular triggered drug release based on pH-responsive gatekeepers was investigated in collaboration with the groups of Prof. Bräuchle and Prof. Carell. In this study, the enzyme carbonic anhydrase was attached to the external surface of MSNs via linkage to sulfonamide derivatives. By changing the pH to slightly acidic values (5.5), the efficient sealing of the mesoporous channels with these bulky bio-macromolecules became reversible. Consequently, loaded cargo molecules could be released. *In vitro* studies showed a controlled intracellular release of the fluorescent model drug DAPI after endocytosis and acidification of the endosomal compartment.

Mesoporous nanoparticles for drug delivery would benefit significantly from further improvements in targeting efficiency and endosomal release. We present a system based on colloidal MSNs with targeting-ligands and a red-light photosensitizer. Furthermore, these

nanocarriers were equipped with a supported lipid bilayer (SLB) as a removable cargo encapsulation. Upon photoactivation of these multifunctional drug delivery vehicles, a successful cargo delivery to the cytosol was observed. This nanoparticle system provides spatial and temporal control of the release of drugs into the cytosol of cancer cells. Our system presents a general platform since it can be loaded with different model drugs and adapted for targeting multiple cell types.

Multifunctional mesoporous silica nanocarriers feature excellent cellular uptake behavior due to their nanometer-scaled size. Nevertheless, after endocytosis of the MSNs, the endosomal entrapment is known to be a major bottleneck for efficient cytosolic cargo release. In a joint project with Prof. Bräuchle and coworkers, PAMAM dendron-coated MSNs exhibiting high buffering capacity were investigated. These adopted buffering properties prevented acidification of the endosomal compartment, ultimately causing endosomal escape via the proton-sponge effect. *In vitro* studies showed a time-dependent release of immobilized fluorescent dye (DAPI) and anticancer drug (colchicine) from the mesopores. Furthermore, targeting specificity to KB cancer cells was achieved by folate receptor-mediated endocytosis and could be observed by fluorescence live-cell imaging.

In summary, different requirements that are of key importance for a controlled and targeted drug delivery have been investigated. Multifunctional mesoporous silica nanoparticles with precisely tailored properties are viewed as a promising and flexible platform for numerous biomedical applications such as targeted drug delivery and bioimaging. In this work, we could show that multifunctional MSNs are suitable for applications as versatile drug delivery vehicles. A co-delivery of different chemotherapeutics for an enhanced combination treatment of cancer cells could also be achieved. We established different successful approaches for the endosomal escape of the multifunctional MSNs via internal and external stimuli. In the future, the combination of many or all of these essential features into one multifunctional nanocarrier is anticipated to result in powerful drug delivery systems.

Table of contents

1 Introduction

This chapter is based on the following perspective article:

Christian Argyo, Veronika Weiss, Christoph Bräuchle, and Thomas Bein, *Chemistry of Materials* **2014**, *26*, 435 – 451.

1.1 Multifunctional Mesoporous Silica Nanoparticles

Multifunctional mesoporous silica nanoparticles (MSNs, size typically < 500 nm) have attracted substantial attention in recent years due to their advantageous structural properties, such as a high internal surface area and pore volume, tunable pore sizes, colloidal stability, and the possibility to specifically functionalize the inner pore system and/or the external particle surface. These highly attractive features make MSNs a promising and widely applicable platform for diverse biomedical applications including bioimaging for diagnostics,[1-2] biosensing,[3-4] biocatalysis,[5-7] bone repair and scaffold engineering,[8-10] and drug delivery.[11-13] Caruso and coworkers established another interesting approach using mesoporous silica particles as a template to create submicron-sized polymer capsules for anticancer drug delivery.[14-16] Periodically ordered mesoporous silica, created by combining surfactant micellar aggregates with reactive silica precursors, was discovered about 20 years ago by researchers at Mobil.[17-18] In particular, inorganic-organic (hybrid) core-shell nanoparticles based on mesoporous silica have received great attention as drug delivery vehicles, where the decoration of the inner or outer surface of the particles with organic molecules can impart important features for successful drug delivery. MSNs have first been proposed around 2001 as nanocarriers for transporting therapeutics.[19] Inspired by this simple concept (at that time still lacking control over cargo uptake or release), many efforts were made in recent years to create multifunctional stimuli-responsive nanocarrier systems consisting of MSNs as host materials.[20] This is based on the excellent material properties of MSNs such as good biocompatibility, high loading capacity and efficient encapsulation of cargo molecules in their mesopores. Additional benefits include the possibility to design stimuli-responsive mechanisms with spatio-temporal control of release of the cargo, and the efficient attachment of organic surface functionalities including hydrophilic polymers, gate keepers, and targeting ligands, respectively.[21-27]

The delivery of anti-cancer therapeutics into cancer cells by employing nanoparticle carriers has made significant progress in recent years. Here, the intention is to overcome common issues of conventional systemic drug supply such as poor solubility, limited stability, rapid metabolization and excretion of the drug, undesired side effects, and to overcome the lack of selectivity towards specific cells types.[28-30] The encapsulation of therapeutics within nanocarriers that selectively target certain cell types or tissues represents a promising strategy to address these problems.

Here, recent research in the field of multifunctional MSNs intended for drug delivery applications is discussed. MSNs can be designed as a multifunctional platform for different stimuli-responsive trigger systems for a specific drug release. Moreover, different strategies for achieving controlled endosomal escape will be discussed. Coating the nanoparticles with different organic shells improves biocompatibility, facilitates attachment of targeting ligands for specific cellular recognition, and can be utilized for the effective encapsulation of cancer therapeutics. Investigation of *in vitro* behavior of colloidal particles, often fluorescently marked to track the particles in cells, with live-cell imaging serves to evaluate targeting specificity and efficient delivery. The implementation of the above strategies and features into one multifunctional drug delivery vehicle provides a promising basis for wide-ranging applications in cancer therapy and diagnosis. These key prerequisites for efficient drug delivery nanocarriers based on MSNs are schematically presented in Scheme 1.1. They will be discussed in more detail in the following sections.

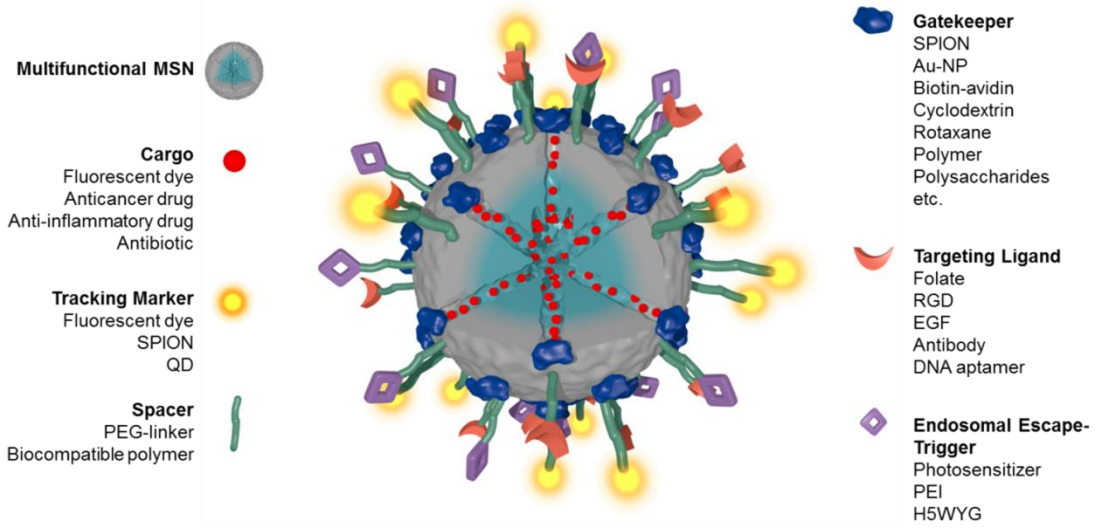

Scheme 1.1: Schematic illustration of a multifunctional mesoporous silica nanoparticle (MSN) containing the necessary features for a stimuli-responsive controlled release of the loaded cargo into the cytosol of a targeted cell (SPION: superparamagnetic iron oxide nanoparticle, QD: quantum dot, PEG: poly(ethylene glycol), Au-NP: gold nanoparticle, RGD: Arg-Gly-Asp amino acid sequence, EGF: epidermial growth factor, PEI: poly(ethylene imine), H5WYG: endosomolytic peptide).

1.2 Multifunctional Drug Delivery Vehicles Based on MSNs

1.2.1 Inorganic Silica Core as a Host System

MSNs acting as host systems for therapeutics provide high loading capacity within the porous system and protection of the guest molecules from degradation and from detection by the immune system. Furthermore, the nanocarrier systems can be utilized for the transport of hydrophobic molecules through biological media, thus increasing the therapeutic effect at the desired location. The synthesis of ordered mesoporous silica materials has been extensively studied in recent years,[31-34] including sol-gel processes to create MCM-41[35] and SBA-15,[36] amongst various different structure types.[37-39] Fine-tuning of the reaction parameters such as concentrations, pH value, chemical nature of the surfactants, temperature and time allows for a precise adjustment of size, morphology and pore structure of the mesoporous silica. The scope of conventional mesoporous materials such as MCM-41 for applications in drug delivery is limited due to their relatively large particle sizes in the micrometer range. Cellular uptake studies of nanoparticles showed that particle sizes less than 120 nm are preferred for endocytic uptake.[40] Thus, efforts have been made to obtain spherical mesoporous silica nanoparticles MSNs in that size range.[41-45] For example, a standard synthesis route following addition of surfactant template, silica source, and organotrialkoxysilanes to a highly basic

aqueous solution (2 M NaOH, pH 12.3) at elevated temperatures to create MCM-41-like nanoparticles, is used by many research groups.[46-51] Another versatile approach for obtaining stable suspensions of MSNs in high yields was developed in our group. Here, triethanolamine is exploited as base and as complexing ligand for the silica precursor and is used to tune the particle size (to about 80 nm).[21, 52] Their worm-like pore structure with pores growing from the center to the periphery suggests a seed-growth mechanism (Figure 1.1c). Delivery of large cargo molecules, such as enzymes or oligonucleotides, leads to a growing interest in the synthesis of MSNs with large pores (10 – 20 nm, Figure 1.1d) and is part of recent research.[53-54]

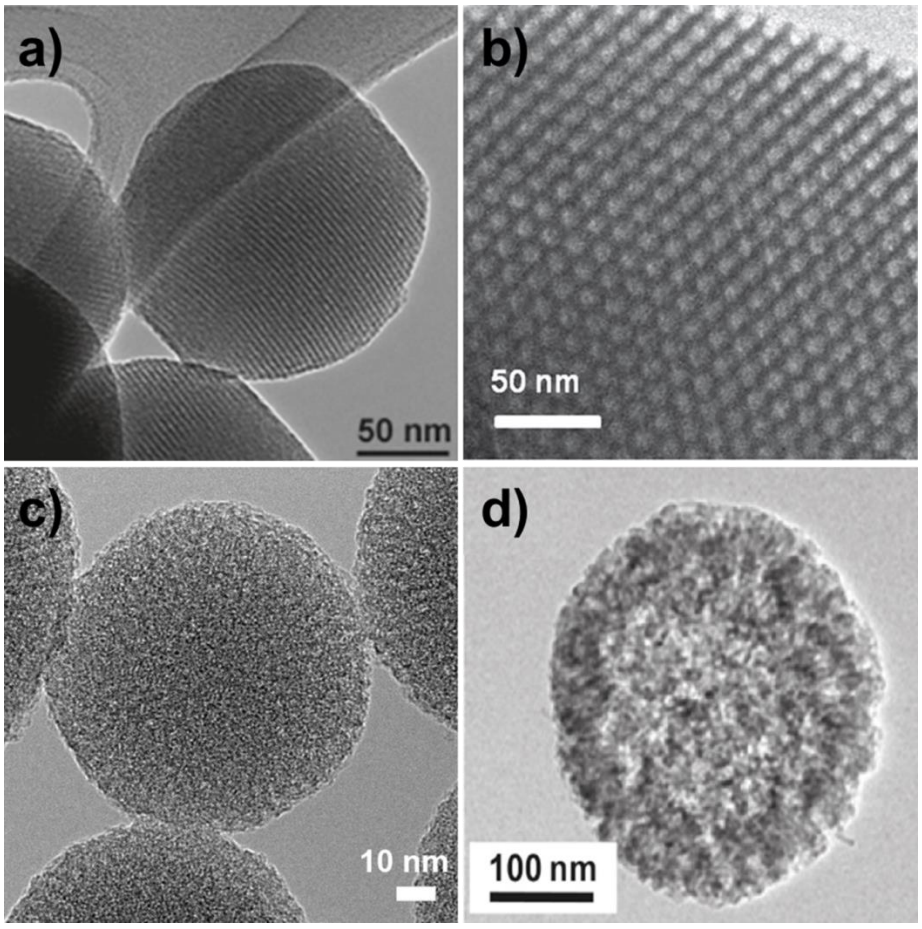

Figure 1.1: Transmission electron micrographs of a) MCM-41-type nanoparticles,[55] b) micron-sized SBA-15 material,[56] c) colloidal MSNs with worm-like pore structure, and d) monodispersed MSNs with large pores (> 15 nm).[53]

In order to gain access to the pores, the templating surfactant molecules have to be removed. This can be achieved either by calcination or with extraction methods. To overcome impediments such as reduction in pore size, particle agglomeration, removal of organic

moieties, or low degree of condensation of the silica network, Cauda *et al*. established a new approach that combines the advantages of both aforementioned methods for template removal (cf. chapter 3).[57] Here, a liquid-phase high temperature "calcination" of MSNs is performed in a high-boiling organic solvent leading to a higher degree of silica condensation while maintaining the colloidal nature of the nanoparticles.

Functionalization. In order to exploit the whole potential of MSNs for drug delivery applications, it is desirable to add functionality to the silica scaffold. Molecular functionality attached to the surfaces of inorganic silica can dramatically change the properties of the obtained material, which is important in host-guest interactions with the cargo. The incorporation of organic moieties at specific locations is intended to fine-tune surface and materials properties and is a subject of current research.[58-59] The spatially selective modification of the internal pore system and the external particle surface with organic and inorganic moieties is often an essential requirement for these materials to operate as multifunctional drug carriers exhibiting the required features. External surface functionalization is particularly important for colloidal and chemical stability as well as for interactions with the environment, such as modifying the particles for specific cell targeting or attaching large molecules for pore gating and improving biocompatibility.[60-64] On the other hand, internal organic moieties can supply enhanced interaction or covalent binding sites for cargo molecules, such as drugs or proteins, which allows for control over diffusional transport, delivery kinetics, and stability of the therapeutic molecules.[65-67]

In general, there are several approaches to achieve functionalization of silica materials. The most important functionalization strategies are via post-synthetic grafting and via co-condensation, besides the synthesis of periodic mesoporous organosilicas (PMO) and employment of metal organic reagents.[35, 68-70] In order to gain control over the location of the functional groups in silica nanoparticles, Bein and co-workers established a site-selective delayed co-condensation approach.[22, 71] Here, bi-functional MSNs with a selective functionalization of the interior and an orthogonal functionality at the external particle surface in different onion-like shells can thus be prepared (Figure 1.2). This strategy opens new possibilities for the design of numerous highly functionalized porous nanoparticles with applications in controlled drug delivery.

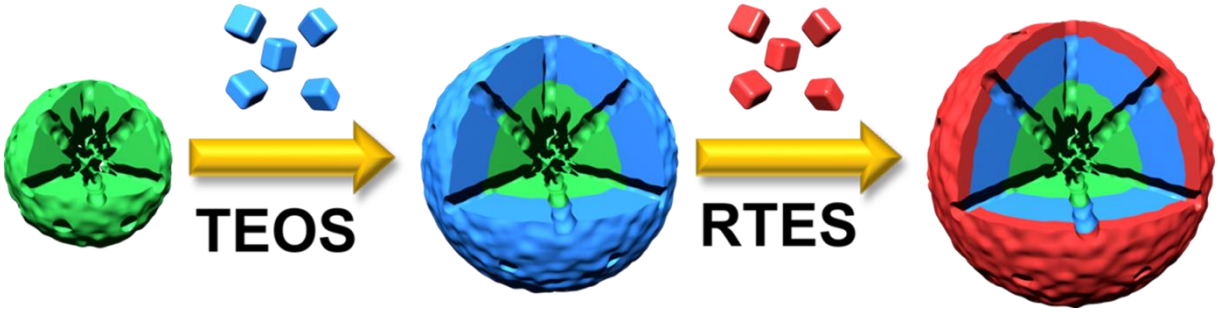

Figure 1.2: Site-selective delayed co-condensation approach for creating bi-functional MSNs. In a first step a mixture of organosilane (green) and tetraethyl orthosilicate (TEOS) in an aqueous solution containing template and catalyst creates a functionalized nanoparticle core. Subsequently, the nanoparticle growth is completed by addition of pure TEOS (blue) resulting in an unfunctionalized silica shell around the core. Finally, the addition of another organotriethoxysilane (RTES, R represents any organic moiety, red) and TEOS forms an external skin with different functionality.

1.2.2 Modification of MSNs with a Functional Shell

The potential to design biocompatible external surfaces of nanoparticles providing tunable interactions with the biological environment by attachment of molecular or macromolecular moieties for biomedical applications has been recently demonstrated.[25-26, 72] Surface modification with organic and inorganic species can introduce a large variety of functionalities for controlling diffusion and release of cargo molecules and cell surface recognition, among others. The combination of the properties of such an external functional shell and the advantageous structural properties of the mesoporous silica core can create multifunctional drug carriers, making the delivery process highly controllable.

Gating. One of the important functionalities in this context is triggered release of the cargo through specially designed gating concepts. In general, gatekeepers can be classified into three different types (cf. Figure 1.3). Pore gating systems can either consist of bulky molecular groups or nanoparticles, such as proteins, superparamagnetic iron oxide nanoparticles (SPIONs), or gold nanoparticles (Au-NPs) which block the pore entrances for efficient sealing of the interior mesoporous environment.[25, 73-74] These macromolecular structures are either degradable or covalently linked to the silica particle surface via linkers that are cleavable upon exposure to certain stimuli.[75-76] Very good pore sealing can also be achieved by a complete coating of the MSNs. For instance, polymers, oligonucleotides, or supported lipid bilayers (SLB) have been shown to prevent premature cargo release.[24, 27, 77-84] Often phase transitions or competitive displacement reactions lead to opening of the pores and

efficient cargo delivery.[85-86] The third strategy for controlled cargo release involves attachment of the cargo molecules in the porous system of the silica nanocarriers. Coordinative or covalent bonds can be cleaved by certain stimuli such as competitive molecules reducing agents or competitive molecules reducing agents to activate cargo release.[87-89] Zink and coworkers have presented different nanocarriers with on-demand controllable release mechanisms, including nanoimpellers consisting of azobenzene groups that have been described to trigger UV-light-activated release of a cell membrane-impermeable dye.[90]

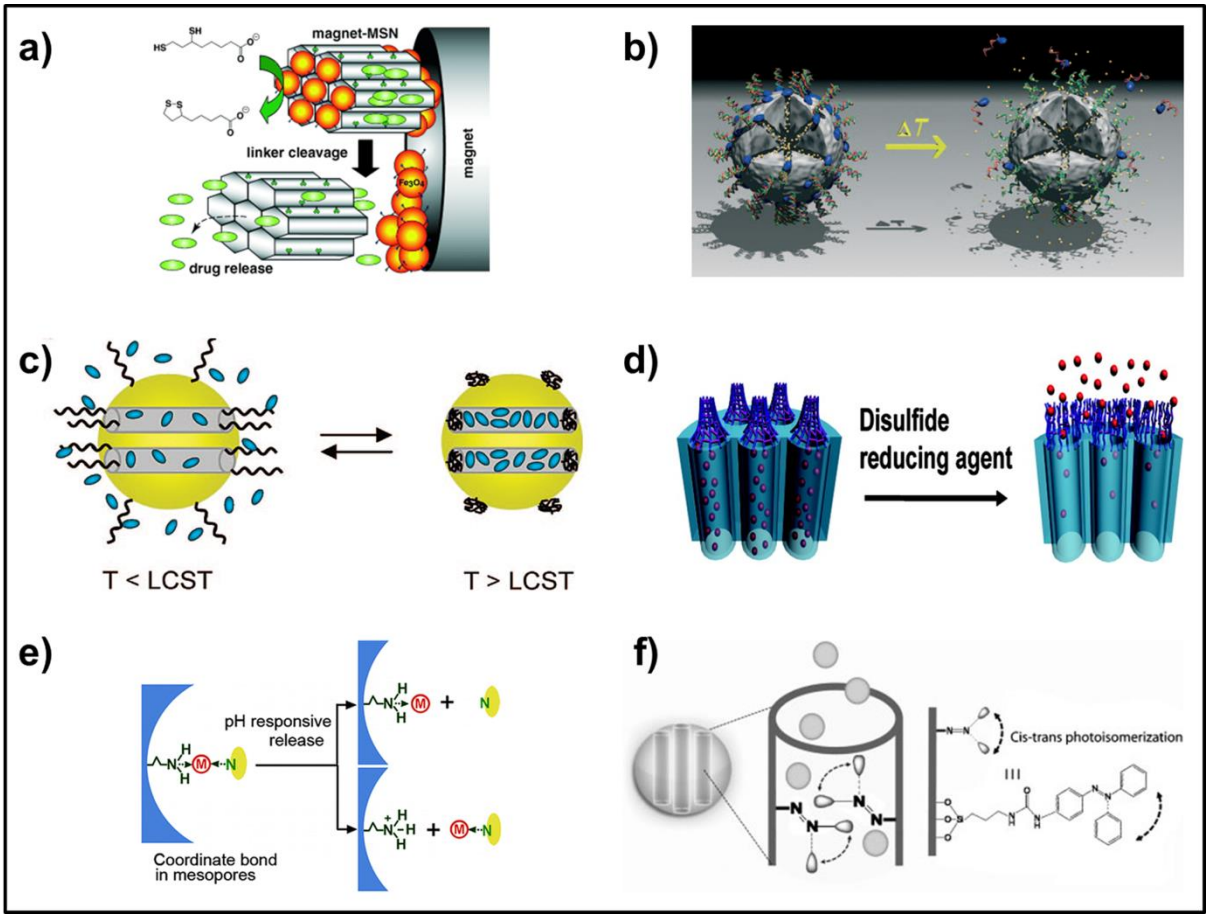

Figure 1.3: Strategies of controlled release can be classified into three different types, molecular/particle pore gating (a,b), surface coating (c,d), and internal pore modification (e,f). a) Mesoporous silica nanorods capped with superparamagnetic iron oxide nanoparticles (SPIONs) containing redox-responsive cleavable disulfide linkers;[73] b) temperature-dependent programmable molecular valve system consisting of avidin caps being opened by melting the DNA linkers;[91] c) temperature-dependent phase transition of PNIPAM-coating on MSNs;[92] d) disulfide-linked polymeric network at the outlet of mesoporous silica allowing redox-responsive controlled release of the cargo;[93] e) schematic release mechanism for a pH-responsive system based on coordination bonding in mesopores;[94] and f) light-activated cis/trans isomerization of azobenzene groups inside mesopores expels the cargo.[90]

Biocompatibility and stability. For applications of MSNs as nanocarriers, biocompatibility and low toxicity are required. A modification of the nanoparticle surface with functional

shells, such as polymer coatings, charged groups, or a supported lipid bilayer (SLB) was found to decrease particle aggregation and improve stability in biological media. For instance, functionalization of the particle surface with phosphonate groups was shown to improve the stability and dispersibility of MSNs in aqueous media.[95-96] This modification helped to prevent interparticle aggregation, and redispersion after a drying process was highly improved.[1] In general, MSNs provide good biocompatibility, but the high surface area and a low degree of condensation of the silica framework can promote a high rate of dissolution.[97-98] Bare, non-functionalized MSNs featuring silanol groups at their surface dissolve fairly rapidly in simulated body fluid (SBF) under physiological conditions and produce soluble silicic acid species (which are found to be nontoxic).[99] The rate of silica dissolution is dependent on particle size, functionalization, degree of silica condensation, and pore morphology. A surface functionalization can prevent fast degradation and provide prolonged stability of MSNs in biological media. For example, a hydrophilic polymer shell such as poly(ethylene glycol) (PEG) or a SLB on colloidal MSNs improves stability in water, maintains monodispersity, and can minimize nonspecific adsorption of proteins on the nanoparticle surface.[20, 79, 96] Such a polymer coating provides a protective shell for the silica surface, which is important when prolonged circulation time in an organism is required for effective drug delivery. PEGylation can hinder capture by organs of the reticuloendothelial system (RES) and consequently slow down biodegradation.[100]

Hemocompatibility is another important attribute of MSNs. Surface functionalization of bare MSNs can reduce or even completely prevent thrombogenic effects and non-specific protein adsorption on MSN surfaces.[101] For example, heparin-coated core-shell MSNs have recently been described (cf. chapter 5).[102] Heparin is a highly sulfated, anionic polysaccharide, known for its anticoagulant properties. This novel nanoscale system combines the efficiency of heparin in preventing blood-clotting with multifunctional core-shell MSNs featuring excellent structural properties and colloidal stability. In general, MSNs with organic shells offer multifunctionality and improved biocompatibility and hemocompatibility and are expected to have potential as blood-stream-injectable drug-delivery systems offering new options for cancer therapy. For illustration, a typical sequence of cytosolic delivery of therapeutics to cancer cells with mesoporous silica nanocarriers is depicted in Scheme 1.2.

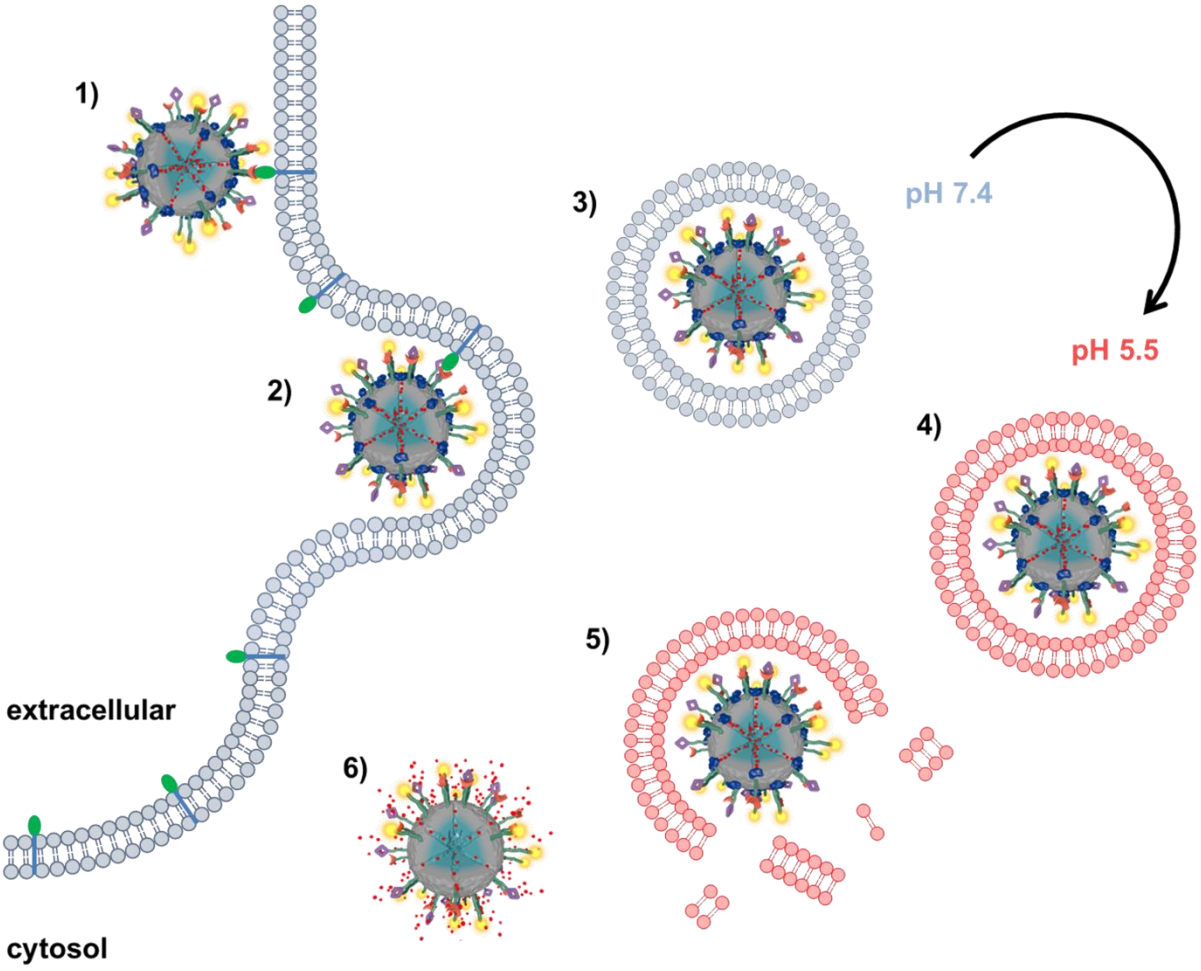

Scheme 1.2: Schematic representation of different stages of a targeted cellular uptake of a multifunctional MSN and controlled release of the cargo into the cytoplasm of cancer cells. 1) Active docking to cell surface receptor of a nanocarrier *via* targeting ligands; 2) process of ligand/receptor-mediated endocytosis; 3) MSN entrapped in endosome; 4) intracellular transport and acidification of endosome; 5) triggered endosomal escape of nanocarrier, thus obtaining access to the cytoplasm; 6) controlled delivery of the cargo inside the cell.

1.3 Drug Delivery and Bioimaging Applications

1.3.1 Targeting and Cellular Uptake

Targeting. Insufficient target selectivity of drugs can cause unwanted side effects and reduce therapeutic efficacy. Especially in anticancer chemotherapy, limited selectivity of cytostatins and cytotoxins towards tumor cells is responsible for many undesired side effects. The efficacy of the treatment can be affected when nonspecific toxicity to normal cells prevents an effective dose that is necessary to eradicate malignant cells.[103-104] Extensive studies showed that passive targeting of nanocarriers in tumor tissue could be observed.[105-106] Well-stabilized nanoparticles with optimal size and appropriate antifouling surface can remain in blood vessels long enough to accumulate at the tumor site. Passive targeting relies on the enhanced permeability and retention (EPR) effect. This effect is described as the tendency of particles of certain sizes, such as liposomes, nanoparticles, and macromolecular drugs, to preferentially accumulate in tumor tissue. Tumor vasculature typically exhibits an increased permeability and is lacking of effective lymphatic drainage.[107] Enhanced passive bioaccumulation via the EPR effect could be achieved by modifying the MSN surface with positively charged groups.[108] However, the EPR effect is not universal for all types of tumor cells and a lack of cell-specific interactions might decrease therapeutic efficacy and induce multiple drug resistance (MDR).[84, 107, 109]

In contrast, employing targeting ligands like folic acid or macromolecules like the epidermal growth factor (EGF) in order to exploit the overexpression of certain receptors on tumor cell surfaces can promote specific and active nanocarrier binding and cellular uptake. Active targeting can be achieved by covalent attachment of targeting molecules (ligands) to the particle surface. The main challenge for targeted nanocarriers is to achieve high targeting specificity and drug delivery efficiency simultaneously, while avoiding nonspecific binding and activation of immunogenic effects. A recent advance has been reported by Brinker and coworkers, who combined a porous, inorganic MCM-41-type silica core coated with a supported lipid bilayer to prevent cargo leakage with a short targeting peptide (SP94).[84] This small peptide was identified by phage display to bind efficiently to hepatocellular carcinoma cells. The complementary receptor is still unknown. In this study, a ligand recruitment

procedure was described leading to efficient receptor-mediated endocytosis of the nanocarriers.

The small molecule folic acid (FA) has been widely investigated as targeting ligand and has shown a notable enhancement in uptake efficiency of MSN nanocarriers (citations see Table 1.3-1). Often long spacers, e.g. PEG chains, are used for the covalent attachment of the targeting ligands to the external surface of the MSNs. This linkage provides high flexibility to obtain efficient binding of the targeting ligands to the cell membrane receptors. Ligands such as FA, mannose, hyaluronic acid, and EGF (amongst others) used as targeting devices are abundantly present in organisms. Moreover, the associated receptors are widely present on many eukaryotic cells. This implies concerns about the achievable targeting specificity. In those cases the significant overexpression of receptors on cancer cells has been exploited. Extensive efforts have been made to create actively targeted nanocarrier vehicles using ligands for specific recognition of the cell-surface receptors as well as antibodies and DNA aptamers. Important examples are summarized in Table 1.1. Studies on antibodies attached to the nanoparticle surface either via electrostatic interactions or covalent linkage showed highly specific binding with high affinity to antigens overexpressed on different cancer cell lines.[110-111] MSN bioconjugates with DNA-aptamers were also investigated and showed specific binding to nucleolin, a cell membrane protein overexpressed on breast cancer cells.[112] However, concerns may arise about the stability of these systems in body fluids due to potential degradation of the targeting ligands by extracellular nucleases or proteases, which may reduce targeting efficiency of antibody- and aptamer-aided delivery concepts.

Table 1.1: Diverse targeting ligands used for active and specific cell recognition of nanocarriers based on MSNs.

Targeting Ligand	Cell Membrane Receptor	Targeted Cell Line	Ref.
Folic acid (FA)	Folate receptor (FR-α)	HeLa, KB	[27, 79, 113-121]
RGD motifs	Integrins	HeLa, MCF-7, U87-MG, HT-29, SCC-7	[122-124]
Antibody ME1	Mesothelin	MM	[110]
Antibody ab2428	ErbB 2	MCF-7	[111]
Antibody Herceptin	HER2/neu	BT-474	[125]
Aptamer AS 1411	Nucleolin	MCF-7, MDA-MB-231	[112]
Mannose	Mannose receptor	MDA-MB-231	[126]
Galactose	Galactose receptor	HCT-116, Capan-1, MDA-MB-231	[127]
Hyaluronic acid	CD44 (RHAMM, CD168, HARE)	MDA-MB-231	[128]
Anisamide	Sigma-receptor	ASPC-1	[129]
EGF	EGF-R	HuH-7	[27]
SP94	Unknown	Hep3B	[84]
FA, TEM-7, CD31	FR-α, TEM-7 antibody, CD31 antibody	MCF-7, HUVEC	[130]

Endocytosis. In general MSNs are internalized into the cells via endocytosis.[12] The endocytic pathway is the most common uptake mechanism of cells for many different nanoparticles and macromolecules. Endocytosis is a very complex process by which cells absorb such particles by engulfing them with a lipid bilayer forming vesicles. Therefore a part of the cell membrane is used for creating an endosome.[131] Size and morphology of the silica nanoparticles and functional groups on the external particle surface influence the ability of MSNs to be internalized via endocytosis.[132-137] Utilizing such modifications of the MSNs can aid in specific cellular uptake in a precisely controlled manner. In a study of Slowing *et al*.,[63] endocytosis of aminopropyl-functionalized MSNs was shown to be affected by caveolar inhibition suggesting a cellular uptake via a caveolae-mediated mechanism. Endocytosis of MSNs can be investigated via flow cytometry, transmission electron microscopy, confocal microscopy and other techniques.[138]

1.3.2 Endosomal Escape

Recent studies have demonstrated that MSNs are able to undergo smooth cell internalization, but endosomal escape has been identified as a bottleneck for the efficient delivery of macromolecular substances or nanoparticles.[72] The entrapment in the endosomes could lead to degradation of the nanocarriers and their cargo molecules by specific digestive enzymes when fusion with a lysosome occurs. Thus, an important step in achieving an appropriate therapeutic effect is to facilitate the endosomal escape and to ensure cytosolic delivery of the therapeutics. Many anticancer therapeutics such as doxorubicin (DOX) feature cell membrane permeability and consequently a trigger for endosomal escape is not required. These permeable drugs only require means of preventing premature release from the nanocarrier to avoid global distribution in the organism and targeted transport into cancer tissue to achieve a sufficiently high local drug concentration. Nevertheless, a large number of molecular and macromolecular therapeutics are either hydrophobic or membrane-impermeable. Therefore the multifunctional nanocarrier vehicles should provide an efficient endosomal escape mechanism for the local delivery of the drug molecules into the cytoplasm, thus gaining access to the targeted cell compartments or to the nucleus. Excellent strategies for achieving endosomal escape are provided by nature. Evolution created bacteria and viruses, which are able to penetrate membranes via different mechanisms to escape the endosomal pathway and to reach their target sites. Thus, it would be desirable to transfer these very efficient natural mechanisms to the drug delivery vehicles. Different mechanisms such as pore formation in the endosomal membrane, pH-buffering effects of protonable groups (“proton sponge”) or fusion into the lipid bilayer of endosomes have been proposed to facilitate the endosomal escape.[139] In addition, photochemical methods to rupture the endosomal membrane have been introduced to MSNs.[27, 72, 140]

In a study by Sauer *et al.*,[72] MSNs were taken up into cells and transported within endosomes, but no release of the cargo into the cytoplasm could be detected during incubation. In order to overcome the barrier of endosomal entrapment, photoinduced endosomal release via excitation of a photosensitizer was employed. Photochemical internalization (PCI) using photosensitizers (PS) that generate reactive oxygen species upon photoactivation is a powerful tool to overcome trapping by the endosomal membrane.[141] Initial approaches of combining PS with mesoporous silica as a drug carrier did not provide a covalent bond of the PS to the particles. This could lead to uncontrolled spreading of the compounds and toxic effects on the cells. To achieve a more spatially controlled activity of

nanodevices operating with PS, it is desirable to bind the PS directly to the surface of the mesoporous particles. Thus, a mesoporous core–shell system with covalently surface-linked photosensitizer was designed that provides an on-board trigger for light-activated endosomal membrane rupture.[140] The nanocarriers can be loaded with model drugs in a broad size-range and are encapsulated by a SLB. The controlled release mechanism in living cells operates in a two-step cascaded manner, where the SLB is disintegrated by singlet oxygen in a first step and, secondly, the endosomal membrane is ruptured causing efficient cytosolic drug release. This nanodevice for drug delivery is capable of stimuli-responsive and localized endosomal escape and drug release without the systemic cell toxicity exhibited by common (dissolved) PS. In order to create a general photoactivatable drug delivery platform being applicable in biological environments, such as cancer tissue, further improvements have to be accomplished. Strategies for red-light activation have already been investigated (cf. chapter 6).[27, 127] The activation of the photosensitizer with light of low energy reduces the phototoxicity and significantly increases the depth of tissue penetration, which will be crucial when activation *in vivo* is required.

Another promising endosomal release strategy is based on the proton sponge effect, in which osmotic swelling and membrane rupture of endosomes is initiated by macromolecules with high buffering capacities (cf. chapter 9).[142] This mechanism does not require an external stimulus and custom-made nanocarriers can activate an ”automatic” pathway for endosomal escape. Several cationic lipids and polymers, such as poly(ethylene imine) (PEI), possess substantial buffering capacity below the physiological pH which is a potential trigger to escape the endosomal entrapment.[143-144] The cationic polymers or particles enter the cell via endocytosis, subsequently being entrapped in the endosome. Upon intracellular trafficking to late endosomes or lysosomes, the compartment is acidified from an initial physiological pH value of 7.4 to 5.5.[145] Thus, the overall protonation level for PEI increases drastically.[146] The accumulation of positive charge inside the endosome is coupled with a passive influx of chloride anions through ion channels to maintain electroneutrality. The large increase of ion concentration within the endosome in turn results in an inflow of water molecules, which causes osmotic swelling and subsequent membrane rupture. Employment of the proton sponge effect would provide an elegant solution for the problem of endosomal entrapment of MSNs. However, the exact mechanism is not fully understood. It is still an open question whether there has to be a high-capacity buffering agent present that is subsequently

protonated and highly charged, or if an already highly charged surface of particles is also sufficient to cause counter-ion influx, endosome swelling and rupture. Lin and coworkers reported on MSNs with negatively charged surface functionalization achieving endosomal escape via the proton sponge effect.[63] More negatively charged nanoparticles would escape more easily from endosomes of cancer cells owing to their high buffering capacity. The zeta potential of the silica nanoparticles seems to have a great impact on the ability of particles to escape the endolysosomal pathway. However, such highly negatively charged nanoparticles exhibit unfavorable cellular uptake behavior due to electrostatic repulsion with the negatively charged cell membrane. Nanocarriers providing protonable groups at mildly acidic conditions should result in much more efficient cellular uptake and subsequent drug release to the cytosol. In general, the proton sponge effect is a promising intrinsic endosomal escape pathway that should be further investigated.

As an alternative mechanism, endosomolytic peptides can be utilized to achieve endosomal release.[147] The lipid bilayer-enclosed MSNs established by Brinker and coworkers were decorated with such an endosomolytic peptide (H5WYG) (Figure 1.4).[84] This peptide sequence is a subunit of the glycoprotein hemagglutinin of the influenza virus A, and undergoes a conformational change upon protonation. H5WYG peptides were often employed in combination with nanocarriers, but experimental evidence for the exact molecular mechanism was not provided so far.[148-150] Different endosomal escape pathways were believed to take place, such as the proton sponge effect (protonation of the histidine residues of the peptide) or fusion of the endosomal membrane with the SLB. Further investigations are needed to evaluate the exact mechanism, which could lead to full exploitation of this endosomal escape pathway.

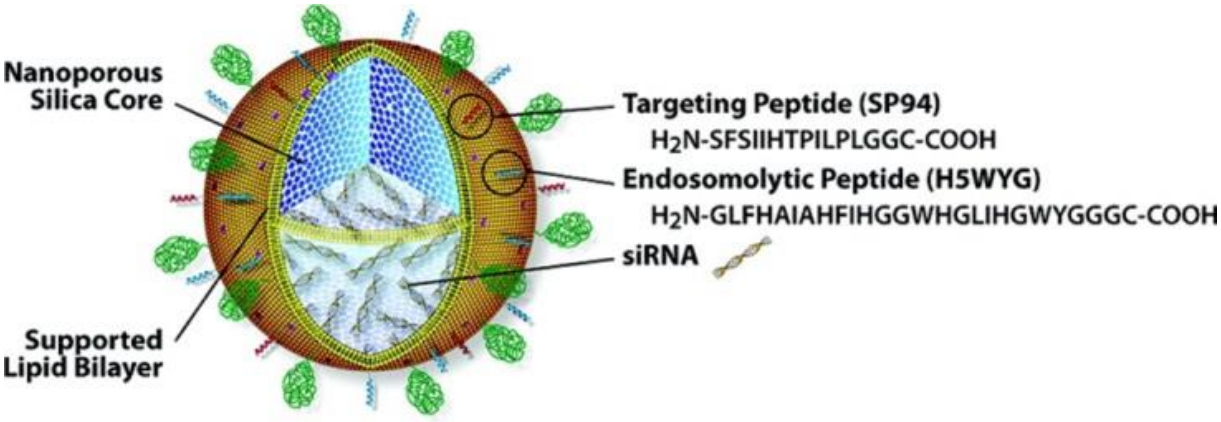

Figure 1.4: "Protocell" consisting of MSN-supported lipid bilayers with targeting peptides (SP94) and endosomolytic peptides (H5WYG) attached to the outer periphery of the nanoconstructs.[83]

In general, endosomal entrapment was found to be a bottleneck in efficient cytosolic delivery of non-permeable drug molecules and further efforts have to be made to overcome this entrapment. Complete understanding of the diverse escape mechanisms is highly desirable. Internalized multifunctional MSNs with an integrated trigger could rapidly escape from endolysosomal vesicles into the cytoplasm and resist the lysosomal degradation and thus protect the loaded drugs from bioerosion.

1.3.3 Controlled Release of Cargo

Extensive *in vitro* studies have been performed to gain insights regarding the feasibility of MSNs as drug nanocarriers. Cargo release in a controlled manner is highly desirable, since side effects can be drastically reduced by locating delivery to single cells or target tissue and since the optimal amount of drug can be liberated. MSNs serving as drug delivery vehicles can be functionalized on the external particle surface with stimuli-responsive molecules, nanoparticles, polymers, and proteins acting as caps and gatekeepers for such a controlled release of various cargos. Delivery of antitumor drugs and other pharmaceutical cargos such as enzymes or oligonucleotides requires effective protection from undesired degradation in harsh environments, such as the stomach and intestines. On the other hand, when injected into the blood stream such a drug delivery device should offer perfect enclosure of the cargo to prevent undesired premature release and systemic distribution before reaching the targeted tissue or cells.

The most common pore sealing strategies can be classified into three different types of gate keepers, i.e. molecular/particle pore gating, coating of the external particle surface, and internal pore binding. Reported *in vial* and *in vitro* studies and the diverse opening mechanisms based on external or internal stimuli are presented in Table 1.2 and Table 1.3, respectively.

Table 1.2: Controlled cargo release mechanisms triggered by external stimuli.

Stimulus	Gating system	Opening mechanism	Cargo	Release experiments	Ref.
External					
UV-Vis light (λ = 240 – 639 nm)	**Molecular pore gating**				
	Thymidine dimers	Cleavage	Dye	*In vial*	[151]
	Cylcodextrin (CD)	Dethreading	Dye	*In vial*	[152]
	Cucurbit[6]uril	Photothermal dethreading	Dye	*In vial*	[153]
	Nitroveratryl carbamate	Cleavage	Anticancer drug	*In vial*	[154]
	Coating				
	Polymer shell	Photolysis, dethreading	Dye	*In vial*, *in vitro*	[155-156]
	Supported lipid bilayer (SLB)	Photolysis	Dye, therapeutic	*In vitro*	[27, 140, 157]
	Internal pore modification				
	Coordinative bonds	Cleavage	Dye	*In vial*	[87]
IR-light (λ = 808 nm)	**Coating**				
	Aptamer DNA shell	Photothermal dehybridization	Anticancer drug	*In vitro*	[78]
	Pore modification				
	Coordinative bonds	Photothermal cleavage	Anticancer drug	*In vitro*	[89]
Magnetic field + absorber	**Molecular/Particle pore gating**				
	DNA	Thermal cleavage	Dye	*In vial*	[158]
	SPIONs	Heat-shock induced cleavage of disulfide linker	Dye	*In vitro*	[73]
	Au-NPs	Cleavage of boroester linker	Dye	*In vial*	[159]
	Coating				
	PEI/NIPAM	Thermal phase transition	Dye , enzyme	*In vial*	[160]
Temperature	**Molecular/Particle pore gating**				
	Biotin-Avidin	Cleavage of DNA linker	Dye	*In vial*	[91]
	Au-NPs	Cleavage DNA linker	Dye	*In vial*	[161]
	Coating				
	Paraffin	Melting	Dye, anticancer drug	*In vitro*	[162]
	Polymer	Phase transition	Dye, antibiotic, anticancer drug	*In vial*, *in vitro*	[85, 92, 163]
Molecules	**Molecular pore gating**				
	DNA	Competitive displacement	Dye	*In vial*, *in vitro*	[86, 164-165]
	Glycoprotein	Cleavage of boroester linker	Dye, antifungal drug	*In vitro*	[166]
	18-crown-6	Competitive displacement	Antiinflammatory drug	*In vial*	[167]
	SLB	Lysis	Dye, colchicine	*In vitro*	[24]

Table 1.3: Controlled cargo release mechanisms triggered by internal stimuli.

Stimulus	Gating system	Opening mechanism	Cargo	Release experiments	Ref.
Internal					
pH (acidic)	**Molecular/Particle pore gating**				
	SPIONs	Cleavage of boroester linker	Antiinflammatory drug	*In vitro*	[76]
	Au-NPs	Cleavage of boroester linker	Dye	*In vial*	[159, 168]
	CD	Dethreading	Dye, anticancer drug	*In vial, in vitro*	[169-172]
	[2]pseudorotaxane	Dethreading	Dye	*In vial*	[173]
	Curcubit[6]uril	Dethreading	Dye	*In vial*	[174-175]
	Coating				
	Saccharides	Cleavage of boroester linker	Dye	*In vial*	[176]
	Layered double hydroxides (LDH)	Dissolution	Dye	*In vial*	[177]
	Polymer	Phase transition	Anticancer drug, insulin, dye	*In vial, in vitro*	[67, 77, 85, 154, 178-181]
	Coordination polymer	Cleavage	Anticancer drug	*In vitro*	[182]
	Chitosan	Phase transition	Anti-inflammatory drug, Anticancer drug	*In vial, in vitro*	[48, 111, 183]
	Internal pore modification				
	Coordinative bonds	Cleavage	Anticancer drug	*In vial, in vitro*	[89, 94]
	Acetal linkage	Cleavage	Peptide	*In vitro*	[184]
	Electrostatic interactions	Cleavage	Anticancer drug	*In vitro*	[185]
	Template	Extraction	Anticancer drug	*In vitro, in vivo*	[186]
	Hydrazone linkage	Cleavage	Anti-inflammatory drug	*In vitro*	[187]
pH (basic)	**Molecular pore gating**				
	β-Lactoglobulin	Phase transition	Dye, anti-inflammatory drug	*In vial*	[188]
	Lysozyme	Detaching	Dye	*In vitro*	[189]
	Sulfophenyl isothiocyanate	Cleavage	Anti-inflammatory drug	*In vial*	[26]
Enzymes	**Molecular pore gating**				
	Azopyridine derivatives	Cleavage	Dye, anticancer drug	*In vitro*	[190]
	Cucurbit[7]uril	Competitive displacement	Dye	*In vial*	[191]
	[2]pseudorotaxane	Cleavage of ester linker	Dye	*In vial*	[192]
	Biotin-Avidin	Enzymatic digestion	Dye	*In vial*	[25]
	Coating				
	Hyaluronic acid	Cleavage	Dye, anticancer drug	*In vitro*	[128]
	Ethylene glycol ester	Cleavage	Dye, anticancer drug	*In vitro*	[193]
	Peptides	Cleavage	Dye	*In vial*	[194]
	Starch derivatives	Enzymatic digestion	Dye, anticancer drug	*In vitro*	[75]
	Lactose derivatives	Enzymatic digestion	Dye	*In vial*	[195]

Reducing agent	**Molecular pore gating**				
	CD	Cleavage of disulfide linker	Dye	*In vial*	[172]
	ssDNA	Cleavage of disulfide linker	Anticancer drug, ssDNA	*In vitro*	[196]
	Coating				
	Collagen	Cleavage of disulfide linker	Dye	*In vial*	[197]
	Polymer	Cleavage of disulfide linker	Dye	*In vial, in vitro*	[93, 156, 181]
	Internal pore modification				
	Disulfide linkage	Cleavage	Enzyme, cysteine	*In vial, In vitro*	[72, 88]
Molecules	**Molecular pore gating**				
	ATP aptamer	Competitive displacement	Dye	*In vial, in vitro*	[198-200]
	Insulin derivatives	Competitive displacement	Insulin, cAMP	*In vial*	[201]
	Au-NPs	Dehybridization of DNA linker	Dye	*In vial*	[74]
	Coating				
	Enzyme multilayers	Phase transition	Insulin	*In vial*	[202]

A broad spectrum of triggers for specific cargo release has been described. External triggers, such as light, external magnetic fields, and temperature, require activation of the release mechanism from the outside.[152, 160, 162] These systems provide perfect control over temporal and spatial release of the drugs into the targeted tissue or cells, but tissue penetration in *in vivo* studies can limit performance. Temperature changes have been investigated to release encapsulated molecules.[162-163] Light can also be used to activate various opening mechanisms.[151, 153] Recently, Bein, Bräuchle and co-workers could demonstrate an improved system consisting of MSNs coated with a supported lipid bilayer (SLB) and equipped with a covalently attached photosensitizer (PS).[27] The SLB was shown to seal the pores and to prevent premature release of the loaded cargo. Upon photoactivation of the PS with red light, generation of reactive oxygen species initiated cargo release due to rupture of the SLB (cf. chapter 6). Photosensitizers are promising components of nanocarrier systems for efficient drug delivery because they can simultaneously serve as a means for endosomal escape and for triggering controlled release in combination with SLB-coated MSNs. Changes in pH, enzymatic reactions, and reducing agents are internal triggers that can provide intrinsic and autonomous release of the loaded cargo molecules from the mesoporous host system. Many mechanisms for controlled closure and release have been developed in recent years, often with a view on utilizing such biologically relevant changes in the cell environment encountered by the particles upon endocytosis. Thus, pH changes have been used to open gates at the pores of the mesoporous nanoparticles and changes in redox potential could be used to cleave disulfide bridges. pH-responsive nanocarriers have been designed to achieve a

site-selective controlled release, because tumor and inflammatory tissues are more acidic than normal tissue and blood. Importantly, the acidification of endosomes inside targeted cells can be utilized to trigger pH-responsive intracellular release of the cargo molecules.[111, 182, 187] Zink and coworkers have described a pH-responsive dethreading of bulky β–cycodextrin molecules upon protonation of a complementary stalk located at the pore entrances, and the resulting efficient DOX release *in vitro*. In the context of oral administration, nanocarrier systems have been designed with acid-stable gatekeepers to be able to pass the stomach without premature release. After passing the acidic environment, pH-responsive caps can be cleaved in the basic milieu of the intestines to efficiently release the loaded pharmaceuticals.[26, 188-189] Enzyme-responsive controlled release can be highly efficient once the nanocarriers have entered the cancer tissue or the cytosol of targeted cells. Many intracellular and extracellular enzymes are overexpressed in cancer tissue and exhibit increased activity, resulting in preferential cargo release at those locations.[190-194] Summarizing, molecular and particle-based pore gating or coatings, removable by either intracellular or external triggers, can provide exquisite control over the location and time of cargo release during drug delivery.

1.3.4 Biological and Pharmaceutical Activity

On-demand cargo release from the mesopores of silica nanoparticles has been proven to be feasible. To understand the biological and pharmaceutical activity of the MSN drug delivery systems *in vitro* and *in vivo*, it is useful to investigate the response of cells, such as knock-down of certain genes, stimuli-responsive labeling of cell compartments, destruction of the microtubule network, or apoptosis of cancer cells.[24, 140, 203-204] Dependent on the charge of the cargo, the surface of the nanocarriers has to be tuned and the release systems need to be adjusted to the scope of the application. Diverse model systems have been devised to learn more about the complex processes during cellular uptake of MSNs and subsequent drug release. Here, the focus is not to give insight to the challenges of preclinical studies, but to provide information about the mode of operation of multifunctional MSNs in the biological environment. For instance, attaching fluorescent dyes to the MSNs provides the possibility to directly observe the behavior of the nanocarriers and the cells. Common dyes include rhodamine or fluorescein derivatives, as well as ATTO or ALEXA dyes.[72, 118, 135, 205] Fluorescent cargo and/or labeling of cell compartments also aids to examine the intracellular

processes. Drug loading of small anti-cancer therapeutics can be achieved by simple immersion of the particles into a concentrated solution of the desired drug, followed by sealing with the gating mechanism under study. Efficient loading was shown by Bein and co-workers upon adsorbing colchicine, propidium iodide, phalloidin, chromobodies, calcein or a rhodamine derivative into MSNs, which were subsequently sealed by a supported lipid bilayer.[24, 27, 140] Doxorubicin (DOX) is a commonly used anti-cancer therapeutic due to its efficient induction of apoptosis in cancer cells, and it is fluorescent thus enabling direct microscopic observation.[206] Several DOX-containing systems have been investigated, ranging from Fe_3O_4@mSiO_2 nanocapsules[207] to hollow MSNs,[208-210] mesoporous silica-coated gold nanorods,[78] and to MSNs including targeting functionalities like aptamers.[112] Our groups (Bein, Bräuchle and coworkers) could show an efficient release behavior of calcein in HeLa cells over time driven by photoactivation of an on-board photosensitizer ($AlPcS_{2a}$, cf. chapter 6).

In vitro methods can verify the encapsulation of a large amount of drug molecules in MSN carriers, which increases their efficiency. This was proven in a study of Tian and co-workers.[203] They demonstrated a significant increase of early and late apoptosis of paclitaxel-loaded MSNs on MCF-7 cells compared to free drug molecules. Gene transfection or oligonucleotide delivery with MSNs has not been studied to a large extent yet, and in most reported cases the oligonucleotides are only adsorbed on the external surface of the MSNs or incorporated in a polymer shell of coated MSNs.[211] Milligan and co-workers used so called "protocells" for GFP and IL-10 gene delivery *in vitro* and *in vivo*, but no proof of gene adsorption inside the pores was provided.[82, 211] Tamanoi and co-workers attached siRNA to the external surface of coated MSNs with the aid of PEI and observed gene silencing of EGFP.[212] Attachment of the oligonucleotides exclusively on the external particle surface could cause concerns about premature degradation via abundantly available ribonucleases. Therefore, controlled loading of siRNA into large pores of MSNs is a highly desirable approach that is expected to provide efficient protection from bioerosion. In addition to extensive *in vitro* investigations, the first *in vivo* application of MSNs was reported in 2008.[213] Recently Nel and co-workers presented a successful proof of principle aimed to overcome DOX resistance in a mouse xenograft model with PEI-PEG functionalized MSNs.[214] Unfortunately, heterogeneity in the tumor microenvironment, such as differences in the vascularity, possibly influences the efficacy of drug delivery *in vivo*. Further research is necessary to evaluate the MSN distribution in tumor models, particularly with targeting ligands to ensure the capability of the delivery systems to efficiently reach all cells within the

tumor tissue. Nevertheless, these early experiments provide strong evidence that MSNs are promising candidates for improved cancer therapy and that they are able to reduce side effects for healthy tissues.[47, 215] Furthermore, very promising results for siRNA delivery were obtained by Min and co-workers.[204] They showed successful delivery of GFP downregulating siRNA in a tumor xenograft mouse model (Figure 1.5). The reduction of GFP fluorescence could be observed with optical imaging *in vivo* (Figure 1.5a/b) and more clearly in tissue sections (Figure 1.5c). Although the results demonstrate the feasibility of this approach, the system is still lacking control over pore sealing and a release mechanism.

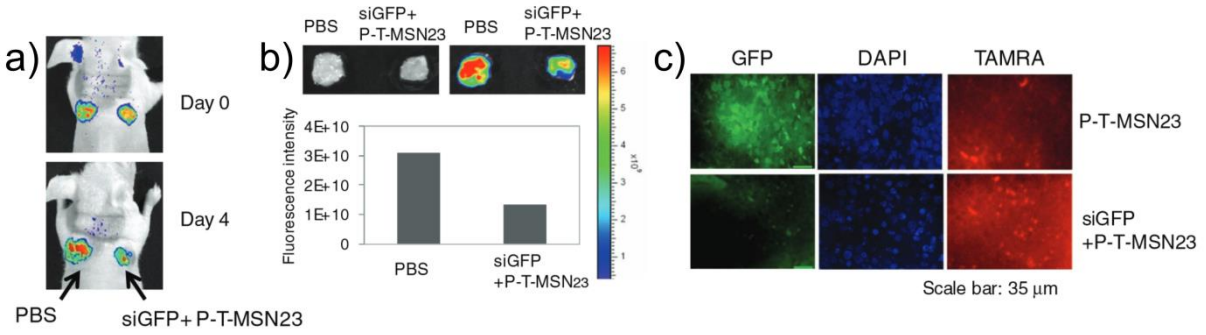

Figure 1.5: Knockdown of GFP genes with siRNA-loaded, PEGylated (P), and carboxytetramethylrhodamine-labeled (T) MSN with a pore diameter of 23 nm (P-T-MSN23) *in vivo*. a,b) *In vivo* optical images before (a) and after removal of tumors (b) and quantitative analysis of GFP-expressing tumors. c) Optical microscopic images of a tissue section after 4′,6-diamidino-2-phenylindole (DAPI) staining show considerable reduction in GFP expression in the siGFP–P-T-MSN23-treated tumor, compared with tissue treated with P-T-MSN23.[204]

In addition to possible cancer therapeutics and gene delivery there are also studies for inhibitor delivery and delivery of cytokines.[148, 216] A detailed overview on *in vivo* bio-safety evaluations and diagnostic/therapeutic applications of MSNs has recently been provided by Shi and co-workers.[217]

1.3.5 Imaging

The imaging possibilities for MSNs and their combinations with other materials range from optical microscopy to magnetic resonance imaging, and to ultrasonic imaging, near infrared imaging and other techniques. Here, we will focus on optical microscopy and its applicability to gain real-time observation of MSNs in cell cultures and tissues. Other imaging techniques and the preparation methods for functionalized hybrid nanoparticles, such as silica nanoparticles containing magnetic cores, have been extensively discussed elsewhere.[2, 217-219] In this context MSNs are used as a platform for incorporation of nanocrystals or doping with active ions including iron oxide nanocrystals, quantum dots, gold nanoparticles, and manganese or gandolinium ions. These multifunctional nanocarriers gain high interest in theranostic applications. There are different possibilities to fluorescently label MSNs. Depending on the desired type of labeling (removable or not), fluorescent dye molecules can be attached to the inner and outer particle surface by covalent linkage via post-synthetic grafting, incorporation into the silica framework, or pH-/redox-sensitive linkage. Diffusion of dye molecules or nanoparticles like quantum dots inside the pores has been investigated as well.[220] In that case, an efficient enclosure of the fluorescent cargo in the mesopores can be achieved by supported lipid bilayers or other bulky molecules used as valves. Diffusion dynamics of fluorescent molecules in porous silica materials were intensively studied with fluorescence microscopy. Bräuchle and co-workers could image single dye molecules[221-223] as well as the anticancer agent DOX[224] moving inside mesoporous channels of silica materials. Such studies are crucial for understanding diffusion processes and confirm the need for defined surface modifications for controlling adsorption and desorption processes of the cargo molecules in the mesoporous system. Functionalization of the mesoporous interior with amino-groups in order to achieve positively charged surfaces resulted in preferential and increased uptake of negatively charged siRNA constructs.[225] Issues of cargo loading efficacy may arise due to electrostatic repulsion when negatively charged molecules like double stranded DNA should be absorbed into nanocontainers featuring negative surface charge.[226] On the other hand, electrostatic interactions may not be too strong, otherwise they can cause entrapment in the porous system and consequently cargo release is inhibited. The stability of the cargo to be transported is a key factor in particle design, especially if the goal is to efficiently deliver sensitive cargos like siRNA. Fluorescent donor-acceptor pairs offer the possibility to investigate the stability of oligonucleotides inside the pores by measuring the Förster resonance energy transfer (FRET).[225-226] Thus, the stability of oligonucleotides in specifically functionalized mesopores after adsorption was demonstrated. Since nanocarriers

provide protection against diverse biological attacks, incorporation of oligonucleotides into the mesopores of silica materials is very promising for future experiments in gene delivery, especially because previous efforts in delivery so far have focused on oligonucleotides attached to the external particle surface, as already discussed in chapter 3.4.[211-212] FRET is also a useful method to monitor the release of payload from the pores of MSNs in real-time. For that purpose Lee and co-workers attached a FRET donor-acceptor pair of coumarin and fluorescein isothiocyanate (FITC) to the cap system β-cyclodextrin located at the pore entrances of MSNs. After light activation, cleavage of the gatekeepers occurred and subsequently the FRET-signal vanished due to great distance of the donor-acceptor pair.[227] Optical imaging is also the most widely used technique to study the feasibility of custom-made drug nanocarriers based on MSNs. The direct release and distribution of cargo inside cells can be monitored via fluorescence microscopy. Furthermore, precise investigations of uptake behavior and cellular internalization mechanisms of MSNs in single cells can be realized. Methods that were developed to evaluate the uptake behavior of viruses and single polymeric gene carriers (polyplexes) were extensively exploited by Bräuchle and co-workers.[228-231] Subsequently, the internalization of epidermal growth factor receptor (EGFR) targeted MSNs into living cells was also investigated. Detailed information on the internalization pathway, the behavior of the MSNs inside the cells, and information on unexpected interactions between the particles and the cell can be gathered by life-cell imaging and consequently possible challenges can be monitored. Similar to the behavior of polyplexes it was observed that porous silica nanoparticles exhibit three phases of motion during their internalization (Figure 1.6). The particle motion was measured on a sensitive fluorescence wide field microscope and analyzed with single particle tracking methods. In the first phase the particles attach to the cell membrane and consequently show a slow directed movement, provoked by movement of the subjacent actin cytoskeleton mediated by the EGF receptor and linker proteins. With the transition to phase II the particles are internalized into the cells. Phase II consists either of normal, anomalous and confined diffusion or a combination of all three. Normal diffusion is often hindered in the cytoplasm by the local microenviroment (cytoskeleton, organelles, large molecules etc.). Phase III shows much faster, active transport of the particles entrapped inside endosomes along the microtubule network via motor proteins with velocities up to 2 µm/s.

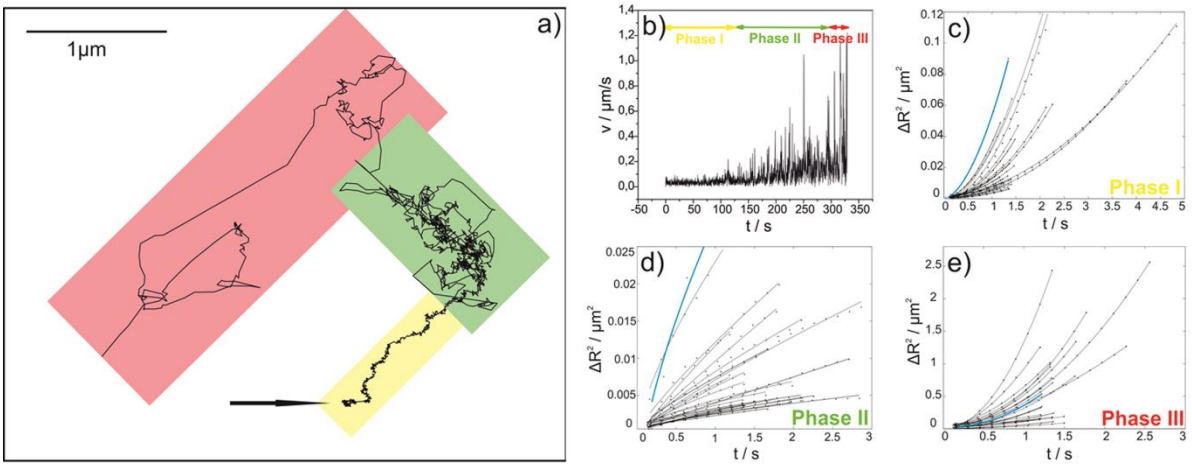

Figure 1.6: Internalization of epidermal growth factor receptor (EGFR)-MSNs with supported lipid bilayer.[27] (a) Trajectory of an MSN during uptake into a HuH7 cells. The particle was tracked 4 minutes after addition of the particles on top of the cells, for 5 minutes and 50 seconds at a temporal resolution of 150 ms/frame. Three phases are typically observed during the internalization process.[229] The starting point of the trajectory is indicated with an arrow. The overlying color boxes indicate the three phases. Yellow: phase I – slow active transport; green: phase II – anomalous and confined diffusion; red: phase III – active transport with back and forth movement. (b) Instantaneous velocities of the trajectory shown in (a), and (c)-(e) the mean square displacement (MSD) plots of the three phases obtained from several trajectories. The corresponding plots from the trajectory are indicated in blue. The analysis of the trajectories was performed with the help of the viro-tracker developed by Godinez *et al.*[232] to localize the xy-coordinates and with the help of the transport-program developed by Arcizet *et al.*[233] to calculate MSD plots.

Optical microscopy also provides the capability to image *in vivo*. However, attenuation of photon propagation and a poor signal to noise ratio due to auto-fluorescence of the tissue can cause difficulties and should be considered in the selection of the type of dye and its concentration. Nevertheless, the high loading capability of MSNs makes them promising candidates to overcome this problem. Thus, Lo and co-workers could study the spatial distribution of MSNs with positive surface charge and loaded with indocyanine green (ICG) via near infrared microscopy inside anesthetized rats.[234] In that case the biodistribution of the optical MSN probe was evaluated in comparison to FITC-labeled MSNs. FITC seems to be not appropriate for *in vivo* optical imaging, since tissue penetration depth of the fluorescent signal of this dye is too small and consequently not detectable. NIR fluorescent dyes can be clearly detected after intravenous injection for evaluating particle accumulation inside the liver and kidney, and partially in lungs, spleen and heart. Further verification of the biodistribution in the dissected organs can be seen in Figure 1.7. Optical microscopy utilizing NIR fluorescent dyes offers the possibility to investigate long-term biodistribution of nanocarrier systems, since it is a non-invasive method and animal models do not need to be sacrificed. As can be seen in this experiment, bare MSNs seem to face the problem to be cleared through the reticuloendothelial system (RES), such as spleen or liver, and

subsequently the EPR effect is decreased.[99, 105, 234] Further modifications of the particle surface including PEGylation of the MSNs have to be done to avoid the activation of the immune system.[235]

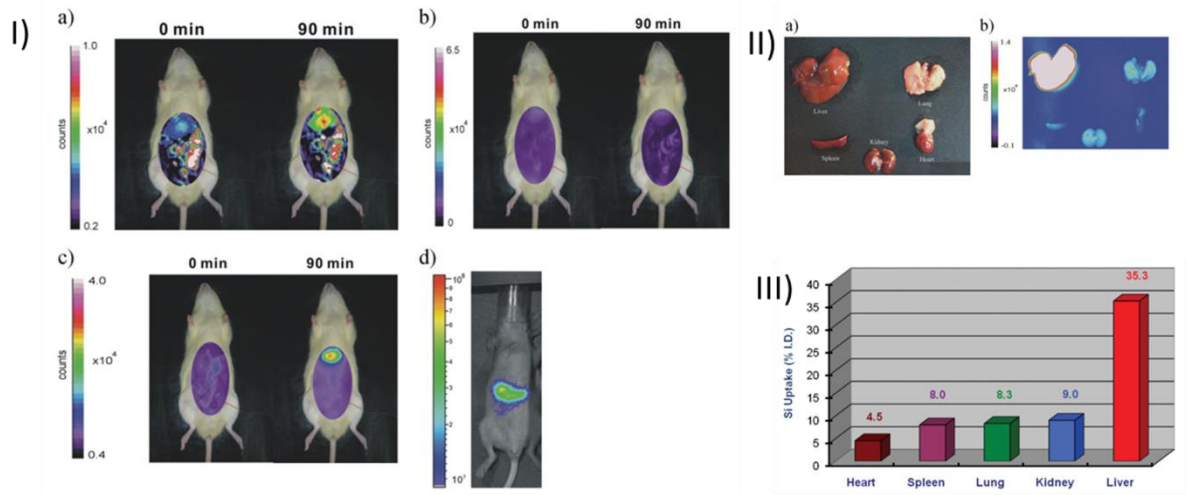

Figure 1.7: I) Comparison of FITC-tagged MSN with ICG-tagged MSN (50-100 nm) (a)/(b) Biodistribution of MSN-NH_2-FITC in an anesthetized rat before and after (90 min) i.v. injection. The experimental conditions were set at 492 nm (excitation) and 518 nm (emission) and (a) a longer shutter time (60 s) for a visible imaging and (b) 30 s shutter time. (c) Biodistribution of MSN-TA-ICG in an anesthetized rat before and after i.v. injection for 90 min. MSN-TA-ICG sample showed less interference of autofluorescence in a shorter shutter period (30 s). (d) MSN-TA-ICG in nude mice after i.v. injection for 3 h. II) Dissected organs from a rat sacrificed after i.v. injection of MSN-TA-ICG for 3 h. (a) representative white-light and (b) fluorescent images. III) *In vivo* biodistribution of silicon percentage in various organs of rat after i.v. injection of MSN-TA-ICG for 6 h.[234]

1.4 Future Perspectives

Colloidal MSNs have attracted great attention as potential drug delivery systems for cancer cell targeting, and as bioimaging devices. In addition to their biocompatibility and biodegradability, they can be selectively modified at their inner and outer surface. Guest molecules can be efficiently encapsulated in their tunable pore system. Furthermore, it is possible to functionalize their outer surface with targeting ligands, biomimetic and other pore gating molecules, fluorescent dyes, and biocompatible polymers. Compared to most other prominent organic carriers, such as liposomes and polyplexes, MSNs offer several advantages including high loading capacity, high stability, and the ability to protect the guest molecules from various biochemical attacks causing degradation of the bioactive cargo molecules. Extensive *in vitro* studies on the controlled release of therapeutics and the evaluation of cytotoxicity have proven the feasibility of multifunctional MSNs for a sustainable and efficient drug delivery to cancer cells. Today's challenge is the investigation of

pharmacokinetics and pharmacodynamics of mesoporous silica nanoconstructs for *in vivo* diagnostic and therapeutic applications. Issues and opportunities have been recently reviewed by several groups.[32, 217, 236-237] The biological effects of MSNs at different levels ranging from molecules, cells, and blood to tissue and organs, involving cytotoxicity, biodegradability, blood compatibility, biodistribution and excretion are currently under investigation. Oral administration and injection into the blood stream of such nanocarriers require specific properties for long-term stability during circulation in the organism, specific targeting of the desired location, and controllable release of the loaded drugs to obtain the desired therapeutic outcome. Controlling all these requirements is important to avoid side effects harming healthy tissue. Researchers are still faced with many challenges, especially *in vivo* applicable stimuli-responsive release mechanisms, targeting specificity, and bio-safety issues, which need to be fully understood to achieve efficient and safe drug delivery. A complete understanding of the mechanisms for intracellular uptake, trafficking, and the fate of multifunctional MSNs in the body would be highly desirable. Up to now only a few *in vivo* studies of the pharmacokinetics of multifunctional MSNs including biodistribution, biodegradation, and excretion and clearance have been performed and additional work in this area is clearly needed.[99, 238-241] Additional functional groups, such as PEG chains, on the external surface of MSNs seem to be important for achieving the EPR effect and were shown to decrease the clearance through the RES.[99, 105] Selected strategies and model systems are needed to gain insights to such complex processes before reaching the stage of clinical trials. Comprehensive reviews address the state of the art for preclinical studies.[217, 237] Here, model systems for investigations on the way to clinical trials are discussed including chorioallantoic membrane, zebrafish embryo and mouse, amongst others.[242-244] Pharmacokinetics of nanomaterials is closely related to *in vivo* toxicity, biocompatibility and retention. The issue of potential toxicity to cells or organisms caused by nanocarriers seems to be strongly influenced by several particle properties including size, morphology and surface functionality.[64] Studies on the dissolution of silica nanoparticles concerning retention and clearance in the body showed that the silica was adsorbed or excreted in the urine in the form of silicic acid or organic silica species.[99] For future applications of multifunctional MSNs as drug delivery devices and to pave the way to clinical trials, these nanocarriers could be designed with two very different operating modes in mind. One approach would pursue the design of autonomous drug delivery vehicles, which can perform their tasks as a response to stimuli already present in the organism, including receptors on cell and tissue surfaces, changes of pH and redox potential in endosomes (for opening gate functions), the presence of

enzymes, and autonomous endosomal escape. Reversible opening and closing methods should also be developed further, because it was shown that MSNs can also be exocytosed from cells.[245] Successful re-sealing of the MSNs could efficiently hinder further drug release after leaving the cell or tissue to prevent unintended distribution of the drug. The other approach would rely on the use of external triggers (in combination with internal stimuli) to spatially control the drug release behavior, for example to focus the release to a certain area of tissue or a certain time period. Light activation with red or near infrared light, two-photon activation (to enhance tissue penetration), ultrasound, and local heating by different means such as RF absorption all present intriguing opportunities for future research. External stimuli for endosomal escape and controlled cargo release are also excellent tools for mechanistic studies in cell cultures, because they allow control over time and location of the initial release. Finally, recent studies focus on the ultimate combination of diagnostic and therapeutic capabilities in the multifunctional mesoporous nanoparticles, such that the nanocarrier uses diagnostic information to control or tune its therapeutic actions. One such approach could be the detection of the presence of multiple receptors indicating specific target tissue, where the logical combination of this information leads to release of drug only at this location, another one the detection of several enzymes that together constitute the signature of a target tissue. The future is bright for multifunctional mesoporous nanoparticles in diagnostics and therapy.

1.5 References

[1] M. Liong, J. Lu, M. Kovochich, T. Xia, S. G. Ruehm, A. E. Nel, F. Tamanoi, J. I. Zink, *ACS Nano* **2008**, *2*, 889.

[2] J. E. Lee, N. Lee, T. Kim, J. Kim, T. Hyeon, *Acc. Chem. Res.* **2011**, *44*, 893.

[3] I. I. Slowing, B. G. Trewyn, S. Giri, V. S. Y. Lin, *Adv. Funct. Mater.* **2007**, *17*, 1225.

[4] J. Liu, C. Li, F. Li, *J. Mater. Chem.* **2011**, *21*, 7175.

[5] B. F. G. Johnson, *Top. Catal.* **2003**, *24*, 147.

[6] A. Popat, S. B. Hartono, F. Stahr, J. Liu, S. Z. Qiao, G. Q. Lu, *Nanoscale* **2011**, *3*, 2801.

[7] K. Ariga, Q. Ji, T. Mori, M. Naito, Y. Yamauchi, H. Abe, J. P. Hill, *Chem. Soc. Rev.* **2013**, *42*, 6322.

[8] A. J. Salinas, P. Esbrit, M. Vallet-Regi, *Biomater. Sci.* **2013**, *1*, 40.

[9] N. Ehlert, P. P. Mueller, M. Stieve, T. Lenarz, P. Behrens, *Chem. Soc. Rev.* **2013**, *42*, 3847.

[10] C. Vitale-Brovarone, F. Baino, M. Miola, R. Mortera, B. Onida, E. Verne, *J. Mater. Sci. Mater. Med.* **2009**, *20*, 809.

[11] Z. X. Li, J. C. Barnes, A. Bosoy, J. F. Stoddart, J. I. Zink, *Chem. Soc. Rev.* **2012**, *41*, 2590.

[12] J. L. Vivero-Escoto, I. I. Slowing, B. G. Trewyn, V. S. Y. Lin, *Small* **2010**, *6*, 1952.

[13] P. P. Yang, S. L. Gai, J. Lin, *Chem. Soc. Rev.* **2012**, *41*, 3679.

[14] Y. J. Wang, A. M. Yu, F. Caruso, *Angew. Chem. Int. Ed.* **2005**, *44*, 2888.

[15] Y. J. Wang, Y. Yan, J. W. Cui, L. Hosta-Rigau, J. K. Heath, E. C. Nice, F. Caruso, *Adv. Mater.* **2010**, *22*, 4293.

[16] J. W. Cui, Y. Yan, Y. J. Wang, F. Caruso, *Adv. Funct. Mater.* **2012**, *22*, 4718.

[17] J. S. Beck, J. C. Vartuli, W. J. Roth, M. E. Leonowicz, C. T. Kresge, K. D. Schmitt, C. T. W. Chu, D. H. Olson, E. W. Sheppard, S. B. McCullen, J. B. Higgins, J. L. Schlenker, *J. Am. Chem. Soc.* **1992**, *114*, 10834.

[18] C. T. Kresge, M. E. Leonowicz, W. J. Roth, J. C. Vartuli, J. S. Beck, *Nature* **1992**, *359*, 710.

[19] M. Vallet-Regi, A. Ramila, R. P. del Real, J. Perez-Pariente, *Chem. Mater.* **2001**, *13*, 308.

[20] S. H. Wu, Y. Hung, C. Y. Mou, *Chem. Commun.* **2011**, *47*, 9972.

[21] K. Möller, J. Kobler, T. Bein, *Adv. Funct. Mater.* **2007**, *17*, 605.

[22] V. Cauda, A. Schlossbauer, J. Kecht, A. Zürner, T. Bein, *J. Am. Chem. Soc.* **2009**, *131*, 11361.

[23] V. Cauda, C. Argyo, T. Bein, *J. Mater. Chem.* **2010**, *20*, 8693.

[24] V. Cauda, H. Engelke, A. Sauer, D. Arcizet, C. Bräuchle, J. Rädler, T. Bein, *Nano Lett.* **2010**, *10*, 2484.

[25] A. Schlossbauer, J. Kecht, T. Bein, *Angew. Chem. Int. Ed.* **2009**, *48*, 3092.

[26] V. Cauda, C. Argyo, A. Schlossbauer, T. Bein, *J. Mater. Chem.* **2010**, *20*, 4305.

[27] S. A. Mackowiak, A. Schmidt, V. Weiss, C. Argyo, C. von Schirnding, T. Bein, C. Bräuchle, *Nano Lett.* **2013**, *13*, 2576.

[28] D. Peer, J. M. Karp, S. Hong, O. C. FaroKhzad, R. Margalit, R. Langer, *Nat. Nanotechnol.* **2007**, *2*, 751.

[29] R. A. Petros, J. M. DeSimone, *Nat. Rev. Drug Discovery* **2010**, *9*, 615.

[30] V. Wagner, A. Dullaart, A. K. Bock, A. Zweck, *Nat. Nanotechnol.* **2006**, *24*, 1211.

[31] S. H. Wu, C. Y. Mou, H. P. Lin, *Chem. Soc. Rev.* **2013**, *42*, 3862.

[32] Y. S. Lin, K. R. Hurley, C. L. Haynes, *J. Phys. Chem. Lett.* **2012**, *3*, 364.

[33] I. I. Slowing, J. L. Vivero-Escoto, B. G. Trewyn, V. S. Y. Lin, *J. Mater. Chem.* **2010**, *20*, 7924.

[34] F. Q. Tang, L. L. Li, D. Chen, *Adv. Mater.* **2012**, *24*, 1504.

[35] F. Hoffmann, M. Cornelius, J. Morell, M. Fröba, *Angew. Chem. Int. Ed.* **2006**, *45*, 3216.

[36] D. Y. Zhao, J. L. Feng, Q. S. Huo, N. Melosh, G. H. Fredrickson, B. F. Chmelka, G. D. Stucky, *Science* **1998**, *279*, 548.

[37] J. C. Vartuli, K. D. Schmitt, C. T. Kresge, W. J. Roth, M. E. Leonowicz, S. B. McCullen, S. D. Hellring, J. S. Beck, J. L. Schlenker, D. H. Olson, E. W. Sheppard, *Chem. Mater.* **1994**, *6*, 2317.

[38] P. T. Tanev, T. J. Pinnavaia, *Science* **1995**, *267*, 865.

[39] G. Herrier, J. L. Blin, B. L. Su, *Langmuir* **2001**, *17*, 4422.

[40] B. D. Chithrani, A. A. Ghazani, W. C. W. Chan, *Nano Lett.* **2006**, *6*, 662.

[41] C. E. Fowler, D. Khushalani, B. Lebeau, S. Mann, *Adv. Mater.* **2001**, *13*, 649.

[42] Y. F. Lu, H. Y. Fan, A. Stump, T. L. Ward, T. Rieker, C. J. Brinker, *Nature* **1999**, *398*, 223.

[43] K. Suzuki, K. Ikari, H. Imai, *J. Am. Chem. Soc.* **2004**, *126*, 462.

[44] M. Grun, I. Lauer, K. K. Unger, *Adv. Mater.* **1997**, *9*, 254.

[45] C. J. Brinker, Y. F. Lu, A. Sellinger, H. Y. Fan, *Adv. Mater.* **1999**, *11*, 579.

[46] S. Huh, J. W. Wiench, J. C. Yoo, M. Pruski, V. S. Y. Lin, *Chem. Mater.* **2003**, *15*, 4247.

[47] J. Lu, M. Liong, J. I. Zink, F. Tamanoi, *Small* **2007**, *3*, 1341.

[48] A. Popat, J. Liu, G. Q. Lu, S. Z. Qiao, *J. Mater. Chem.* **2012**, *22*, 11173.

[49] Q. Cai, Z. S. Luo, W. Q. Pang, Y. W. Fan, X. H. Chen, F. Z. Cui, *Chem. Mater.* **2001**, *13*, 258.

[50] Y. S. Lin, N. Abadeer, K. R. Hurley, C. L. Haynes, *J. Am. Chem. Soc.* **2011**, *133*, 20444.

[51] K. Ma, U. Werner-Zwanziger, J. Zwanziger, U. Wiesner, *Chem. Mater.* **2013**, *25*, 677.

[52] J. Kobler, K. Möller, T. Bein, *ACS Nano* **2008**, *2*, 791.

[53] M. H. Kim, H. K. Na, Y. K. Kim, S. R. Ryoo, H. S. Cho, K. E. Lee, H. Jeon, R. Ryoo, D. H. Min, *ACS Nano* **2011**, *5*, 3568.

[54] K. Zhang, L.-L. Xu, J.-G. Jiang, N. Calin, K.-F. Lam, S.-J. Zhang, H.-H. Wu, G.-D. Wu, B. Albela, L. Bonneviot, P. Wu, *J. Am. Chem. Soc.* **2013**, *135*, 2427.

[55] X. Sun, Y. Zhao, V. S. Y. Lin, I. I. Slowing, B. G. Trewyn, *J. Am. Chem. Soc.* **2011**, *133*, 18554.

[56] H. Vallhov, N. Kupferschmidt, S. Gabrielsson, S. Paulie, M. Stromme, A. E. Garcia-Bennett, A. Scheynius, *Small* **2012**, *8*, 2116.

[57] V. Cauda, C. Argyo, D. G. Piercey, T. Bein, *J. Am. Chem. Soc.* **2011**, *133*, 6484.

[58] A. Stein, B. J. Melde, R. C. Schroden, *Adv. Mater.* **2000**, *12*, 1403.

[59] D. M. Ford, E. E. Simanek, D. F. Shantz, *Nanotechnology* **2005**, *16*, S458.

[60] C. Park, K. Oh, S. C. Lee, C. Kim, *Angew. Chem. Int. Ed.* **2007**, *46*, 1455.

[61] Y. S. Lin, C. P. Tsai, H. Y. Huang, C. T. Kuo, Y. Hung, D. M. Huang, Y. C. Chen, C. Y. Mou, *Chem. Mater.* **2005**, *17*, 4570.

[62] C.-Y. Lai, B. G. Trewyn, D. M. Jeftinija, K. Jeftinija, S. Xu, S. Jeftinija, V. S. Y. Lin, *J. Am. Chem. Soc.* **2003**, *125*, 4451.

[63] I. Slowing, B. G. Trewyn, V. S. Y. Lin, *J. Am. Chem. Soc.* **2006**, *128*, 14792.

[64] X. Huang, L. Li, T. Liu, N. Hao, H. Liu, D. Chen, F. Tang, *ACS Nano* **2011**, *5*, 5390.

[65] M. Manzano, V. Aina, C. O. Arean, F. Balas, V. Cauda, M. Colilla, M. R. Delgado, M. Vallet-Regi, *Chem. Eng. J.* **2008**, *137*, 30.

[66] J. M. Rosenholm, M. Linden, *J. Control. Rel.* **2008**, *128*, 157.

[67] Q. Yang, S. H. Wang, P. W. Fan, L. F. Wang, Y. Di, K. F. Lin, F. S. Xiao, *Chem. Mater.* **2005**, *17*, 5999.

[68] K. Yamamoto, T. Tatsumi, *Chem. Lett.* **2000**, 624.

[69] J. E. Lim, C. B. Shim, J. M. Kim, B. Y. Lee, J. E. Yie, *Angew. Chem. Int. Ed.* **2004**, *43*, 3839.

[70] J. Kecht, T. Bein, *Langmuir* **2008**, *24*, 14209.

[71] J. Kecht, A. Schlossbauer, T. Bein, *Chem. Mater.* **2008**, *20*, 7207.

[72] A. M. Sauer, A. Schlossbauer, N. Ruthardt, V. Cauda, T. Bein, C. Bräuchle, *Nano Lett.* **2010**, *10*, 3684.

[73] S. Giri, B. G. Trewyn, M. P. Stellmaker, V. S. Y. Lin, *Angew. Chem. Int. Ed.* **2005**, *44*, 5038.

[74] L. Chen, Y. Wen, B. Su, J. Di, Y. Song, L. Jiang, *J. Mater. Chem.* **2011**, *21*, 13811.

[75] A. Bernardos, L. Mondragon, E. Aznar, M. D. Marcos, R. Martinez-Manez, F. Sancenon, J. Soto, J. M. Barat, E. Perez-Paya, C. Guillem, P. Amoros, *ACS Nano* **2010**, *4*, 6353.

[76] Q. Gan, X. Lu, Y. Yuan, J. Qian, H. Zhou, X. Lu, J. Shi, C. Liu, *Biomaterials* **2011**, *32*, 1932.

[77] R. Liu, P. Liao, J. Liu, P. Feng, *Langmuir* **2011**, *27*, 3095.

[78] X. Yang, X. Liu, Z. Liu, F. Pu, J. Ren, X. Qu, *Adv. Mater.* **2012**, *24*, 2890.

[79] L.-S. Wang, L.-C. Wu, S.-Y. Lu, L.-L. Chang, I. T. Teng, C.-M. Yang, J.-A. A. Ho, *ACS Nano* **2010**, *4*, 4371.

[80] G. Nordlund, J. B. S. Ng, L. Bergstrom, P. Brzezinski, *ACS Nano* **2009**, *3*, 2639.

[81] J. Liu, X. Jiang, C. Ashley, C. J. Brinker, *J. Am. Chem. Soc.* **2009**, *131*, 7567.

[82] J. Liu, A. Stace-Naughton, X. Jiang, C. J. Brinker, *J. Am. Chem. Soc.* **2009**, *131*, 1354.

[83] C. E. Ashley, E. C. Carnes, K. E. Epler, D. P. Padilla, G. K. Phillips, R. E. Castillo, D. C. Wilkinson, B. S. Wilkinson, C. A. Burgard, R. M. Kalinich, J. L. Townson, B. Chackerian, C. L. Willman, D. S. Peabody, W. Wharton, C. J. Brinker, *ACS Nano* **2012**, *6*, 2174.

[84] C. E. Ashley, E. C. Carnes, G. K. Phillips, D. Padilla, P. N. Durfee, P. A. Brown, T. N. Hanna, J. W. Liu, B. Phillips, M. B. Carter, N. J. Carroll, X. M. Jiang, D. R. Dunphy, C. L. Willman, D. N. Petsev, D. G. Evans, A. N. Parikh, B. Chackerian, W. Wharton, D. S. Peabody, C. J. Brinker, *Nat. Mater.* **2011**, *10*, 389.

[85] X. Hu, X. Hao, Y. Wu, J. Zhang, X. Zhang, P. C. Wang, G. Zou, X.-J. Liang, *J. Mater. Chem. B* **2013**, *1*, 1109.

[86] E. Climent, A. Bernardos, R. Martinez-Manez, A. Maquieira, M. Dolores Marcos, N. Pastor-Navarro, R. Puchades, F. Sancenon, J. Soto, P. Amoros, *J. Am. Chem. Soc.* **2009**, *131*, 14075.

[87] N. Z. Knezevic, B. G. Trewyn, V. S. Y. Lin, *Chem. Commun.* **2011**, *47*, 2817.

[88] J. Mendez, A. Monteagudo, K. Griebenow, *Bioconjugate Chem.* **2012**, *23*, 698.

[89] W. Fang, J. Yang, J. Gong, N. Zheng, *Adv. Funct. Mater.* **2012**, *22*, 842.

[90] J. Lu, E. Choi, F. Tamanoi, J. I. Zink, *Small* **2008**, *4*, 421.

[91] A. Schlossbauer, S. Warncke, P. M. E. Gramlich, J. Kecht, A. Manetto, T. Carell, T. Bein, *Angew. Chem. Int. Ed.* **2010**, *49*, 4734.

[92] Y.-Z. You, K. K. Kalebaila, S. L. Brock, D. Oupicky, *Chem. Mater.* **2008**, *20*, 3354.

[93] R. Liu, X. Zhao, T. Wu, P. Feng, *J. Am. Chem. Soc.* **2008**, *130*, 14418.

[94] C. Gao, H. Zheng, L. Xing, M. Shu, S. Che, *Chem. Mater.* **2010**, *22*, 5437.

[95] A. M. Mumin, J. W. Barrett, G. A. Dekaban, J. Zhang, *J. Colloid Interface Sci.* **2011**, *353*, 156.

[96] H. Meng, M. Liong, T. Xia, Z. Li, Z. Ji, J. I. Zink, A. E. Nel, *ACS Nano* **2010**, *4*, 4539.

[97] Q. He, J. Shi, M. Zhu, Y. Chen, F. Chen, *Microporous and Mesoporous Mater.* **2010**, *131*, 314.

[98] V. Cauda, A. Schlossbauer, T. Bein, *Microporous and Mesoporous Mater.* **2010**, *132*, 60.

[99] Q. He, Z. Zhang, F. Gao, Y. Li, J. Shi, *Small* **2011**, *7*, 271.

[100] Y.-S. Lin, C. L. Haynes, *J. Am. Chem. Soc.* **2010**, *132*, 4834.

[101] A. Yildirim, E. Ozgur, M. Bayindir, *J. Mater. Chem. B* **2013**, *1*, 1909.

[102] C. Argyo, V. Cauda, H. Engelke, J. Rädler, G. Bein, T. Bein, *Chem. - Eur. J.* **2012**, *18*, 428.

[103] A. E. Nel, L. Maedler, D. Velegol, T. Xia, E. M. V. Hoek, P. Somasundaran, F. Klaessig, V. Castranova, M. Thompson, *Nat. Mater.* **2009**, *8*, 543.

[104] M. Ferrari, *Nat. Rev. Cancer* **2005**, *5*, 161.

[105] H. Meng, M. Xue, T. Xia, Z. Ji, D. Y. Tarn, J. I. Zink, A. E. Nel, *ACS Nano* **2011**, *5*, 4131.

[106] J. E. Lee, N. Lee, H. Kim, J. Kim, S. H. Choi, J. H. Kim, T. Kim, I. C. Song, S. P. Park, W. K. Moon, T. Hyeon, *J. Am. Chem. Soc.* **2010**, *132*, 552.

[107] H. Maeda, J. Wu, T. Sawa, Y. Matsumura, K. Hori, *J. Control. Rel.* **2000**, *65*, 271.

[108] D. Tarn, C. E. Ashley, M. Xue, E. C. Carnes, J. I. Zink, C. J. Brinker, *Acc. Chem. Res.* **2013**, *46*, 792.

[109] M. M. Gottesman, T. Fojo, S. E. Bates, *Nat. Rev. Cancer* **2002**, *2*, 48.

[110] K. Cheng, S. R. Blumen, M. B. MacPherson, J. L. Steinbacher, B. T. Mossman, C. C. Landry, *ACS Appl. Mater. Interf.* **2010**, *2*, 2489.

[111] Z. Deng, Z. Zhen, X. Hu, S. Wu, Z. Xu, P. K. Chu, *Biomaterials* **2011**, *32*, 4976.

[112] L.-L. Li, Q. Yin, J. Cheng, Y. Lu, *Adv. Healthcare Mater.* **2012**, *1*, 567.

[113] J. M. Rosenholm, A. Meinander, E. Peuhu, R. Niemi, J. E. Eriksson, C. Sahlgren, M. Linden, *ACS Nano* **2009**, *3*, 197.

[114] Q. Zhang, F. Liu, N. Kim Truc, X. Ma, X. Wang, B. Xing, Y. Zhao, *Adv. Funct. Mater.* **2012**, *22*, 5144.

[115] J. Pang, L. Zhao, L. Zhang, Z. Li, Y. Luan, *J. Colloid Interface Sci.* **2013**, *395*, 31.

[116] D. Chen, M. Jiang, N. Li, H. Gu, Q. Xu, J. Ge, X. Xia, J. Lu, *J. Mater. Chem.* **2010**, *20*, 6422.

[117] F. Wang, X. Chen, Z. Zhao, S. Tang, X. Huang, C. Lin, C. Cai, N. Zheng, *J. Mater. Chem.* **2011**, *21*, 11244.

[118] V. Mamaeva, J. M. Rosenholm, L. T. Bate-Eya, L. Bergman, E. Peuhu, A. Duchanoy, L. E. Fortelius, S. Landor, D. M. Toivola, M. Linden, C. Sahlgren, *Mol. Ther.* **2011**, *19*, 1538.

[119] C. Zhou, A. Kunzmann, M. Rakonjac, B. Fadeel, A. Garcia-Bennett, *Nanomedicine* **2012**, *7*, 327.

[120] J. Fan, G. Fang, X. Wang, F. Zeng, Y. Xiang, S. Wu, *Nanotechnology* **2011**, *22*.

[121] Y. Zhu, Y. Fang, S. Kaskel, *J. Phys. Chem. C* **2010**, *114*, 16382.

[122] I. J. Fang, I. I. Slowing, K. C. W. Wu, V. S. Y. Lin, B. G. Trewyn, *Chem. - Eur. J.* **2012**, *18*, 7787.

[123] S.-H. Cheng, C.-H. Lee, M.-C. Chen, J. S. Souris, F.-G. Tseng, C.-S. Yang, C.-Y. Mou, C.-T. Chen, L.-W. Lo, *J. Mater. Chem.* **2010**, *20*, 6149.

[124] J. Zhang, Z.-F. Yuan, Y. Wang, W.-H. Chen, G.-F. Luo, S.-X. Cheng, R.-X. Zhuo, X.-Z. Zhang, *J. Am. Chem. Soc.* **2013**, *135*, 5068.

[125] C.-P. Tsai, C.-Y. Chen, Y. Hung, F.-H. Chang, C.-Y. Mou, *J. Mater. Chem.* **2009**, *19*, 5737.

[126] D. Brevet, M. Gary-Bobo, L. Raehm, S. Richeter, O. Hocine, K. Amro, B. Loock, P. Couleaud, C. Frochot, A. Morere, P. Maillard, M. Garcia, J.-O. Durand, *Chem. Commun.* **2009**, 1475.

[127] M. Gary-Bobo, O. Hocine, D. Brevet, M. Maynadier, L. Raehm, S. Richeter, V. Charasson, B. Loock, A. Morere, P. Maillard, M. Garcia, J.-O. Durand, *Inter. J. Pharm.* **2012**, *423*, 509.

[128] Z. Chen, Z. Li, Y. Lin, M. Yin, J. Ren, X. Qu, *Chem. - Eur. J.* **2013**, *19*, 1778.

[129] J. L. Vivero-Escoto, K. M. L. Taylor-Pashow, R. C. Huxford, J. Della Rocca, C. Okoruwa, H. An, W. Lin, W. Lin, *Small* **2011**, *7*, 3519.

[130] S. Veeranarayanan, A. C. Poulose, M. S. Mohamed, S. H. Varghese, Y. Nagaoka, Y. Yoshida, T. Maekawa, D. S. Kumar, *Small* **2012**, *8*, 3476.

[131] S. D. Conner, S. L. Schmid, *Nature* **2003**, *422*, 37.

[132] H. Meng, S. Yang, Z. Li, T. Xia, J. Chen, Z. Ji, H. Zhang, X. Wang, S. Lin, C. Huang, Z. H. Zhou, J. I. Zink, A. E. Nel, *ACS Nano* **2011**, *5*, 4434.

[133] Z. Tao, B. B. Toms, J. Goodisman, T. Asefa, *Chem. Res. Toxicol.* **2009**, *22*, 1869.

[134] G. Begum, S. Singh, N. Rangaraj, G. Srinivas, R. K. Rana, *J. Mater. Chem.* **2010**, *20*, 8563.

[135] J. Yu, H. Zhao, L. Ye, H. Yang, S. Ku, N. Yang, N. Xiao, *J. Mater. Chem.* **2009**, *19*, 1265.

[136] J. Zhu, J. Tang, L. Zhao, X. Zhou, Y. Wang, C. Yu, *Small* **2010**, *6*, 276.

[137] T.-H. Chung, S.-H. Wu, M. Yao, C.-W. Lu, Y.-S. Lin, Y. Hung, C.-Y. Mou, Y.-C. Chen, D.-M. Huang, *Biomaterials* **2007**, *28*, 2959.

[138] W. Sun, N. Fang, B. G. Trewyn, M. Tsunoda, I. I. Slowing, V. S. Y. Lin, E. S. Yeung, *Anal. Bioanal. Chem.* **2008**, *391*, 2119.

[139] A. K. Varkouhi, M. Scholte, G. Storm, H. J. Haisma, *J. Control. Rel.* **2011**, *151*, 220.

[140] A. Schlossbauer, A. M. Sauer, V. Cauda, A. Schmidt, H. Engelke, U. Rothbauer, K. Zolghadr, H. Leonhardt, C. Bräuchle, T. Bein, *Adv. Healthcare Mater.* **2012**, *1*, 316.

[141] K. G. de Bruin, C. Fella, M. Ogris, E. Wagner, N. Ruthardt, C. Bräuchle, *J. Control. Rel.* **2008**, *130*, 175.

[142] J. P. Behr, *Chimia* **1997**, *51*, 34.

[143] O. Boussif, F. Lezoualch, M. A. Zanta, M. D. Mergny, D. Scherman, B. Demeneix, J. P. Behr, *Proc. Natl. Acad. Sci. U.S.A.* **1995**, *92*, 7297.

[144] A. Akinc, M. Thomas, A. M. Klibanov, R. Langer, *J. Gene Med.* **2005**, *7*, 657.

[145] J. Gruenberg, F. R. Maxfield, *Curr. Opin. Cell Biol.* **1995**, *7*, 552.

[146] J. Suh, H. J. Paik, B. K. Hwang, *Bioorg. Chem.* **1994**, *22*, 318.

[147] S. Oliveira, I. van Rooy, O. Kranenburg, G. Storm, R. M. Schiffelers, *Inter. J. Pharm.* **2007**, *331*, 211.

[148] E. S. Lee, H. J. Shin, K. Na, Y. H. Bae, *J. Control. Rel.* **2003**, *90*, 363.

[149] K. Yamada, N. Kamada, M. Odomi, N. Okada, T. Nabe, T. Fujita, S. Kohno, A. Yamamoto, *Inter. J. Pharm.* **2005**, *293*, 63.

[150] T. Kakudo, S. Chaki, S. Futaki, I. Nakase, K. Akaji, T. Kawakami, K. Maruyama, H. Kamiya, H. Harashima, *Biochemistry* **2004**, *43*, 5618.

[151] D. He, X. He, K. Wang, J. Cao, Y. Zhao, *Langmuir* **2012**, *28*, 4003.

[152] D. P. Ferris, Y.-L. Zhao, N. M. Khashab, H. A. Khatib, J. F. Stoddart, J. I. Zink, *J. Am. Chem. Soc.* **2009**, *131*, 1686.

[153] J. Croissant, J. I. Zink, *J. Am. Chem. Soc.* **2012**, *134*, 7628.

[154] N. Z. Knezevic, B. G. Trewyn, V. S. Y. Lin, *Chem. - Eur. J.* **2011**, *17*, 3338.

[155] J. Lai, X. Mu, Y. Xu, X. Wu, C. Wu, C. Li, J. Chen, Y. Zhao, *Chem. Commun.* **2010**, *46*, 7370.

[156] R. Liu, Y. Zhang, P. Feng, *J. Am. Chem. Soc.* **2009**, *131*, 15128.

[157] M. P. Dobay, A. Schmidt, E. Mendoza, T. Bein, J. O. Rädler, *Nano Lett.* **2013**, *13*, 1047.

[158] E. Ruiz-Hernandez, A. Baeza, M. Vallet-Regi, *ACS Nano* **2011**, *5*, 1259.

[159] E. Aznar, M. Dolores Marcos, R. Martinez-Manez, F. Sancenon, J. Soto, P. Amoros, C. Guillem, *J. Am. Chem. Soc.* **2009**, *131*, 6833.

[160] A. Baeza, E. Guisasola, E. Ruiz-Hernandez, M. Vallet-Regi, *Chem. Mater.* **2012**, *24*, 517.

[161] Y. Wen, L. Xu, C. Li, H. Du, L. Chen, B. Su, Z. Zhang, X. Zhang, Y. Song, *Chem. Commun.* **2012**, *48*, 8410.

[162] E. Aznar, L. Mondragon, J. V. Ros-Lis, F. Sancenon, M. Dolores Marcos, R. Martinez-Manez, J. Soto, E. Perez-Paya, P. Amoros, *Angew. Chem. Int. Ed.* **2011**, *50*, 11172.

[163] Y. Zhu, S. Kaskel, T. Ikoma, N. Hanagata, *Microporous and Mesoporous Mater.* **2009**, *123*, 107.

[164] D. He, X. He, K. Wang, M. Chen, J. Cao, Y. Zhao, *J. Mater. Chem.* **2012**, *22*, 14715.

[165] E. Climent, R. Martinez-Manez, F. Sancenon, M. D. Marcos, J. Soto, A. Maquieira, P. Amoros, *Angew. Chem. Int. Ed.* **2010**, *49*, 7281.

[166] J. Geng, M. Li, L. Wu, C. Chen, X. Qu, *Adv. Healthcare Mater.* **2012**, *1*, 332.

[167] Y. L. Choi, J. Jaworski, M. L. Seo, S. J. Lee, J. H. Jung, *J. Mater. Chem.* **2011**, *21*, 7882.

[168] R. Liu, Y. Zhang, X. Zhao, A. Agarwal, L. J. Mueller, P. Feng, *J. Am. Chem. Soc.* **2010**, *132*, 1500.

[169] Y.-L. Zhao, Z. Li, S. Kabehie, Y. Y. Botros, J. F. Stoddart, J. I. Zink, *J. Am. Chem. Soc.* **2010**, *132*, 13016.

[170] H. Meng, M. Xue, T. Xia, Y.-L. Zhao, F. Tamanoi, J. F. Stoddart, J. I. Zink, A. E. Nel, *J. Am. Chem. Soc.* **2010**, *132*, 12690.

[171] L. Du, S. Liao, H. A. Khatib, J. F. Stoddart, J. I. Zink, *J. Am. Chem. Soc.* **2009**, *131*, 15136.

[172] C. Wang, Z. Li, D. Cao, Y.-L. Zhao, J. W. Gaines, O. A. Bozdemir, M. W. Ambrogio, M. Frasconi, Y. Y. Botros, J. I. Zink, J. F. Stoddart, *Angew. Chem. Int. Ed.* **2012**, *51*, 5460.

[173] N. M. Khashab, M. E. Belowich, A. Trabolsi, D. C. Friedman, C. Valente, Y. Lau, H. A. Khatib, J. I. Zink, J. F. Stoddart, *Chem. Commun.* **2009**, 5371.

[174] S. Angelos, N. M. Khashab, Y.-W. Yang, A. Trabolsi, H. A. Khatib, J. F. Stoddart, J. I. Zink, *J. Am. Chem. Soc.* **2009**, *131*, 12912.

[175] J. Liu, X. Du, *J. Mater. Chem.* **2010**, *20*, 3642.

[176] E. Aznar, C. Coll, M. Dolores Marcos, R. Martinez-Manez, M. Sancenon, J. Soto, P. Amoros, J. Cano, E. Ruiz, *Chem. - Eur. J.* **2009**, *15*, 6877.

[177] Q. Zheng, Y. Hao, P. Ye, L. Guo, H. Wu, Q. Guo, J. Jiang, F. Fu, G. Chen, *J. Mater. Chem. B* **2013**, *1*, 1644.

[178] F. Yu, X. Tang, M. Pei, *Microporous and Mesoporous Mater.* **2013**, *173*, 64.

[179] L. Sun, X. Zhang, C. Zheng, Z. Wu, C. Li, *J. Phys. Chem. B* **2013**, *117*, 3852.

[180] Y. L. Choi, J. H. Lee, J. Jaworski, J. H. Jung, *J. Mater. Chem.* **2012**, *22*, 9455.

[181] B. Chang, D. Chen, Y. Wang, Y. Chen, Y. Jiao, X. Sha, W. Yang, *Chem. Mater.* **2013**, *25*, 574.

[182] L. Xing, H. Zheng, Y. Cao, S. Che, *Adv. Mater.* **2012**, *24*, 6433.

[183] F. Chen, Y. Zhu, *Microporous and Mesoporous Mater.* **2012**, *150*, 83.

[184] A. Schlossbauer, C. Dohmen, D. Schaffert, E. Wagner, T. Bein, *Angew. Chem. Int. Ed.* **2011**, *50*, 6828.

[185] Y. Ma, L. Zhou, H. Zheng, L. Xing, C. Li, J. Cui, S. Che, *J. Mater. Chem.* **2011**, *21*, 9483.

[186] Q. He, Y. Gao, L. Zhang, Z. Zhang, F. Gao, X. Ji, Y. Li, J. Shi, *Biomaterials* **2011**, *32*, 7711.

[187] S.-H. Cheng, W.-N. Liao, L.-M. Chen, C.-H. Lee, *J. Mater. Chem.* **2011**, *21*, 7130.

[188] R. Guillet-Nicolas, A. Popat, J.-L. Bridot, G. Monteith, S. Z. Qiao, F. Kleitz, *Angew. Chem. Int. Ed.* **2013**, *52*, 2318.

[189] M. Xue, G. H. Findenegg, *Langmuir* **2012**, *28*, 17578.

[190] N. Mas, A. Agostini, L. Mondragon, A. Bernardos, F. Sancenon, M. Dolores Marcos, R. Martinez-Manez, A. M. Costero, S. Gil, M. Merino-Sanjuan, P. Amoros, M. Orzaez, E. Perez-Paya, *Chem. - Eur. J.* **2013**, *19*, 1346.

[191] J. Liu, X. Du, X. Zhang, *Chem. - Eur. J.* **2011**, *17*, 810.

[192] K. Patel, S. Angelos, W. R. Dichtel, A. Coskun, Y.-W. Yang, J. I. Zink, J. F. Stoddart, *J. Am. Chem. Soc.* **2008**, *130*, 2382.

[193] A. Agostini, L. Mondragon, L. Pascual, E. Aznar, C. Coll, R. Martinez-Manez, F. Sancenon, J. Soto, M. Dolores Marcos, P. Amoros, A. M. Costero, M. Parra, S. Gil, *Langmuir* **2012**, *28*, 14766.

[194] C. Coll, L. Mondragon, R. Martinez-Manez, F. Sancenon, M. Dolores Marcos, J. Soto, P. Amoros, E. Perez-Paya, *Angew. Chem. Int. Ed.* **2011**, *50*, 2138.

[195] A. Bernardos, E. Aznar, M. Dolores Marcos, R. Martinez-Manez, F. Sancenon, J. Soto, J. Manuel Barat, P. Amoros, *Angew. Chem. Int. Ed.* **2009**, *48*, 5884.

[196] X. Ma, K. T. Nguyen, P. Borah, C. Y. Ang, Y. Zhao, *Adv. Healthcare Mater.* **2012**, *1*, 690.

[197] Z. Luo, K. Cai, Y. Hu, L. Zhao, P. Liu, L. Duan, W. Yang, *Angew. Chem. Int. Ed.* **2011**, *50*, 640.

[198] X. He, Y. Zhao, D. He, K. Wang, F. Xu, J. Tang, *Langmuir* **2012**, *28*, 12909.

[199] C.-L. Zhu, C.-H. Lu, X.-Y. Song, H.-H. Yang, X.-R. Wang, *J. Am. Chem. Soc.* **2011**, *133*, 1278.

[200] V. C. Özalp, T. Schäfer, *Chem. - Eur. J.* **2011**, *17*, 9893.

[201] Y. Zhao, B. G. Trewyn, I. I. Slowing, V. S. Y. Lin, *J. Am. Chem. Soc.* **2009**, *131*, 8398.

[202] W. Zhao, H. Zhang, Q. He, Y. Li, J. Gu, L. Li, H. Li, J. Shi, *Chem. Commun.* **2011**, *47*, 9459.

[203] L. Jia, J. Shen, Z. Li, D. Zhang, Q. Zhang, G. Liu, D. Zheng, X. Tian, *Int. J. Pharm.* **2013**, *445*, 12.

[204] H.-K. Na, M.-H. Kim, K. Park, S.-R. Ryoo, K. E. Lee, H. Jeon, R. Ryoo, C. Hyeon, D.-H. Min, *Small* **2012**, *8*, 1752.

[205] A. Agostini, L. Mondragon, A. Bernardos, R. Martinez-Manez, M. Dolores Marcos, F. Sancenon, J. Soto, A. Costero, C. Manguan-Garcia, R. Perona, M. Moreno-Torres, R. Aparicio-Sanchis, J. Ramon Murguia, *Angew. Chem. Int. Ed.* **2012**, *51*, 10556.

[206] P. Changenet-Barret, T. Gustavsson, D. Markovitsi, I. Manet, S. Monti, *Phys. Chem. Chem. Phys.* **2013**, *15*, 2937.

[207] Y. Chen, H. Chen, D. Zeng, Y. Tian, F. Chen, J. Feng, J. Shi, *ACS Nano* **2010**, *4*, 6001.

[208] T. Wang, F. Chai, Q. Fu, L. Zhang, H. Liu, L. Li, Y. Liao, Z. Su, C. Wang, B. Duan, D. Ren, *J. Mater. Chem.* **2011**, *21*, 5299.

[209] Y. Gao, Y. Chen, X. Ji, X. He, Q. Yin, Z. Zhang, J. Shi, Y. Li, *ACS Nano* **2011**, *5*, 9788.

[210] Y. Chen, Q. Yin, X. Ji, S. Zhang, H. Chen, Y. Zheng, Y. Sun, H. Qu, Z. Wang, Y. Li, X. Wang, K. Zhang, L. Zhang, J. Shi, *Biomaterials* **2012**, *33*, 7126.

[211] E. C. Dengler, J. Liu, A. Kerwin, S. Torres, C. M. Olcott, B. N. Bowman, L. Armijo, K. Gentry, J. Wilkerson, J. Wallace, X. Jiang, E. C. Carnes, C. J. Brinker, E. D. Milligan, *J. Control. Rel.* **2013**, *168*, 209.

[212] C. Hom, J. Lu, M. Liong, H. Luo, Z. Li, J. I. Zink, F. Tamanoi, *Small* **2010**, *6*, 1185.

[213] S.-H. Wu, Y.-S. Lin, Y. Hung, Y.-H. Chou, Y.-H. Hsu, C. Chang, C.-Y. Mou, *ChemBioChem* **2008**, *9*, 53.

[214] H. Meng, W. X. Mai, H. Zhang, M. Xue, T. Xia, S. Lin, X. Wang, Y. Zhao, Z. Ji, J. I. Zink, A. E. Nel, *ACS Nano* **2013**, *7*, 994.

[215] L. Li, F. Tang, H. Liu, T. Liu, N. Hao, D. Chen, X. Teng, J. He, *ACS Nano* **2010**, *4*, 6874.

[216] F. Sharif, F. Porta, A. H. Meijer, A. Kros, M. K. Richardson, *Int. J. Nanomed.* **2012**, *7*, 1875.

[217] Y. Chen, H. Chen, J. Shi, *Adv. Mater.* **2013**, *25*, 3144.

[218] J. L. Vivero-Escoto, R. C. Huxford-Phillips, W. Lin, *Chem. Soc. Rev.* **2012**, *41*, 2673.

[219] T. L. Doane, C. Burda, *Chem. Soc. Rev.* **2012**, *41*, 2885.

[220] G. Bardi, M. A. Malvindi, L. Gherardini, M. Costa, P. P. Pompa, R. Cingolani, T. Pizzorusso, *Biomaterials* **2010**, *31*, 6555.

[221] B. Rühle, M. Davies, T. Lebold, C. Bräuchle, T. Bein, *ACS Nano* **2012**, *6*, 1948.

[222] A. Zürner, J. Kirstein, M. Döblinger, C. Bräuchle, T. Bein, *Nature* **2007**, *450*, 705.

[223] J. Kirstein, B. Platschek, C. Jung, R. Brown, T. Bein, C. Bräuchle, *Nat. Mater.* **2007**, *6*, 303.

[224] T. Lebold, C. Jung, J. Michaelis, C. Bräuchle, *Nano Lett.* **2009**, *9*, 2877.

[225] T. Lebold, A. Schlossbauer, K. Schneider, L. Schermelleh, H. Leonhardt, T. Bein, C. Bräuchle, *Adv. Funct. Mater.* **2012**, *22*, 106.

[226] F. Feil, V. Cauda, T. Bein, C. Bräuchle, *Nano Lett.* **2012**, *12*, 1354.

[227] J. Lai, B. P. Shah, E. Garfunkel, K.-B. Lee, *ACS Nano* **2013**, *7*, 2741.

[228] G. Seisenberger, M. U. Ried, T. Endress, H. Buning, M. Hallek, C. Bräuchle, *Science* **2001**, *294*, 1929.

[229] K. de Bruin, N. Ruthardt, K. von Gersdorff, R. Bausinger, E. Wagner, M. Ogris, C. Bräuchle, *Mol. Ther.* **2007**, *15*, 1297.

[230] F. M. Mickler, L. Möckl, N. Ruthardt, M. Ogris, E. Wagner, C. Bräuchle, *Nano Lett.* **2012**, *12*, 3417.

[231] N. Ruthardt, D. C. Lamb, C. Bräuchle, *Mol. Ther.* **2011**, *19*, 1199.

[232] W. J. Godinez, M. Lampe, S. Wörz, B. Müller, R. Eils, K. Rohr, *Med. Image Anal.* **2009**, *13*, 325.

[233] D. Arcizet, B. Meier, E. Sackmann, J. O. Rädler, D. Heinrich, *Phys. Rev. Lett.* **2008**, *101*.

[234] C.-H. Lee, S.-H. Cheng, Y. Wang, Y.-C. Chen, N.-T. Chen, J. Souris, C.-T. Chen, C.-Y. Mou, C.-S. Yang, L.-W. Lo, *Adv. Funct. Mater.* **2009**, *19*, 215.

[235] Q. He, J. Zhang, J. Shi, Z. Zhu, L. Zhang, W. Bu, L. Guo, Y. chen, *Biomaterials* **2010**, *31*, 1085.

[236] V. Mamaeva, C. Sahlgren, M. Linden, *Adv. Drug Delivery Rev.* **2013**, *65*, 689.

[237] J. M. Rosenholm, V. Mamaeva, C. Sahlgren, M. Linden, *Nanomedicine* **2012**, *7*, 111.

[238] J. Lu, M. Liong, Z. Li, J. I. Zink, F. Tamanoi, *Small* **2010**, *6*, 1794.

[239] B. Fadeel, A. E. Garcia-Bennett, *Adv. Drug Delivery Rev.* **2010**, *62*, 362.

[240] Q. He, Z. Zhang, Y. Gao, J. Shi, Y. Li, *Small* **2009**, *5*, 2722.

[241] Z. Tao, M. P. Morrow, T. Asefa, K. K. Sharma, C. Duncan, A. Anan, H. S. Penefsky, J. Goodisman, A.-K. Souid, *Nano Lett.* **2008**, *8*, 1517.

[242] R. Wittig, J. M. Rosenholm, E. von Haartman, J. Hemming, F. Genze, L. Bergman, T. Simmet, M. Linden, C. Sahlgren, *Nanomedicine* **2013**.

[243] J. Duan, Y. Yu, Y. Li, Y. Yu, Z. Sun, *Biomaterials* **2013**, *34*, 5853.

[244] H. HogenEsch, A. Y. Nikitin, *J. Control. Rel.* **2012**, *164*, 183.

[245] I. I. Slowing, J. L. Vivero-Escoto, Y. Zhao, K. Kandel, C. Peeraphatdit, B. G. Trewyn, V. S. Y. Lin, *Small* **2011**, *7*, 1526.

2 Characterization

The synthesis and functionalization of MSNs can be characterized by various techniques. Structural and morphological parameters are obtained by X-ray diffraction, nitrogen physisorption measurements and transmission electron microscopy (TEM). By means of dynamic light scattering (DLS) the size of the MSNs and their agglomeration behavior can be investigated. Furthermore, zeta potential was used to characterize the charge of the particle surface. Vibrational spectroscopy (IR- and Raman spectroscopy) elucidates the properties of chemical bonding in materials. The complementary selection rules for either IR- or Raman-active vibrations make these two approaches versatile tools for the analysis of the synthesized samples. Additionally, nuclear magnetic resonance spectroscopy of liquids and solid state NMR shows chemical bonding in the samples. Thermogravimetric analysis (TGA) was used to evaluate the amount of functional organic compounds attached to the MSNs. Fluorescence spectroscopy was performed to gain information about the time-based release of fluorescent model drugs such as fluorescein from the mesoporous nanocarriers.

2.1 Dynamic Light Scattering (DLS)

Dynamic light scattering (DLS) measurements provide information about the size of particles suspended in a liquid.[1-2] This technique is valuable for the analysis of nano-sized particles typically having a diameter between 1 – 1000 nm. The size of particles is correlated with the Brownian motion which is the random movement of particles in a liquid caused by constant collisions with the surrounding solvent molecules. The smaller the particles, the more effective these collisions are, causing rapid movement. Slow Brownian motion is observed for large particles. The velocity of the Brownian motion is related to the translational diffusion coefficient *D*, from which the particle size can be calculated following the Stokes-Einstein equation (2.1).

$$d(H) = \frac{kT}{3\pi\eta D} \tag{2.1}$$

Stokes-Einstein equation: *d(H)* is the hydrodynamic diameter, *D* is the translational diffusion coefficient, *k* is the Boltzmann's constant, *T* is the temperature, *η* is the viscosity.

DLS measures the hydrodynamic diameter *d(H)*, which is related to the diffusion properties of a particle in a liquid. The translational diffusion coefficient *D* depends on several parameters, including the ionic strength of the suspension, the texture of the particle surface, and the shape of the particles. Upon illumination of the particles by laser light, the intensity fluctuations in the scattered light are analyzed during DLS measurements. These intensity fluctuations occur by constructive and destructive interferences of the scattered light being detected. The size of the particles will determine the rate of occurrence of these intensity fluctuations. The particle size distribution which is obtained by DLS measurements is based on intensity. This intensity-derived size distribution is suitable for small particles (size smaller than one-tenth of the wavelength of the illuminating light) in a suspension featuring monodispersity, and is well described by Rayleigh scattering. The Rayleigh approximation (2.2) presents the relation between the light scattering intensity I and the particle diameter d.

$$I \propto d^6 \tag{2.2}$$

Rayleigh approximation: *I* is the intensity of scattered light and *d* is the particle diameter.

The scattering intensity is proportional to d^6. Thus, large particles and agglomerations would dominate the intensity size distribution even if only present in small amounts. For particles that have a size similar to the wavelength of the laser, and broad particle size distributions or a suspension containing different particle size populations, Mie theory has to be applied. Here, a conversion to volume size distribution or number size distribution is more accurate, taking into account the refractive index of the sample. Volume size distribution and number size distribution are proportional to d^3 and d, respectively, which gives a more realistic view of particle aggregation and polydispersity.

2.2 Zeta Potential Measurements

Particles in an aqueous suspension feature a zeta potential, which is the electrokinetic potential difference between a stationary layer of ions in a liquid attached to the dispersed particle and the liquid medium in the surroundings.[3] Particles in colloidal suspensions can exhibit surface charges, which can originate from ionization of functional groups at the external particle surface, differential loss of ions from the particle, or adsorption of charged

species, such as ions and ionic surfactants. The charged particle surfaces affect the distribution of ions in the dispersion medium generating different layers of counter ions, close to the surface, thus forming an electrical double layer which exists around single particles (Figure 2.1).[4]

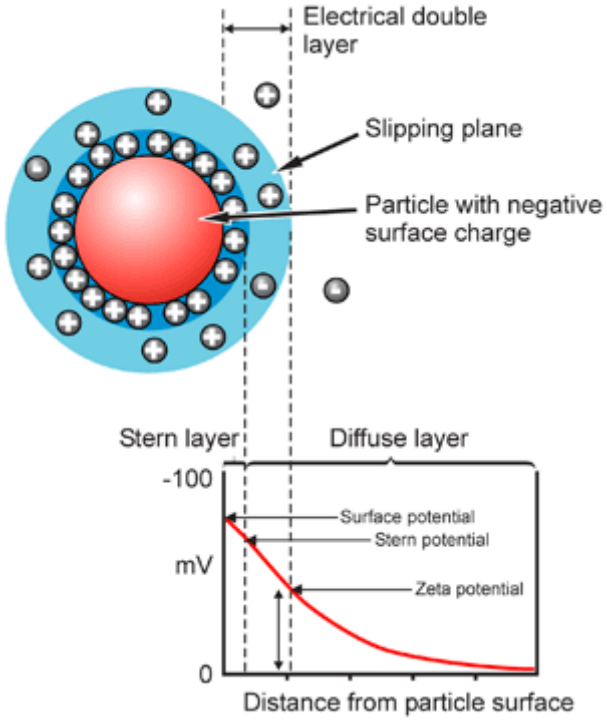

Figure 2.1: Schematic representation of the electric double layer around a negatively charged particle and location of the zeta potential.[5]

Zeta potential measurements are used to investigate the charge of the particle surface depending on the pH value of the solution. The zeta potential of particles is highly affected by environmental changes in pH causing protonation or deprotonation of functional groups, such as amino or carboxy groups, on the particle surface. This results in an increased or decreased surface charge. Zeta potential is measured indirectly by determination of the electrophoretic mobility. By applying an external electric field, charged particles move towards the electrodes. The velocity of particle movement depends on the strength of the external electric field, the dielectric constant, the viscosity of the fluid, and the zeta potential of the particles. The Henry equation (2.3) describes the relation between the electrophoretic mobility and the zeta potential.

$$U_E = \frac{2\varepsilon\zeta f(\kappa a)}{3\eta} \tag{2.3}$$

Henry equation: U_E is the electrophoretic mobility, ε is the dielectric constant of the sample, ζ is the zeta potential, $f(\kappa a)$ is the Henry function, and η is the viscosity.

To obtain the electrophoretic mobility, the velocity of the particles is measured using Laser Doppler Velocimetry (LDV). An electric field of known strength is applied to a capillary cell containing the particle suspension. The frequency shift of the laser light passing through the suspension is used to determine the velocity of the particles. For small particles (< 200 nm) in low dielectric constant media the Henry function $f(\kappa a)$ becomes 1.0, known as the Hückel approximation. The Smoluchowski approximation is suitable for particles lager than 200 nm in diameter and for suspensions containing more than 1 mM salt concentrations. Using these simple approximations for the Henry function, the zeta potential of the particles within the colloidal suspension can finally be calculated.

2.3 IR- and Raman Spectroscopy

IR- and Raman spectroscopy offers the potential to study the properties of the chemical bonds in a molecule by excitation of vibrational modes. In the former, radiation in the infrared region of the electromagnetic spectrum (200 – 4000 cm^{-1}) is used for the excitation in order to receive information about the vibrational and rotational energy states of a molecule.[6-7] The infrared light interacts with the sample and the intensity of the transmitted or scattered light is measured. For detection of vibrational modes it is necessary that the molecule is IR-active, which implies that the dipole moment of the molecule has to change during the vibration. The absorption of the IR radiation results in transitions to higher energy levels and thus a characteristic absorption spectrum providing information about the chemical composition and bonding of the sample can be detected. Fourier transformation of a time-dependent signal which is detected by an interferometer while performing IR spectroscopy measurements, results in a frequency-dependent spectrum with information about characteristic vibrational bands of specific functional groups.[8]

For Raman spectroscopy monochromatic light, usually generated by a laser, is used to characterize the sample. The Raman effect relies on the interaction of light with the electron

shell of the molecules. It is based on the inelastic scattering of the monochromatic light by interaction with the electron cloud of a molecule. The Raman selection rule requires vibrations to induce a change in the polarizability in order to be Raman-active. Figure 2.2 illustrates the possible excitation and relaxation processes occurring during a Raman experiment.

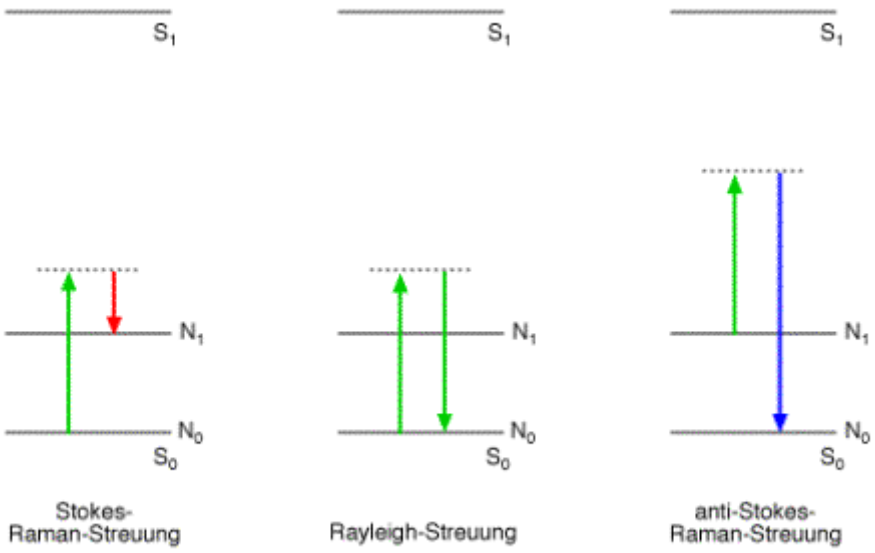

Figure 2.2: Energy states and scattering processes (Stokes-, Rayleigh-, and anti-Stokes scattering, respectively) occurring in a Raman experiment.[9]

An incident photon excites a bound electron from a given vibrational state into a virtual energy state. There are two different possibilities to scatter the incident light. Either the monochromatic light is scattered elastically, which is known as Rayleigh scattering, or inelastically, known as Raman scattering. In Raman scattering, the scattered light is either shifted to higher frequencies (Anti-Stokes scattering) or shifted to lower frequencies (Stokes scattering) with respect to the original frequency. The corresponding absorption frequencies are related to specific functional groups and the nature of a synthesized molecule can be identified.

2.4 Fluorescence Spectroscopy

Fluorescence, a certain kind of photoluminescence, is a physical process in which a substance absorbs photons and subsequently reradiates photons of lower energy. Fluorescence results of a three-stage process in the electron shell of certain molecules, including mainly polyaromatic

hydrocarbons or heterocycles. These molecules consisting of a large conjugated π-electron system are called fluorophores or fluorescent dyes. In Figure 2.3 a Jablonski diagram is depicted, which gives information about the process of fluorescence in a simplified manner.

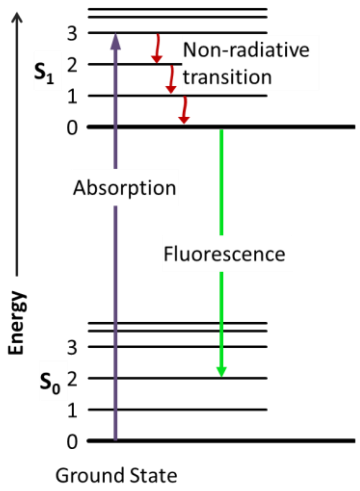

Figure 2.3: Jablonski diagram illustrating the process of fluorescence: Excitation of electrons by absorption of external photons, non-radiative relaxation to vibrational ground state (0) of excited electronical state (S_1), and emission of photons (fluorescence).[10]

First, a photon of energy $h\nu_{ex}$ is absorbed by the fluorophore, which results in an excitation of electrons from the ground state S_0 to an excited state S_1'. These photons are generated externally by incandescent lamp or a laser sources. The absorption occurs in a very short time-scale of about one femtosecond. Subsequently, a non-radiative relaxation process takes place caused by conformational changes of the fluorophore. These conformational changes lead to a loss of energy and are subject to environmental interactions. The electrons need typically about $1 - 10$ nanoseconds to temporarily end up in a relaxed excited state S_1. Finally, the electrons can reach the ground state S_0 by emitting photons $h\nu_{em}$ of lower energy compared to the external photons $h\nu_{ex}$ which led to electron excitation. Fluorescence features a red-shift of the emitted wavelength accompanied with energy loss compared to the initial photons generated by external sources. This phenomenon is called Stokes shift, which is a bathochromic shift of the emission maximum compared to the absorption.[11-12] Fluorescence is not the only process causing a return of the excited molecules to the ground state. Other known processes are quenching, fluorescence energy transfer and intersystem crossing

(phosphorescence) which also can lead to depopulation of the excited state S_1 without emitting a photon.

2.5 Nitrogen Physisorption

Adsorption and desorption measurements of a gas on a porous substrate give information about the shape and pore size distribution, the specific surface area and the pore volume of a material. Nitrogen sorption measurements are suitable to characterize porous materials concerning their pore characteristics, such as pore size, pore arrays, and surface areas.[13] The nitrogen sorption process can be classified as physisorption, since only weak interactions including van-der-Waals forces occur for the adsorbed species and the absorbents. For nitrogen physisorption measurements, the amount of the adsorbed nitrogen gas at different pressures and constant temperature (77 K) is used to generate sorption isotherms (Figure 2.4).

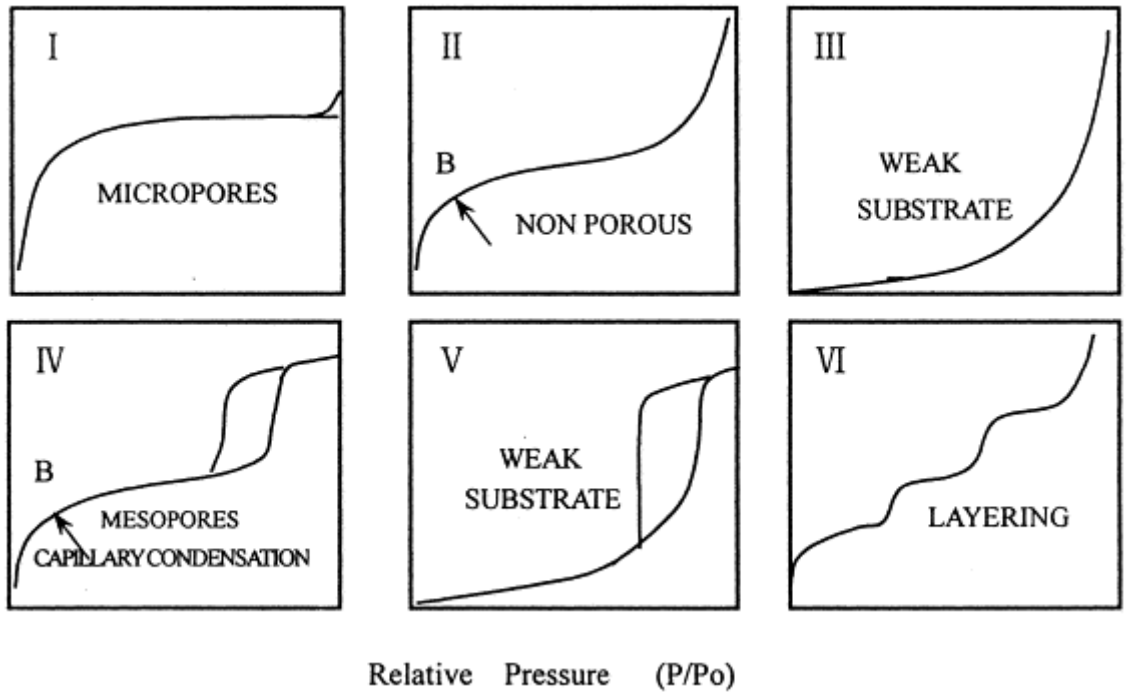

Figure 2.4: IUPAC classification of six different sorption isotherms.[14]

Six different types of sorption isotherms were classified by IUPAC.[14] The different types (I-VI) distinguish porous materials regarding pore structure and size, and the interactions of the adsorbed gas molecules with the adsorbent. The most common models for the description of isotherms are those of Langmuir, Freundlich and Brunauer-Emmett-Teller (BET).[15] The BET isotherm model assumes multilayer adsorption, neglecting interactions of the adsorbates among each other. The initial monolayer serves as a substrate for further adsorption processes,

and consequently a change in adsorption enthalpy between the first and the subsequent layers occurs. With these approximations, the BET-equation can be derived (2.4).

$$\frac{n}{n_m} = \frac{C \cdot \frac{p}{p_0}}{\left(1 - \frac{p}{p_0}\right)\left(1 + C - \frac{p}{p_0}\right)} \tag{2.4}$$

BET equation: *n* is the amount of the adsorbate at the pressure *p*, n_m is the capacity of one monolayer, *C* is the BET constant, *p* is the equilibrium pressure, and p_0 is the saturation vapor pressure of the adsorbate.

Transformation of the BET equation leads to a linear relation between partial pressure and surface occupancy. The capacity of one monolayer n_m can be easily calculated by this linear relation. The specific surface area can be calculated by the required space of one adsorbed molecule. For mesoporous materials, the pore shape influences the shape of the hysteresis loops of IUPAC type IV adsorption isotherms.[16] The pore size distribution function is a very important characteristic of porous materials. The thermodynamic relation between the reduced pore radius r_k (Kelvin radius, defined by the sum of the quotients of principal radii r_1 and r_2 of the curvature of the liquid meniscus in the mesopore)[17] and the relative vapor pressure p/p_0 is described by Kelvin's equation (2.5).

$$r_k = \frac{-2\gamma V_L}{RT \cdot \ln(\frac{p}{p_0})} \tag{2.5}$$

Kelvin's equation: r_k is the reduced radius, γ is the surface tension of the adsorbate, V_L is the molar volume, *R* is the gas constant, *T* is the temperature, *p* is the equilibrium pressure, p_0 is the saturation vapor pressure of the adsorbate.

The reduced pore radius r_k indicates the curvature of the adsorbate's surface. However, pore size calculations using Kelvin's equation are often not accurate, since the expressed pore radius does not include multilayer films. Consequently, pore sizes are underestimated. In the BJH method, corrections are made to account for the film formation. This method however is limited in so far as it disregards the impact of surface curvature on the formation of the film, it is only derived for cylindrical pores, it assumes formation of homogenous films and it does not explicitly account for surface forces between the film and the surface. Due to these limitations the BJH is known to underestimate the pore size, especially for small pores. The calculations involving density functional theory (DFT) can lead to more realistic results. Pore

size analyses with DFT and Monte Carlo methods describe the situation of an adsorbed fluid in equilibrium with a bulk fluid reservoir.[18] The grand canonical Monte Carlo simulation represents the most common computer simulation for the study of adsorption processes. Equilibrium density profiles are obtained by applying the DFT approach. The free-energy function is minimized for a pore system in equilibrium with a bulk phase. This represents the exact situation during a sorption experiment. Two different DFT approaches, the local density functional theory (LDFT) and the non-local density functional theory (NLDFT), were developed for a more exact description of the porous system. NLDFT in combination with Monte Carlo simulations describes very well the local fluid structure near curved solid walls.

2.6 Thermogravimetric Analysis

Thermogravimetric analysis (TGA) can be performed for determining the composition of a sample containing volatile or combustible components.[19-20] This method investigates the mass loss of a sample with increasing temperature. The sample is placed into an adjustable oven, usually heated up to 900 °C in this work, and the weight losses are detected by a coupled thermobalance. The mass loss results either from desorption of adsorbed molecules or from the decomposition of the material. The temperature is raised with a constant heating rate $\beta = dT/dt$ in inert gas atmosphere or in synthetic air that passes the sample and removes desorbed components. The resulting thermogravimetric data contain information about the temperature stability of the observed sample. Furthermore, the thermogravimetric analysis of porous compounds can also quantify the amount of adsorbed cargo molecules in the mesopores.

2.7 X-Ray Diffraction (XRD)

X-ray diffraction measurements can be performed to gain direct information about the crystallinity of the investigated material. Furthermore, the particle shape and size of nanostructured materials can be analyzed in the nanometer range.[21] The (ordered) pore structure of mesoporous silica materials can be analyzed by small angle X-ray scattering (SAXS). Here, the identification of the mesostructure of the synthesized silica materials was carried out at small angles ranging from $2\theta = 0.1 – 10$ °. X-ray radiation is emitted from a metal source, normally copper, with a characteristic wavelength (Cu-K_α is 1.54182 Å).[22] This wavelength has about the same order of magnitude as the distances of atoms in solids

possibly causing scattering of an incident X-ray beam. Therefore, constructive and destructive interferences of X-rays scattered by the lattice planes of the porous materials gives information on the atomic structure of the material. The relationship between the incident X-ray beam and the lattice plane distance of porous materials is described by Bragg's law 2.6.

$$\sin\theta = \frac{n\lambda}{2d} \tag{2.6}$$

Bragg's relation: θ is the angle of incidence, d is the lattice plane distance, λ is the wavelength, and n is the order of interference.

2.8 Transmission Electron Microscopy (TEM)

Electron microscopy is a powerful imaging technique - achieving a spatial resolution down to 0.1 nm - to observe structures at the atomic length scale, which makes it a very important characterization technique in nanotechnology.[23] For imaging, highly accelerated electrons are generated by an electron gun and focused by using electromagnetic lenses. The strong interaction of electrons with matter requires ultrahigh vacuum to achieve the highest resolution. Limiting factors for high resolution are spherical aberrations, chromatic aberrations, and astigmatism.[24] Various processes occur upon electron irradiation of a material, generating X-rays and a variety of resulting electrons, such as secondary, backscattered, and Auger electrons, which can be detected and are subsequently used to image the specimen. The described effects are utilized for different techniques in electron microscopy including selected area electron diffraction (SAED), energy dispersive X-ray (EDX) analysis, and electron energy loss spectroscopy (EELS). Another type of generated electrons are transmitted electrons that are not subjected to energy loss or directional change. Consequently, they are not influenced by the investigated material. For transmission electron microscopy (TEM), the transmitted electrons are detected by a fluorescent screen or a CCD camera. This technique offers the investigation of the internal structure of the specimen. A schematic construction of a transmission electron microscope is depicted in Figure 2.5, including the pathway of the electron beam.

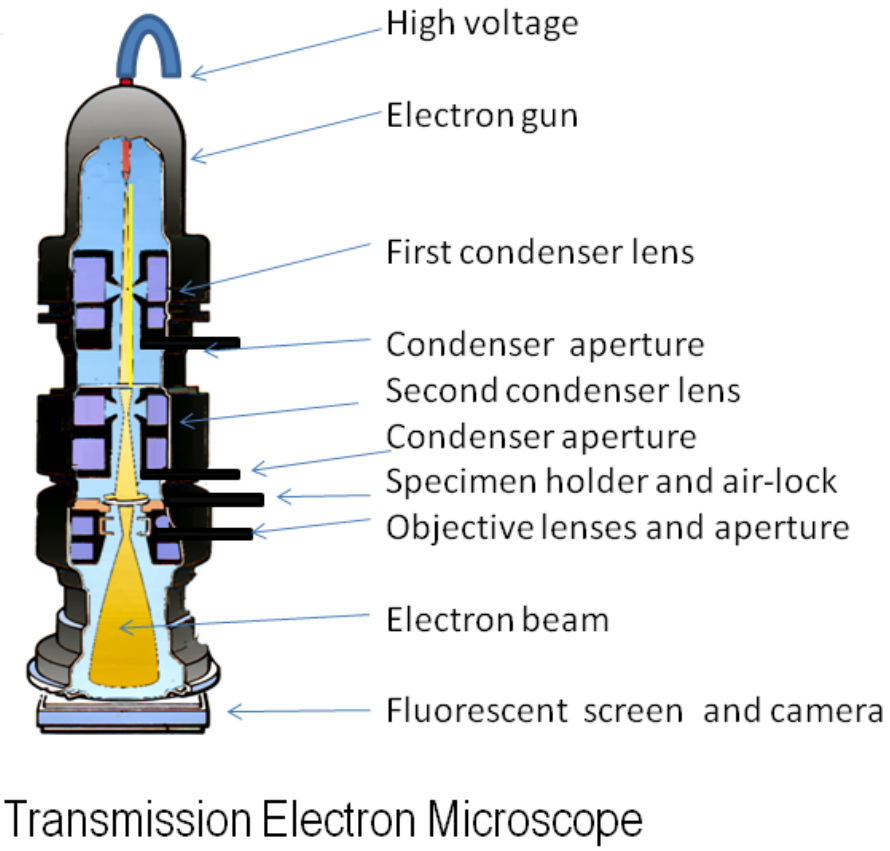

Figure 2.5: Schematic representation of a transmission electron microscope. The pathway of the electron beam is presented in yellow.[25]

Information about the structure and morphology of the material, cell parameters, pore dimensions and wall thickness can be obtained from TEM investigations, since resolution down to the atomic level is provided by this technique. Structural results for porous materials derived from XRD and physisorption measurements can be verified by TEM analysis. Samples for TEM investigation have to be very thin to allow electron transmission. MSNs studied here have a diameter of about 80 nm and so they are in the appropriate range for TEM measurements. The sample has to be penetrated by radiation, this is possible due to the high acceleration voltage for electrons (80 – 300 keV).

2.9 Nuclear Magnetic Resonance (NMR)

Nuclear magnetic resonance (NMR) spectroscopy investigates the absorption of electromagnetic radiation by magnetic nuclei in a static magnetic field. The evaluation of NMR data provides information about the chemical environment and structural properties of nuclear isotopes, including chemical bonds, connectivity within molecules, and coordination

numbers. The elements need to have a non-zero nuclear spin which is, for instance, present in ^{1}H, ^{13}C, and ^{29}Si. The applied external magnetic field influences the energy states of the nuclei possessing a permanent magnetic dipole moment. Consequently, this results in a differentiation of the magnetic energy levels into (2J+1) distinct energy states (J indicates the nuclear spin). This strictly depends on the alignment of the nuclear spins relative to the external magnetic field. A transition between these quantum states can be induced by electromagnetic radiation with radiofrequency, typically ranging from a few kHz to several hundred MHz (2.7).

$$\omega = \gamma(B_0 + B_{int}) \tag{2.7}$$

ω is the frequency of electromagnetic radiation at resonance conditions, γ is the gyromagnetic ratio, B_0 is applied external magnetic field, and B_{int} is the internal field arising from electronic environments and surrounding magnetic moments.

Nuclear magnetic resonance spectroscopy of liquids typically gives sharp spectra at high resolution. The mobility of the nuclei in liquid samples creates an averaging process, leading to an intrinsic elimination of the line broadening related to dipole-dipole interactions. In contrast, the investigation of solids by solid state NMR requires special methods to give comparable structural information. These dipole-dipole interactions between the magnetic moments of nearby nuclei lead to line broadening in the spectra. The “magic angle spinning” (MAS) technique provides a method to eliminate this anisotropic effect and sharpen the obtained broad peaks in solid state NMR, by rotating the sample at high velocity at an angle of 54.74° relative to the applied magnetic field.

2.10 References

[1] http://www.malvern.de/malvern/kbase.nsf/allbyno/KB000792/$file/MRK656-01_An_Introduction_to_DLS.pdf

[2] R. Pecora, *Dynamic Light Scattering: Applications of Photon Correlation Spectroscopy*, Plenum Press, **1985**.

[3] H. Butt, K. Graf, M. Kappl, *Physics and Chemistry of Interfaces*, Wiley VCH, **2003**.

[4] http://www.malvern.de/malvern/kbase.nsf/allbyno/KB000734/$file/MRK654-01%20An%20Introduction%20to%20Zeta%20Potential%20v3.pdf

[5] http://www.malvern.com/labeng/technology/images/zeta_potential_schematic.png

[6] M. Hesse, H. Meier, B. Zeeh, *Spectroscopic Methods in Organic Chemistry.*, Thieme, **2008**.

[7] H. Günzler, H. Gremlich, *IR-Specktroskopie: Eine Einführung*, Wiley VCH, **2003**.

[8] J. Mermet, M. Otto, R. Kellner, M. Cases, *Analytical Chemistry: A Modern Approach to Analytical Science.*, Wiley VCH, **2004**.

[9] http://www.raman.de/assets/images/energie.gif

[10] http://upload.wikimedia.org/wikipedia/commons/8/89/Jablonski_Diagram_of _Fluorescence_Only.png

[11] J. R. Lakowicz, *Principles of Fluorescence Spectroscopy.*, Plenum Press, **1983**.

[12] P. W. Atkins, *Physikalische Chemie*, Wiley VCH, **2001**.

[13] S. Lowell, J. E. Shields, M. A. Thomas, M. Thommes, *Characterization of Porous Solids and Powders: Surface Area, Pore Size and Density.*, Springer, **2006**.

[14] Z. Y. Ryu, J. T. Zheng, M. Z. Wang, B. J. Zhang, *Carbon* **1999**, *37*, 1257.

[15] S. Brunauer, P. H. Emmett, E. Teller, *J. Am. Chem. Soc.* **1938**, *60*, 309.

[16] J. H. de Boer, *The Structures and Properties of Porous Materials*, Butterworth, London, **1958**.

[17] K. S. W. Sing, D. H. Everett, R. A. W. Haul, L. Moscou, R. A. Pierotti, J. Rouquerol, T. Siemieniewska, *Pure Appl. Chem.* **1985**, *57*, 603.

[18] P. I. Ravikovitch, A. Vishnyakov, A. V. Neimark, *Physical Review E* **2001**, *64*.

[19] L. S. K. Pang, J. D. Saxby, S. P. Chatfield, *J. Phys. Chem.* **1993**, *97*, 6941.

[20] M. P. Sepe, *Thermal Analysis of Polymers*, Rapra Technology Limited, **1997**.

[21] P. Fratzl, *J. Appl. Crystallogr.* **2003**, *36*, 397.

[22] B. D. Cullity, S. R. Stock, *Elements of X-Ray Diffraction.*, Prentice Hall, **2001**.

[23] D. B. Williams, C. B. Carter, *The Transmission Electron Microscope*, Springer, **1996**.

[24] B. Fultz, J. Howe, *Transmission Electron Microscopy and Diffractometry of Materials*, Springer, **2008**.

[25] http://edu.glogster.com/media/5/32/8/90/32089069.png

3 "Liquid-Phase Calcination" of Colloidal Mesoporous Silica Nanoparticles in High-Boiling Solvents

This chapter is based on the following publication:

Valentina Cauda, Christian Argyo, Davin G. Piercey, and Thomas Bein, *Journal of the American Chemical Society* **2011**, *133*, 6484 – 6486.

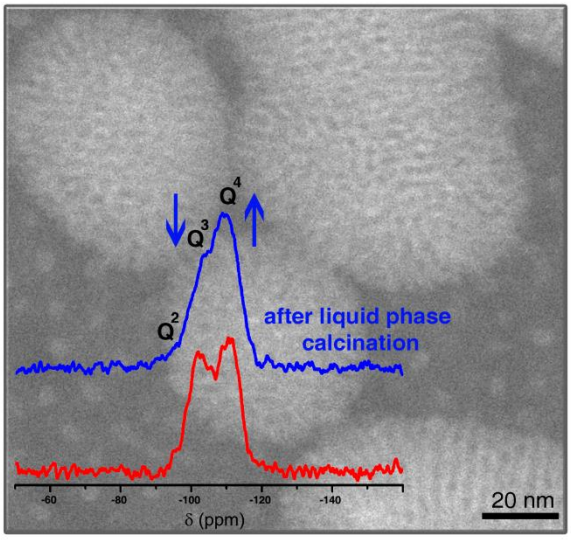

3.1 Introduction

Colloidal mesoporous silica nanoparticles (MSNs) are of great interest for their unique properties regarding catalysis, separation, chemical sensing, and drug delivery.[1-2] The defining factor of the synthesis of mesoporous silica is the use of a templating surfactant causing self-assembly of the material at mild temperatures. The subsequent removal of this template is the key step for obtaining accessible mesopores, large surface areas, and pore volumes.[3-4] Established methods of template removal include calcination in air, extraction in ethanol with various solutes, microwave irradiation, and UV light.[5-8] However, all these methods except the solution-phase ethanol-based template extraction are conducted in the solid phase, which is appropriate for bulk mesoporous silica or for particles with a size far greater than 100 nm.[9-10] During calcination, condensation of silanol groups (Si-OH) into siloxane (Si-O-Si) bridges takes place, thus consolidating the mesoporous structure.[11] However, when colloidal MSNs (e.g., 20-100 nm in size) are calcined, strong aggregation prevents their subsequent redispersion as isolated nanoparticles in a colloidal solution. For

this reason only solvent extraction, hydrogen peroxide oxidation, or dialysis can be applied,[12-14] but no further condensation of the silica network after the room temperature sol-gel synthesis is obtained. This implies the low stability of the extracted MSNs in aqueous media, which can pose a serious impediment for applications such as drug delivery. We have previously shown that the silanol groups are the point of initial attack and silica degradation, leading to rapid particle destruction in simulated biological fluids.[15] Current attempts at increasing the stability of MSNs in biological media have mainly involved polymeric-shell functionalization of the outer particle surface.[16]

Here we present for the first time the use of a liquid-phase high temperature "calcination" of MSNs in high boiling point organic solvents (HBS), leading to significant silica condensation and also to template removal. Trioctylphosphine oxide (TOPO), known for its stabilizing effect in nanoparticle and quantum dot synthesis,[17-18] was used as solvent for high temperature treatment of the MSNs, in both thermal and microwave-assisted liquid calcination. In addition we have examined two other HBS, tri-*n*-octylamine (TOA, $C_{24}H_{51}N$) and squalene ($C_{30}H_{50}$).[19]

3.2 Results and Discussion

The synthesis of MSNs (sample UN-CMS) was carried out as previously reported.[20] The ability of the HBS treatment to enhance the degree of silica condensation in the already template-extracted MSNs (sample ex-CMS) was examined with thermal liquid calcination at 400 °C in squalene (sample LC-1), TOA (sample LC-2), and TOPO (sample LC- 3), in this last case also at 275 °C (sample LC-4), for 5 h under a N_2 atmosphere. Moreover, we have combined the ability of the TOPO treatment to enhance silica condensation with the removal of the template phase in as-synthesized MSNs (template: cetyltrimethylammonium chloride (CTAC)). This was achieved in a thermal liquid calcination at both 275 °C (sample LC-5) and 400 °C (sample LC-6) on UN-CMS nanoparticles. Microwave (MW) heating has been demonstrated to enhance reaction rates, selectivity, and product yields in chemical synthesis.[21-22] Due to its polarity, TOPO can couple with microwaves and efficiently convert electromagnetic energy into heat, resulting in rapid heating of the bulk solution. TOPO microwave-assisted liquid calcination was carried out at 200 °C for 30 min (sample LC-7) or 2 h (sample LC-8) with template-extracted MSNs (ex-CMS). All TOPO-calcined samples

were thoroughly washed. The degree of condensation of the silica network in the as-synthesized (UN-CMS) and template-extracted MSNs (ex-CMS) is strongly enhanced by all the liquid-phase calcinations treatments, as observed by ^{29}Si-MAS NMR spectroscopy (Figure 3.1).

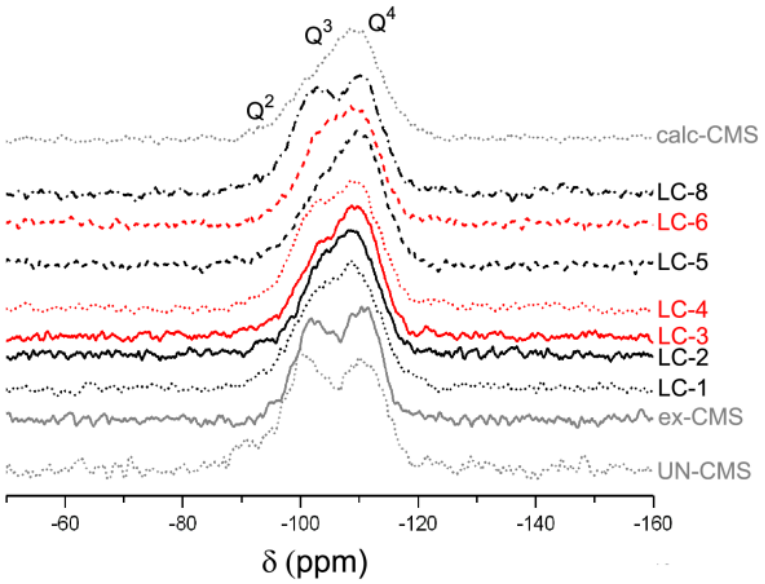

Figure 3.1: ^{29}Si-MAS NMR spectra of the as-synthesized (UN-CMS), template-extracted (ex-CMS), and air-calcined (calc-CMS) MSNs and the liquid-phase-calcined MSNs with squalene (LC-1), TOA (LC-2), and TOPO (from LC-3 to LC-8).

Table 3.1: Quantification of the Integrated Area of Q^3 and Q^4 Peaks and Their Relative Change upon Thermal Treatment.

Sample	Treatment	Q^3/Q^4 ratio	Increase of Condensation[a] (%)
UN-CMS	-	1.08	-
ex-CMS	EtOH@78 °C	1.02	+ 5.56
LC-1	Sqa@400 °C	0.755	+ 30.1
LC-2	TOA@400 °C	0.795	+ 26.2
LC-3	TOPO@400 °C	0.816	+ 24.5
LC-4	TOPO@275 °C	0.801	+ 25.8
LC-5	TOPO@275 °C	1.04	+ 2.78
LC-6	TOPO@400 °C	0.910	+ 15.7
LC-8	TOPO@200 °C MW	1.01	+ 6.48
calc-CMS	550 °C (air)	0.549	+ 49.2

[a]Based on the decrease in % of the Q^3/Q^4 ratio of each sample with respect to the reference one (UN-CMS).

Quantification of the integrated area of the Q^n peaks is given in Table 3.1, clearly indicating a strengthening of the silica network due to the HBS calcination treatments. In order to quantitatively evaluate the degree of silica condensation after the TOPO-calcination process,

the Q^3 and Q^4 peaks from the single-pulse ^{29}Si-MAS NMR measurements were deconvoluted by using the deconvolution software Deconv2Dxy.[23] The ratio of Gaussian to Lorentzian fit was set to 0.5 and the area under each Q^n peak was calculated. The results of this fitting procedure are shown in Table 3.1 and in Appendix 3.5. To better estimate the effect of the silica condensation, we also calculated the ratio of the Q^3/Q^4 areas for each sample and the percentage of variation of the Q^3/Q^4 ratio for one given sample after HBS-treatment with respect to the ratio values of the starting materials (Table 3.1). The general trend in all samples is an increase of the Q^4 area after the HBS-thermal treatment. In particular, a clear indication of this trend is given by the decrease of the relative ratio Q^3/Q^4 for the samples LC-1 to LC-4. It has to be noted that sample LC-4, thermally calcined in TOPO for 5 h at 275 °C, shows a similar Q^3/Q^4 area ratio as compared to sample LC-3, calcined at the same conditions at 400 °C. This indicates that a similar degree of silica condensation is already obtained at 275 °C and no significant improvement is obtained by further increasing the temperature. In contrast, the microwave-calcined sample LC-8 shows no significant reduction of the Q^3/Q^4 area ratio, thus indicating that the treatment with TOPO at only 200 °C for 2 h is not enough to improve the silica condensation. A reduction of the ^{29}Si-MAS NMR peak area is also observed for the TOPO-calcined particles LC-5 and LC-6 starting from the unextracted ones (sample UN-CMS): the reduction of the Q^3/Q^4 area ratio is consistently higher as the temperature of TOPO treatment increases from 275 to 400 °C. It has to be noted that the ratio Q^4/Q^3 of the sample ex-CMS (template-containing MSNs) and sample UN-CMS (extracted MSNs) are quite similar, thus indicating that poor silica network condensation is retained using conventional solvent-extraction methods and that only a "liquid-calcination" procedure is able to consolidate the network of colloidal MSNs. Specifically, a consistent increase of the Q^4 peak at -110 ppm [$Q^n = Si(OSi)_n(OH)_{4-n}$ with n = 2-4, 4 representing the fully condensed silica] upon "liquid calcination" is observed with respect to the Q^3 peak at -102 ppm (silica with one terminal hydroxyl group) in all HBS-calcined samples, except the MW-treated ones (only LC-8 is reported in Figure 3.1). We attribute the lower efficiency of the MW treatment to both its lower temperature (200 °C) and shorter time (2 h). For the two TOPO-calcined samples at 275 °C (sample LC-4) and 400 °C (LC-3), a similar Q^3/Q^4 ratio is obtained, thus indicating that no further increase of silica condensation is obtained above 275 °C. The highest Q^4 fraction, implying the highest degree of silica condensation, was obtained upon calcination in squalene (LC-1). Air calcination at a still higher temperature (550 °C) can lead

to an even higher degree of condensation (sample calc- CMS); however, such a sample cannot be dispersed again as colloidal solution. Dynamic Light Scattering (DLS, Figure 3.2) shows that the colloidal stability in ethanol of all the MSNs is not affected after high-temperature treatment with HBS, and particle sizes do not change significantly as a result of different solvents and thermal treatments.

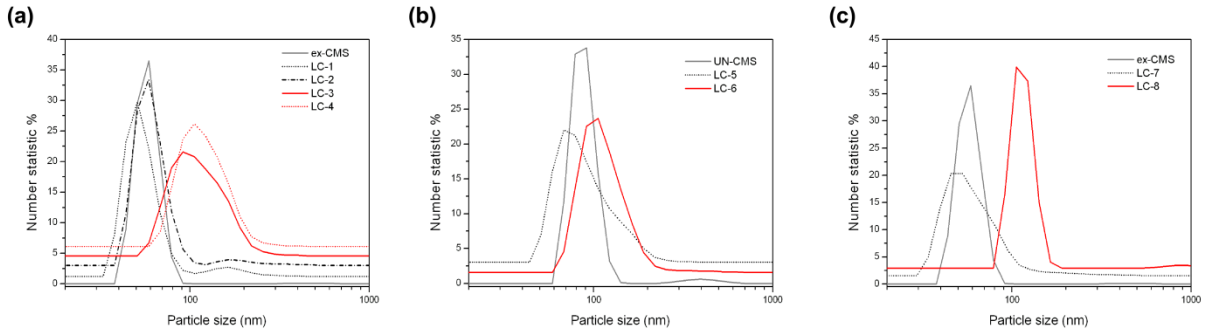

Figure 3.2: Dynamic Light Scattering (DLS) measurements of as-synthesized (UN-CMS), template-extracted (ex-CMS) and liquid-phase-calcined MSNs with TOPO (from LC-3 to LC-8), TOA (LC-2) and squalene (LC-1). For clarity reasons, the DLS measurements are shifted along the y-axis by 1.25 units.

As previously mentioned, air-calcined MSNs are no longer able to form colloidal solutions. All the HBS-treated samples do not show any structural difference by X-ray diffraction; in particular no shift of the (100)-like reflection to higher angles is observed (Figure 3.4c). This indicates the absence of the unit cell shrinkage, in contrast to conventional air-calcined MSNs.[24] Complete removal of TOPO by repetitive washing was confirmed by IR spectroscopy, whereas residual squalene and TOA are still present in both samples LC-1 and LC-2 (Figures 3.4 and 3.5). For this reason, the use of TOPO solvent is preferred with respect to squalene and TOA, even if the degree of silica condensation shown by ^{29}Si-MAS NMR is slightly lower with TOPO treatments. The enhancement of silica condensation in combination with the template extraction ability of the TOPO treatment was investigated with the unextracted MSNs (UN-CMS), using the thermal calcination method. Indeed, the resulting sample LC-6 shows a strengthening of the silica network in ^{29}Si-MAS NMR spectroscopy (Figure 3.1 and Table 3.1) and good colloidal stability in ethanolic solution with a homogeneous particle size distribution (Figure 3.2). TGA and IR spectroscopy show almost complete removal of the template (see Figure 3.8). The corresponding nitrogen sorption measurements (Figure 3.3) demonstrate that calcining unextracted MSNs in TOPO at 400 °C is as efficient as the solution-phase ethanol extraction method (see Table 3.2).

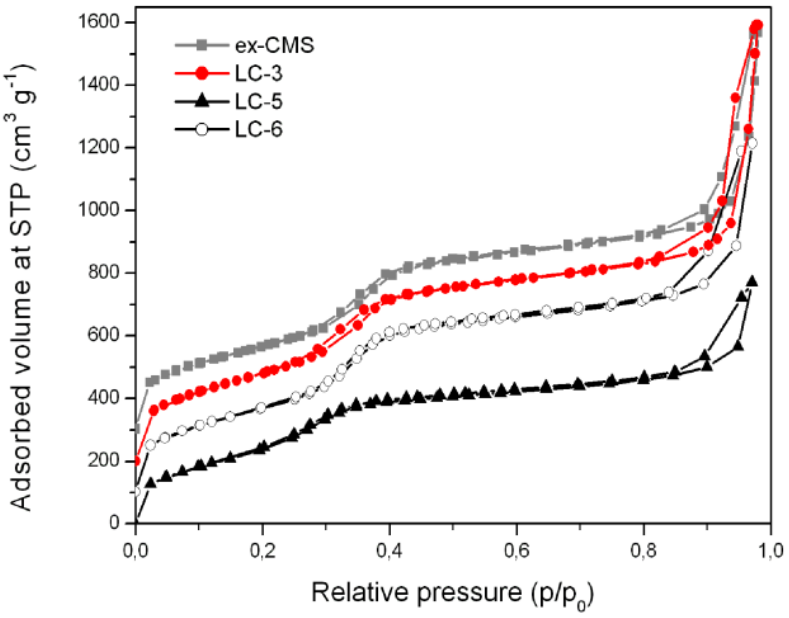

Figure 3.3: Nitrogen sorption isotherms of the unextracted/TOPO-calcined MSNs (LC-5 and LC-6), compared to the template-extracted MSNs (ex-CMS) and extracted/TOPO-calcined MSNs (LC-3). The curves are shifted by 100 units each.

However, calcination of the unextracted MSNs in TOPO at 275 °C (LC-5) is not sufficient to completely remove the template and to enhance the silica condensation as in the sample treated at 400 °C (LC-6). HBS-calcined CMS samples also exhibit a comparable porosity. The N_2 sorption isotherms of the other HBS-treated samples are shown in Table 3.2.

Table 3.2: Characterization of the Samples before and after HBS "Liquid-Calcination" Treatments.

Sample	BET surface area (m^2/g)	Pore volume[a] (cm^3/g)	DFT pore diameter[b] (nm)	DLS particle size[b] (nm)
ex-CMS	978	0.78	3.9	59
LC-1	918	0.71	3.5	51
LC-2	968	0.76	3.8	59
LC-3	1032	0.78	3.9	91
LC-4	1052	0.80	3.9	106
LC-5	928	0.60	3.5	68
LC-6	998	0.77	3.9	106
LC-7	850	0.75	3.9	59

LC-8	1087	0.83	3.8	106

[a]Pore volume was calculated only up to a pore size of 8 nm to remove the contribution of textural porosity.
[b]Referred to the peak value of the size distribution.

Characterization of the MSNs after thermal liquid calcination (samples from LC-1 to LC-4)

The high-boiling solvent (HBS) calcination was carried out thermally in reflux conditions for 5 hours at 400 °C in squalene (LC-1), TOA (LC-2) and TOPO (LC-3) and at 275 °C in TOPO (LC-4). After repetitive washing to remove the residual HBS, as described in the Experimental section, the samples were characterized by nitrogen sorption measurements. Figure 3.4a compares the nitrogen sorption isotherms of the HBS calcination (from LC-1 to LC-4) with the starting template–extracted MSNs (ex-CMS). All the thermally calcined MSN samples retained their surface area and pore volume (see also Table 3.2).

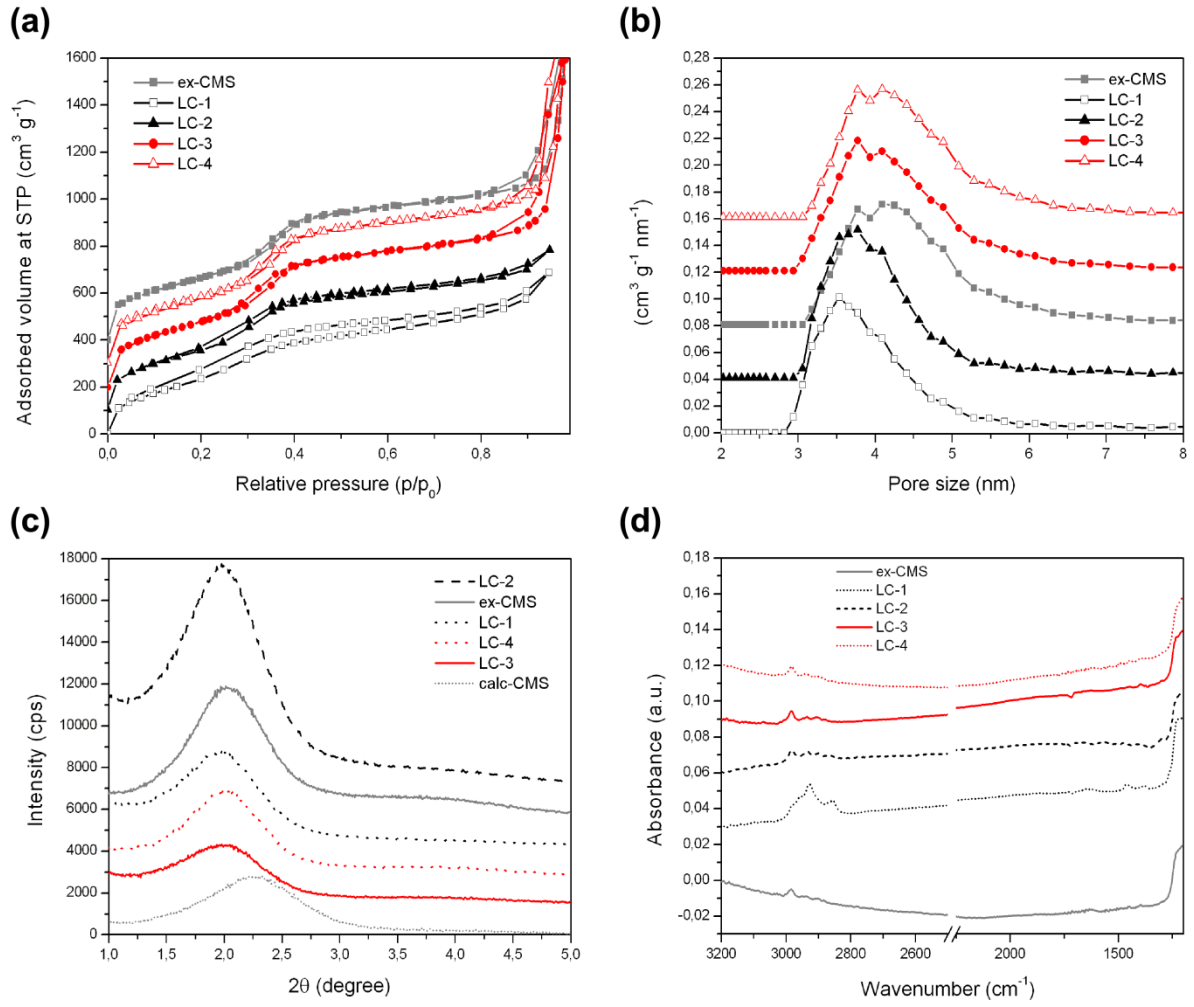

Figure 3.4: (a) Nitrogen sorption isotherms; (b) DFT pore size distributions; (c) small-angle XRD; and (d) infrared spectra for the thermal HBS-calcination at 400 °C with Squalene (LC-1), TOA (LC-2) and TOPO (LC-3) and at 275 °C in TOPO (LC-4), compared with ethanol-extracted MSNs (ex-CMS) and air-

calcined MSNs (calc-CMS in (c)). For clarity reasons, the nitrogen sorption isotherms in (a) are shifted along the y-axis by 100 units, the pore size distributions in (b) by 0.04 units, the XRD pattern in (c) by 1500 units and the IR spectra in (d) by 0.03 units.

Pore filling occurs at similar relative pressures in the type IV isotherms as for the initial particles (ex-CMS) and for both temperature of the TOPO calcination experiments, 400 and 275 °C. Similarly, the DFT pore size distributions show only minor differences between the template-extracted MSNs (ex-CMS) and the TOPO calcinations at 400 (LC-3) and 275 °C (LC-4), showing mesopores of 3.9 nm (Figure 3.4b) In contrast, the squalene- and TOA-calcined samples (LC-1 and LC-2 respectively) show a slight reduction of the DFT pore size distribution (3.5 for sample LC-1 and 3.8 for sample LC-2, see also Table 3.2). Small-angle X-ray diffraction shows that the first-order (100)-like reflection at 1.93°, diagnostic of the worm-like mesoporous structure, was maintained after thermal HBS-calcination (Figure 3.4c). It has to be noted that the (100)-like reflection at 1.93° of HBS-treated samples shows no shift to higher angles with respect to the ex-CMS nanoparticles. This indicates the absence of unit cell shrinkage, in contrast to the conventional air-calcined MSNs at 550 °C (calc-CMS), with a peak position at 2.28°. IR spectra were measured for the thermal HBS-calcined samples (from LC-1 to LC-4) and are shown in comparison to the template extracted one (ex-CMS, see Figure 3.4d). The spectra of all MSNs show strong vibrations typical of the silica framework at around 1240 – 1050 cm^{-1} (not shown here). In addition, for all samples small C-H stretching modes at 2983, 2935 and 2904 cm^{-1} are observed, corresponding to the asymmetric CH_3, asymmetric CH_2, and symmetric CH_3 stretch vibrations respectively of the ethoxy groups formed during the ethanolic template extraction.[13] Similarly, C-H bending modes at 1396 and 1384 cm^{-1} are observed. After calcination with squalene (sample LC-1), additional C-H stretching bands at 2927 and 2854 cm^{-1} and –CH bending at 1459 and 1381 cm^{-1} are observed. These bands correspond to the position of the alkyl vibrations of squalene,[25] indicating that a small amount of squalene remains at the surface of sample LC-1 after the repetitive washing. Thermogravimetry measurements (Figure 3.5a) on HBS-calcined samples in comparison with the template-extracted nanoparticles (ex-CMS) indeed show a higher weight loss for sample LC-1, treated with squalene, and sample LC-2, calcined with TOA. We assume that residual solvent, even after repetitive washing, is present in both samples. Figure 3.5b shows the scanning transmission electron microscopy (STEM) image detailing the small particle size and the worm-like mesoporous structure for the sample LC-4.

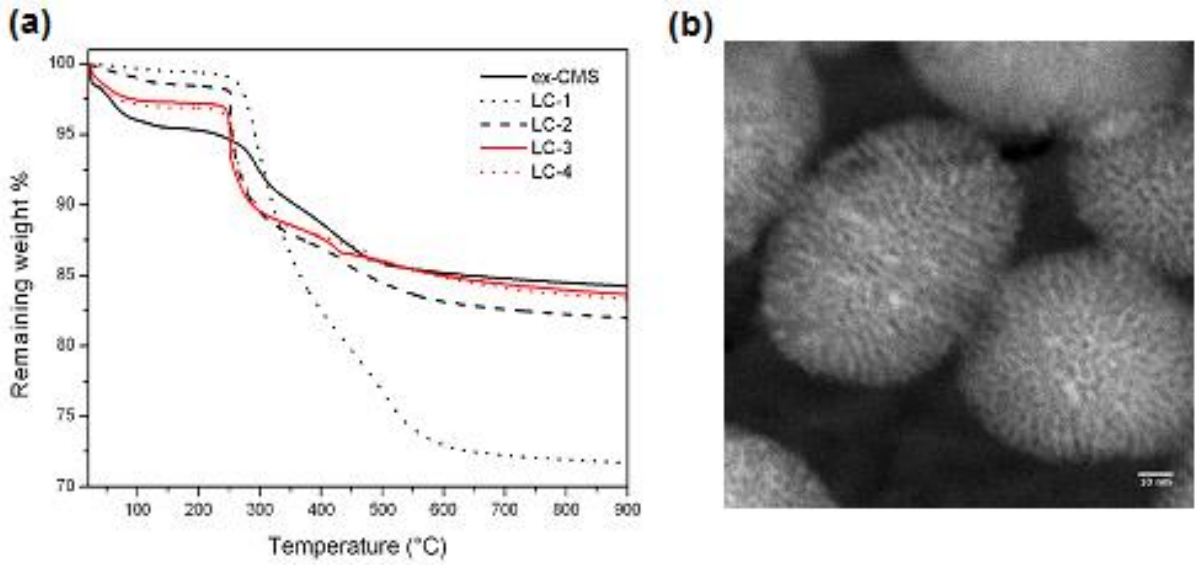

Figure 3.5: (a) Thermogravimetric measurements on thermal HBS-calcined samples (from LC-1 to LC-4) in comparison with the template extracted nanoparticles (ex-CMS); (b) STEM image of thermal TOPO-calcined MSNs at 275 °C (LC-4).

Characterization of the MSNs after microwave-assisted liquid calcination (samples LC-7 and LC-8)

Microwave-assisted calcinations of the template-extracted MSNs (ex-CMS) were only performed at 200 °C and conducted for thirty minutes and two hours. The nitrogen sorption isotherms (Figure 3.6a) show similar features for the 30 min microwave-calcined sample (LC-7) and the 2 h microwave-calcined sample (LC-8) as compared to the starting MSNs (ex-CMS). For both the thirty minutes (LC-7) and the two hour (LC-8) microwave-assisted calcinations the nitrogen sorption isotherm and DFT pore size distributions were similar to the initial MSNs (ex-CMS) (Figure 3.6a and b).

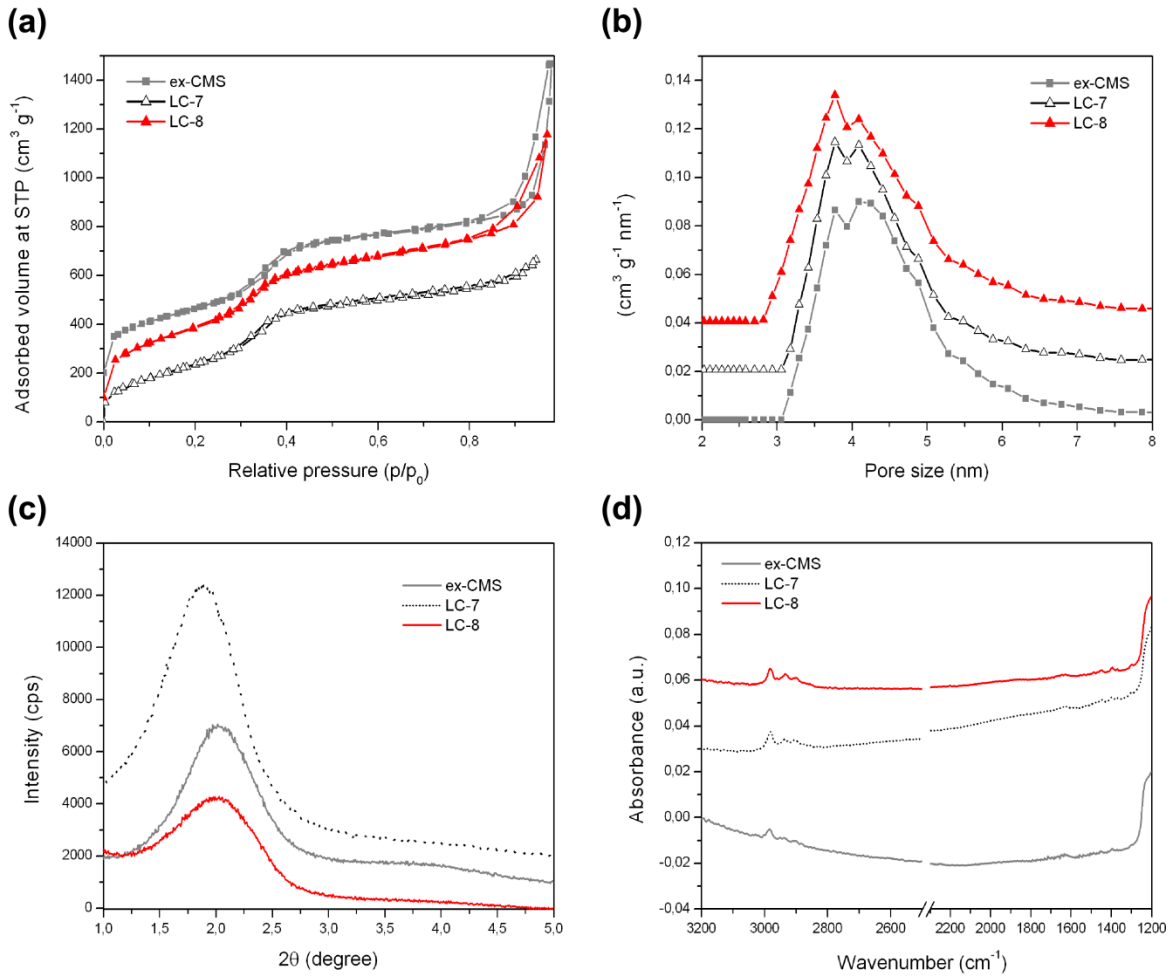

Figure 3.6: (a) Nitrogen sorption isotherms; (b) DFT pore size distributions; (c) small-angle XRD; and (d) infrared spectra for the microwave-assisted TOPO calcinations at 200 °C for 30 min (LC-7) and 2 h (LC-8) compared to the starting template-extracted MSNs (ex-CMS). For clarity reasons, the nitrogen sorption isotherms in (a) are shifted along the y-axis by 100 units, the pore size distributions in (b) by 0.02 units, the XRD pattern in (c) by 1000 units and the IR spectra in (d) by 0.03 units.

The small-angle X-ray diffraction measurements (Figure 3.6c) show the retention of the worm-like nature of the pore structure, as evidenced by the (100)-like reflection after microwave calcination at 200 °C for either 30 minutes (LC-7) or 2 hours (LC-8). The calcined materials were studied by infrared spectroscopy (Figure 3.6d) and compared with the starting material, sample ex-CMS. The C-H stretching modes at 2983, 2935 and 2904 cm^{-1}, corresponding to the asymmetric CH_3, asymmetric CH_2, and symmetric CH_3 stretching vibrations respectively of the ethoxy groups formed during the ethanolic template extraction,[13] are observed for the template-extracted sample ex-CMS, as well as for both the 30 min (LC-7) and 2 h microwave-calcined (LC-8) samples. The lack of the C-H stretching

intensity at 3019, 2967, 2892 cm^{-1} assigned to TOPO,[25] is indicative of efficient TOPO removal after the microwave calcination. Figure 3.7 shows the scanning transmission electron microscopy (STEM) image detailing the small particle size and the worm-like mesoporous structure for the sample LC-8.

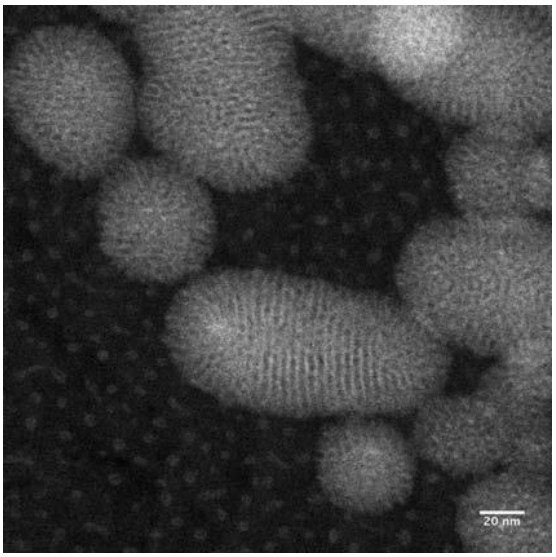

Figure 3.7: STEM image of 2 h microwave-assisted TOPO-calcined MSNs (LC-8).

Characterization of the unextracted MSNs after thermal liquid calcination (samples LC-5 and LC-6)

It was of interest to determine whether the thermal calcinations that have been shown to increase the degree of silica condensation would simultaneously extract template from unextracted MSNs (UN-CMS); this would save a work-up step while preparing a more stable MSNs. Calcinations were done at 275 °C and 400 °C via the thermal method. From the nitrogen absorption isotherms (Figure 3.3) one can conclude that calcination in TOPO is as efficient as the solution-phase ethanolic template extraction, as similar surface areas and pore volumes are obtained. The DFT pore size distribution for sample LC-5 prepared from non-extracted MSNs (UN-CMS) features slightly decreased values, due to a minimal residue of the template. Sample LC-6 shows a similar DFT pore size distribution as compared to the ex-CMS sample.

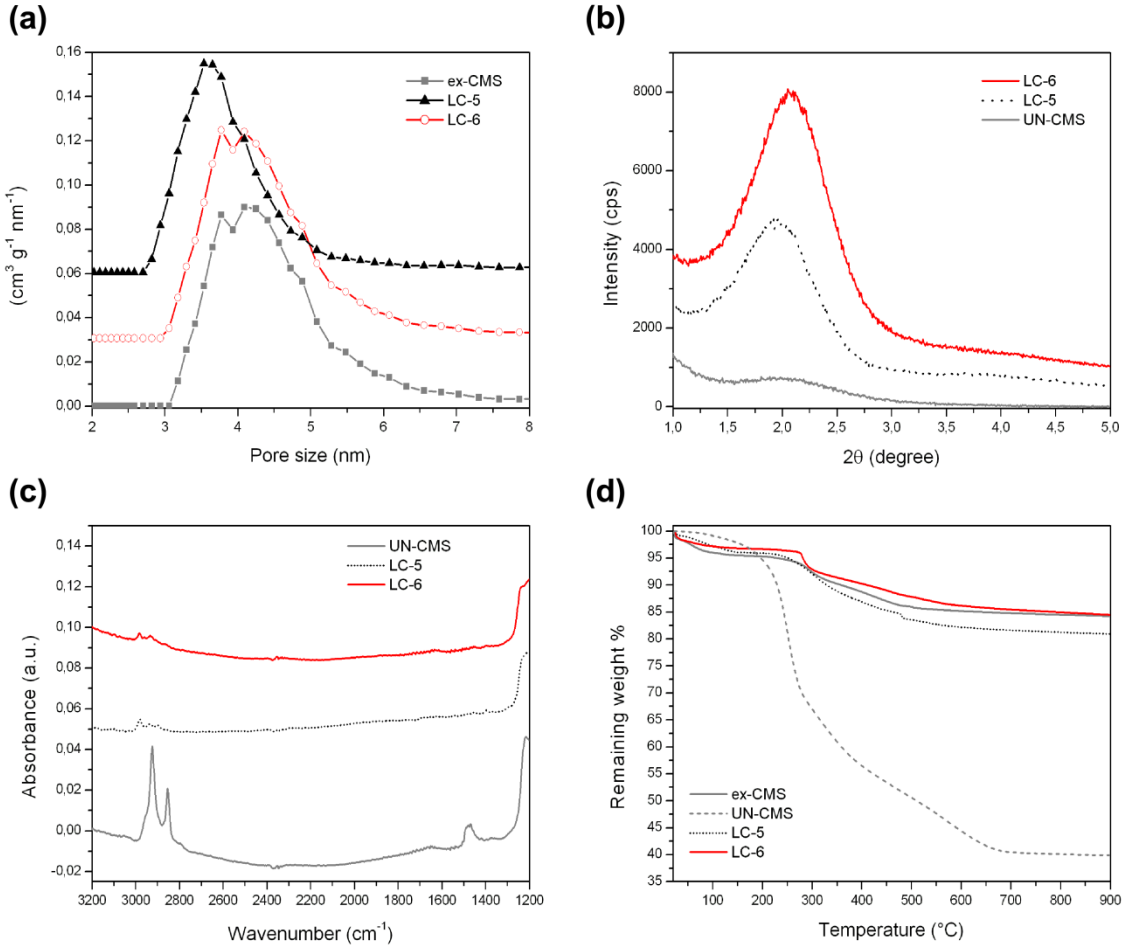

Figure 3.8: (a) DFT pore size distributions, (b) small angle XRD, (c) IR spectroscopy, and (d) thermogravimetric analysis (TGA) for the liquid-calcined MSNs with TOPO at 275 °C (LC-5) and 400 °C (LC-6) prepared from non-extracted particles (UN-CMS). For comparison the template-extracted non-calcined MSNs (ex-CMS) are also shown. For clarity reasons, the pore size distributions in (a) are shifted along the y-axis by 0.03 units, the XRD patterns in (b) by 500 units and the IR spectra in (c) by 0.05 units.

Small angle X-ray diffraction of both samples LC-5 and LC-6 shows an increase in intensity of the (100)-like reflection with respect to the UN-CMS pattern, as expected after the template removal from the mesopores. Only small shifts of the (100)-like reflection are observed for both samples LC-5 and LC-6, indicating only minor changes in the mesoporous structure (Figure 3.8b). Infrared spectroscopy was used to assess the removal of both the TOPO and of the template during the calcination step (Figure 3.8c). The spectrum of non-extracted MSNs (UN-CMS) shows the typical vibration modes of the CTAC template alkyl chains (C-H stretching at 2853 and 2925 cm^{-1} and a weaker band at 1480 cm^{-1}). The absence of these stretching vibrations in the calcined particles (LC-5 and LC-6) indicates that the calcination in TOPO successfully removed most of the template. In addition, the absence of stretching

modes at 3019, 2967, 2892 cm^{-1} assigned to TOPO is indicative of efficient TOPO removal after thermal calcinations in both samples LC-5 and LC-6. At small intensities, C-H stretching modes at 2983, 2935 and 2904 cm^{-1} of ethoxy groups in both samples LC-5 and LC-6 are observed; they may be attributed to the repetitive washing steps in ethanol. Figure 3.8d illustrates the TGA profiles for both TOPO-calcined MSNs (LC-5 and LC-6) in comparison to the unextracted MSNs (UN-CMS) and the template extracted MSNs (ex-CMS). The first significant weight loss for the template-containing MSNs (UN-CMS) begins at around 200 °C, corresponding to template loss, and results in a weight loss of about 55 wt%. For both samples LC-5 and LC-6 the initial 4-5% weight loss (up to about 100 °C) is attributed to physically adsorbed water at the MSN surface. The other weight loss occurs between 300 and 600 °C, with a weight loss of 14 wt% for sample LC-5 calcined at 275 °C and of 10 wt% for sample LC-6, calcined at 400 °C. Similarly, the solvent extracted MSNs (ex-CMS) show a weight loss of 5 wt%, due to the loss of physisorbed water, occurring at 100 °C, and of 10 wt% due to the decomposition of ethoxy groups and silanol condensation at temperatures above 300 °C. Therefore, no difference in weight loss is observed between the ex-CMS nanoparticles and sample LC-6, indicating in this last sample the complete removal of the template CTAC. The slight difference in weight loss (4 wt%) between the extracted sample (ex-CMS) and the TOPO-calcined MSNs at 275 °C(LC-5) could be mainly attributed to residual CTAC template due to the lower temperature used during the TOPO-treatment.

3.3 Conclusion

Summarizing, we describe a novel "liquid calcination" method for preparing highly condensed mesoporous silica nanoparticles that form stable colloidal suspensions. The MSNs calcined in high-boiling solvents (HBS) retain their original pore size, experience no unit cell shrinkage or particle agglomeration, and exhibit a significant decrease in silanol content. The thermal liquid calcination of unextracted MSNs in TOPO at 400 °C produces calcined MSNs with similar characteristics compared to the MSNs obtained from the liquid calcination of extracted MSNs; the surface area, pore volume, pore sizes, particle sizes, pore morphology and degree of silica condensation are all comparable. The high degree of condensation and the resulting stability will open up new fields of application for colloidal mesoporous nanoparticles.

3.4 Experimental

3.4.1 Synthesis of MSNs

A mixture of 14.2 g (95.6 mmol) of triethanolamine (TEA, Aldrich, 98%) and 1.92 g (9.22 mmol) of tetraethyl orthosilicate (TEOS, Fluka, >98%) was heated for 20 minutes at 90 °C without stirring in a 100 mL polypropylene reactor (Solution 1). Meanwhile, a mixture (Solution 2) of 2.41 mL (7.29 mmol) of cetyltrimethylammonium chloride (CTAC, Fluka, 25 wt% in H_2O) and 21.7 g (1.21 mol) of bi-distilled water from a Millipore system (Milli-Q Academic A10) was heated at 60 °C and then added to the Solution 1. The resulting mixture, having a molar composition of 1 TEOS: 0.20 CTAC: 10.4 TEA: 130.2 H_2O, was then stirred (500 rpm) at room temperature overnight. After addition of 100 mL ethanol, the UN-CMS nanoparticles were separated by centrifugation (19.000 rpm, 43.146 RCF, 20 min) and redispersed in ethanol. The MSN concentration was determined by drying and weighing a known volume of the colloidal suspension.

3.4.2 Template Extraction

Extraction of the organic template from the mesoporous silica nanoparticles (UN-CMS) was performed by heating the colloidal suspension for 45 minutes under reflux (90 °C oil bath) in 100 mL of an ethanolic solution containing 2 g ammonium nitrate, followed by 45 minutes under reflux in a solution of 10 mL of concentrated hydrochloric acid and 90 mL absolute ethanol. The MSNs were then separated by centrifugation (19.000 rpm, 43.146 RCF, 30 min). The material was washed with ethanol after each extraction step. Ex-CMS materials were then redispersed in absolute ethanol, obtaining clear ethanolic colloidal suspensions.

3.4.3 Thermal Liquid-Phase Calcination

100 mg of the unextracted (UN-CMS) or the template-extracted MSNs (ex-CMS) in ethanolic suspension were respectively added to 7 g of molten trioctylphosphine oxide (TOPO), 10 mL of squalene or 10 mL of tri-*n*-octylamine (TOA) in a round bottom flask equipped with a reflux condenser. The ethanol was separated from the solution under vacuum (175 mbar at 60 °C). The solution was heated to 275 °C or 400 °C using a silicon carbide (SiC) grain bath under a nitrogen atmosphere and the solution was maintained at this temperature for 5 h. At the end of this period, the solutions were cooled to 50 °C where TOPO is still liquid (whereas squalene and TOA are liquid also at RT), and 10 mL of absolute ethanol was added. The

ethanol solutions were centrifuged (19.000 rpm, 43.146 RFC, 20 min) to isolate the particles, which were then rinsed with ethanol, redispersed in 100 mL ethanol and centrifuged again under the same conditions. This process was repeated for a total of five times, in order to remove the residual high-boiling-point solvents. After the final centrifugation the particles were resuspended in absolute ethanol.

For comparison, air-calcined MSNs were also prepared starting from the template-extracted ones (sample ex-CMS). This calc-CMS sample was heated in air to 550 °C for 7 h with a heating rate of 1,5 °C/min.

3.4.4 Microwave-Assisted Liquid-Phase Calcination

The amount of 100 mg of the template-extracted MSNs (ex-CMS) in ethanol was added to 7 g of molten TOPO in a 20 mL microwave-compatible vial. The ethanol was separated from the solution under vacuum (175 mbar at 60 °C). The solution was stirred and heated at 200 °C by means of microwave irradiation for two different times: 30 min (LC-7) and 120 min (LC-8). The solution was allowed to cool to 50 °C and was diluted with 10 mL absolute ethanol. The ethanolic solution was centrifuged (19.000 rpm, 43.146 RCF, 20 min) to isolate the particles, which were then rinsed with ethanol, redispersed in 100 mL ethanol and centrifuged again under the same conditions. This process was repeated for a total of five centrifugations. After the final centrifugation the particles were resuspended in absolute ethanol.

3.4.5 Characterization

All MSN samples were characterized by nitrogen sorption measurements, performed on a Quantachrome Instruments NOVA 4000e at -196 °C. Sample outgassing was performed at 120 °C for 12 hours at a vacuum of 10 mTorr. Pore size and pore volume were calculated using a NLDFT equilibrium model of N_2 on silica, based on the desorption branch of the isotherm. A BET model was used in the range of 0.05 – 0.20 p/p_0 to estimate the specific surface area. Dynamic light scattering (DLS) measurements were carried out on ~1 mg/mL ethanolic colloidal solutions using a Malvern Zetasizer-Nano instrument with a 4 mW He-Ne laser (633 nm) with an avalanche photodiode detector. Thermogravimetric analyses (TGA) of the bulk samples (about 10 mg of powder dried at 60 °C) were performed on a Netzsch STA 440 Jupiter thermobalance with a heating rate of 10 °C/min in a stream of synthetic air of about 25 mL/min. X-ray diffraction patterns were collected on solid samples at small angles on a Bruker D8 Discover with Ni-filtered Cu-K_α radiation and a position-sensitive detector (Vantec). Single pulse ^{29}Si-MAS solid-state NMR measurements were performed on a Bruker

DSX Advance500 FT spectrometer in a 4 mm ZrO_2 rotor at a frequency of 50 MHz. Infrared spectra were collected on a Bruker Equinox 55 operating under attenuated total reflectance (ATR) (spectra were background subtracted). For scanning transmission electron microscopy (STEM) at 300 kV using a Titan 80-300 kV microscope, samples were prepared by adding 3 drops of the ethanolic MSN suspension (~3 wt%) to 4 mL absolute EtOH and drying of a drop of the resulting diluted colloidal suspension on a carbon-coated copper grid.

3.5 Appendix

Table 3.3: Quantification of the Q^3/Q^4 area ratio deconvolved by Gaussian/Lorentzian fitting using Deconv2Dxy software.[23] The values for the shift, area and width of both peaks (Q^3 and Q^4) are obtained from ^{29}Si-MAS NMR spectra.

Sample	Shift (ppm)	Area (a.u.)	Width (ppm)	Chi²	Q^3/Q^4
UN-CMS	-101 -109	$2.62*10^6$ $2.42*10^6$	8.42 8.13	0.0473	1.08
ex-CMS	-102 -110	$1.65*10^6$ $1.61*10^6$	7.47 6.68	0.0401	1.02
LC-1	-102 -110	$2.89*10^6$ $3.83*10^6$	10.3 9.60	0.0481	0.755
LC-2	-103 -110	$2.99*10^6$ $3.76*10^6$	8.82 8.09	0.0664	0.795
LC-3	-103 -110	$3.99*10^6$ $4.89*10^6$	9.23 7.55	0.0160	0.816
LC-4	-102 -110	$3.10*10^6$ $3,87*10^6$	8.85 9.19	0.0264	0.801
LC-5	-103 -110	$4.21*10^6$ $4.03*10^6$	8.89 7.52	0.0182	1.04
LC-6	-103 -110	$3.83*10^6$ $4.21*10^6$	11.7 8.59	0.0540	0.910
LC-8	-102 -110	$4.00*10^6$ $3.97*10^6$	9.01 8.06	0.0399	1.01
calc-CMS	-102 -110	$3.22*10^6$ $5.87*10^6$	9.51 9.06	0.0142	0.549

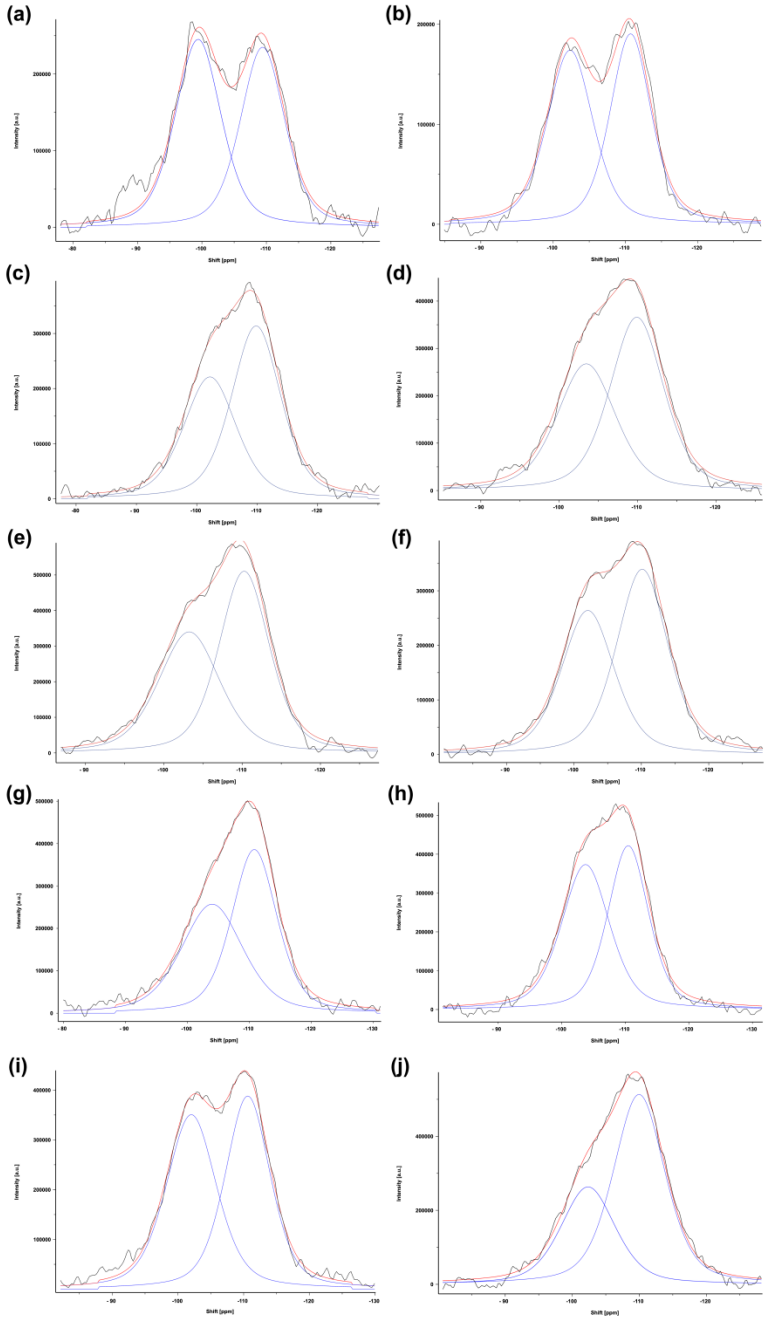

Figure 3.9: Deconvolution results of the Q^3 and Q^4 peaks from ^{29}Si-MAS NMR measurements of the samples: (a) UN-CMS (unextracted MSNs); (b) ex-CMS (solvent extracted MSNs); (c) LC-1 (thermal squalene-calcined extracted MSNs at 400 °C for 5 h); (d) LC-2 (thermal TOA-calcined extracted MSNs at 400 °C for 5 h); (e) LC-3 (thermal TOPO-calcined extracted MSNs at 400 °C for 5 h); (f) LC-4 (thermal TOPO-calcined extracted MSNs at 275 °C for 5 h); (g) LC-5 (thermal TOPO-calcined unextracted MSNs at 275 °C for 5 h); (h) LC-6 (thermal TOPO-calcined unextracted MSNs at 400 °C for 5 h); (i) LC-8 (microwave-assisted TOPO-calcined extracted MSNs at 200 °C for 2 h); and (j) calc-CMS (air-calcined extracted MSNs at 550 °C for 7 h).

3.6 References

[1] Y. Wan, D. Zhao, *Chem. Rev.* **2007**, *107*, 2821.

[2] F. Hoffmann, M. Cornelius, J. Morell, M. Fröba, *Angew. Chem. Int. Ed.* **2006**, *45*, 3216.

[3] F. Schüth, *Chem. Mater.* **2001**, *13*, 3184.

[4] G. S. Attard, J. C. Glyde, C. G. Göltner, *Nature* **1995**, *378*, 366.

[5] C. T. Kresge, M. E. Leonowicz, W. J. Roth, J. C. Vartuli, J. S. Beck, *Nature* **1992**, *359*, 710.

[6] M. Kruk, M. Jaroniec, C. H. Ko, R. Ryoo, *Chem. Mater.* **2000**, *12*, 1961.

[7] K. W. Gallis, C. C. Landry, *Adv. Mater.* **2001**, *13*, 23.

[8] A. Hozumi, Y. Yokogawa, T. Kameyama, K. Hiraku, H. Sugimura, O. Takai, M. Okido, *Adv. Mater.* **2000**, *12*, 985.

[9] C.-Y. Lai, B. G. Trewyn, D. M. Jeftinija, K. Jeftinija, S. Xu, S. Jeftinija, V. S. Y. Lin, *J. Am. Chem. Soc.* **2003**, *125*, 4451.

[10] A. Katiyar, S. Yadav, P. G. Smirniotis, N. G. Pinto, *J. Chromatogr., A* **2006**, *1122*, 13.

[11] C.-Y. Chen, H.-X. Li, M. E. Davis, *Microporous Mater.* **1993**, *2*, 17.

[12] V. Cauda, A. Schlossbauer, J. Kecht, A. Zürner, T. Bein, *J. Am. Chem. Soc.* **2009**, *131*, 11361.

[13] J. Kecht, T. Bein, *Microporous and Mesoporous Mater.* **2008**, *116*, 123.

[14] C. Urata, Y. Aoyama, A. Tonegawa, Y. Yamauchi, K. Kuroda, *Chem. Commun.* **2009**, 5094.

[15] V. Cauda, A. Schlossbauer, T. Bein, *Microporous and Mesoporous Mater.* **2010**, *132*, 60.

[16] V. Cauda, C. Argyo, T. Bein, *J. Mater. Chem.* **2010**, *20*, 8693.

[17] M. Ghosh, K. Biswas, A. Sundaresan, C. N. R. Rao, *J. Mater. Chem.* **2006**, *16*, 106.

[18] Y. Hou, H. Kondoh, T. Ohta, S. Gao, *Appl. Surf. Sci.* **2005**, *241*, 218.

[19] N. Zaitseva, Z. R. Dai, C. D. Grant, J. Harper, C. Saw, *Chem. Mater.* **2007**, *19*, 5174.

[20] K. Möller, J. Kobler, T. Bein, *Adv. Funct. Mater.* **2007**, *17*, 605.

[21] J. A. Gerbec, D. Magana, A. Washington, G. F. Strouse, *J. Am. Chem. Soc.* **2005**, *127*, 15791.

[22] R. N. Gedye, J. B. Wei, *Can. J. Chem.* **1998**, *76*, 525.

[23] *The deconvolution software was kindly provided by Dr. Jörn Schmedt auf der Günne*.

[24] C.-Y. Chen, S. L. Burkett, H.-X. Li, M. E. Davis, *Microporous Mater.* **1993**, *2*, 27.

[25] *Trioctylphosphine oxide, squalene, and tri-n-octylamine FTIR-Raman data sheets from www.sigma-aldrich.com/catalog.*

4 Superparamagnetic Nanocomposites with Multifunctional Mesoporous Silica Shells

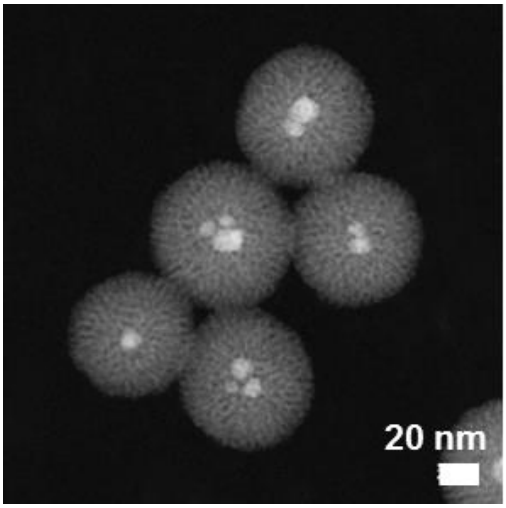

4.1 Introduction

Magnetic nanocomposites consisting of magnetic cores and mesoporous silica shells have been extensively studied in the past decade, both in terms of precise control over the synthesis and appropriate applications.[1-3] These magnetic nanoparticles have a wide range of applications including magnetic resonance imaging (MRI), hyperthermia treatment, and targeted drug delivery, since they combine different advantageous properties in one multifunctional nanocomposite.[4-5] Their characteristics enable magnetic separation and targeting, surface modification, and high cargo loading capacity along with high chemical stability and biocompatibility.[6-8] An on-demand magnetic behavior can be achieved by employing magnetic nanocrystals (NCs) as a core. For example, nano-sized iron oxide particles consisting of only one single crystal domain (diameter < 20 nm) exhibit superparamagnetic properties. Such NCs do not have permanent magnetic moments but allow for targeting of biological objects, such as tissues or organs, by exposure to an external magnetic field.[9-10] Various synthesis strategies including thermal decomposition,[11-12] co-precipitation,[13-14] and hydrothermal approaches[15-16] have resulted in various precisely tunable magnetic properties, morphologies and structural phases such as cubic magnetite (Fe_3O_4) or maghemite (γ-Fe_2O_3) exhibiting an inverse spinel structure. Today, coated

superparamagnetic iron oxide NCs are widely used in biomedical applications, particularly as contrast agents for MRI.[17-18] A coating with a mesoporous silica shell provides protection against fast degradation and improved dispersibility in biological fluids due to prevention of aggregation, accompanied by the ability to create functionalized surfaces and storage characteristics for cargo molecules.[19] In 2008, Hyeon and coworkers first reported the synthesis of magnetic NCs coated with fluorescently labeled mesoporous silica shells that were utilized as drug nanocarriers.[20] Surfactants such as cetyltrimethylammonium bromide (CTAB) simultaneously perform two different tasks in this synthesis approach. First, these molecules permit transfer of the hydrophobic NCs to the aqueous phase via a ligand-exchange process. Secondly, the surfactant molecules act as a template for the subsequent sol-gel reaction of the silica source creating mesoporous silica shells around the magnetic NCs. Nanovehicles with magnetic cores based on mesoporous silica can respond to an external magnetic field and feature high surface area and pore volume, along with the ability to implement functional groups which makes them promising candidates for controlled drug delivery.[21-23] These multifunctional magnetic silica nanocomposites designed for magnetically targeted cell uptake and drug delivery in combination with imaging capabilities have already been synthesized and *in vitro* and *in vivo* investigations have been performed before.[19-20] However, the imaging and targeting performance of many magnetic nanocomposites is seriously affected by only low magnetization due to high non-magnetic silica content.[24-25] The magnetic properties can be improved by doping the iron oxide NCs, for instance with Zn^{2+} and Mn^{2+} ions, resulting in ferrite nanoparticles which offer precisely tunable and high magnetization values.[26-28]

Here, we report on a new synthesis strategy to create multifunctional mesoporous silica nanoparticles (MSNs) consisting of a superparamagnetic Zn-doped manganese ferrite core. The mesoporous silica shell itself consists of several compartments enclosing functional groups for further modification. An inner functional pore modification allows for hosting cargo molecules and fluorescent labels, and an external functional layer offers selective grafting of required organic molecules such as stabilizing agents or targeting ligands. These magnetic nanocomposites hold promise as drug nanocarrier systems providing physical targeting capability in an external magnetic field. Moreover, they can additionally serve as imaging agents for magnetic resonance and fluorescence imaging.

4.2 Results and Discussion

Magnetic nanocomposites based on mesoporous silica nanoparticles have been synthesized in two steps. First, a one-pot thermal decomposition procedure resulted in zinc-doped manganese ferrite NCs (Zn-MnFe NCs), as previously described.[26] In brief, the precursors iron(III) acetylacetonate ($Fe(acac)_3$), zinc chloride ($ZnCl_2$) and manganese chloride ($MnCl_2$) were dissolved in octylether. By addition of oleic acid and oleylamine which serve as capping agents, the particle growth can be limited. The reaction mixture was heated to 300 °C for 1 h under nitrogen atmosphere and dark-brown NCs were subsequently collected by centrifugation. Dynamic light scattering (DLS) measurements feature an average particle size of 10 nm with narrow particle size distribution and no agglomeration could be observed in toluene (Figure 4.1).

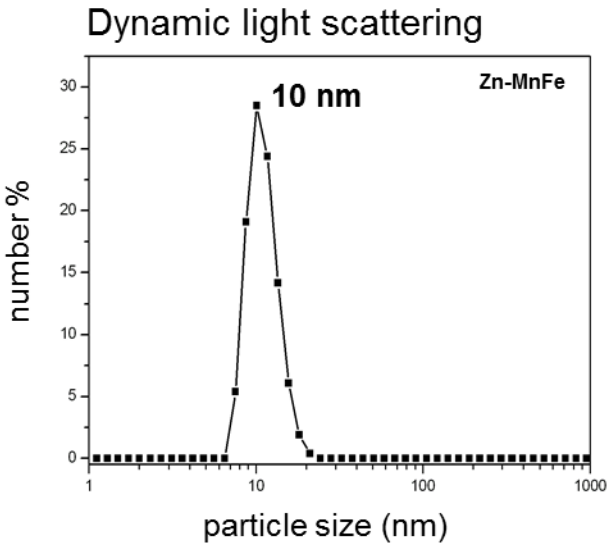

Figure 4.1: Dynamic light scattering (DLS) measurement of Zn-doped manganese ferrite nanocrystals (Zn-MnFe NCs).

Transmission electron micrographs (TEM) provide information about morphology, size and crystallinity of the ferrite NCs (Figure 4.2 a). The NCs consist of single crystal domains with an average size of about 8 nm. The lattice fringes of a single NC embedded in silica can be clearly seen in a high resolution TEM (HRTEM) image (Appendix 4.5). Crystallinity is further proven by selected area electron diffraction (SAED) (inset Figure 4.2 a). The doping of the manganese ferrite NCs with zinc ions can be confirmed by energy dispersive X-ray (EDX) analysis (Figure 4.2 b). The additional content of copper belongs to the sample holder for TEM specimen consisting of a carbon-coated copper grid.

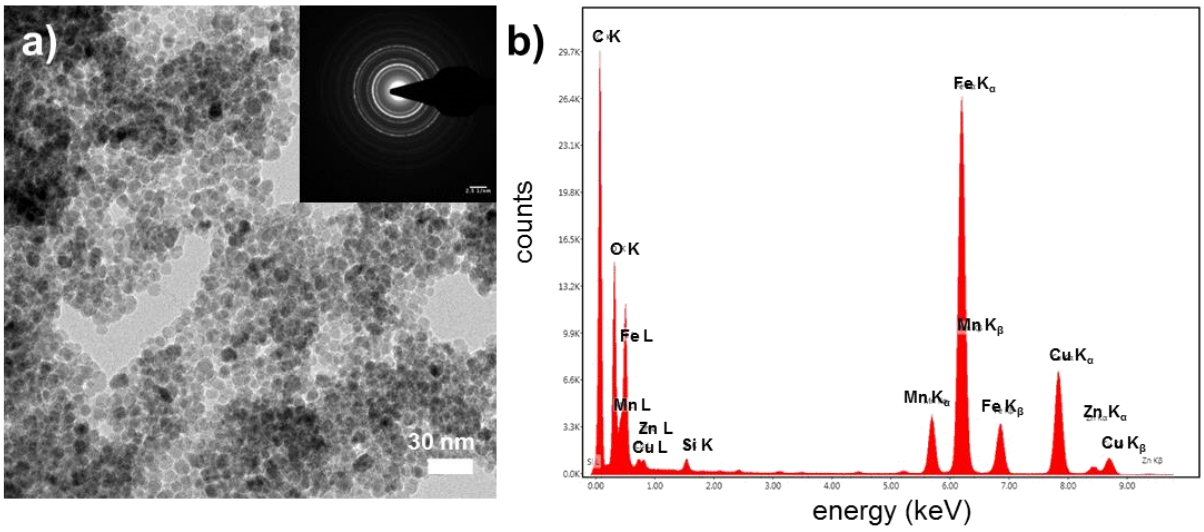

Figure 4.2: (a) Transmission electron micrograph of Zn-doped manganese ferrite NCs. The inset shows a SAED pattern proving crystallinity of the sample. (b) Energy dispersive X-ray (EDX) analysis of the sample Zn-MnFe.

Further information about the crystallinity of the ferrite nanoparticles can be obtained by X-ray diffraction (XRD) measurements. The XRD pattern in Figure 4.3a was collected with Cu-K_α radiation and show several distinct reflections. Due to fluorescent interference of the ferrite NCs with the Cu-K_α radiation, a low signal-to-noise ratio is obtained. Therefore, another diffractogram (Figure 4.3b) was recorded with Co-K_α radiation. Both XRD patterns showed the formation of crystalline Zn-MnFe material. A Scherrer calculation suggests a crystalline domain size of about 9 nm. Since the sizes of the nanoparticles obtained from DLS measurements and TEM images are also on this scale, the synthesized NCs consist of only one single crystalline domain. This is an important requirement for superparamagnetism. Only nanoparticles sizes smaller than 20 nm exhibit superparamagnetic properties.[29]

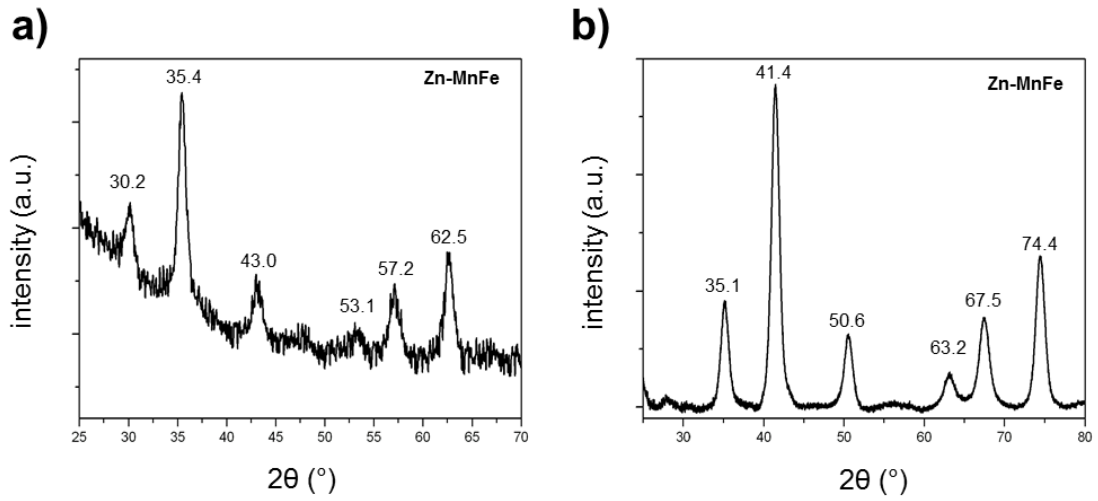

Figure 4.3: X-ray Diffraction (XRD) patterns of Zn-doped manganese ferrite nanocrystals (Zn-MnFe) performed (a) with Cu-K_α radiation and (b) with Co-K_α radiation.

Vibrational spectroscopy gives information about organic compounds within the sample. Oleic acid and oleylamine was used during the synthesis procedure to limit the particle growth by forming an organic capping shell around single NCs. Their existence in the Zn-MnFe sample can be observed by infra-red (IR) spectroscopy (Figure 4.4a). Distinct bands at 2923 and 2854 cm^{-1} can be assigned to the characteristic C-H stretching vibration of the alkyl chains of both capping agents. The characteristic band for the C=O stretching vibration of carboxyl groups is shifted to lower wavenumbers (1589 cm^{-1}). This significant shift can be attributed to the coordination of the carboxy groups to iron or manganese metal centers at the interface of the NCs. Additional bands at 3205 cm^{-1} (broad, N-H_{str}), 2422 and 2167 cm^{-1} (C=C_{str}), 1411 cm^{-1} (N-H_{def}), and 910 cm^{-1} (C-H_{def}) further prove the presence of oleylamine and oleic acid in the ferrite NC sample.

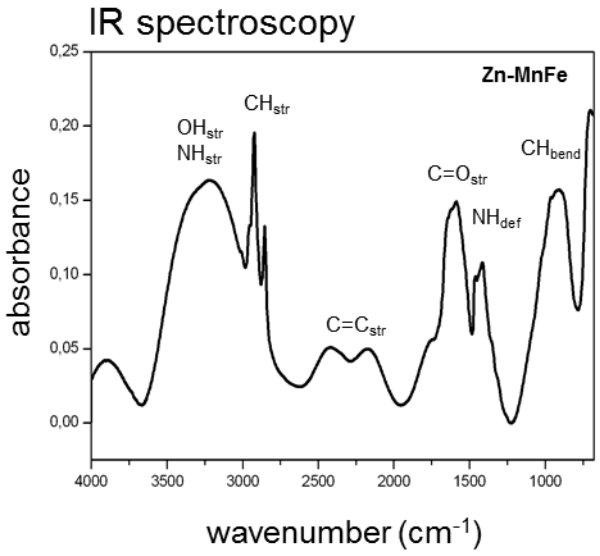

Figure 4.4: Infrared spectroscopy data of Zn-doped manganese ferrite nanocrystals (Zn-MnFe).

The magnetization behavior of the ferrite NCs can be obtained with a superconducting quantum interference device (SQUID). The measurement of magnetic properties showed that the sample is superparamagnetic at room temperature (300 K). The field-dependent magnetization curve of the sample Zn-MnFe showed quick magnetization in an external magnetic field (10 kOe) with saturation magnetization values of about 200 emu/g (Figure 4.5). In comparison, for superparamagnetic iron oxide nanoparticles magnetization values of only about 50 emu/g can be obtained.[29] Doping with zinc ions efficiently modulates the manganese ferrite NCs resulting in 4-fold improved magnetization properties. The absence of a hysteresis proves the absence of remanence of magnetization and indicates a superparamagnetic character of the Zn-MnFe NCs.

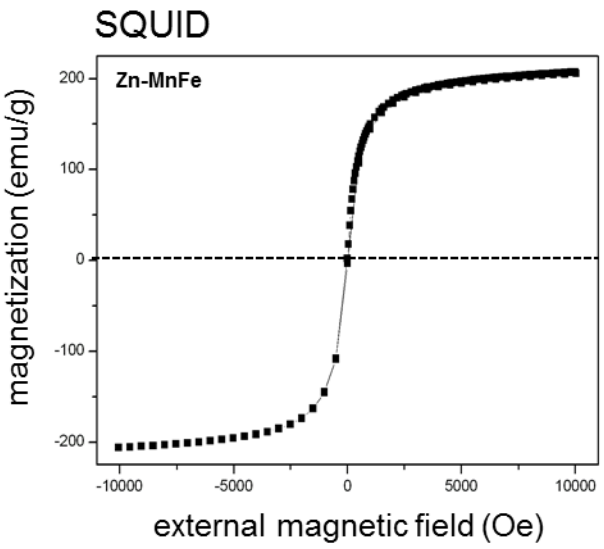

Figure 4.5: Superconducting quantum interference device (SQUID) data of superparamagnetic Zn-doped manganese ferrite nanocrystals (Zn-MnFe).

The second step to create magnetic nanocomposites with functionalized mesoporous silica shells was performed via a sol-gel synthesis approach. Before generating a mesoporous silica shell around the NCs, a phase transfer of the ferrite NCs capped with organic ligands from the organic phase to the aqueous phase was needed. This transfer was achieved by addition of a surfactant (cetyltrimethylammonium chloride, CTAC) following a previously described method.[20] The ferrite NCs dispersed in chloroform were mixed with an aqueous solution of CTAC to gain water-dispersibility (Figure 4.6).

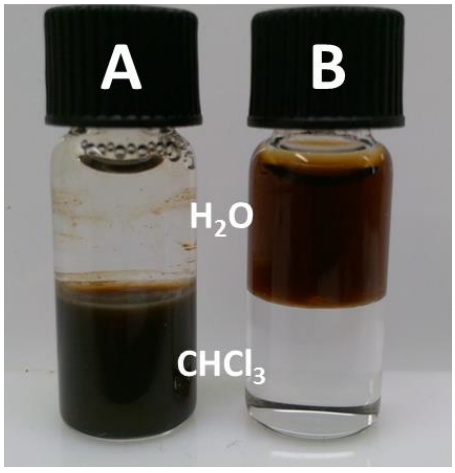

Figure 4.6: Phase transfer of Zn-doped manganese ferrite nanocrystals (Zn-MnFe, brown) with surfactant molecules (CTAC) from A) chloroform (oleate-capped NCs) to B) aqueous solution (CTAC-stabilized NCs).

This emulsion was sonicated and the organic solvent was evaporated at elevated temperatures (70 °C). An excess of CTAC additionally served as a template in the following silica condensation reaction to form an outer mesoporous silica shell. For a heterogeneous nucleation to create magnetic cores and mesoporous silica shells, it was very important to avoid agglomeration of the ferrite NCs. We found intensive sonication to be essential to obtain monodispersed nanocrystals which can serve as nucleation seeds for the silica framework. Triethanolamine (TEA) was added as base catalyst for the hydrolysis of the silica precursor tetraethyl orthosilicate (TEOS) together with various organoalkoxysilanes. Simultaneously, TEA served as a stabilizing agent lowering the condensation rate to create particles at the nanoscale. A stepwise addition of silica precursors in small portions resulted in functionalized silica shells in a layer-by-layer manner. By using a delayed co-condensation approach, which has been established in our group for core-shell functionalized MSNs,[30] we were able to create separate silica shells in the particles, bearing different functional groups in an onion-like structure. In the present work, we synthesized three different magnetic nanocomposite constructs, namely Zn-MnFe@MSN-$NH_{2\ OUT}$, Zn-MnFe@MSN-Ph/$NH_{2\ IN}$, and Zn-MnFe@MSN-SH_{IN}-$NH_{2\ OUT}$. Ethanolic extraction with ammonium nitrate was carried out to remove the organic template, thus obtaining an accessible mesoporous system.

DLS measurements showed an average particle size of about 106 nm and a narrow particle size distribution for all samples (cf. Table 4.1 and Appendix 4.5). No agglomeration occurred in ethanolic suspensions. All samples showed good colloidal stability. TEM images provide information about the morphology and structure of the nanocomposite systems (Figure 4.7). A typical mesoporous worm-like structure of spherically shaped nanoparticles with integrated magnetic cores could be observed for all samples. The mesoporous channels are clearly visible with near radial alignment. Small nanoparticles (about 8 nm) with higher contrast that were embedded in the center of the silica particles could be identified as crystalline magnetic ferrite NCs (Appendix 4.5). The total size of the nanocomposite particles ranges from 50 – 80 nm depending on the number of integrated magnetic NCs. All samples feature homogeneous morphology and distribution of magnetic cores. For all samples only a small number of encapsulated cores (1 – 5) have been observed. Additionally, scanning TEM (STEM) images provide an even better contrast of the different composites of the samples (Appendix 4.5).

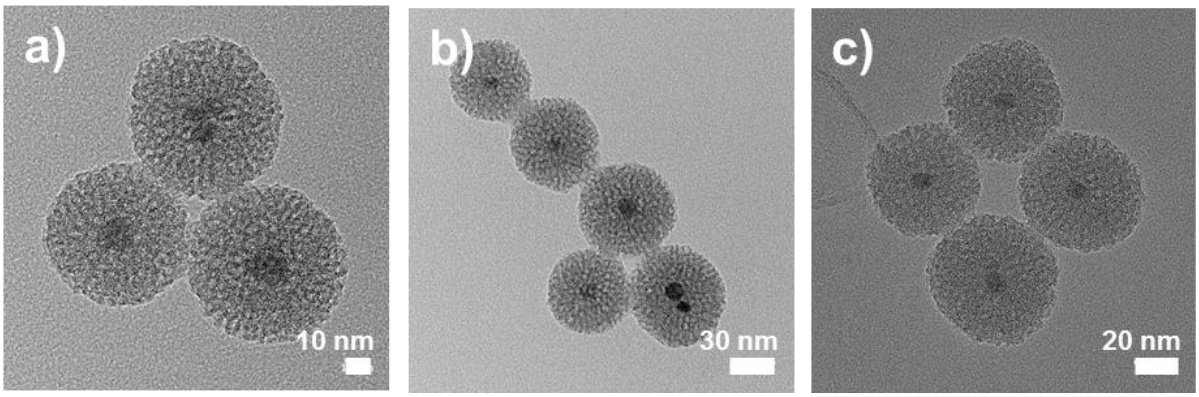

Figure 4.7: Transmission electron micrographs of magnetic nanocomposites. (a) Zn-MnFe@MSN-$NH_{2\ OUT}$, (b) Zn-MnFe@MSN-Ph/$NH_{2\ IN}$ and (c) Zn-MnFe@MSN-SH_{IN}-$NH_{2\ OUT}$ (blue).

Nitrogen sorption measurements give information about the porosity of the silica shell. For all samples, a typical type IV isotherm with inflection points at around 0.3 p/p_0 could be observed indicating a mesoporous structure. Interparticle textural porosity is shown for all samples by a second hysteresis loop at partial pressures of about 0.9 p/p_0. All samples feature high BET surface area, high pore volume, and a defined pore size distribution (Table 4.1). The DFT pore size distribution exhibits an average pore size of 4.3 nm for all samples.

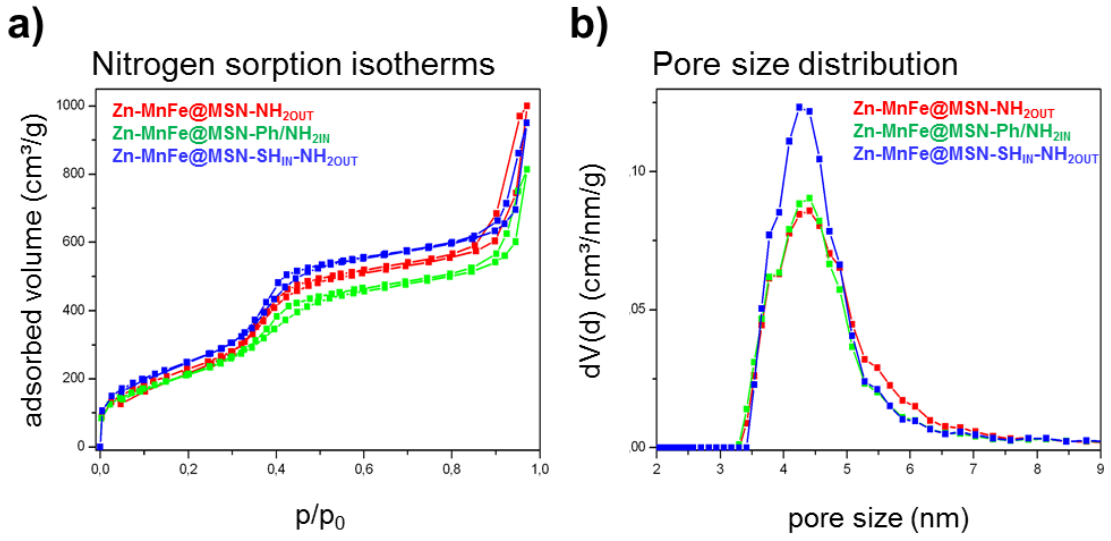

Figure 4.8: (a) Nitrogen sorption isotherms and (b) pore size distribution of magnetic nanocomposites. Zn-MnFe@MSN-$NH_{2\ OUT}$ (red), Zn-MnFe@MSN-Ph/$NH_{2\ IN}$ (green) and Zn-MnFe@MSN-SH_{IN}-$NH_{2\ OUT}$ (blue).

Table 4.1: Structural parameters of magnetic nanocomposites.

Sample	Particle size[a] (nm)	BET surface area (m^2/g)	Pore volume[b] (cm^3/g)	Pore size[c] (nm)
Zn-MnFe@MSN-$NH_{2\ OUT}$	106	860	0.72	4.3
Zn-MnFe@MSN-Ph/$NH_{2\ IN}$	106	800	0.67	4.3
Zn-MnFe@MSN-SH_{IN}-$NH_{2\ OUT}$	106	930	0.80	4.3

[a]Average particle size refers to the peak value of the particle size distribution derived from DLS measurements; [b]Pore volume is calculated up to a pore size of 8 nm to remove the contribution of interparticle porosity; [c]DFT pore size refers to the peak value of the pore size distribution.

The existence of functional groups in the samples can be confirmed with Raman spectroscopy (Figure 4.9a). The sample Zn-MnFe@MSN-SH_{IN}-$NH_{2\ OUT}$ shows a characteristic band at 2585 cm^{-1} (#), which can be assigned to thiol groups (S-H stretching vibration). Bands at 3060 cm^{-1} (*) (C-H stretching vibration of aromatic rings) and 999 cm^{-1} (*) (C-H deformation vibration of aromatic rings) are typical for the phenyl groups of the nanoparticles Zn-MnFe@MSN-Ph/$NH_{2\ IN}$. All samples show additional bands at 2980, 2936 and 2899 cm^{-1}, which indicate C-H stretching vibration modes deriving from alkyl chains including ethoxy groups of the silica framework and capping agents of the ferrite NCs (oleic acid, oleylamine, CTAC). Amino groups can barely be detected since they feature only characteristic bands similar to hydroxyl groups which are also abundant in our nanocomposite materials. Data derived from IR spectroscopy show typical bands of the silica framework appearing at 1245 – 1050 cm^{-1} which can be assigned to asymmetric stretching vibration of Si-O-Si. Two additional bands at 965 cm^{-1} and 795 cm^{-1} for the asymmetric bending and stretching vibration of Si-OH are dominantly present in all samples. Complementary to Raman spectroscopy, the bands for the C-H stretching vibration (2981 – 2904 cm^{-1}) and the C-H bending vibration (1446 cm^{-1}) of alkyl groups were obtained.

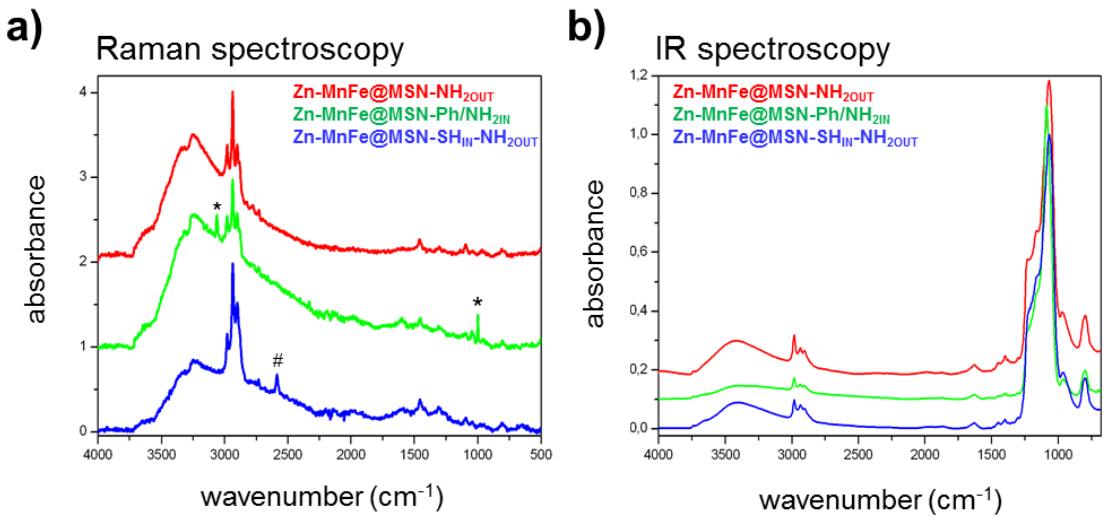

Figure 4.9: (a) Raman and (b) IR spectroscopy data of magnetic nanocomposites: Zn-MnFe@MSN-$NH_{2\ OUT}$ (red), Zn-MnFe@MSN-Ph/$NH_{2\ IN}$ (green) and Zn-MnFe@MSN-SH_{IN}-$NH_{2\ OUT}$ (blue). For clarity reasons, the curves for Raman spectroscopy are shifted along the y-axis by 1.0 units and for IR spectroscopy by 0.1 units.

The zeta potential of the nanoparticles is dependent on the pH value of the aqueous solution. Zeta potential measures the surface charge of nanoparticles which provides information about functional groups at the external particle surface. Positive surface charge refers to protonated amino groups in an acidic milieu. The samples Zn-MnFe@MSN-$NH_{2\ OUT}$ and Zn-MnFe@MSN-SH_{IN}-$NH_{2\ OUT}$ show highly positive zeta potential values over the whole acidic pH range. The isoelectric point (IEP) is around pH 6.5 for both samples featuring amino groups at the outer particle surface. Sample Zn-MnFe@MSN-Ph/$NH_{2\ IN}$ features a more neutral surface charge which is comparable to unfunctionalized MSNs (data not shown). Here, a significant shift of the IEP to lower pH values (4.6) can be observed. Only hydroxyl groups are present at the particle surface leading to a more negative surface charge when deprotonation occurs. The phenyl and amino groups need to be located at the inner part of the silica shell and are not able to influence the zeta potential of these nanoparticles. We assume that only for the samples Zn-MnFe@MSN-$NH_{2\ OUT}$ and Zn-MnFe@MSN-SH_{IN}-$NH_{2\ OUT}$ the amino groups are located at the outer surface of the nanocomposite materials.

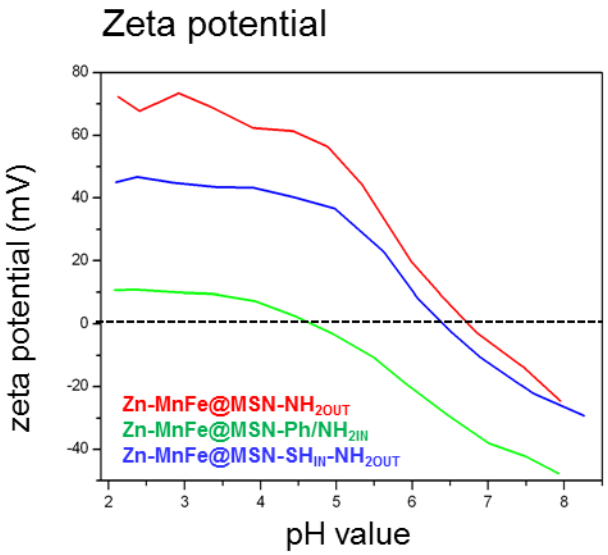

Figure 4.10: Zeta potential titrations of magnetic nanocomposites. Zn-MnFe@MSN-$NH_{2\ OUT}$ (red), Zn-MnFe@MSN-Ph/$NH_{2\ IN}$ (green) and Zn-MnFe@MSN-SH_{IN}-$NH_{2\ OUT}$ (blue).

To prove the physical targeting ability of our magnetic samples, the nanoparticles were exposed to an external magnetic field. As depicted in Figure 4.11 the sample Zn-MnFe@MSN-$NH_{2\ OUT}$ can be collected by a magnet from a well-dispersed aqueous solution.

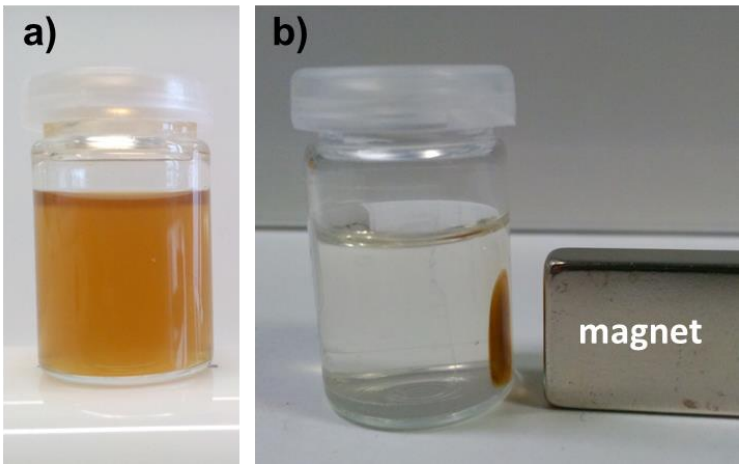

Figure 4.11: Magnetic nanocomposite particles (sample Zn-MnFe@MSN-$NH_{2\ OUT}$) (a) colloidally dispersed in an aqueous solution (b) can be collected by applying an external magnetic field (magnet).

4.3 Conclusion

From the above data, we conclude the successful synthesis of superparamagnetic Zn-doped manganese ferrite NCs, which have been incorporated into multifunctional mesoporous silica nanoparticles as a magnetic core. Different functional silica shells can be created following a delayed co-condensation approach. In the future, a more precise characterization of the location of the functional groups within the silica shell could be performed by quenching experiments with gold colloids (<5 nm) and dye molecules which are covalently attached to the amino groups. Furthermore, the formation of iridium clusters at the location of amino groups can be investigated by tomography analysis, as has already been shown for colloidal MSNs in our group.[31] The combination of superparamagnetic NCs with a multifunctional mesoporous silica shell may enable the generation of an integrated system for imaging-guided, physically targeted drug delivery that comprises functions for triggered drug release at the targeted site.

4.4 Experimental

Materials. Iron(III) acetylacetonate ($Fe(acac)_3$, Aldrich, 97 %), zinc(II) chloride ($ZnCl_2$, Merck) manganese(II) chloride ($MnCl_2$, Merck), octylether (Aldrich, 99%), tetraethyl orthosilicate (TEOS, Fluka, > 99 %), triethanolamine (TEA, Aldrich, 98 %), cetyltrimethylammonium chloride (CTAC, Fluka, 25 % in H_2O), (3-aminopropyl)-triethoxysilane (APTES, ABCR, 96 %), (3-mercaptopropyl)-triethoxysilane (MPTES, ABCR, > 92 %), (3-phenyl)-triethoxysilane (PTES, Sigma, > 98 %), ammonium nitrate, were used as received. Absolute ethanol (EtOH, Aldrich), chloroform ($CHCl_3$, Aldrich) and toluene (Aldrich) were used as solvents without further purification. Bidistilled water was obtained from a Millipore system (Milli-Q Academic A10). Oleic acid (Alfa Aesar, 90 %) and oleylamine (Aldrich, 70 %) were freshly distilled prior to use.

Synthesis of superparamagnetic ferrite nanocrystals. Zn-doped MnFe NCs were synthesized following a thermal decomposition process as previously described.[26] In brief, 0.353 g (1.00 mmol) $Fe(acac)_3$, 30.0 mg (0.220 mmol) $ZnCl_2$ and 63.3 mg (0.320 mmol) $MnCl_2$ were placed in a 50 mL three-neck flask equipped with a refluxer under nitrogen atmosphere. 2.00 mL oleic acid, 4.00 mL oleylamine and 2.06 mL octylether were added and the reaction mixture was heated to 300 °C (SiC bath) for 1 h. The reaction mixture was cooled to room temperature and absolute ethanol was added. The resulting nanoparticles were

washed three times with a mixture of toluene and ethanol (1:9) by centrifugation (10 min, 15,000 rpm, 26,892 rcf) and finally redispersed in 15 ml toluene.

Synthesis of multifunctional nanocomposites.

Fe_3O_4@MSN-$NH_{2\ OUT}$. Prior to the sol-gel reaction, the ferrite NCs were transferred form the organic phase to the aqueous phase. 30 mg of ferrite NCs were dispersed in 10 mL chloroform and placed in a polypropylene reactor. 21.7 g H_2O and 2.41 mL of aqueous CTAC solution (25 wt%) was added generating a second phase. The mixture was sonicated for 15 min (60 % of continuous power (250 W), frequency 20 KHz) using a sonication horn and subsequently the chloroform was evaporated at elevated temperatures (70 °C) for 2 h. After a second sonication step lasting 15 min, the mixture was added to 14.3 g TEA and stirred (700 rpm) at 60 °C. The silica source TEOS (10-times 155 µL, 692 µmol) was added stepwise every 10 min over a total time period of 90 min at constant temperature of 60 °C. After 30 min of stirring, a mixture of TEOS (20.5 µL, 92.2 µmol) and APTES (21.5 µL, 92.2 µmol) was added and the synthesis mixture was stirred at 1000 rpm at room temperature for 12 hours. After addition of ethanol (100 mL), the Zn-MnFe@MSNs were separated by centrifugation (19.000 rpm, 43.146 RCF.for 20 min) and redispersed in ethanol. The template extraction was performed twice by heating the Zn-MnFe@MSN suspension under reflux at 90 °C (oil bath) for 45 min in an ethanolic solution (100 mL) containing ammonium nitrate (2 g). The Zn-MnFe@MSNs were purified by centrifugation and washed with ethanol after each extraction step. The resulting nanoparticles were stored in an ethanolic solution.

Fe_3O_4@MSN-Ph/$NH_{2\ IN}$. 30 mg of ferrite NCs were dispersed in 10 mL chloroform and placed in a polypropylene reactor. 21.7 g H_2O and 2.41 mL of aqueous CTAC solution (25 wt%) was added generating a second phase. The mixture was sonicated for 15 min using a sonication horn and subsequently the chloroform was evaporated at elevated temperatures (70 °C) for 2 h. After a second sonication step for 15 min, the mixture was added to 14.3 g TEA and stirred (700 rpm) at 60 °C. The silica source TEOS (147 µL, 658 µmol) was added and the reaction mixture was stirred for 10 min. Subsequently, a mixture of TEOS (5-times 147 µL, 658 µL), APTES (5-times 8.1 µL, 34.6 µmol) and PhTES (5-times 8.4 µL, 34.6 µmol) was added stepwise every 10 min over a total time period of 40 min at constant temperature of 60 °C. Afterwards, TEOS (4-times 147 µL, 658 µmol) was added stepwise every 10 min and finally the synthesis mixture was stirred at 1000 rpm at room temperature for 12 hours. After addition of ethanol (100 mL), the Zn-MnFe@MSNs were separated by

centrifugation (19.000 rpm, 43.146 RCF.for 20 min) and redispersed in ethanol. The template extraction was performed twice by heating the Zn-MnFe@MSN suspension under reflux at 90 °C (oil bath) for 45 min in an ethanolic solution (100 mL) containing ammonium nitrate (2 g). The Zn-MnFe@MSNs were purified by centrifugation and washed with ethanol after each extraction step. The resulting nanoparticles were stored in an ethanolic solution.

Fe_3O_4@MSN-SH_{IN}-$NH_{2\ OUT}$. 30 mg of ferrite NCs were dispersed in 10 mL chloroform and placed in a polypropylene reactor. 21.7 g H_2O and 2.41 mL of aqueous CTAC solution was added generating a second phase. The mixture was sonicated for 15 min using a sonication horn and subsequently the chloroform was evaporated at elevated temperatures (70 °C) for 2 h. After a second sonication step for 15 min, the mixture was added to 14.3 g TEA and stirred (700 rpm) at 60 °C. The silica source TEOS (147 µL, 658 µmol) was added and the reaction mixture was stirred for 10 min. Subsequently, a mixture of TEOS (5-times 147 µL, 658 µL) and MPTES (5-times 16.7 µL, 69.2 µmol) was added stepwise every 10 min over a total time period of 40 min at constant temperature of 60 °C. Then, TEOS (4-times 147 µL, 658 µmol) was added stepwise every 10 min. After 30 min of stirring, a mixture of TEOS (20.5 µL, 92.2 µmol) and APTES (21.5 µL, 92.2 µmol) was added and finally the synthesis mixture was stirred at 1000 rpm at room temperature for 12 hours. After addition of ethanol (100 mL), the Zn-MnFe@MSNs were separated by centrifugation (19.000 rpm, 43.146 RCF for 20 min) and redispersed in ethanol. The template extraction was performed twice by heating the Zn-MnFe@MSN suspension under reflux at 90 °C (oil bath) for 45 min in an ethanolic solution (100 mL) containing ammonium nitrate (2 g). The Zn-MnFe@MSNs were purified by centrifugation and washed with ethanol after each extraction step. The resulting nanoparticles were stored in an ethanolic solution.

Characterization. DLS and zeta potential measurements were performed on a Malvern Zetasizer Nano instrument equipped with a 4 mW He-Ne-Laser (633 nm) and an avalanche photodiode detector. DLS measurements were directly recorded in diluted colloidal suspensions of the particles at a concentration of 1 mg/mL. Zeta potential measurements were performed using the add-on Zetasizer titration system (MPT-2) based on diluted NaOH and HCl as titrants. For this purpose, 1 mg of the particles was diluted in 10 mL bi-distilled water. Thermogravimetric analyses (TGA) of the bulk extracted samples (approximately 10 mg) were recorded on a Netzsch STA 440 C TG/DSC. The measurements proceed at a heating rate of 10 °C/min up to 900 °C in a stream of synthetic air of about 25 mL/min. Nitrogen sorption measurements were performed on a Quantachrome Instrument NOVA 4000e at -196 °C.

Sample outgassing was performed for 12 hours at a vacuum of 10 mTorr at 120 °C. Pore size and pore volume were calculated by an NLDFT equilibrium model of N_2 on silica, based on the desorption branch of the isotherms. In order to remove the contribution of the interparticle textural porosity, pore volumes were calculated only up to a pore size of 8 nm. A BET model was applied in the range of 0.05 – 0.20 p/p_0 to evaluate the specific surface area. Infrared spectra of dried sample powder were recorded on a ThermoScientific Nicolet iN10 IR-microscope in reflexion-absorption mode with a liquid-N_2 cooled MCT-A detector. Raman spectroscopy measurements were performed on a Bruker Equinox 55 with a Nd:YAG laser (λ= 1064 nm) at a laser power of 50 mW and 20,000 scans. X-ray diffraction patterns were collected in the range of 20-80 ° on a STOE Stadi P powder diffractometer equipped with an image plate detector system, in transmission geometry, with Cu-K_α radiation and on a STOE Stadi MP with Co-K_α radiation. For transmission electron microscopy (TEM) at 300 kV using a Titan 80-300 kV microscope, samples were prepared by adding 3 drops of the ethanolic particle suspension (~3 wt%) to 4 mL absolute EtOH and drying of a drop of the resulting diluted colloidal suspension on a carbon-coated copper grid. Field-dependent magnetization measurements were performed on a superconducting quantum interference device (SQUID) magnetometer at 300 K.

4.5 Appendix

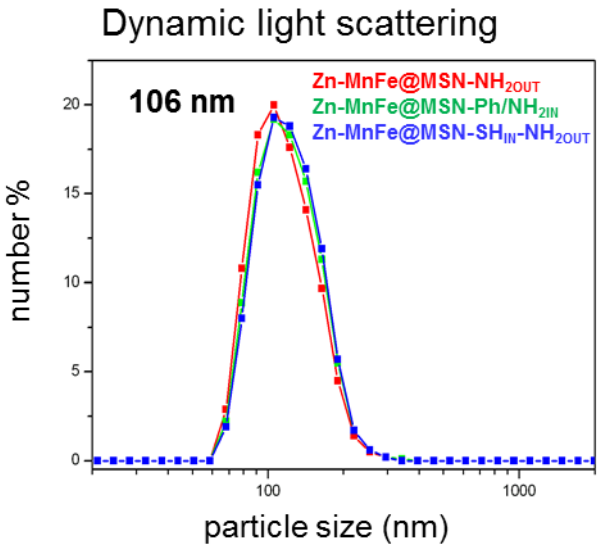

Figure 4.12: Dynamic light scattering (DLS) measurements of magnetic nanocomposites. Zn-MnFe@MSN-$NH_{2\ OUT}$ (red), Zn-MnFe@MSN-Ph/$NH_{2\ IN}$ (green) and Zn-MnFe@MSN-SH_{IN}-$NH_{2\ OUT}$ (blue).

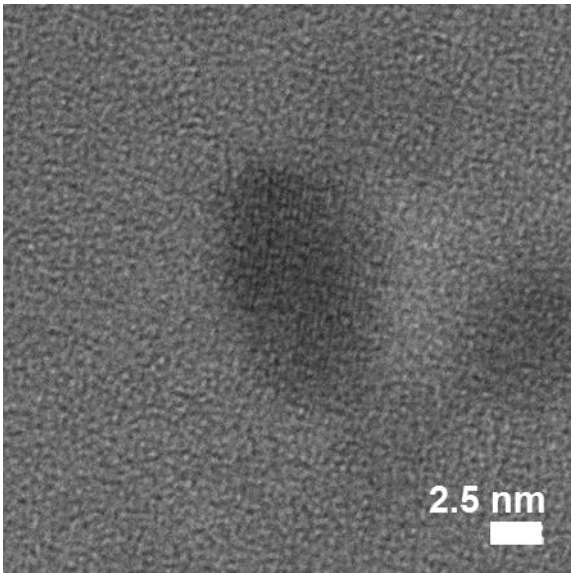

Figure 4.13: High resolution Transmission electron micrograph of sample Zn-MnFe@MSN-SH_{IN}-$NH_{2\ OUT}$. The lattice fringes of the cryystalline ferrite core are clearly visible.

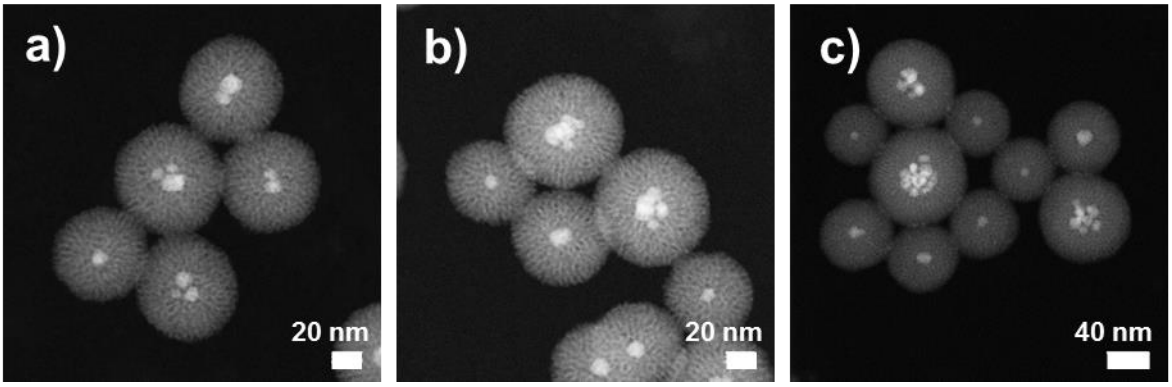

Figure 4.14: Scanning transmission electron micrographs of magnetic nanocomposites.

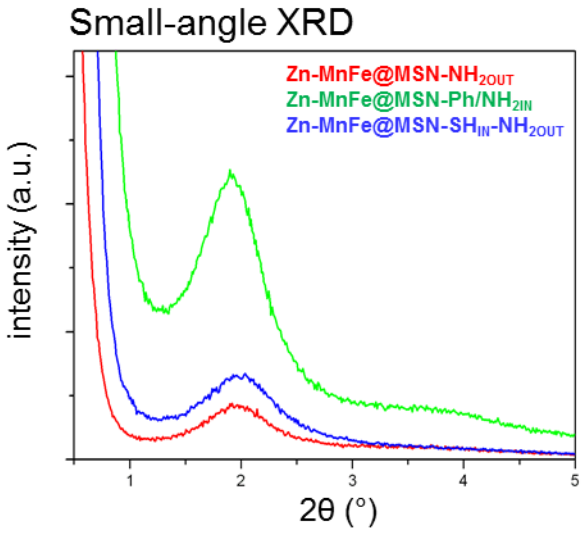

Figure 4.14: Small-angle XRD pattern of magnetic nanocomposites. Zn-MnFe@MSN-$NH_{2\ OUT}$ (red), Zn-MnFe@MSN-Ph/$NH_{2\ IN}$ (green) and Zn-MnFe@MSN-SH_{IN}-$NH_{2\ OUT}$ (blue).

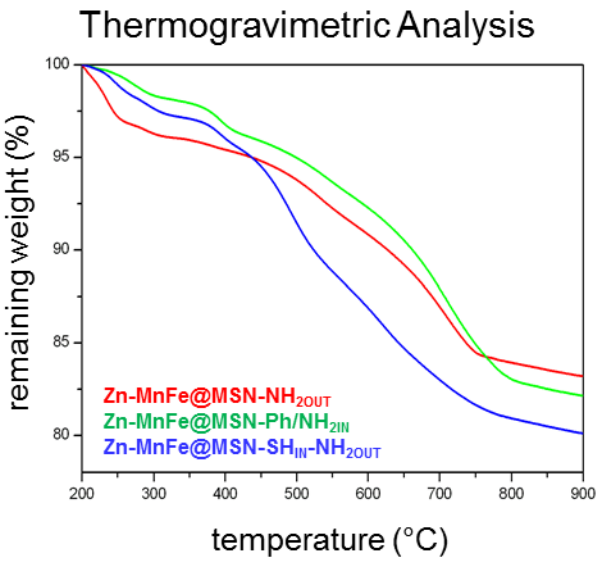

Figure 4.15: Thermogravimetirc analysis (TGA) of magnetic nanocomposites. Zn-MnFe@MSN-$NH_{2\ OUT}$ (red), Zn-MnFe@MSN-Ph/$NH_{2\ IN}$ (green) and Zn-MnFe@MSN-SH_{IN}-$NH_{2\ OUT}$ (blue).

4.6 References

[1] P. Wu, J. Zhu, Z. Xu, *Adv. Funct. Mater.* **2004**, *14*, 345.

[2] A. Guerrero-Martinez, J. Perez-Juste, L. M. Liz-Marzan, *Adv. Mater.* **2010**, *22*, 1182.

[3] J. Liu, S. Z. Qiao, Q. H. Hu, G. Q. Lu, *Small* **2011**, *7*, 425.

[4] U. Jeong, X. W. Teng, Y. Wang, H. Yang, Y. N. Xia, *Adv. Mater.* **2007**, *19*, 33.

[5] J. E. Lee, N. Lee, T. Kim, J. Kim, T. Hyeon, *Acc. Chem. Res.* **2011**, *44*, 893.

[6] A. H. Lu, E. L. Salabas, F. Schuth, *Angew. Chem. Int. Ed.* **2007**, *46*, 1222.

[7] J. Kim, Y. Piao, T. Hyeon, *Chem. Soc. Rev.* **2009**, *38*, 372.

[8] J. H. Gao, H. W. Gu, B. Xu, *Acc. Chem. Res.* **2009**, *42*, 1097.

[9] Y. W. Jun, Y. M. Huh, J. S. Choi, J. H. Lee, H. T. Song, S. Kim, S. Yoon, K. S. Kim, J. S. Shin, J. S. Suh, J. Cheon, *J. Am. Chem. Soc.* **2005**, *127*, 5732.

[10] H. Zeng, J. Li, J. P. Liu, Z. L. Wang, S. Sun, *Nature* **2002**, *420*, 395.

[11] S. H. Sun, H. Zeng, *J. Am. Chem. Soc.* **2002**, *124*, 8204.

[12] J. Park, K. J. An, Y. S. Hwang, J. G. Park, H. J. Noh, J. Y. Kim, J. H. Park, N. M. Hwang, T. Hyeon, *Nat. Mater.* **2004**, *3*, 891.

[13] S. Peng, S. H. Sun, *Angew. Chem. Int. Ed.* **2007**, *46*, 4155.

[14] J.-P. Jolivet, C. Chaneac, E. Tronc, *Chem. Commun.* **2004**, 481.

[15] X. Wang, J. Zhuang, Q. Peng, Y. D. Li, *Nature* **2005**, *437*, 121.

[16] T. Hyeon, S. S. Lee, J. Park, Y. Chung, H. Bin Na, *J. Am. Chem. Soc.* **2001**, *123*, 12798.

[17] Y. Chen, H. Chen, J. Shi, *Adv. Mater.* **2013**, *25*, 3144.

[18] N. Lee, T. Hyeon, *Chem. Soc. Rev.* **2012**, *41*, 2575.

[19] M. Liong, J. Lu, M. Kovochich, T. Xia, S. G. Ruehm, A. E. Nel, F. Tamanoi, J. I. Zink, *ACS Nano* **2008**, *2*, 889.

[20] J. Kim, H. S. Kim, N. Lee, T. Kim, H. Kim, T. Yu, I. C. Song, W. K. Moon, T. Hyeon, *Angew. Chem. Int. Ed.* **2008**, *47*, 8438.

[21] S. Giri, B. G. Trewyn, M. P. Stellmaker, V. S. Y. Lin, *Angew. Chem. Int. Ed.* **2005**, *44*, 5038.

[22] Y.-S. Lin, C. L. Haynes, *Chem. Mater.* **2009**, *21*, 3979.

[23] E. Ruiz-Hernandez, A. Lopez-Noriega, D. Arcos, I. Izquierdo-Barba, O. Terasaki, M. Vallet-Regi, *Chem. Mater.* **2007**, *19*, 3455.

[24] J. Kim, J. E. Lee, J. Lee, J. H. Yu, B. C. Kim, K. An, Y. Hwang, C. H. Shin, J. G. Park, J. Kim, T. Hyeon, *J. Am. Chem. Soc.* **2006**, *128*, 688.

[25] Y. S. Lin, S. H. Wu, Y. Hung, Y. H. Chou, C. Chang, M. L. Lin, C. P. Tsai, C. Y. Mou, *Chem. Mater.* **2006**, *18*, 5170.

[26] J. T. Jang, H. Nah, J. H. Lee, S. H. Moon, M. G. Kim, J. Cheon, *Angew. Chem. Int. Ed.* **2009**, *48*, 1234.

[27] J. H. Lee, Y. M. Huh, Y. Jun, J. Seo, J. Jang, H. T. Song, S. Kim, E. J. Cho, H. G. Yoon, J. S. Suh, J. Cheon, *Nature Medicine* **2007**, *13*, 95.

[28] C. Liu, B. S. Zou, A. J. Rondinone, J. Zhang, *J. Am. Chem. Soc.* **2000**, *122*, 6263.

[29] A. K. Gupta, M. Gupta, *Biomaterials* **2005**, *26*, 3995.

[30] V. Cauda, A. Schlossbauer, J. Kecht, A. Zürner, T. Bein, *J. Am. Chem. Soc.* **2009**, *131*, 11361.

[31] J. Kecht, A. Schlossbauer, T. Bein, *Chem. Mater.* **2008**, *20*, 7207.

5 Heparin-Coated Colloidal Mesoporous Silica Nanoparticles Efficiently Bind to Antithrombin as an Anticoagulant Drug-Delivery System

This chapter is based on the following publication:

Christian Argyo, Valentina Cauda, Hanna Engelke, Joachim Rädler, Gregor Bein, and Thomas Bein, *Chemistry – A European Journal* **2012**, 18, 428 – 432.

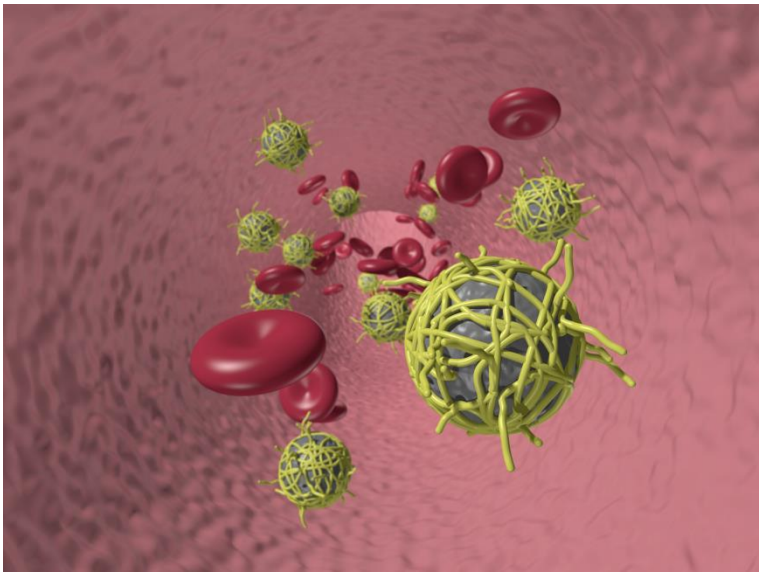

5.1 Introduction

Colloidal mesoporous silica nanoparticles (MSNs) have attracted great attention as potential injectable drug delivery and cancer cell targeting systems.[1] In addition to their high biocompatibility and biodegradability,[2-3] they can be selectively modified at their inner and outer surfaces to efficiently encapsulate molecules in their tunable pore system,[4] and they can be specifically functionalized on their outer surface for the application of interest.[5-9] Recent efforts have addressed the prevention of their fast degradation and hemolytic behavior by poly(ethylene glycol) coating.[10-11] To deliver such multiple core-shell functionalized MSNs to the blood stream additional efforts are critical to guarantee adequate circulation times and to prevent thrombogenic effects. Heparin (Hep), a highly sulfated, anionic polysaccharide, is best known for its anticoagulant properties and is conventionally injected subcutaneously or intravenously.[12] Free Hep always involves an increased bleeding risk and other side effects, for example, Hep-induced thrombocytopenia, while diffusing throughout

the whole blood circulation system. However, specifically tissue-targeted nanocarriers with Hep coating should be harmlessly injectable into the blood stream, and prevent activation of the clotting system only in the immediate vicinity of the nanocarriers without systemic side effects.[13-14] In addition, the Hep coating prolongs the circulation time of the nanoparticles in blood vessels and improves biocompatibility, and thus enhances their chances of serving their purpose *in vivo*, as shown in previous studies.[15-16] Recently, the biological properties of Hep combined with polymeric and metallic nanomaterials and their application as anticoagulants have been reviewed.[17] Here we present heparin-coated core-shell MSNs, in which Hep is covalently bound to the outer surface of amino-functionalized MSNs. The combination of Hep with the highly porous features of MSNs should lead to an efficient multifunctional drug-delivery system that can act as an anticoagulant drug and allow for incorporation of biologically functional molecules as deliverable cargos.

5.2 Results and Discussion

In this work we focus on the efficiency of the anticoagulant coating on MSNs, and thus move towards the first step for the preparation of smart drug-delivery systems by improving biocompatibility and hemocompatibility. The MSNs were synthesized by sol-gel synthesis, as previously reported.[4] In the present case we selectively functionalized the outer nanoparticle surface with aminopropyl groups. After template extraction, the amino groups of the core-shell nanoparticles were treated via EDC amidation with the carboxyl groups of Hep (Scheme 5.1), and thus a heparin coating covalently bound to the outer surface of the colloidal MSNs (CMS–Hep) was obtained.

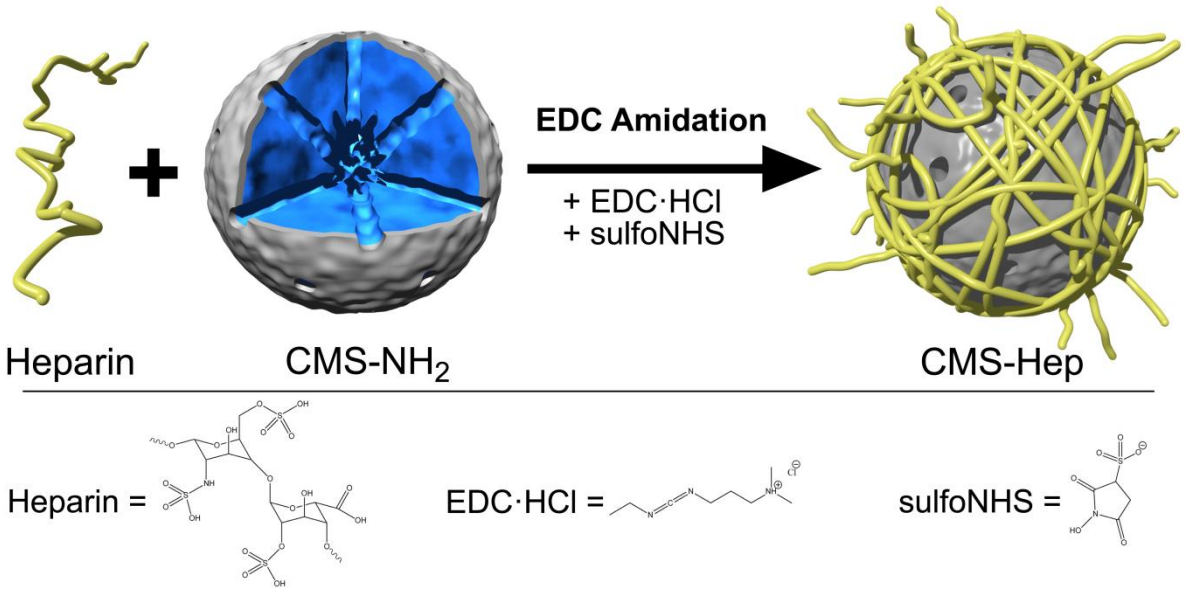

Scheme 5.1: Treatment of the CMS-NH_2 nanoparticles (the external functionalized shell is represented in dark grey) with the carboxylic groups of the polysaccharide chain of Hep, catalyzed by EDC and sulfoNHS to create amide bonds for covalent attachment of Hep (yellow) to the outer particle surface. The molecular structure of Hep and the MSNs are not to scale.

The amino-functionalized sample CMS-NH_2 consists of nano-sized particles of about 50 nm in diameter. The wormlike structure of the mesopores is clearly visible (Figure 5.1a). For CMS–Hep nanoparticles the mesoporous structure was hardly detectable due to the additional organic layer (Figure 5.1b).

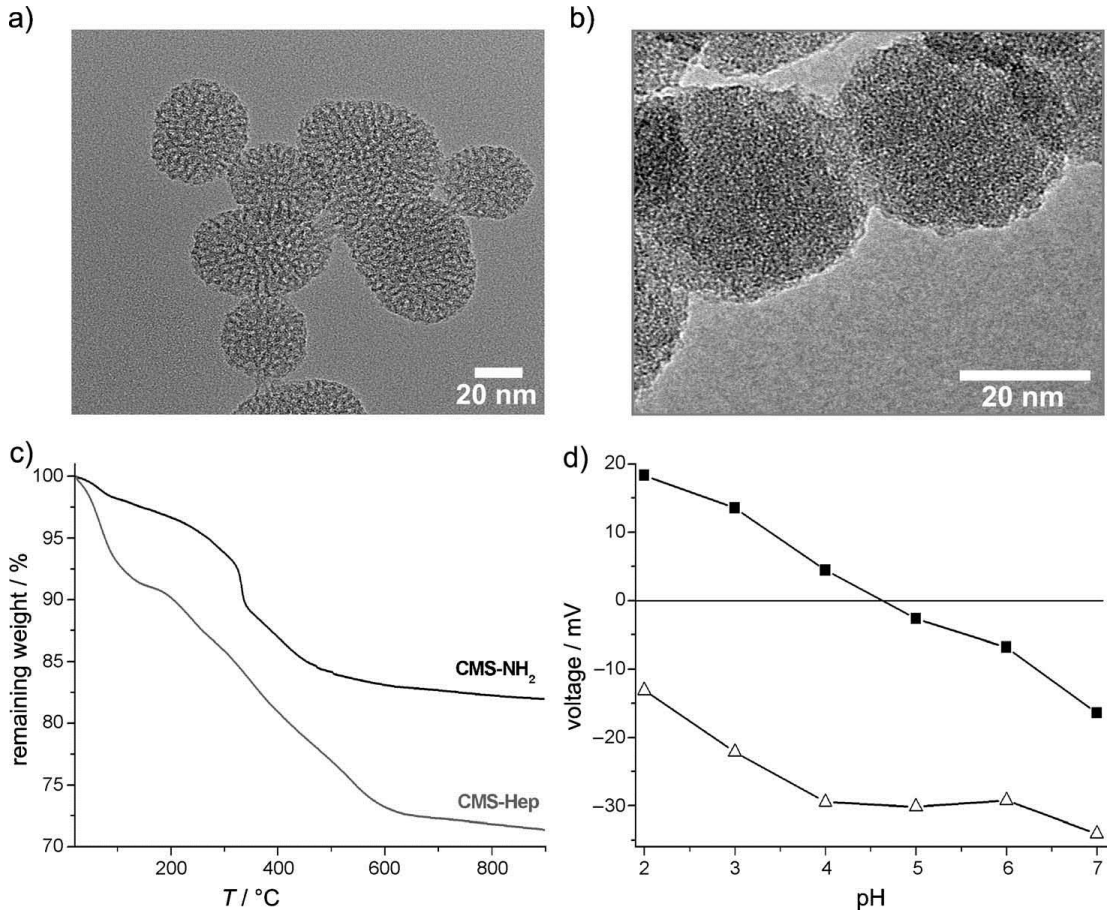

Figure 5.1: Characterization of mesoporous silica nanocarriers. Transmission electron micrographs (TEM) of: a) CMS-NH_2, and b) CMS–Hep. c) Thermogravimetric analysis, and d) ζ-potential measurements of CMS-NH_2 (black squares) and CMS–Hep (empty triangles).

Additional TEM images show that the MSNs, coated with heparin, are surrounded by a thick organic layer (Figure 5.2a). However the mesopores are barely visible. For a better imaging of the mesoporous structure of the heparin-coated MSNs scanning transmission electron micrograph (STEM) is shown in Figure 5.2b. STEM images feature a better contrast correlated with the atomic mass number of the different elements in the specimen. With this technique the mesoporous structure of the MSNs is better visualized, thus confirming the maintenance of the porous features after heparin modification.

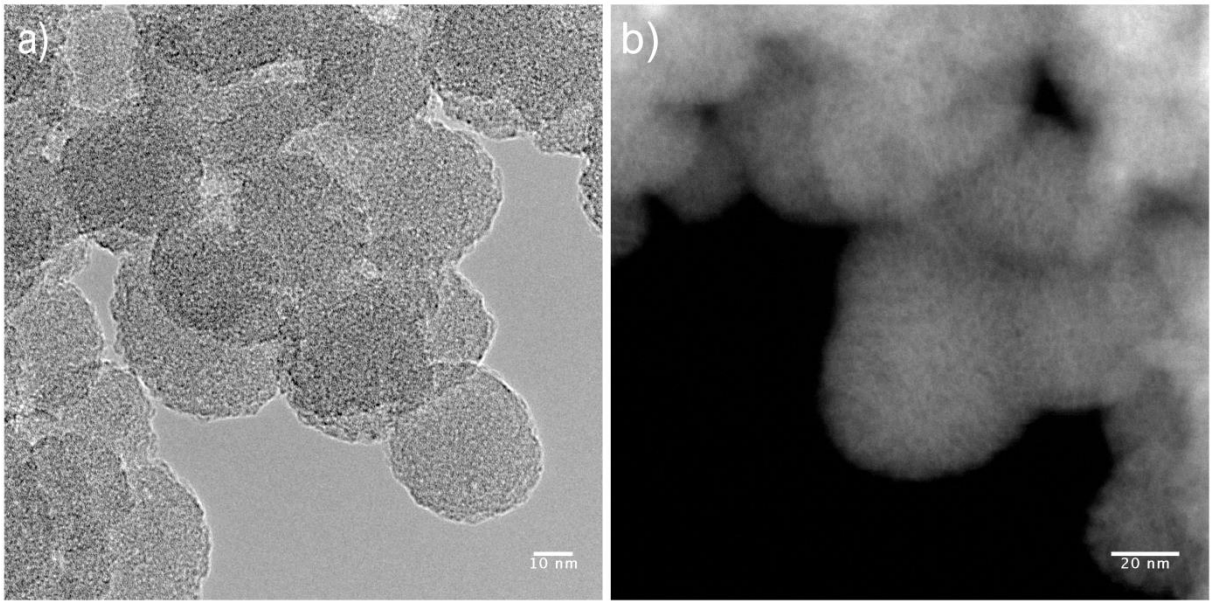

Figure 5.2. (a) Transmission electron micrograph (TEM) and (b) scanning transmission electron micrograph (STEM) of the heparin-coated MSNs (CMS-Hep).

The effective attachment of Hep was confirmed by the higher weight loss (about 5%, w/w) between 170–650 °C in the thermogravimetric analysis with respect to the unmodified CMS-NH_2 (Figure 5.1c). The ζ-potential measurements show the surface charge of the particle at different pH values, and reveal the presence of charged functional groups. The sulfate groups of Hep carry a strong negative charge even at low pH values, thus the negative profile of the CMS–Hep nanoparticles confirms the presence of Hep at the outer surface (Figure 5.1d). In contrast, the ζ-potential profile of the CMS-NH_2 sample shows a high positive charge at acidic pH values, since the unreacted amino groups are positively charged upon protonation. Evidence for the successful attachment of Hep is also provided by ^{13}C solid state NMR spectroscopy (Figure 5.4a, resonances of the propyl chain at 8, 20, and 43 ppm, a broad signal at 69 ppm due to the carbon atoms of the carbohydrate backbone (disaccharide units), and the carboxyl resonance at 174 ppm). The coating with organic moieties of the nanoparticle surface was also investigated by infrared spectroscopy (Figure 5.3a). The spectra A and B related to MSNs with amino groups and heparin coating respectively, indicate strong vibrations of the silica framework at around 1240 – 1050 cm^{-1} (asymmetric stretching vibration of Si-O-Si), and at 964 and 796 cm^{-1} (asymmetric bending and stretching vibration of Si-OH). Furthermore a broad band at 3600 – 3100 cm^{-1} corresponding to water and silanol groups on the particle surface can be observed for both samples. The peak at 1629 cm^{-1} indicates the bending modes of the water molecules adsorbed on the surface of the particles appearing in all spectra. For comparison the spectrum of pure heparin (curve C) is also

reported. Several characteristic peaks for heparin are covered by the massive silica peak. However, by zooming-in in the region between 3500 – 1200 cm^{-1} (Figure 5.3b), it is possible to detect additional bands for the sample CMS-Hep in the range of 2980 – 2850 cm^{-1}, associated with the C-H (2854 cm^{-1}) and CH_2 (2925 cm^{-1}) stretching vibrational modes of the polysaccharide backbone chain. The peak at 1710 cm^{-1} can be related to the carbonyl stretching vibrational mode of the carboxylic acids of Hep. The carbonyl stretching vibration of amide groups is shifted to smaller wavenumbers. Therefore the peak at 1650 cm^{-1} is attributed to the amide group which was built by EDC amidation creating a covalent bond between the amino-functionalized MSNs and carboxy groups of Hep. Further proof for the amide bond formation is shown by the peak at 1577 cm^{-1} for the N-H deformation mode of the amide group. The peak at 1629 cm^{-1} arises due to the N-H deformation vibrational mode of the sulfonamide groups of Hep. The stretching mode of SO_2 at 1456 cm^{-1} shows the presence of the sulfonic groups. We note that the samples were extensively washed with water and ethanol before measurements, thus the detection of only physically adsorbed heparin can be excluded, as also confirmed by ssNMR.

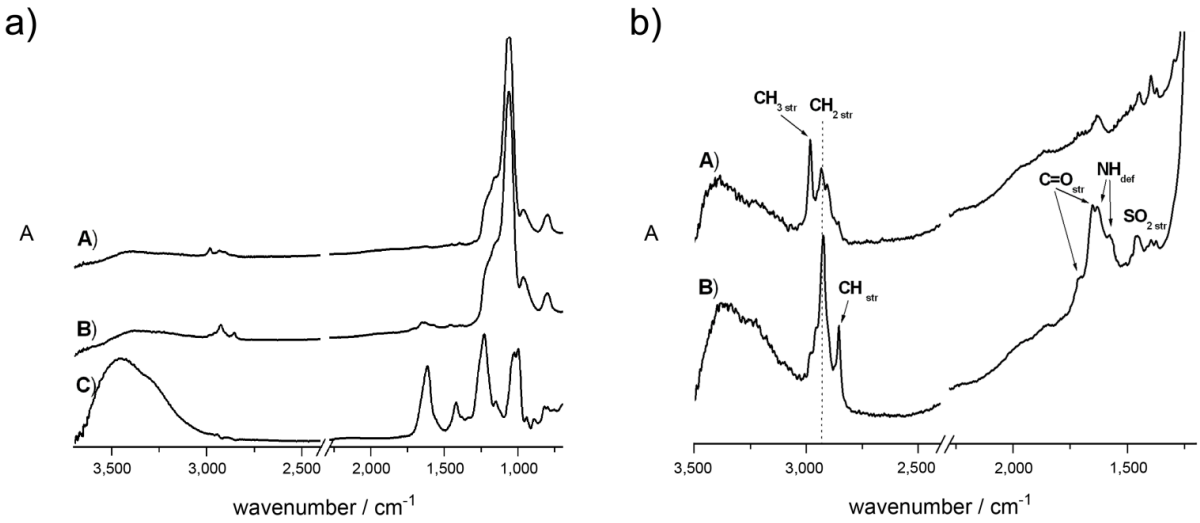

Figure 5.3: (a) Infrared spectra (for clarity reasons, the IR spectra are shifted along the y-axis by 0.2 units each) of the aminopropyl-functionalized (CMS-NH_2, curve A), heparin-coated (CMS-Hep, curve B) MSNs and pure heparin (curve C). (b) Zoom-in in the area of interest for better detection of organic moieties.

Relatively high values of specific surface area and pore volume were obtained for the CMS–Hep nanoparticles (Figure 5.4b and Table 5.1). We attribute the reduced pore volume in comparison with the CMS-NH_2 sample to the increased sample weight by the addition of the

nonporous Hep, and to the blocking of some pores by frozen Hep in the surface layer of the nanoparticles.

Table 5.1: Structural parameters of the heparin-coated MSNs and the unmodified CMS-NH_2.

Sample	DFT pore size[a] [nm]	BET surface area [m^2/g]	Pore volume[b] [cm^3/g]
CMS-NH_2	3.93	949	0.75
CMS-Hep	3.66	465	0.32

[a]DFT pore size refers to the peak value of the pore size distribution
[b]Pore volume is calculated up to a pore size of 8 nm to remove the contribution of interparticle porosity.

As previously found for PEGylated MSNs,[10] the colloidal stability in water was improved by the Hep coating (average particle size: 95 nm) compared to the unmodified CMS-NH_2 particles, for which a fraction of aggregates of up to 700 nm in size was formed (Figure 5.4d).

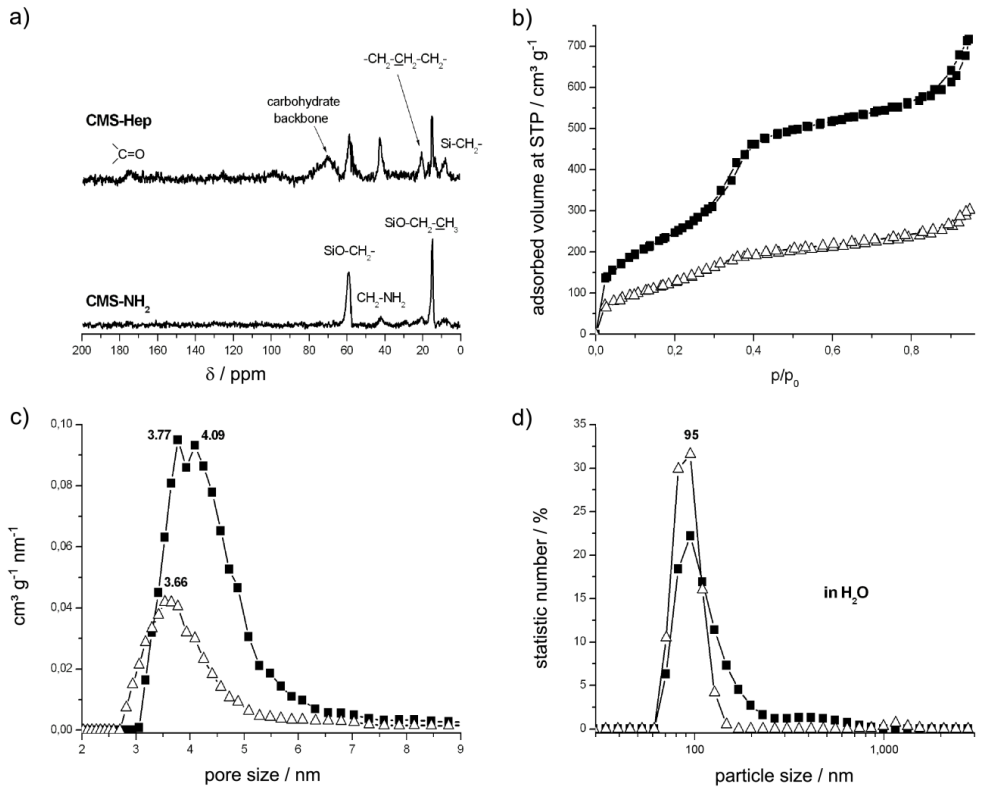

Figure 5.4: a) ^{13}C solid state NMR spectra, b) nitrogen sorption isotherms relative to the total sample weight, c) DFT pore size distributions, and d) dynamic light scattering (DLS) measurements of CMS-NH_2 (black squares) and CMS–Hep (empty triangles).

From this we concluded that the covalent binding of Hep to the outer surface of the MSNs was successful. We preclude the presence of free Hep due to extensive washing steps after the synthesis and the good solubility of Hep in water. Hep specifically binds to antithrombin

(AT), and thus accelerates the inhibiting effect of AT on the coagulation proteins by up to 1000-fold; in this way it prevents the formation of thrombin.[18-19] The specific interaction of Hep at the outer surface of MSNs with AT and hence thrombin (TR) was evaluated with binding experiments by using fluorescence correlation spectroscopy (FCS). FCS measures the amount of bound protein as a function of the MSN concentration based on the size dependence of diffusion.[20] The isotherms in Figure 5.5 confirm binding of AT to the CMS–Hep (binding constant: 160 mL/mg).

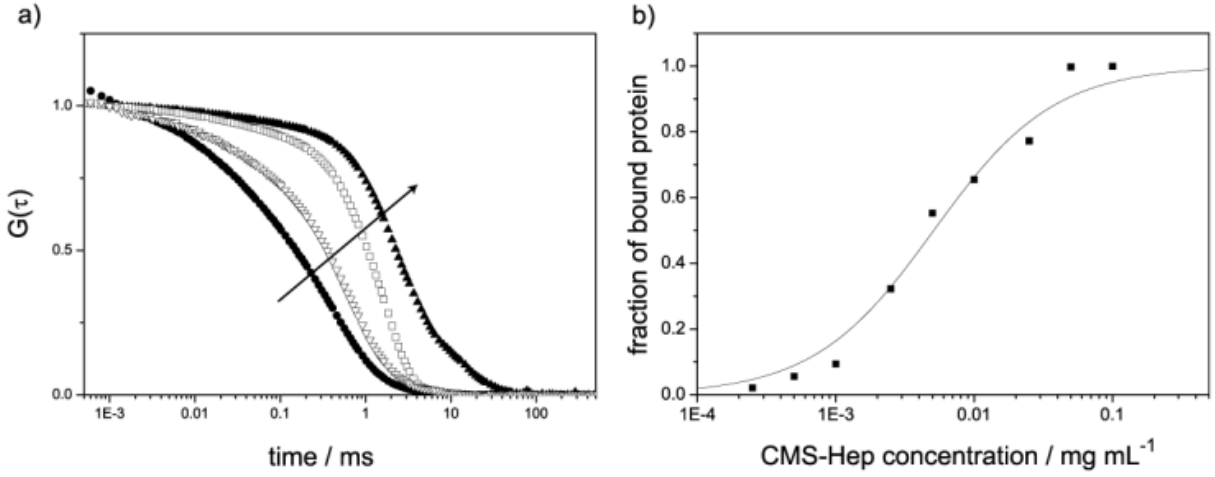

Figure 5.5: a) Fluorescence correlation spectroscopy (FCS) curves: the characteristic decay of the autocorrelation curve resulting from freely diffusing fluorescently labeled proteins (AT, black circles) is shifted towards longer timescales with increasing amount of protein bound to CMS–Hep nanoparticles (30%, empty triangles; 70%, empty squares; 100% black triangles) as indicated by the arrow. b) Binding isotherm of AT to the CMS–Hep.

Additional FCS experiments were carried out in order to gain an understanding of the influence of CMS-Hep on TR (see Appendix 5.5). To evaluate the anticoagulant activity of CMS–Hep nanoparticles, activated partial thromboplastin time (aPTT) and antifactor Xa (FXa) activity assays were performed. The physiological target proteases of AT are those of the contact activation pathway, mainly the activated forms of factor X (FXa) and factor II (TR); these activate the formation of fibrin, which polymerizes and creates the blood clot with thrombocytes. For these measurements we prepared three samples of CMS–Hep with different Hep contents (0.4–1.0 IU/mL). As reference, we provided three samples of CMS-NH_2 nanoparticles with the same particle concentration as the CMS–Hep samples and pure Hep solutions without nanoparticles with the same Hep concentration. Since the effect of identical doses of Hep varies between individuals, all experiments were carried out with plasma samples from three different consenting adult donors. The anti-FXa test is a

chromogenic assay for determining Hep activity in plasma.[21] The CMS–Hep samples showed significant Hep activity, which was only slightly lower than that of free Hep in solution in the reference sample (Figure 5.6a and Table 5.2) with almost exactly the calculated Hep concentration. More than half of the covalently bound Hep was still able to form the inhibitory complex of the anti-FXa assay. Slight deviations can be attributed to variations in the individual response of each donor to Hep. As expected, the CMS-NH_2 nanoparticles showed no Hep activity. The reference measurements with PBS did not exhibit inhibitory activity. The aPTT is a coagulometric measurement in which the activity of coagulation factors relevant for clinical investigations is evaluated.[22] All reference samples, containing CMS-NH_2 and pure PBS, showed normal blood clotting times (30–35 s). The CMS–Hep nanoparticles showed (for all Hep contents) prolonged blood clotting times of about 160 s and longer; this is comparable with the expected aPTT of the pure Hep solutions (Figure 5.6b and Table 5.3).

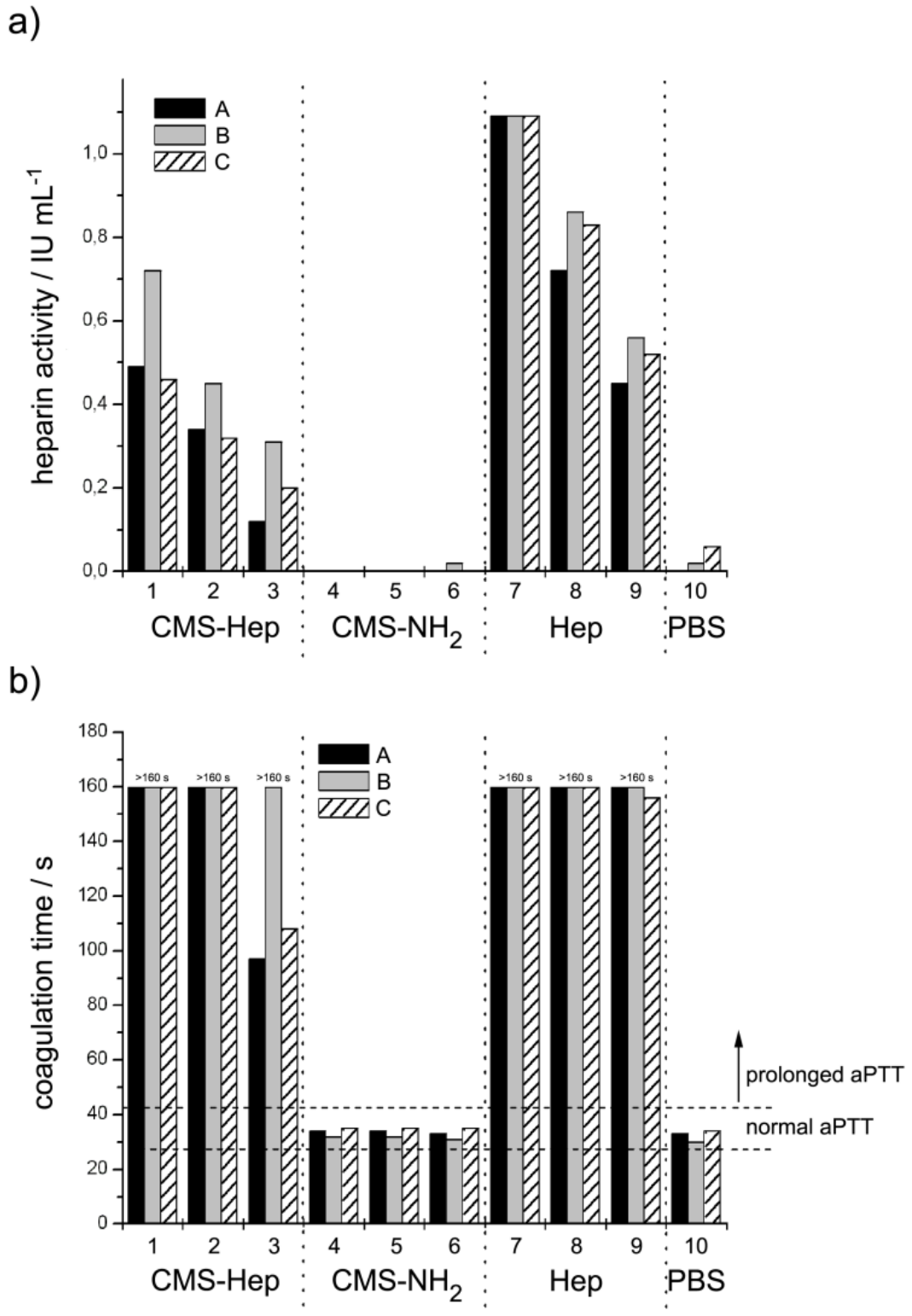

Figure 5.6: a) Hep activity in IU/mL (anti-FXa assay), and b) the aPTT assay (in seconds) evaluated for the CMS–Hep samples (1, 2 and 3) with various Hep concentrations (1.0, 0.7 and 0.4 IU/mL, respectively). Reference samples: CMS-NH_2 nanoparticles with the same particle concentration as CMS–Hep: 1.0 IU/mL (4), 0.7 IU/mL (5) and 0.4 IU/mL (6); free Hep in solution with calculated concentrations of 1.0 IU/mL (7), 0.7 IU/mL (8) and 0.4 IU/mL (9); sample 10 contains PBS only (no particles or Hep). All samples were added to the citrated blood plasma of three different consenting adult subjects (A, B, C). The BCS coagulation system measures coagulation time only up to 160 s.

Table 5.2: The heparin activity in IU/mL was evaluated by the anti-FXa activity test. The MSN samples with various heparin concentrations and diverse reference samples were added to the citrated blood plasma of three different subjects (A, B, C).

Sample	A [IU/mL]	B [IU/mL]	C [IU/mL]
CMS-Hep (1.0 IU/mL)	0.49	0.72	0.46
CMS-Hep (0.7 IU/mL)	0.34	0.45	0.32
CMS-Hep (0.4 IU/mL)	0.12	0.31	0.20
CMS-NH_2 (1.0)[a]	0.00	0.00	0.00
CMS-NH_2 (0.7)[a]	0.00	0.00	0.00
CMS-NH_2 (0.4)[a]	0.00	0.02	0.00
Hep (1.0 IU/mL)	1.09	1.09	1.09
Hep (0.7 IU/mL)	0.72	0.86	0.83
Hep (0.4 IU/mL)	0.45	0.56	0.52
PBS	0.00	0.02	0.06

[a]These samples of unmodified CMS-NH_2 nanoparticles feature the same particle concentration as the CMS-Hep ones. Obviously they cannot contain any heparin activity in IU/mL.

Table 5.3: The aPTT in seconds was evaluated for all samples and references added to the citrated blood plasma of three different subjects (A, B, C). The BCS Coagulation System measures coagulation time only up to 160 s. Blood clotting times about and above 160 s are presented in this way: > 160 s.

Sample	A	B	C
CMS-Hep (1.0 IU/mL)	> 160 s	> 160 s	> 160 s
CMS-Hep (0.7 IU/mL)	> 160 s	> 160 s	> 160 s
CMS-Hep (0.4 IU/mL)	97 s	> 160 s	108 s
CMS-NH_2 (1.0)[a]	34 s	32 s	35 s
CMS-NH_2 (0.7)[a]	34 s	32 s	35 s
CMS-NH_2 (0.4)[a]	33 s	31 s	35 s
Hep (1.0 IU/mL)	> 160 s	> 160 s	> 160 s
Hep (0.7 IU/mL)	> 160 s	> 160 s	> 160 s
Hep (0.4 IU/mL)	160 s	> 160 s	156 s
PBS	33 s	30 s	34 s

[a]These samples of unmodified CMS-NH_2 nanoparticles feature the same particle concentration as the CMS-Hep ones. Obviously they cannot contain any heparin activity in IU/mL.

The graph of one measurement of the chromogenic assay for determination of the heparin activity in human blood plasma is shown in Figure 5.8a (Appendix 5.5). Heparin considerably accelerates inactivation of coagulation factor FXa and thrombin (FIIa) by antithrombin (AT).

During the incubation phase of the test FXa is inactivated by AT catalyzed by the presence of heparin. The quantity of FXa which remains after incubation is determined via the increase in absorbance at the wavelength 405 nm, since the coagulation factor is able to crack a chromogenic substrate into a tripeptide and a dye. The curve in Figure 5.8a shows a linear increase in absorbance during time. The slope of this curve is determined for 60 s. This value is evaluated on a reference curve resulting in the heparin activity of the analyzed sample (here sample CMS-Hep (1.0 IU/mL) features heparin activity of 1.09 IU/mL). The activated partial thromboplastin time (aPTT) test was accomplished to determine the coagulation time of citrated human blood plasma in presence of modified heparin-coated and unmodified MSNs. The incubation of citrated plasma with phospholipids and a surface activator leads to the activation of several factors of the intrinsic coagulation system. The addition of Ca^{2+} cations triggers the coagulation process. The time until the formation of fibrin clot starts is measured and detected photo optically. Figure 5.8b shows the aPTT for two different samples. Amino-functionalized MSNs (filled squares) feature normal blood clotting time within 32 s. These particles are not able to influence the coagulation system. On the contrary the heparin-coated MSNs (empty triangles) show prolonged blood clotting time up to 97 s. The covalently attached heparin on the external surface of the MSNs is able to catalyze the inhibition of the coagulation system. Both the anti-FXa and aPTT assays indicate that a high amount of Hep is covalently bound to the outer nanoparticle surface, which offers enough free active sites for efficient inhibition of coagulation. Previous studies on the immobilization of Hep on substrates have shown low nonspecific protein adsorption behavior when in contact with blood or plasma.[23-24]

5.3 Conclusion

To the best of our knowledge, this is the first report on covalently bound Hep at the outer surface of nano-sized mesoporous silica particles showing efficient anticoagulant properties; these could possibly reduce unintended immunogenic response. The CMS–Hep nanoparticles are expected to have potential as a blood-stream-injectable drug-delivery system, and offer new options for cancer therapy. As a future outlook, their selectivity could be further enhanced by functionalizing the heparin layer with site-specific targeting ligands.

5.4 Experimental

Chemicals. Tetraethyl orthosilicate (TEOS, Fluka, >98%), triethanolamine (TEA, Aldrich, 98%), cetyltrimethylammonium chloride (CTAC, Fluka, 25% in water), aminopropyl-triethoxy silane (APTES, Sigma Aldrich, 99%), heparin sodium salt (HEP, Alfa Aesar, 100%), *N*-(3-dimethylaminopropyl)-*N'*-ethylcarbodiimide hydrochloride (EDC, Aldrich), *N*-hydroxysulfosuccinimide sodium salt (sulfoNHS, Aldrich), antithrombin (AT, 50 IU/mL, American Diagnostics INC.), thrombin (Human Thrombin, 500 IE/mL, Baxter), Atto 488 NHS-ester (ATTOTEC), Atto 633 NHS-ester (ATTO-TEC), ammonium nitrate (Fluka) and hydrochloric acid (37%) were used as received. Ethanol (absolute, Aldrich) was used as solvent without further purification. Bidistilled water was obtained from a Millipore system (Milli-Q Academic A10).

Synthesis procedures. Particle synthesis. For the outer aminopropyl-functionalized MSNs, tetraethyl orthosilicate (TEOS) (1.92 g, 9.22 mmol) and triethanolamine (TEA) (14.3 g, 95.6 mmol) were heated to 90 °C without stirring in a 100 mL polypropylene reactor. After 20 min a solution of cetyltrimethylammonium chloride (CTAC, 25% in water) (2.41 mL, 1.83 mmol) in bi-distilled water (21.7 g, 1.21 mol) from a Millipore system (Milli-Q Academic A10), preheated to 60 °C, was added to the polypropylene reactor. The resulting mixture, having a molar composition of 1 TEOS: 0.20 CTAC: 10.4 TEA: 130.2 H_2O, was stirred at 500 rpm at RT for 30 min. Afterwards aminopropyl-triethoxy silane (APTES) (20.4 mg, 0.0922 mmol, 1.0 mol% of the total amount of TEOS) together with TEOS (19.2 mg, 0.0922 mmol) were added and the synthesis mixture was stirred at 500 rpm at RT for 12 hours. After addition of ethanol (100 mL), the MSNs were separated by centrifugation (19.000 rpm, 43.146 RCF.for 20 min) and redispersed in ethanol. The template extraction was performed by heating the MSN suspension under reflux at 90 °C (oil bath) for 45 minutes in an ethanolic solution (100 mL) containing ammonium nitrate (2 g), followed by 45 minutes under reflux in a solution of concentrated hydrochloric acid (10 mL) and ethanol (90 mL). The MSNs were purified by centrifugation and washed with ethanol after each extraction step.

Heparin functionalization. For the surface functionalization of the MSNs with Hep, 216 mg (16.2 μmol, 5 equiv. to the amino groups of the particles) of heparin sodium salt were dissolved in 8 mL bidistilled H_2O. Then 62.1 mg (324 μmol, 20 equiv. to Hep) EDC and 70.4 mg (324 μmol, 20 equiv. to Hep) sulfoNHS were added successively and stirred for 5 min at RT. The amount of 1.12 mL ethanolic solution with 20 mg of the amino-functionalized MSNs (contains 3.25 μmol amino groups) was added to the reaction mixture

and stirred for 12 h at RT. Afterwards the nanoparticles were separated by centrifugation and washed several times with copious amounts of water and ethanol to remove additional free polysaccharide. Finally they were redispersed in 5 mL ethanol, leading to a colloidal solution.

AT labeling. For labeling the AT with the dye Atto 488, the lypholized AT (50 IU/mL) was dissolved in 0.5 mL bidistilled H_2O. 50 µL of this solution were added to 1 mL of a 0.1 M $NaHCO_3$ buffer solution in an eppendorf tube. A pH value of 8.3 is desired for the labeling reaction. A threefold molar excess (65 µL, 2 mg/mL) of an ethanolic solution of Atto 488 NHS-ester was added to the AT solution and the reaction mixture was incubated for 1 h at RT in the dark. Afterwards the solution was dialyzed against 500 mL bidistilled H_2O for 12 h.

Thrombin labeling. For TR labeling with the dye Atto 633, the lyophilized TR (500 IU/mL) was dissolved in 5 mL bidistilled H_2O. 50 µL of this solution were added to 1 mL of a 0.1 M $NaHCO_3$ buffer solution in an Eppendorf tube, showing a pH value of 8.3. A threefold molar excess (38.8 µL, 2 mg/mL) of an ethanolic solution of Atto 633 NHS-ester was added to the thrombin solution and the reaction mixture was incubated for 1 h at RT in the dark. Afterwards the solution was dialyzed against 500 mL bidistilled H_2O for 12 h.

Characterization. Nitrogen sorption measurements were performed on a Quantachrome Instrument NOVA 4000e at -196 °C. Sample outgassing was performed for 12 hours at a vacuum of 10 mTorr at 120 °C, thus the functional groups should remain unaffected at this temperature. Pore size and pore volume were calculated by a NLDFT equilibrium model of N_2 on silica, based on the desorption branch of the isotherms. In order to remove the contribution of inter-particle textural porosity, pore volumes were calculated only up to a pore size of 8 nm. A BET model was applied in the range of 0.05 – 0.20 p/p0 to evaluate the surface area. Infrared spectra were recorded on a Bruker Equinox 55; the dried powder of the nanoparticles was measured in the Attenuated Total Reflectance (ATR) mode. For all spectra the background was subtracted. Thermogravimetric analyses of the bulk extracted samples were performed on a Netzsch STA 440 C TG/DSC with a heating rate of 10 °C/min in a stream of synthetic air at about 25 mL/min. To evaluate the amount of covalently bound heparin the weight loss was normalized to the weight loss of the CMS-NH_2 sample. Dynamic Light Scattering (DLS) and zeta potential measurements were performed on a Malvern Zetasizer-Nano instrument equipped with a 4 mW He-Ne laser (633 nm) and an avalanche photodiode detector. DLS measurements were directly recorded in diluted colloidal suspensions of the MSNs at a constant concentration of 1 mg/mL for all sample solutions. The

zeta potential measurements were recorded with a mixture of ethanolic suspension of the sample (~3 %wt) and about 1 mL commercial Hydrion Buffer solutions having pH values of 2, 3, 4, 5, 6 and 7. Transmission electron microscopy (TEM) was performed at 300 kV on an FEI Titan 80-300 equipped with a field emission gun. For sample preparation, colloidal mesoporous nanoparticles were diluted in ethanol and a drop of the suspension was then deposited on the sample holder, a copper grid with holey carbon film, and the solvent was allowed to evaporate. Solid state NMR measurements were performed on a BRUKER DSX Avance 500 FT (^{13}C NMR data were acquired at 125.8 MHz under cross-polarization conditions with 13688 transients).

AT-Heparin binding constant measurement with FCS. Binding experiments were performed on an Axiovert 200 microscope equipped with a ConfoCor 2 unit (Carl Zeiss, Jena, Germany). A 40x (NA = 1.4) water immersion objective (Carl Zeiss Jena, Germany) was used for observation and an argon ion laser for Atto 488 excitation at a wavelength of 488 nm and a HeNe laser for Atto 633 excitation at a wavelength of 633 nm. Fluorescence emission was separated from the laser light using a bandpass filter (505-530 nm) and a longpass filter (650 nm), respectively. Samples were measured in 8-well chambers (nunc, Rochester, NY). Data were analyzed and binding isotherms were fitted using Langmuir isotherms according to Ref.[20]

Blood clotting tests, aPTT and anti-FXa activity test. Blood clotting tests were performed on an automatic BCS XP Coagulation System (Siemens Healthcare Diagnostics, Marburg, Germany). For both tests 100 µL of the samples with a heparin content in the therapeutic range of 0.4 – 1.0 IU/mL dispersed in PBS were mixed with 900 µL of citrated blood plasma. For reference measurements unmodified CMS-NH_2 samples and pure heparin solutions were also prepared. Blood from three different blood donors was used for the coagulation tests. Donor's consent was supplied by each individual blood donation. The study was approved by the institutional review board of the Medical Faculty of Justus-Liebig-University Giessen (file number: 05/00). For aPTT measurements, 100 µL of the heparin-coated MSNs are pipette with citrated human blood plasma into a test tube and pre-warmed to 37 °C. After addition of 100 µL Pathromtin SL Reagent (Siemens Healthcare Diagnostics) the solution was incubated for 2 min at 37 °C. This solution contains phospholipids and surface activators, thus leading to the activation of factors of the intrinsic coagulation system. After addition of 100 µL $CaCl_2$ solution the coagulation analyzer was started. The Ca^{2+} triggers the coagulation process leading to clouding of the solution. The formation time of fibrin clots is measured optically.

The resulting coagulation time is given in seconds. As reference, the time of fibrin clot formation is also measured for the unmodified CMS-NH_2 nanoparticles and the free heparin molecules, in the same concentration (in IU/mL) as of the CMS-Hep. The anti-FXa activity test is a chromogenic assay determining the heparin activity in plasma. During the incubation phase of the test, FXa is inactivated upon formation of an inhibitory complex with AT in the presence of heparin. The amount of FXa remaining after the incubation phase is determined in a kinetic test via an increase in absorbance at 405 nm, since the coagulation factor FXa is able to cleave a chromogenic substrate into a tripeptide and a dye. The results are evaluated upon comparison with a calibration curve, showing the heparin activity of the examined sample. For the anti-FXa activity measurements, 50 µL of the particle containing plasma sample, 50 µL AT reagent and 500 µL factor Xa reagent were mixed and incubated for exactly 1 minute at 37 °C. Then 100 µL of the chromogenic substrate reagent were added and the absorbance at 405 nm was detected.

5.5 Appendix

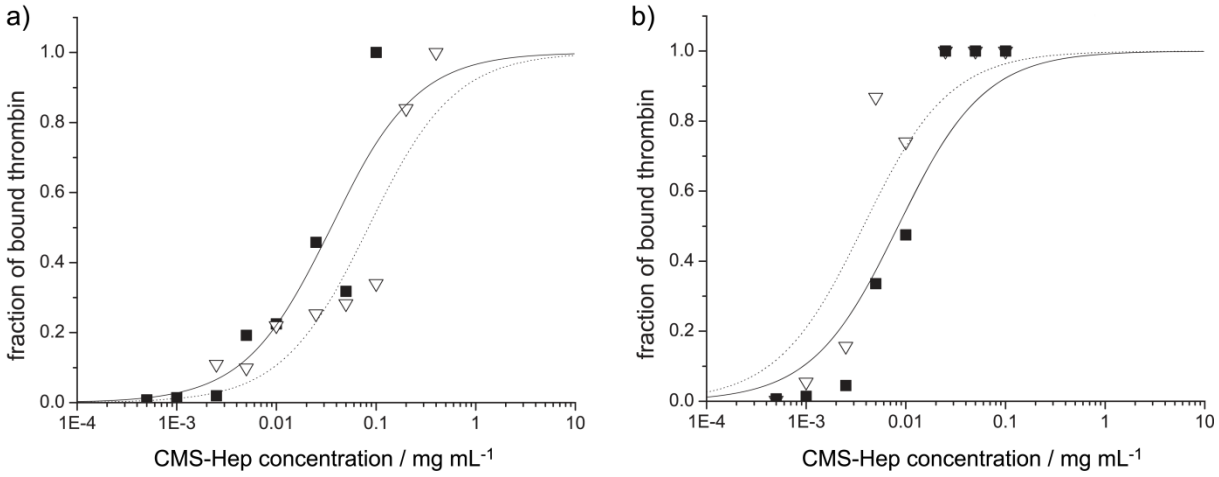

Figure 5.7. (a) Binding of TR to CMS-Hep in the presence of AT (filled squares) is enhanced as compared to the binding without AT (empty triangles). (b) Binding of TR to MSNs without Hep in the absence of AT (empty triangles) is reduced upon addition of AT (filled squares).

Figure 5.7a reveals the experiments on TR binding to CMS-Hep in the presence and absence of AT. Comparison of the resulting binding isotherms shows a clear shift towards enhanced binding upon addition of AT, indicating a specific interaction of CMS-Hep bound AT and TR. A control experiment on MSNs without Hep (Figure 5.7b) shows that in this case,

addition of AT leads to a decrease of binding possibly due to competitive binding effects, which indicates the absence of the specific interaction observed for CMS-Hep. This suggests, that AT bound to CMS-Hep exhibits specific interaction with TR and thus leads to the observed influence of CMS-Hep on blood coagulation. In the presence of AT, the binding of TR to the nanoparticles was enhanced; this indicates a specific interaction between CMS–Hep bound AT and TR. In the absence of CMS–Hep, no binding of AT and TR could be detected. We concluded that the MSN-bound Hep induces a specific interaction between AT and TR, and thus should show a pronounced anticoagulation effect.

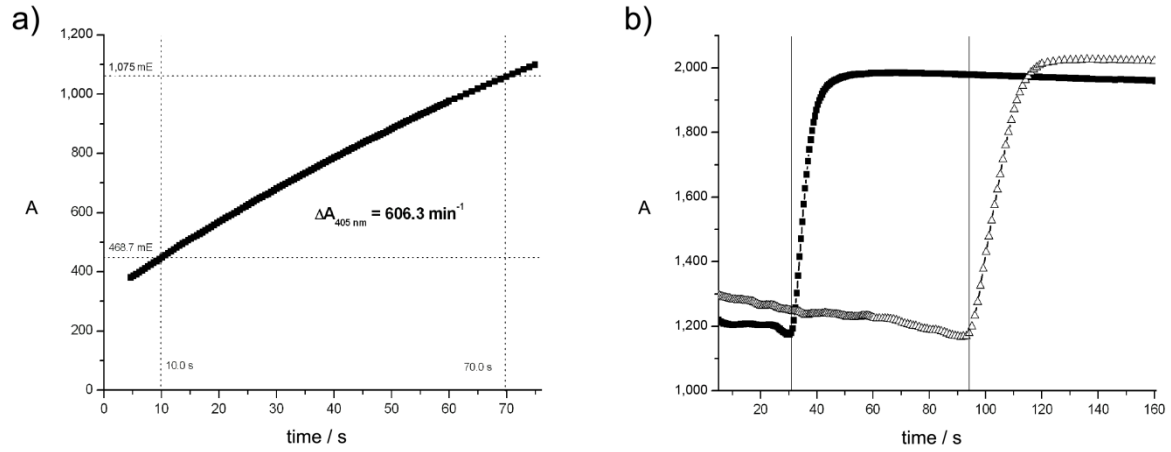

Figure 5.8. (a) FXa activity test of the sample CMS-Hep(1.0 IU/mL) and (b) the aPTT test of the aminopropyl functionalized MSNs (CMS-NH_2(0.4), filled squares) and heparin-coated ones (CMS-Hep(0.4 IU/mL), empty triangles). The absorbance on the y-axis is given in arbitrary units.

5.6 References

[1] I. I. Slowing, B. G. Trewyn, S. Giri, V. S. Y. Lin, *Adv. Funct. Mater.* **2007**, *17*, 1225.

[2] J. Lu, M. Liong, Z. Li, J. I. Zink, F. Tamanoi, *Small* **2010**, *6*, 1794.

[3] V. Cauda, A. Schlossbauer, T. Bein, *Microporous and Mesoporous Mater.* **2010**, *132*, 60.

[4] V. Cauda, A. Schlossbauer, J. Kecht, A. Zürner, T. Bein, *J. Am. Chem. Soc.* **2009**, *131*, 11361.

[5] A. Schlossbauer, S. Warncke, P. M. E. Gramlich, J. Kecht, A. Manetto, T. Carell, T. Bein, *Angew. Chem. Int. Ed.* **2010**, *49*, 4734.

[6] M. Liong, J. Lu, M. Kovochich, T. Xia, S. G. Ruehm, A. E. Nel, F. Tamanoi, J. I. Zink, *ACS Nano* **2008**, *2*, 889.

[7] C. Hom, J. Lu, M. Liong, H. Luo, Z. Li, J. I. Zink, F. Tamanoi, *Small* **2010**, *6*, 1185.

[8] V. Cauda, H. Engelke, A. Sauer, D. Arcizet, C. Bräuchle, J. Rädler, T. Bein, *Nano Lett.* **2010**, *10*, 2484.

[9] V. Cauda, C. Argyo, A. Schlossbauer, T. Bein, *J. Mater. Chem.* **2010**, *20*, 4305.

[10] V. Cauda, C. Argyo, T. Bein, *J. Mater. Chem.* **2010**, *20*, 8693.

[11] Y.-S. Lin, C. L. Haynes, *J. Am. Chem. Soc.* **2010**, *132*, 4834.

[12] J. Piper, *Acta Pharmacol. Toxicol.* **1946**, *2*, 138.

[13] C. Chauvierre, M. C. Marden, C. Vauthier, D. Labarre, P. Couvreur, L. Leclerc, *Biomaterials* **2004**, *25*, 3081.

[14] T.-Y. Liu, L.-Y. Huang, S.-H. Hu, M.-C. Yang, S.-Y. Chen, *J. Biomed. Nanotechnol.* **2007**, *3*, 353.

[15] C. Passirani, G. Barratt, J.-P. Devissaguet, D. Labarre, *Pharm. Res.* **1998**, *15*, 1046.

[16] M. M. Kemp, A. Kumar, S. Mousa, T.-J. Park, P. Ajayan, N. Kubotera, S. A. Mousa, R. J. Linhardt, *Biomacromolecules* **2009**, *10*, 589.

[17] M. M. Kemp, R. J. Linhardt, *WIREs Nanomed. Nanobiotechnol.* **2010**, *2*, 77.

[18] W. H. Seegers, J. F. Johnson, C. Fell, *Am. J. Physiol.* **1954**, *176*, 97.

[19] E. T. Yin, S. Wessler, P. J. Stoll, *J. Biol. Chem.* **1971**, *246*, 3712.

[20] L. Rusu, A. Gambhir, S. McLaughlin, J. Rädler, *Biophys. J.* **2004**, *87*, 1044.

[21] A. N. Teien, M. Lie, *Thromb. Res.* **1977**, *10*, 399.

[22] C. Wagner, F. Dati, *Clinical Laboratory Diagnostics*, TH-Books Verlagsgesellschaft, **1998**.

[23] H. Chen, Y. Chen, H. Sheardown, M. A. Brook, *Biomaterials* **2005**, *26*, 7418.

[24] A. Wang, J. P. McAllister Ii, P. Finlayson, J. Li, K. Brabant, H. Tang, C. Black, T. Cao, X. Liang, S. O. Salley, G. W. Auner, K. Y. S. Ng, *Mater. Sci. Eng. C* **2007**, *27*, 237.

6 Matrix Metalloproteinase-9 Responsive Mesoporous Silica Nanoparticles for Local Drug Delivery to Tumor Cells

This chapter is based on the following manuscript:

Christian Argyo[†], Deniz A. Bölükbas[†], Silke Meiners, Oliver Eickelberg, Thomas Bein*, and Sabine van Rijt*, *submitted*.

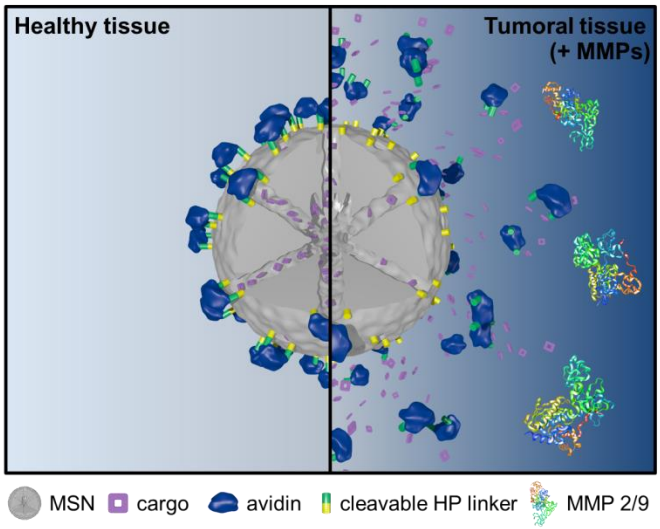

6.1 Introduction

In the past decade, the use of nanoparticles as inert carriers for therapeutic drugs with the possibility to target specific cells or tissues has revolutionized the field of drug delivery. Up to date, many kinds of nanoparticles such as liposomes, micelles, and polymer-based particles are being investigated for their therapeutic use as drug delivery devices.[1] Such nanocarrier systems have shown advantageous features resulting in improved accumulation of active drugs at the disease site and have contributed to reduced drug toxicity.[2] However, the release system of many of these drug carriers relies on spontaneous degradation *in vivo* (e.g., hydrolysis) of the nanoparticle and does not allow for controlled release of the cargo. Recent breakthroughs in the development of multifunctional mesoporous silica nanoparticles (MSNs) have made them attractive alternative carriers for drug delivery.[3-6] MSNs offer unique porous properties, providing high loading capacity that allows for efficient encapsulation of guest molecules. They feature tunable pore sizes and volumes for the specific transport of a wide variety of cargo molecules with different sizes, including chemotherapeutic molecules,

peptides, and oligonucleotides.[7] More importantly, these particles can be selectively functionalized at specific sites within the nanoparticle.[8] For example, decoration of the particle core with organic moieties can offer covalent attachment of cargos via cleavable linkers or binding of fluorescent dye molecules for particle tracking in *in vitro* and *in vivo* studies.[9-11] In addition, orthogonal shell functionalizations enable the attachment of external functions, exclusively on the outer particle surface, that do not interfere with the pore environment. This can be exploited to create stimuli-responsive pore sealing and opening for controlled drug release by surface coating and/or external functions.[9, 12-14] More specifically, MSN pore closing can be achieved by utilizing the biotin-avidin complexation, which can serve as a bulky biomolecule-based valve to efficiently block the pore entrances of MSNs.[15-16]

Lung cancer accounts for more than 30 % of all cancer deaths, and is by far the leading cause of cancer deaths in the Western world (http://globocan.iarc.fr/). Disease survival continues to be poor with a 5-year mortality of about 90 %. The two major lung cancer forms are non–small cell lung cancer and small cell lung cancer, the latter of which exhibits only very limited treatment options. Furthermore, lung cancer treatment is complicated by limitations in early detection and the correspondingly advanced stages at diagnosis. Most patients face an intensive and invasive treatment regimen comprising surgery, radiotherapy, chemotherapy, or combinations thereof.[17] Cisplatin is a commonly used chemotherapeutic agent used to treat many solid cancers, including lung cancer.[18] Drawbacks of the use of cisplatin include nephrotoxicity, nausea, hair loss, and acquired resistance of tumors towards cisplatin. A more targeted and local delivery of cisplatin may result in lower administrated therapeutic doses, and consequently reduced systemic toxicity. To overcome the problem of acquired resistance, cisplatin is often given in a combination treatment with other chemotherapeutics.[17] Multiple clinical trials suggest the use of proteasome inhibitors as combinatorial drugs as they effectively inhibit proliferation of lung tumor cells, sensitize these cells to apoptosis, and overcome drug resistance.[19] The proteasome inhibitor Bortezomib (Bz) is FDA approved for treatment of multiple myeloma, and currently tested in phase II clinical trials for lung cancer. Accordingly, local and targeted drug delivery of proteasome inhibitors in combination with cisplatin into the lung may reduce systemic side effects as well as overcome acquired resistance towards cisplatin, and represents a novel approach for combating lung cancer.

Matrix metalloproteinases (MMPs) are zinc-dependent endopeptidases that can cleave many extracellular matrix proteins and are overexpressed during advanced stages of cancer while they are minimally expressed in normal tissue.[20] For tumor cells, increased expression of MMP-9 is favorable as MMP-mediated matrix degradation increases the metastatic potential of tumor cells. Accordingly, tumor-cell mediated MMP-9 expression correlates with tumor progression, angiogenesis, and metastasis.[21] In particular, increased expression of MMP-9 has been associated with poor prognosis of lung cancer patients. Thus, the use of MMP-9 cleavable peptides for controlled drug release from drug carriers represents a promising targeting strategy for local drug delivery and controlled treatment of lung cancer.

In this work, we present avidin-coated MSNs that have been functionalized with linkers that can be specifically cleaved by matrix metalloproteinases (MMPs) 2 and 9,[22] allowing controlled release of chemotherapeutic drugs from the MSNs in the presence of high levels of MMP-2/9. These biomolecule-coated MSNs showed efficient protease sequence-specific controlled release of the incorporated chemotherapeutic cisplatin. Furthermore, this newly designed nanocarrier system is capable of highly efficient drug combination treatment. This novel drug delivery system represents a promising platform for controllable site-specific drug delivery and shows potential for new clinical applications to combat malignant growth of (lung) tumor cells.

6.2 Results and Discussion

Synthesis and Characterization of the MMP-9 Responsive MSNs. According to previous reports,[8, 23] the MSNs were synthesized by a sol-gel procedure using tetraethyl orthosilicate (TEOS) as a silica source and cetyltrimethylammonium chloride (CTAC) as template. In the present work, we created core-shell functionalized MSNs (MSN-SH_{IN}-$NH_{2\ OUT}$) via a delayed co-condensation approach, providing a thiol-functionalized core of the nanoparticles and an external particle surface decorated with amino groups. The amino groups on the external surface of the MSNs were treated via EDC amidation with the carboxyl groups of the heptapeptide (HP) linker consisting of a biotin functionality on the periphery (HP-biotin), resulting in the coating of the MSNs with HP-biotin (MSN-HP). This HP sequence is known to be selectively cleaved by MMP-9. For reference, MSNs containing a non-cleavable heptapeptide attached at the outer particle surface were also synthesized (MSN-NHP). In this NHP-biotin linker, the specific cleavage site for MMP-9 is lost due to exchange of one single amino acid. After dye/drug uptake into the mesopores of both particle types, the glycoprotein

avidin (66 kDa, av. diameter ~8 nm) was attached to the outer particle surface via linkage to the biotin groups (samples MSN-HP-AVI or MSN-NHP-AVI). Avidin shows a high affinity to biotin and therefore acts as bulky gatekeeper to block the mesopores of the silica nanoparticles. The complete synthesis strategy is depicted in Figure 6.1.

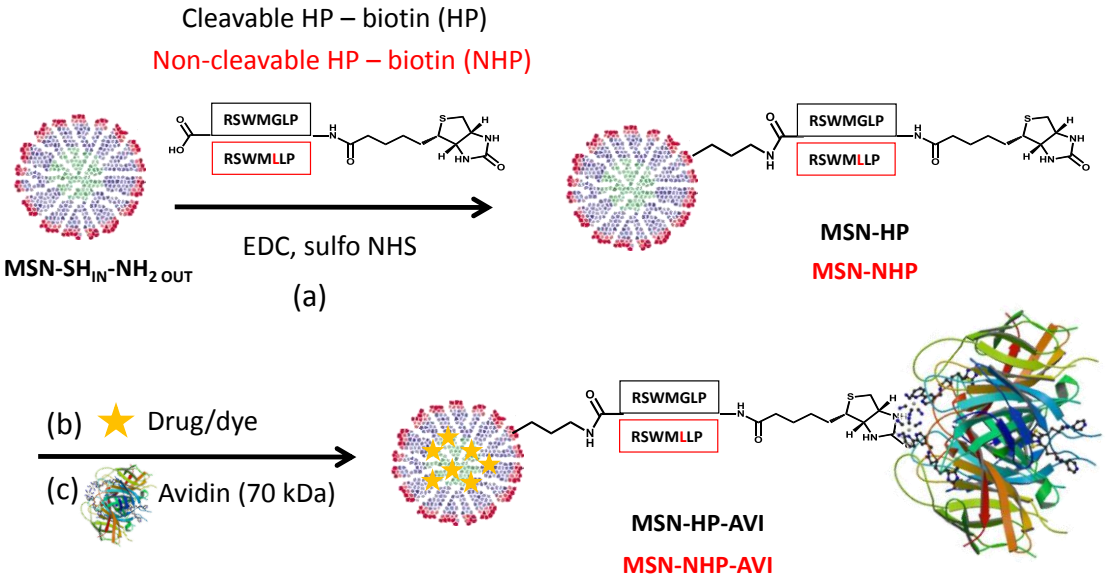

Figure 6.1. Synthesis scheme of core(green)-shell(red) functionalized mesoporous silica nanoparticles (MSN-SH$_{IN}$-NH$_{2\ OUT}$). (a) EDC amidation of amino groups with carboxy groups of the cleavable HP biotin linker (HP, black) or the non-cleavable HP-biotin linker (NHP, red) for a covalent attachment to the external particle surface (MSN-HP, MSN-NHP). (b) After cargo incorporation (drug or dye, yellow star), (c) the strong binding affinity of biotin to avidin leads to a blocking of the mesopores (MSN-HP-AVI, MSN-NHP-AVI).

The core-shell functionalized sample MSN-SH$_{IN}$-NH$_{2\ OUT}$ consisted of nano-sized mesostructured particles of about 70 nm as derived from transmission electron microscopy (TEM, Appendix 6.5). Dynamic Light Scattering (DLS) measurements revealed a mean particle size of 106 nm (Table 6.1) and good colloidal stability. This increase in particle size compared to TEM was attributed to the involvement of the hydrodynamic diameter and weak transient agglomeration of a few nanoparticles during the DLS measurements.[24] After the modification of the MSNs with the short HP linkers and further attachment of avidin, the mean particle sizes slightly increased due to these additional organic layers. Importantly, a narrow particle size distribution and no significant agglomeration were observed after each synthesis step (particle size distribution, see Appendix 6.5). Thermogravimetric analysis showed a stepwise additional weight loss for the samples MSN-HP and MSN-HP-AVI

compared to MSN-SH_{IN}-$NH_{2\ OUT}$ during heating from 150 – 900 °C (Figure 6.1a). This confirmed an effective attachment of the short organic heptapeptide linker (+ 3 % additional weight loss) and the bulky protein avidin (+ 43 % additional weight loss). The zeta potential measurements showed no significant change in the surface charge at different pH values of the MSN-HP and MSN-NHP samples compared to MSN-SH_{IN}-$NH_{2\ OUT}$, since the quantity of charged groups at the external surface was not increased by the attachment of the heptapeptide linkers (mainly consisting of unprotonable residues). The isoelectric points were around pH = 6. Only after attachment of the avidin (MSN-HP-AVI), a drastic change in the surface charge of the coated nanoparticles occurred at pH values of about 7 (Figure 6.1b). Due to various functional groups in the protein sequence including arginine, lysine and histidine residues, avidin-coated MSNs still showed positive surface charge at neutral pH values. Nitrogen sorption measurements were performed to gain information about the porosity and the surface area of the functionalized MSNs. Figure 6.2c shows typical type IV isotherms for samples MSN-SH_{IN}-$NH_{2\ OUT}$, MSN-HP, and MSN-NHP with inflection points at around 0.3 p/p_0, indicating mesoporous structure for all these samples. Relatively high BET surface area and pore volume were obtained for the MSN-SH_{IN}-$NH_{2\ OUT}$ nanoparticles. A summary of the porosity parameters is given in Table 6.1. A slight reduction in specific surface area and pore volume occurred for the MSNs containing the HP linkers (MSN-HP and MSN-NHP, for more details see Appendix 6.5). The narrow pore size distribution with a maximum at around 3.6 nm confirmed an accessible porous system even after modification with the HP linkers. After the attachment of avidin to the silica nanoparticles, we obtained a type II isotherm indicating a massive loss of specific surface area and pore volume (Figure 2c). These data showed that the mesopores of the avidin-coated MSNs almost completely blocked the access of nitrogen molecules, proving that avidin is a suitable gatekeeper to efficiently seal the mesopores of our nanoparticles. Infrared spectroscopy showed a band at 1629 $cm^{-1}$for non-coated particles (i.e. MSN-SH_{IN}-$NH_{2\ OUT}$), indicating the bending modes of physisorbed water (Figure 6.1d). This band was present in all spectra but was partially covered by other more intensive bands of the coated particles. The nanoparticles MSN-HP and MSN-NHP showed an additional band at 1654 cm^{-1} (C=O stretching vibration), which can be attributed to the amide bonds of the short HP linkers. Subsequently, this band was fully obscured after modification with avidin, and typical amide vibration bands (amide I: C=O stretching vibration at 1643 cm^{-1}; amide II: N-H deformation and C-N stretching vibration at 1535 cm^{-1}) of high intensities were detected giving evidence for the presence of the protein. From these

data, we conclude that the attachment of the avidin gatekeepers via short HP-biotin linkers (cleavable and non-cleavable for MMP-9) to the external surface of MSNs was successful.

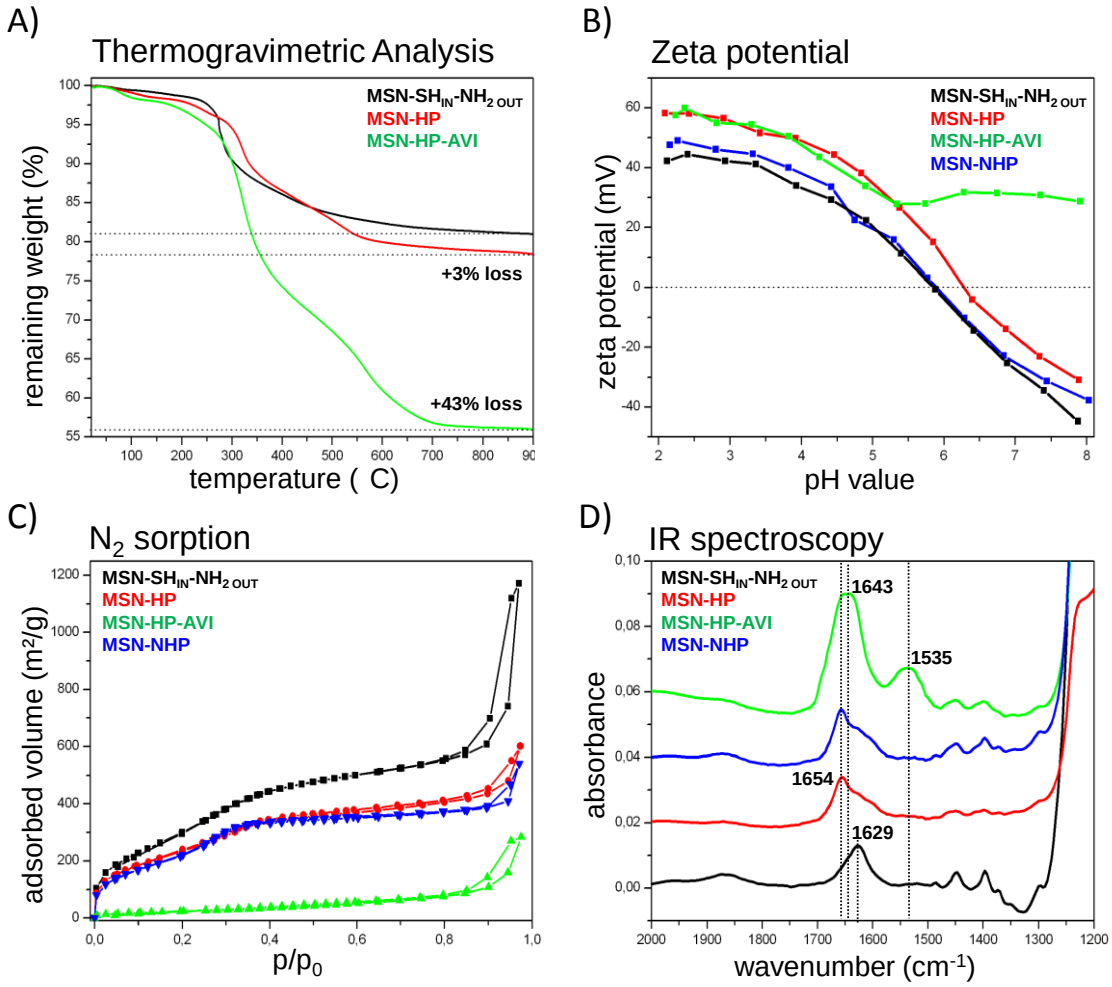

Figure 6.2. Characterization of functionalized mesoporous silica nanoparticles. a) Thermogravimetric analysis, b) zeta potential measurements, c) nitrogen sorption isotherms, and d) infrared spectroscopy (all curves are shifted by a value of 0.02 along the y-axis for clarity) of MSN-SH$_{IN}$-NH$_{2\ OUT}$ (black), MSN-HP (red), MSN-NHP (blue), and MSN-HP-AVI (green).

Table 6.1. Structural parameters of functionalized MSNs.

Sample	Particle size[a] (nm)	BET surface area (m^2/g)	Pore volume[b] (cm^3/g)	DFT pore size[c] (nm)
MSN-SH_{IN}-$NH_{2\ OUT}$	106	1150	0.67	3.6
MSN-HP	142	882	0.55	3.6
MSN-HP-AVI	164	90	0.05	-
MSN-NHP	142	825	0.52	3.6

[a]Particle size refers to the peak value of the size distribution derived from DLS measurements. [b]Pore volume was calculated up to a pore size of 8 nm to remove the contribution of inter-particle textural porosity. [c]DFT pore size refers to the peak value of the pore size distribution.

Stimuli-Responsive Release of Fluorescein. To prove MMP-9 stimuli-responsive release behavior of our nanoparticle system, time-based release experiments of the fluorescent guest fluorescein were performed at 37 °C as previously reported.[16] The avidin-coated sample (MSN-HP-AVI) preloaded with fluorescein showed no premature release of the cargo molecules. Moreover, long-term stability of the capping system for at least up to 16 h was observed (Figure 6.3 and Appendix 6.5) indicating that the avidin gatekeepers result in a perfect sealing of the mesopores and prevent unintended release of the cargo. Only upon addition of recombinant MMP-9 (1 µg/mL) to the particle solution, an increase in fluorescence intensity over time was observed (Figure 6.3). This release behavior gave evidence for protease-responsive release behavior of our nanoparticle system. After around 16 h, a plateau was reached, which suggests a complete release of the loaded cargo molecules within this time range. Additionally, we investigated the release behavior of MSNs containing a non-cleavable heptapeptide linker (MSN-NHP-AVI) after addition of MMP-9. No release of the loaded fluorescein was observed, showing that neither the NHP-biotin linkers nor the avidin gatekeepers are cleavage targets for the MMP-9 enzyme. Consequently, this experiment proved a highly specific release behavior of the MSN-HP-AVI by MMP-9. Because the HP linker can also be cleaved by MMP-2, we investigated the ability of recombinant MMP-2 to release the cargo from the same system. MMP-2 was also able to release fluorescein from the particles, but with slower kinetics compared to MMP-9 (Appendix 6.5). We therefore chose to continue with MMP-9 throughout the following studies. However, it is important to note that both enzymes are overexpressed in lung cancer and so we expect a cumulative effect on cargo release *in vivo*.

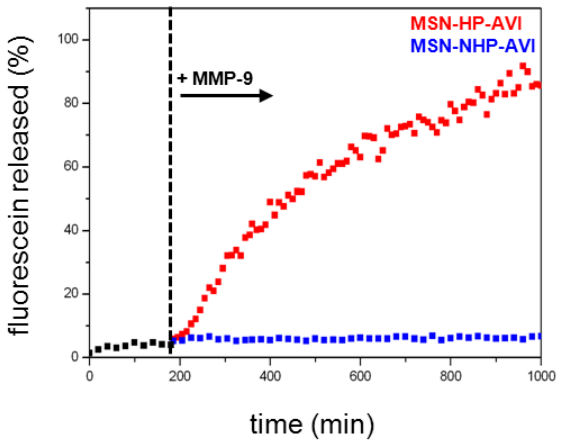

Figure 6.3. Release kinetics of fluorescein from the MSNs before and after addition of MMP-9. Before addition of MMP-9 almost no premature release of the cargo can be observed, which indicates a near perfect closure of the mesopores. Only MSN-HP-AVI (red) shows a significant increase in fluorescence intensity in the presence of MMP-9, demonstrating a protease-responsive release behavior. Specific cleavage of the HP-biotin linker by MMP-9 is proven by the absence of cargo release of the reference MSN-NHP-AVI (blue).

Toxicity Studies. The toxicity of the novel drug delivery particles was assessed in non-small-cell lung cancer (NSCLC) cell lines A549 and H1299 using the WST-1 assay. WST-1 is a stable tetrazolium salt that is cleaved to form a soluble formazan by a complex cellular mechanism that is largely dependent on the glycolytic production of NAD(P)H in viable cells. Therefore, the colorimetric analysis of the formed formazan dye directly correlates to the number of metabolically active cells in the cell culture. To determine whether the avidin functionalization had an effect on the toxicity of these particles, the non-coated particles (i.e. MSN-SH_{IN}-$NH_{2\ OUT}$) were included in the study as well. Thus, A549 and H1299 cells were directly exposed to either MSN-HP-AVI or MSN-SH_{IN}-$NH_{2\ OUT}$ particles at different concentrations at normal cell growing conditions. After 4 h of particle exposure, no toxic effects could be detected in either cell line even at high particle concentrations of 500 µg/mL (Appendix 6.5). After 24 h of exposure, a minor reduction in cell viability for both cell lines at high particle concentrations (> 200 µg/mL) was observed, with H1299 cells being more affected (Figure 6.4a, right panel). Interestingly, in both cell lines the non-coated particles (MSN-SH_{IN}-$NH_{2\ OUT}$) showed increased toxicity at these high particle concentrations compared to the avidin-capped particles (MSN-HP-AVI).

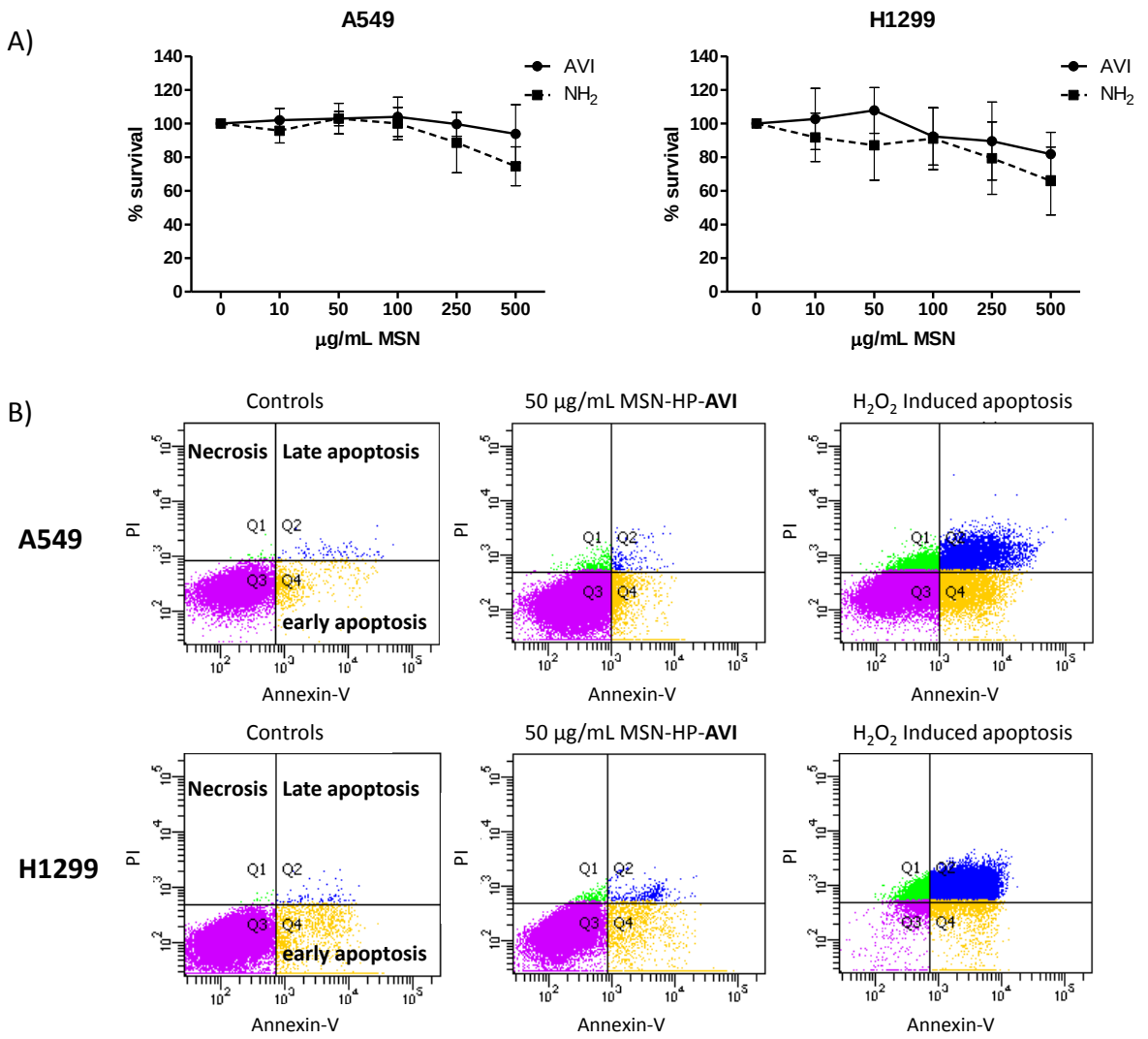

Figure 6.4. Toxicity of different concentrations of MSNs containing the MMP-9 responsive release system (MSN-HP-AVI) and of non-coated particles (MSN-SH_{IN}-$NH_{2\,OUT}$) after 24 h exposure, determined by a) WST-1 assay in A549 (left) and H1299 lung cancer cell lines (right) and b) Annexin-V/PI staining and FACS analysis.

To assess whether these particles induce a specific form of cell death, namely necrosis or apoptosis, at high concentrations, we performed a live/dead assay using Annexin-V-FITC and propidium iodide (PI) staining. Externalization of phosphatidylserine (PS) from the inner face of the plasma membrane to the cell surface is a hallmark of early apoptosis. The FITC labeled Annexin-V binds to PS, resulting in fluorescent staining of early apoptotic cells (lower right quadrant, Figure 6.4b). In late stage apoptotic and in necrotic cells, propidium iodide (fluorescent DNA intercalating agent) is able to enter the cell and binds strongly to DNA (upper left quadrant for necrotic cells PI and upper right quadrant for late stage apoptotic cells). Similar to the results obtained with the WST-1 assay, no apoptotic or necrotic cell death was detected at low particle concentrations of below 100 µg/mL at both 4 and 24 h

time-points (Table 6.2 and 6.3 for 24 h exposure). Importantly, at the dose we used in the following experiments (50 µg/mL) no induction of apoptosis/necrosis could be observed after 24 h in either cell line (Figure 6.4b). At high particle concentrations of 250 µg/mL, some cells were undergoing early apoptosis already after 4 h of exposure (Appendix 6.5), whereas after 24 h, the apoptotic cells were mainly in the late apoptotic phase (Appendix 6.5). Furthermore, as was observed with the WST-1 assay, the avidin capping system had a positive effect on the toxicity, where particles with the avidin capping system induced less apoptosis compared to the amino-functionalized particles (Table 6.2 and 6.3, Appendix 6.5). This was especially evident in the H1299 cell line (Table 6.3, Appendix 6.5).

Table 6.2. Percentage of A549 cells in different stages of cell death after 24 h exposure to MSNs containing MMP-9 responsive release system (MSN-HP-AVI) and non-coated particles (MSN-SH_{IN}-$NH_{2\ OUT}$), as quantified by FACS analysis of Annexin-V/PI stained cells. The values given are average of two independent experiments ± SD.

A549	healthy	necrotic	early apoptotic	late apoptotic
non treated control	92.2 ± 1.1	2.4 ± 2.3	4.5 ± 1.8	0.8 ± 0.3
50 µg/mL MSN-HP-AVI	91.9 ± 2.0	0.8 ± 0.3	6.4 ± 1.8	0.6 ±0.1
50 µg/mL MSN-SH_{IN}-$NH_{2\ OUT}$	93.6 ± 0.6	0.8 ± 0.2	4.9 ±0.9	0.8 ± 0.1
100 µg/mL MSN-HP-AVI	92.8 ± 0.8	1.1 ± 0.6	5.2 ± 1.3	0.9 ± 0.1
100 µg/mL MSN-SH_{IN}-$NH_{2\ OUT}$	91.7 ± 1.8	0.7 ± 0.1	6.3 ± 1.8	1.3 ± 0.1
250 µg/mL MSN-HP-AVI	89.2 ± 2.7	2.5 ± 0.9	6.5 ± 3.6	1.8 ± 0.1
250 µg/mL MSN-SH_{IN}-$NH_{2\ OUT}$	83.2 ± 0.1	1.2 ± 0.9	12.1 ± 1.3	3.6 ±0.4

Table 6.3. Percentage of H1299 cells in different stages of cell death after 24 h exposure to MSNs containing MMP-9 responsive release system (MSN-HP-AVI) and non-coated particles (MSN-SH_{IN}-$NH_{2\ OUT}$), as quantified by FACS analysis of Annexin-V/PI stained cells. The values given are average of two independent experiments ± SD.

H1299	healthy	necrotic	early apoptotic	late apoptotic
non treated control	92.8 ± 2.3	0.2 ± 0.1	5.2 ± 0.1	0.4 ± 0.1
50 µg/mL MSN-HP-AVI	81.4 ± 2.3	8.0 ± 0.4	5.0 ± 0.5	6.5 ± 1.0
50 µg/mL MSN-SH_{IN}-$NH_{2\ OUT}$	73.2 ± 1.3	6.2 ± 0.5	9.6 ± 0.6	8.9 ± 0.3
100 µg/mL MSN-HP-AVI	74.3 ± 2.3	7.2 ± 1.0	7.5 ± 0.3	6.7 ± 0.4
100 µg/mL MSN-SH_{IN}-$NH_{2\ OUT}$	67.1 ± 0.4	6.3 ± 0.3	8.6 ± 0.4	16.8 ± 0.7
250 µg/mL MSN-HP-AVI	68.2 ± 4.0	6.2 ± 0.4	9.2 ± 0.6	12.4 ± 0.9
250 µg/mL MSN-SH_{IN}-$NH_{2\ OUT}$	51.8 ± 3.9	3.5 ± 0.3	19.1 ± 1.5	20.6 ± 1.6

Although MSNs are widely considered as potential drug delivery carriers, only few studies report on their biomedical applications and *in vivo* toxicity.[25] Moreover, assessing the biocompatibility of specific MSN systems is complicated due to the great variation of characteristics possible for MSNs such as the chemical composition, surface chemistry, and diameter that cannot be easily compared between studies. For instance, Huang *et al.* found that only altering the shape of MSNs without changing other characteristics effected their cellular uptake and modulation of cellular function.[26] Similarly, particle functionalization such as PEGylation has shown to greatly impact their biodistribution.[27] It is therefore necessary to evaluate the biocompatibility for each specific MSN system. Here we showed that functionalizing MSNs with avidin protein has a positive effect on the toxicity of these particles and may be a promising strategy to increase their overall biocompatibility.

MMP-9 Responsive Release of Calcein-AM. Triggered drug release from the particles was first assessed with confocal microscopy using the model drug, calcein-AM in both H1299 and A549 cell lines. Calcein-AM is a non-fluorescent cell-membrane permeable compound that is hydrolyzed by intracellular esterases into non-cell permeable, green fluorescent calcein. More specifically, calcein-AM is taken up in the cells via endocytosis and can be detected even at low doses (Figure S6). In this system, calcein-AM functions as a model drug that is released in the extracellular region, and is subsequently actively taken up by the cancerous cells where it is metabolized and becomes active (starts fluorescing). MSNs containing MMP-9 cleavable and non-cleavable linkers (MSN-HP-AVI and MSN-HP-AVI) encapsulating either 20 or

50 µM solutions of calcein-AM were incubated with 0, 1 or 2 µg/mL recombinant MMP-9 in HBSS buffer for 2 h at 37 °C. After the incubation time, particles were removed from the suspension by centrifugation and the cells were exposed to the supernatant for 30 min allowing endosomal uptake of the released calcein-AM dye. Cells were counterstained with Hoechst nuclei stain (blue channel) to allow for the identification of all live adherent cells. After only 2 h of incubation with the different concentrations of recombinant MMP-9, calcein delivery to the cytosol could be observed in both cell lines (Figure 6.5, left panel). Notably, the amount of calcein delivery was dependent on both MMP-9 concentration and the amount calcein-AM encapsulated in the MSNs in both cell lines. The MSNs containing non-cleavable linkers (i.e. MSN-NHP-AVI, differing only one amino acid from HP) displayed only limited release of the calcein dye (Figure 6.5, right panel). The minor calcein-AM release observed for the non-cleavable particles could be due to some dye leakage out of the particles and/ or due to a small amount of dye sticking to the outside of the particles during the preparation step, which is then released over time. Because the dye concentration does not need to be very high to get a visible signal (Appendix 6.5), this could already result in some staining. Nevertheless, MSN-HP-AVI particles that were pre-activated with MMP-9 showed a significant increase in fluorescence intensity and consequently resulted in efficient and stimuli-responsive release of the cargo. The H1299 cells were more sensitive to calcein staining compared to the A549 cells, with already significant release observed when 20 µM solution of calcein-AM encapsulated MSNs were exposed to 1 µg/mL MMP-9. This coincides with the observation that H1299 cells were more sensitive towards calcein staining, as seen in the calcein-AM titration curves (Appendix 6.5) and may relate to an increased endosomal uptake capacity of these cells.

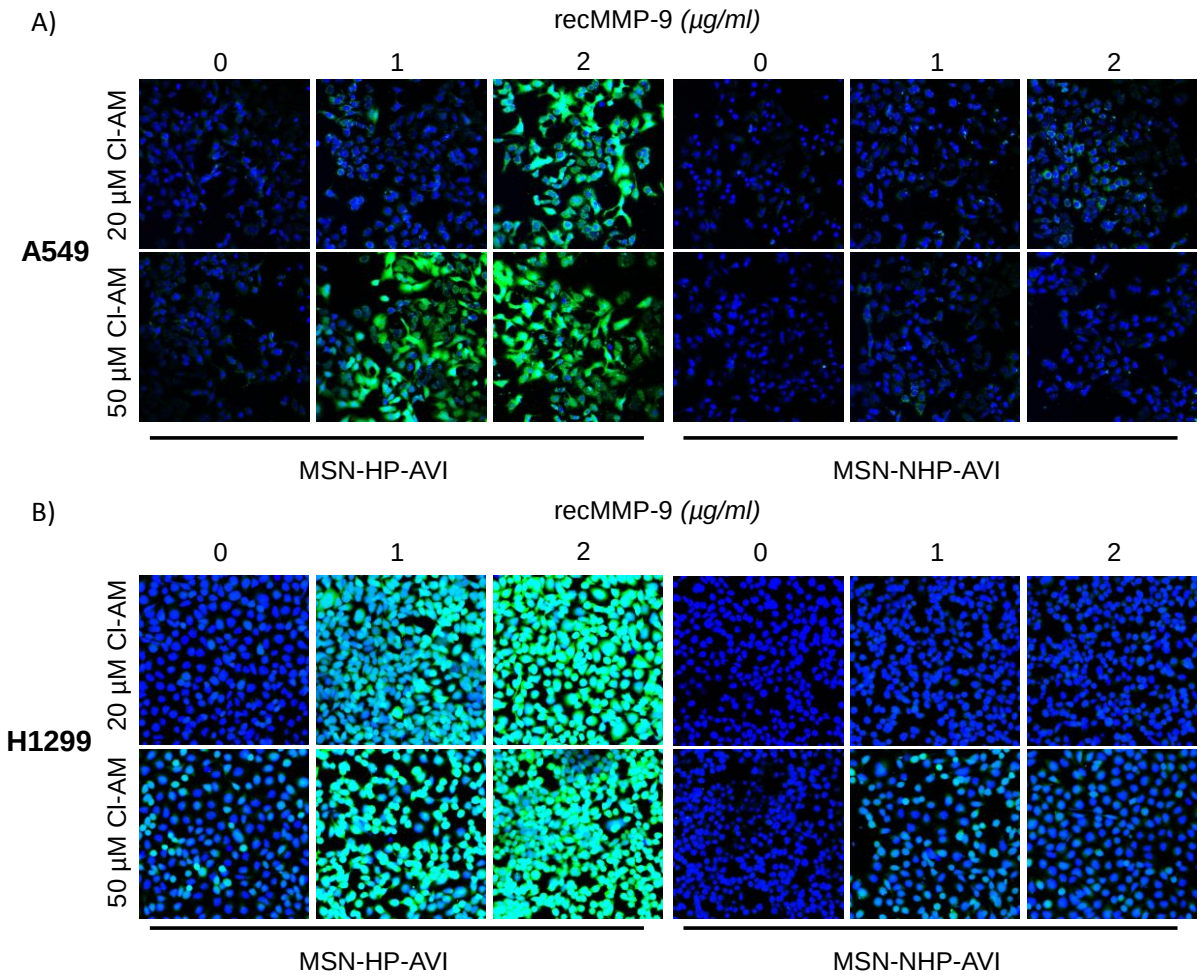

Figure 6.5. Confocal images showing MMP-9 responsive release of calcein-AM (Cl-AM, green) from MSNs containing MMP-9 cleavable linkers (MSN-HP-AVI) and MSNs containing non-cleavable linkers (MSN-NHP-AVI) after 2 h incubation with 0, 1, or 2 µg/mL MMP-9 in a) A549 cells and b) H1299 cells. Hoechst dye was used as counterstain (nuclei, blue). Pictures show representative micrographs from three independent experiments.

MMP-9 Responsive Release of Cisplatin. Next, we assessed whether the functionalized MSNs were also able to efficiently release the chemotherapeutic drug cisplatin to the cells. For this purpose, MSN-HP-AVI particles encapsulating increasing amounts of cisplatin were directly incubated with the cells in media containing 0, 0.5 or 1 µg/mL of recombinant MMP-9. Due to the longer exposure time of 24 h to allow cisplatin-mediated cell death, compared to 2 h for the calcein-AM release experiments, we chose to use lower concentrations of MMP-9 for this experiment. After 24 h of particle exposure, cell viability was tested. A low particle dose of 50 µg/mL was used, as this dose is a non-toxic dose after 24 h of incubation (Figure 6.4). Cells exposed to particles loaded with cisplatin, but with no MMP-9 present in the media, showed only minor loss of cell viability compared to non-treated control cells in both cell lines (white bars in Figure 6.6a and b). This clearly demonstrates the tight sealing of

the cisplatin-loaded MSNs by the peptide-biotin-avidin system. Interestingly, release of cisplatin from the particles was dependent on both the MMP-9 and the cisplatin dose in both cell lines (Figure 6.6a and b). Significant cell death could already be observed for cells exposed to particles loaded with a 10 µM solution of cisplatin when 1 µg/mL MMP-9 was present in the medium, and exposed to particles loaded with a 20 µM solution of cisplatin when 0.5 µg/ml MMP-9 was present. H1299 cells were slightly more sensitive towards the cisplatin-loaded MSNs, in analogy to the calcein release experiments. Importantly, MSNs with non-cleavable linkers (MSN-NHP-AVI) did not induce any cell death in either cell line, indicating that the linker is cleaved specifically by MMP-9 enzymes and that the sealing of the MSN pores is tight (Appendix 6.5). It is important to note that the particles were loaded by diffusing a cisplatin solution into the particles, after which the particles were sealed and washed. This is referred to in the figures as cisplatin concentration used to load the particles. The amount of cisplatin released from the particles and therefore the cisplatin concentration the cells were exposed to is much lower since the volume inside the MSNs is very small. To estimate what the actual concentration of released cisplatin was, we performed a dose-responds curve of cisplatin alone in A549 and H1299 cells. Comparing cell death caused by the cisplatin released from the MSNs to that of cisplatin alone we can estimate that the cisplatin concentration released is about 10-20x diluted (e.g. 1 µM cisplatin caused 43 % cell survival compared to 33 % survival after exposure to 20 µM cisplatin loaded particles in H1299 cells). This can also be observed when comparing the calcein titration curve to the release of calcein loaded particles (Figure 6.5 and Appendix 6.5).

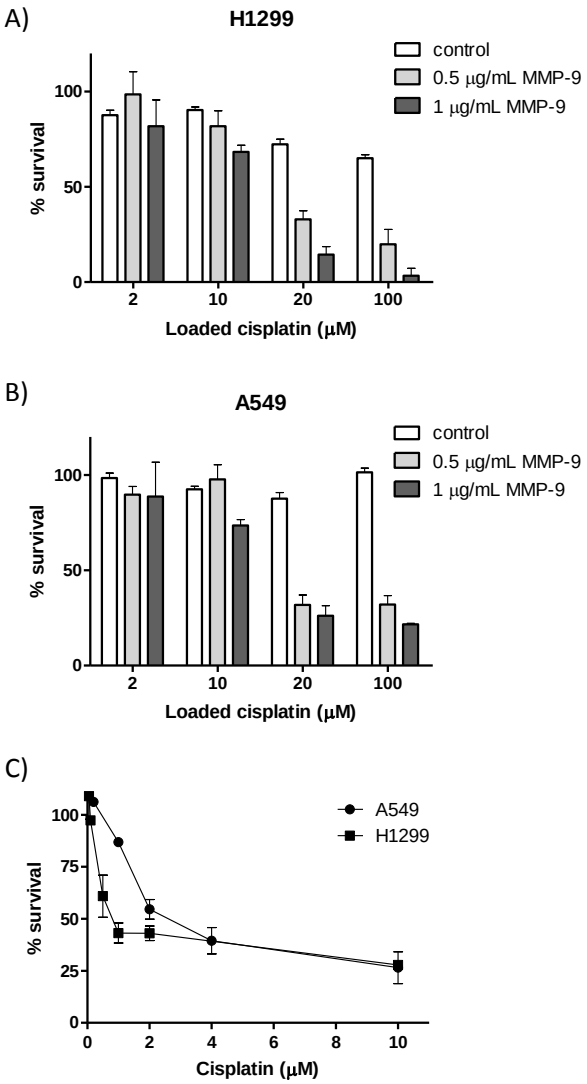

Figure 6.6. Controlled release of cisplatin from MSN-HP-AVI (particles loaded with 2, 10, 20 or 100 μM solutions of cisplatin) incubated with 0 (white bars), 0.5 (light-grey bars), or 1 μg/mL (dark-grey bars) MMP-9 as measured by cell survival using the MTT assay after 24 h exposure for a) H1299 cells and b) A549 cells (non-exposed cells were set to 100 % survival).

To assess whether biologically relevant conditions and physiological concentrations of MMP-9 are able to efficiently trigger cisplatin release from the MSNs, A549 and H1299 cells were transiently transfected with MMP-9 cDNA to induce MMP-9 expression in these cells. Secretion of the soluble MMP-9 into the cell supernatant was validated by zymography. This method uses denaturing SDS-gels which contain 1 % of the MMP-9 substrate gelatin. Proteins from the cell supernatant are separated according to their molecular weight and the presence of active MMP-9 complexes can be detected by digestion of the gelatin inside the gel which results in a clear band after gel protein staining. Endogenous secretion of MMP-9 is very low in both cell lines, as only a low signal was detected in the zymography for cells transfected with a non-coding control vector (Figure 6.7A, first two lanes). However, when cells were

transfected with the cDNA encoding MMP-9, both cell lines could secrete significant amounts of MMP-9 as detected by distinct zymography signals. Expression levels of active MMP-9 were higher for H1299 compared to A549, but lower compared to the signal obtained with 0.25 µg/mL of recombinant MMP-9 run on the same gel (Figure 6.7). These results indicate that the biologically relevant expression level of MMP-9 is lower compared to *in vitro* addition of recombinant MMP-9. To assess cisplatin release under these physiological conditions, MMP-9 cDNA and a non-coding control vector transfected cells were exposed to MSN-HP-AVI cisplatin containing particles. Transfected cells with non-coding control vector (white bars in Figure 6.7b and c) were slightly more sensitive to particle exposure compared to the non-transfected cells (white bars in Figure 6.6) which might be due to the additional stress of the cells undergoing the transfection procedure. Importantly, cisplatin loaded MSNs showed a significant increase in cell death compared to control transfected cells, clearly indicating that biologically relevant concentrations of cellular MMP-9 are able to trigger release of chemotherapeutic drugs from the stimuli responsive MSNs. Similar to the previous experiments, H1299 cells were more sensitive, and significant cell death was observed with particles loaded with 20 µM cisplatin solution. In A549 cells, only a minor albeit significant cytotoxic effect was seen at the highest cisplatin dose of 100 µM. This reduced responsiveness of A549 cells corresponds well with the reduced expression of MMP-9 in these cells, suggesting that with lower levels of MMP-9 longer exposure times are needed to open the MSNs.

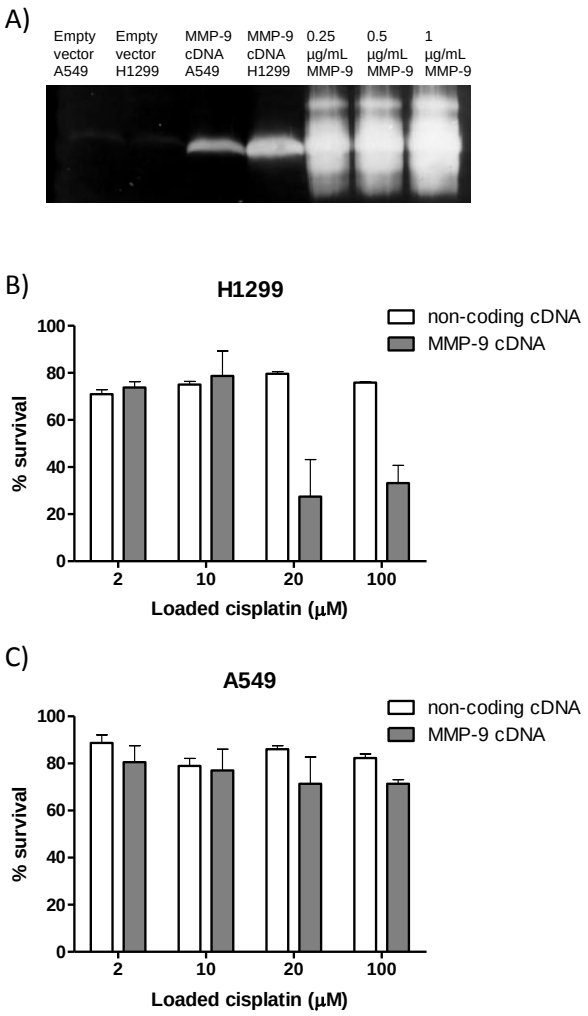

Figure 6.7. Controlled release of cisplatin from MSN-HP-AVI (loaded with 2, 10, 20 or 100 µM solutions of cisplatin) incubated with either MMP-9 cDNA (grey bars) or empty vector transfected cells (white bars) as measured by cell survival after 24 h exposure for a) H1299 cells and b) A549 cells (non-exposed cells were set to 100 % survival).

In conclusion, we were able to show that MSN-HP-AVI particles loaded with cisplatin induce cell death in a both MMP-9 and cisplatin dose-dependent manner. In addition, the effectiveness of this system was validated in a relevant biological setting using MMP-9 cDNA transfected human lung tumor cells. A few recent studies report on the use of MMP-2/9 sensitive peptides for targeted delivery of chemotherapeutics.[28-30] MMP-responsive MSNs were reported only recently by Zhang *et al.*,[31] who could show tumor-triggered cell targeting by utilizing cellular-uptake-shielding multifunctional envelope-type MSNs. Turn-on targeting properties of the multifunctional MSNs were observed via cleavage of a protection shell by MMPs to achieve a specific cellular uptake by cancer cells. After cell uptake, the cargo release (doxorubicin) was obtained by redox-driven release mechanism. In another study by Xu *et al.*,[32] gelatin was used simultaneously as a gatekeeper and degradable substrate for

MMPs in gelatin-coated MSNs. Nevertheless, the efficiency of pore sealing to prevent premature drug release was poor in this system. Here we show efficient protease sequence-specific controlled release of incorporated chemotherapeutic cisplatin from our novel biomolecule-coated MSN system in two non-small cell lung cancer cell lines.

Cisplatin and Bortezomib Combination Treatment. Cisplatin is often used in combination treatment with other chemotherapeutics to overcome the problem of acquired tumor resistance towards cisplatin for treatment of lung cancer.[17] As MSNs can encapsulate multiple drugs in their mesoporous system with high efficiency, they offer an opportunity for controlled local delivery of two drugs at the same time. This is anticipated to result in lower administered doses of chemotherapeutics necessary to achieve a similar therapeutic effect. Proteasome inhibitor Bz is a selective inhibitor of the proteasome, an enzyme that is responsible for the degradation of over 90 % of all cellular proteins. As such, Bz induced proteasome inhibition interferes with many cellular processes, including cell cycle control.[33] The application of proteasome inhibitors in cancer therapy is hampered by difficulties in administration and high systemic toxicity.[34] In addition, high doses and long exposure times are needed to induce toxicity. Several clinical trials suggest that these inhibitors would be better suited for combination therapy since they effectively inhibit proliferation of tumor cells, sensitize these cells to apoptosis, and overcome drug resistance.[19]

To investigate whether we could reduce the amount of cisplatin to achieve a similar therapeutic effect when Bz was present, we exposed A549 cells to MSNs loaded with a solution containing 2, 10 or 20 µM cisplatin and 1 µM of Bz. MSN-HP-AVI particles loaded with only 1 µM Bz (and no cisplatin) were included as controls and did not show an effect on cell viability after 24 h of exposure (Appendix 6.5). Cells exposed to MSNs loaded with 2, 10 or 20 µM cisplatin and 1 µM Bz, but with no MMP-9 present also showed no significant loss in cell viability (Figure 6.8, white bars). Interestingly, when using toxic doses of cisplatin, the concomitant release of Bz had no significant effect on cell death. However, when non-toxic doses of cisplatin were used (i.e., particles loaded with 2 and 10 µM solutions), a significant increase in cell death was observed for particles that contained both drugs in A549 cells (Figure 6.8). Remarkably, this increase was largest for the lowest cisplatin dose (2 µM), with an increased cell death of over 35 % when Bz was present. The effect of 2 µM cisplatin + Bz is in-between that of 10 and 20 µM when cisplatin alone is used. This is a remarkable 5 to 10 x increase in potency when Bz is added. For 10 µM cisplatin loaded particles this

difference was 17 %. These results are in accordance with the combinatorial treatment of cisplatin and proteasome inhibitor on ovarian cancer cells where both drugs were directly applied to the tumor cells.[35] Using proteasome inhibitors in combination with a known cytotoxic drug is a new approach in the treatment of cancer in general and lung cancer in particular. Several clinical and preclinical trials have shown that Bz can be successfully combined with multiple cytotoxic agents as well as radiotherapy, showing good tolerability and without significant overlapping toxicity.[36-37] In particular, the phase II clinical trial study with Bz in combination with carboplatin (another platinum based chemotherapeutic) showed promising progression-free and improved overall survival rates in the treatment of non-small cell lung cancer.[38] To our knowledge, this is the first report in which nanoparticle-based controlled release of a proteasome inhibitor combined with cisplatin shows vastly enhanced antitumor activity.

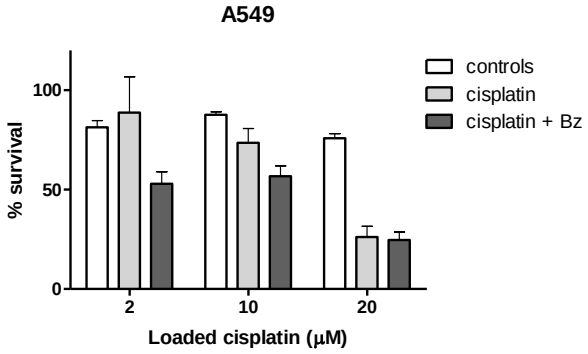

Figure 8. Effect of particle mediated cisplatin and Bortezomib (Bz) combination treatment on cell survival. MSN-HP-AVI particles co-encapsultaed with 2, 10, or 20 µM solutions of cisplatin and 1 µM solution of Bz incubated with 1 µg/mL MMP-9 for 24 h in A549 cells (non-exposed cells were set to 100 % survival).

6.3 Conclusions

In this study, we report the synthesis of novel mesoporous silica nanoparticles containing an MMP-9 responsive avidin capping system. Since MMP-9 enzymes are overexpressed during advanced stages of cancer, whereas they are minimally expressed in normal tissue, this system allows for stimuli-responsive local delivery of cytotoxic drugs in cancer therapy. We demonstrate stimuli-responsive controlled drug release from MSNs only in the presence of MMP-9 enzymes in two non-small-cell lung cancer cell lines. Specifically, dose-dependent release was shown for model cargo calcein-AM as well as chemotherapeutic cisplatin. These results were also validated in a more biological setting, using MMP-9 cDNA transfected cells. Importantly, the MSNs were non-toxic up to high concentrations, where the avidin

functionalization reduced the toxicity of these particles. Additionally, in this work we show for the first time that this novel drug delivery system can be used to efficiently deliver a combination of two drugs, Bz and cisplatin, in a stimuli-controlled manner. Remarkably, MSNs that contained non-toxic doses of cisplatin along with the proteasome inhibitor Bz resulted in a 5 to 10 x increase in potency compared to cisplatin alone.

6.4 Experimental

Materials. Tetraethyl orthosilicate (TEOS, Fluka, > 98 %), triethanolamine (TEA, Aldrich, 98 %), cetyltrimethylammonium chloride (CTAC, Fluka, 25 % in H_2O), mercaptopropyl triethoxysilane (MPTES, Fluka, > 80 %), aminopropyl triethoxysilane (APTES, Sigma Aldrich, 99 %), ammonium fluoride (NH_4F, Fluka), ammonium nitrate (NH_4NO_3, Fluka), hydrochloric acid (HCl, 37 %), Bio-PLGMWSR (HP-biotin, GenScript, 96.3 %), Bio-PLLMWSR (NHP-biotin, GenScript, 90.1 %), *N*-(3-dimethylaminopropyl)-*N*'-ethylcarbodiimide hydrochloride (EDC, Aldrich), *N*-hydroxysulfosuccinimide sodium salt (sulfoNHS, Aldrich), Avidin, egg white (Merck, Calbiochem), fluorescein disodium salt dihydrate (Acros), calcein acetoxymethyl ester (calcein-AM, Sigma Aldrich), cisplatin (Sigma Aldrich), Bortezomib (Bz, Velcade, Millennium Pharmaceuticals), were used as received. Ethanol (EtOH, Aldrich, absolute), dimethylsulfoxide (DMSO, Aldrich), and HBSS buffer (Gibco) were used as solvents without further purification. Bi-distilled water was obtained from a Millipore system (Milli-Q Academic A10).

Synthesis procedures. Particle synthesis (MSN-SH_{IN}-$NH_{2\ OUT}$). Core-shell functionalized MSNs were synthesized according to a slightly modified method, as previously reported.[8] In brief, a mixture of tetraethyl orthosilicate (TEOS, 1.63 g, 7.82 mmol), mercaptopropyl triethoxysilane (MPTES, 112 mg, 0.48 mmol) and triethanolamine (TEA, 14.3 g, 95.6 mmol) was heated under static conditions at 90 °C for 20 min in a polypropylene reactor. Then, a solution of cetyltrimethylammonium chloride (CTAC, 2.41 mL, 1.83 mmol, 25 wt% in H_2O) and ammonium fluoride (NH_4F, 100 mg, 2.70 mmol) in H_2O (21.7 g, 1.21 mmol) was preheated to 60 °C and added quickly to the TEOS solution. The reaction mixture was stirred vigorously (700 rpm) for 20 min while cooling down to room temperature. Subsequently, TEOS (138.2 mg, 0.922 mmol) was added in four equal increments every three minutes. After another 30 min of stirring at room temperature, TEOS (19.3 mg, 92.5 µmol) and aminopropyl

triethoxysilane (APTES, 20.5 mg, 92.5 µmol) were added to the reaction. The resulting mixture was then allowed to stir at room temperature overnight. After addition of ethanol (100 mL), the MSNs were collected by centrifugation (19,000 rpm, 43,146 rcf for 20 min) and re-dispersed in absolute ethanol. The template extraction was performed by heating the MSN suspension under reflux (90 °C oil bath temperature) for 45 min in an ethanolic solution (100 mL) containing ammonium nitrate (NH_4NO_3, 2 g), followed by 45 min under reflux in a solution of concentrated hydrochloric acid (HCl, 10 mL) and absolute ethanol (90 mL). The mesoporous silica nanoparticles were collected by centrifugation and washed with absolute ethanol after each extraction step.

Heptapeptide functionalization (MSN-HP and MSN-NHP). Bio-PLGMWSR (HP-biotin 96.3 %, 5.1 mg, 4.6 µmol) or Bio-PLLMWSR (NHP-biotin, 90.1 %, 5.0 mg, 4.0 µmol) were dissolved in 100 µL DMSO. The solution was diluted by addition of 400 µL H_2O. Then, EDC (0.8 mg, 5.2 µmol) was added and the reaction mixture was stirred for 5 min at room temperature. Subsequently, sulfoNHS (1 mg, 5.0 µmol) was added and the reaction mixture was stirred for another 5 min at room temperature. This mixture was added to a suspension containing 50 mg of MSN-SH_{IN}-$NH_{2\ OUT}$ in a total volume of 8 mL (EtOH:H_2O 1:1). The resulting mixture was then allowed to stir at room temperature overnight. The MSNs were thoroughly washed by EtOH and H_2O (3 times) and finally collected by centrifugation (19,000 rpm, 43,146 rcf, 20 min). The HP-biotin or NHP-biotin functionalized MSNs were stored as colloidal suspension in absolute ethanol.

Cargo-loading. 1 mg of MSNs (MSN-HP or MSN-NHP) were immersed in 500 µl HBSS buffer solution containing fluorescein disodium salt dihydrate (1 mM), calcein-AM (20 µM or 50 µM), cisplatin (2 µM, 10 µM, 20 µM, or 100 µM), or a combination of cisplatin and Bz (2 µM + 1 µM, 10 µM + 1 µM, or 20 µM + 1 µM) for 2 h at room temperature. Afterwards the particles were coated with avidin. Fluorescein-loaded particles have been washed once by centrifugation and redispersion prior to the addition of avidin. All other samples have been coated with avidin without a previous washing procedure.

Avidin-coating (MSN-HP-AVI and MSN-NHP-AVI). 1 mg of loaded or non-loaded MSNs (in 500 µL HBSS buffer) were added to 500 µL HBSS buffer containing 1 mg of avidin. The solution was mixed by using 5 s of vortexing and allowed to react for 30 min under static conditions at room temperature. The resulting suspension was then centrifuged (5000 rpm, 2200 rcf, 4 min, 15 °C) and washed three times with HBSS buffer solution. The particles were

finally re-dispersed in HBSS buffer and used for cuvette release experiments or *in vitro* studies.

Characterization methods. Transmission electron microscopy (TEM) was performed at 300 kV on an FEI Titan 80-300 equipped with a field emission gun. For sample preparation, the colloidal solution of MSNs was diluted in absolute ethanol and one drop of the suspension was then deposited on a copper grid sample holder. The solvent was allowed to evaporate. Dynamic light scattering (DLS) and zeta potential measurements were performed on a Malvern Zetasizer-Nano instrument equipped with a 4 mW He-Ne laser (633 nm) and an avalanche photodiode detector. DLS measurements were directly recorded in diluted colloidal aqueous suspensions of the MSNs at a constant concentration of 1 mg/mL for all sample solutions. Zeta potential measurements were performed using the add-on Zetasizer titration system (MPT-2) based on diluted NaOH and HCl as titrants. For this purpose, 1 mg of the MSN sample was diluted in 10 mL bi-distilled water. Thermogravimetric analyses (TGA) of the bulk extracted samples (approximately 10 mg) were recorded on a Netzsch STA 440 C TG/DSC. The measurements proceed at a heating rate of 10 °C/min up to 900 °C in a stream of synthetic air of about 25 mL/min. Nitrogen sorption measurements were performed on a Quantachrome Instrument NOVA 4000e at -196 °C. Sample outgassing was performed for 12 hours at a vacuum of 10 mTorr at 120 °C. Pore size and pore volume were calculated with an NLDFT equilibrium model of N_2 on silica, based on the desorption branch of the isotherms. In order to remove the contribution of the interparticle textural porosity, pore volumes were calculated only up to a pore size of 8 nm. A BET model was applied in the range of 0.05 – 0.20 p/p_0 to evaluate the specific surface area. Infrared spectra were recorded on a ThermoScientific Nicolet iN10 IR-microscope in reflexion-absorption mode with a liquid-N_2 cooled MCT-A detector. Time-based fluorescence spectra were recorded on a PTI spectrofluorometer equipped with a xenon short arc lamp (UXL-75XE USHIO) and a photomultiplier detection system (model 810/814). The measurements were performed in HBSS buffer solution at 37 °C to simulate human body temperature. For time-base release experiments of fluorescein a custom-made container consisting of a Teflon tube, a dialysis membrane (ROTH Visking type 8/32, MWCO 14,000 g/mol) and a fluorescence cuvette were used (Appendix 6.5).[16] The excitation wavelength was set to $\lambda = 495$ nm for fluorescein-loaded MSNs. Emission scans (505 – 650 nm) were performed every 5 min. All slits were adjusted to 1.0 mm, bandwidth 8 nm).

Cell culture. The NSCLC A549 human alveolar epithelial and the H1299 human lung cancer cell lines were obtained from ATCC (American Type Culture Collection, Manassas, USA). Both cell lines were maintained in DMEM media (LifeSciences). Media were supplemented with 10 % FBS (fetal bovine serum) and 1 % penicillin/streptomycin. All cells were grown at 37 °C in a humidified atmosphere containing 5 % CO_2.

WST-1 assay. Cytotoxicity of the MSNs was assessed using the WST-1 assay (Roche). Briefly, 1.5 x 10^4 cells/well were seeded in 96-well plates. 24 h after seeding, the cells were exposed to MSN-HP-AVI or MSN-SH_{IN}-$NH_{2\ OUT}$ particles for 4 or 24 h. After treatment, 10 µL of WST-1 reagent solution (Roche) was added to each well and incubated at 37 °C for 30 min. Absorbance was measured at 450 nm using a Tristar LB 941 plate-reader (Berthold Technologies).

Live/dead assay using Annexin-V. Induction of apoptosis or necrosis was investigated in both cell lines using Annexin-V-FITC and propidium iodide (PI) double staining. Initially, 4 x 10^5 cells were seeded per well in 6-well plates. After 24 h, the cells were treated with MSN-HP-AVI or MSN-SH_{IN}-$NH_{2\ OUT}$ for 4 or 24 h. The particle containing media were then removed, cells were washed, trypsinized, and stained with Annexin-V-FITC and propidium iodide in binding buffer (10 mM HEPES, 140 mM NaCl, 2.5 mM $CaCl_2$, pH 7.4) at 37 °C for 15 min. Samples were then analyzed by FACS analysis (BD LSRII).

MTT assay. The MTT assay was performed to assess cell viability after cisplatin release from the particles. Briefly, 1 x 10^4 cells/well for H1299 and 0.5 x 10^4 cells/well for A549 were seeded in 96-well plates. 48 h after seeding, cells were exposed to 50 µg/mL MSN-HP-AVI particles that had been loaded with 2, 10, 20 or 100 µM solutions of cisplatin with or without 1 µM solution of Bz, to 0, 0.5 or 1 µg/mL recombinant MMP-9 (Enzo life sciences) in 50 µL of fresh media. In the case of transfected cells, 24 h after seeding, the cells were transfected with 0.15 µg of MMP-9 cDNA (DNASU) or empty vector cDNA per well using SatisFection™ transfection reagent (Agilent Technologies) according to manufacturer's instructions. 24 h after transfection, the cells were exposed to 50 µg/mL MSN-HP-AVI particles that had been loaded with 2, 10, 20 or 100 µM solutions of cisplatin, in 50 µL of fresh media. After treatment, 10 µL of freshly prepared solution of 5 mg Thiazolyl Blue Tetrazolium Bromide/mL PBS (Sigma) was added to each well and incubated at 37 °C for 1 h. The supernatant was then aspirated, and the blue crystals were dissolved in 500 µL isopropanol + 0.1 % Triton X-100. Absorbance was measured at 570 nm, using a Tristar LB

941 plate-reader (Berthold Technologies). Experiments were done in triplicate. Data analyses were performed in Prism graphpad (version 6) software.

Calcein-AM release experiments. The release of calcein-AM, hence the staining of the cells from the particles was assessed using confocal microscopy. Thus, freshly prepared calcein-AM containing MSN-HP-AVI or MSN-NHP-AVI particles were incubated with 0, 1 or 2 µg/mL recombinant MMP-9 (Enzo life sciences) for 2 h at 37 °C in a thermoblock that was shaking mildly at 700 rpm. After the incubation time, the particles were removed by centrifugation and the cells were incubated with the supernatant for 30 min, such that the released calcein could be uptaken by the cells. Afterwards, the nuclei of the cells were counterstained using Hoechst dye (Enzo life sciences). The cells were imaged using a confocal microscope (Zeiss LSM 710).

Zymography. To assess catalytically active MMP-9 expression and transfection efficiency in A549 and H1299 cells, gelatin zymography was performed. In short, collected cell culture media were centrifuged to get rid of cellular debris and then electrophoresed on 10 % SDS-gels containing 1 % gelatin substrate in non-reducing conditions (i.e. no β-mercaptoethanol) so that the proteins could renature after electrophoresis. After electrophoresis, the enzymes were renatured to ensure that the proteins were catalytically active by incubation with 2.5 % Triton-X-100 in developing buffer (50 mM Tris, 200 mM NaCl, 5 mM $CaCl_2$, pH 7.5) for 1 h at room temperature. Afterwards, the gels were incubated in developing buffer at 37 °C for 24 h to allow the enzyme reaction. Thereafter, the gels were stained using PAGE-Blue™ (Fermentas) protein staining, according to the manufacturer's instructions. Gels were analyzed using the ChemiDoc™ XRS+ software (BioRad). Band intensity was quantified with the Image Lab™ software package (version 3.0.1 beta 2) from BioRad.

6.5 Appendix

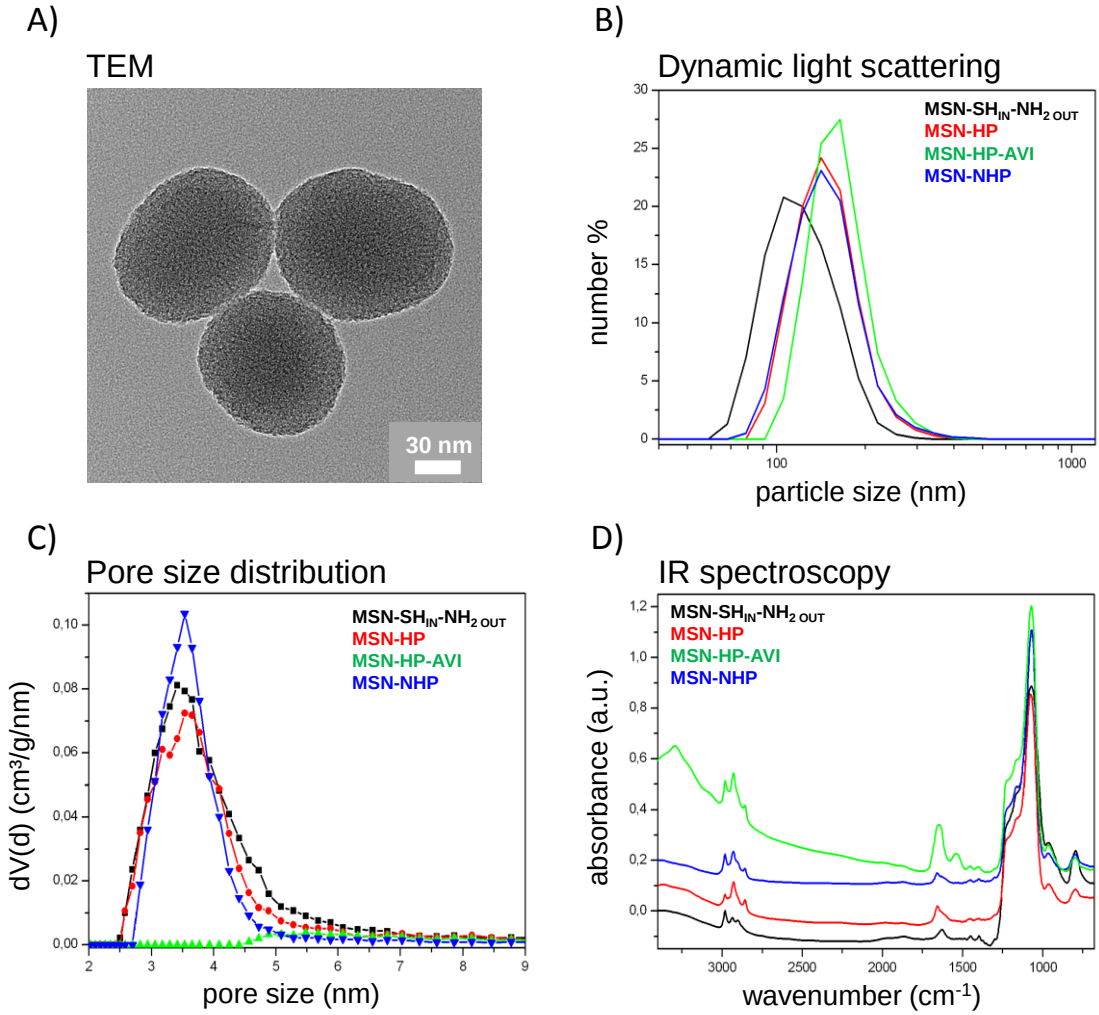

Figure 6.9. Further characterization of functionalized mesoporous silica nanoparticles. a) Transmission electron micrograph of sample MSN-SH$_{IN}$-NH$_{2\ OUT}$. b) Particle size distributions derived from DLS measurements, c) DFT pore size distributions, and d) infrared spectroscopy data (full range) of MSN-SH$_{IN}$-NH$_{2\ OUT}$ (black), MSN-HP (red), MSN-NHP (blue), and MSN-HP-AVI (green).

Further Characterization. The TEM image shows a spherical particle shape, and the worm-like structure of the mesopores is clearly visible (Figure 6.9a). Infrared spectra of all MSNs show typical bands of the silica framework (Si-O-Si) between 1000 and 1300 cm^{-1}. Two additional bands at 780 and 900 cm^{-1} are also present (asymmetric stretching and bending vibrations of Si-OH groups). Furthermore, additional vibrational bands at around 2900 cm^{-1} (C-H stretching modes of ethoxy groups and propyl chains) can be observed for all samples. Nitrogen sorption isotherms show a second hysteresis loop at around 0.9 p/p_0 for all samples, which is attributed to interparticle textural porosity. The slight reduction in BET surface area and pore volume, compared to MSN-SH$_{IN}$-NH$_{2\ OUT}$, can be attributed to the increased sample weight by addition of non-porous organic material (HP-biotin and NHP-biotin), and to the

blocking of some pores towards the access of nitrogen molecules by frozen organic moieties in the surface layer of the nanoparticles.

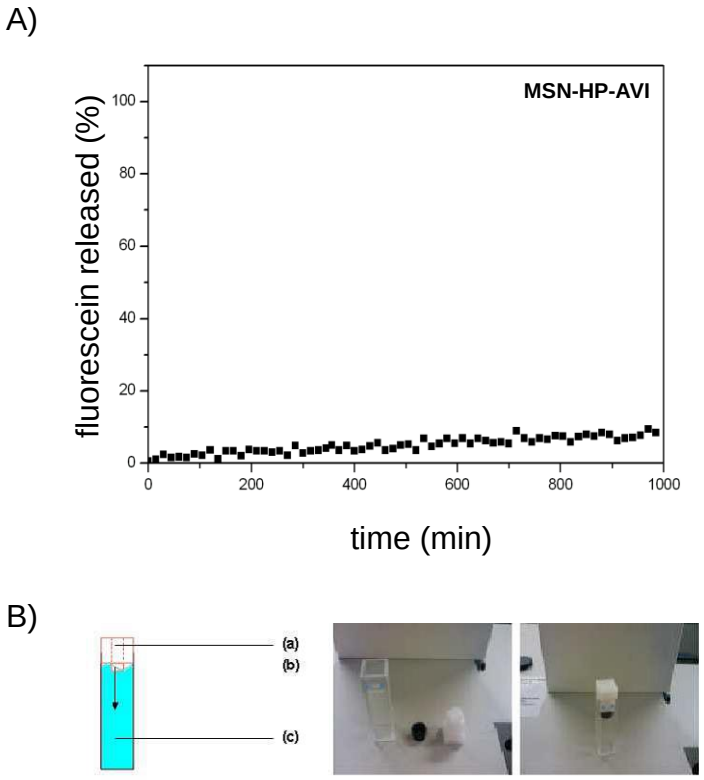

Figure 6.10. A) Long-term stability of avidin capping for MSNs (MSN-HP-AVI) in the absence of MMP-9 (100% of released fluorescein are defined as the total amount being released from MSN-HP-AVI after addition of MMP-9, cf. Figure 3). B) Custom-made release setup consists of a reservoir for the particles (Teflon tube (a), a dialysis membrane (b), and a fluorescence cuvette (c).

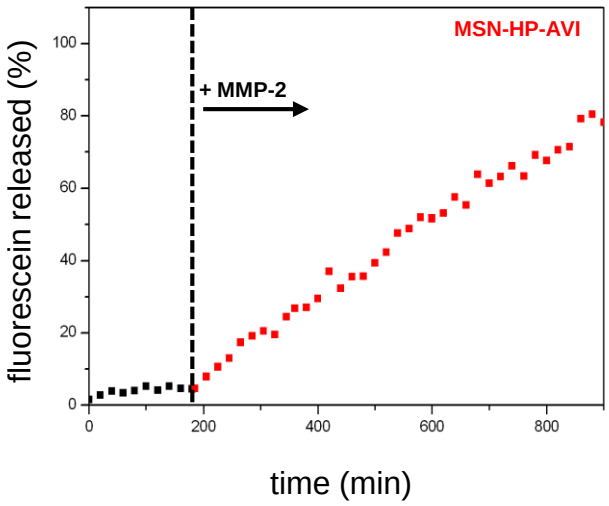

Figure 6.11. Release kinetics of fluorescein from the MSNs (MSN-HP-AVI) before (black dots) and after (red dots) addition of MMP-2 (100% of released fluorescein are defined as the total amount being released from MSN-HP-AVI after addition of MMP-9, cf. Figure 3).

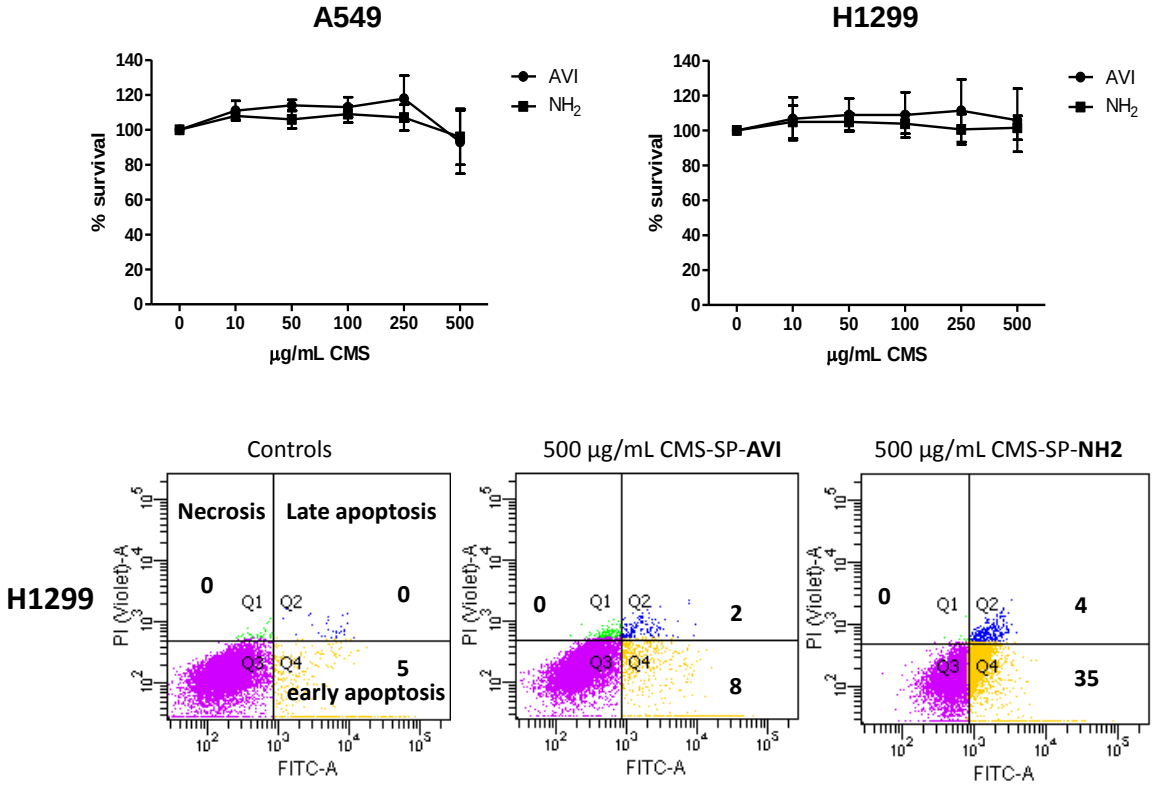

Figure 6.12. Toxicity of different concentrations of MSNs containing the MMP-9 responsive release system (MSN-HP-AVI, denoted as AVI) and of non-coated particles (MSN-SH_{IN}-$NH_{2\ OUT}$) after 4 h of exposure, as determined by a) WST-1 assay in A549 (left) and H1299 (right) lung cancer cell lines and by b) Annexin-V/PI staining and FACS analysis, numbers represent percentage of cells that are counted in marked boxes.

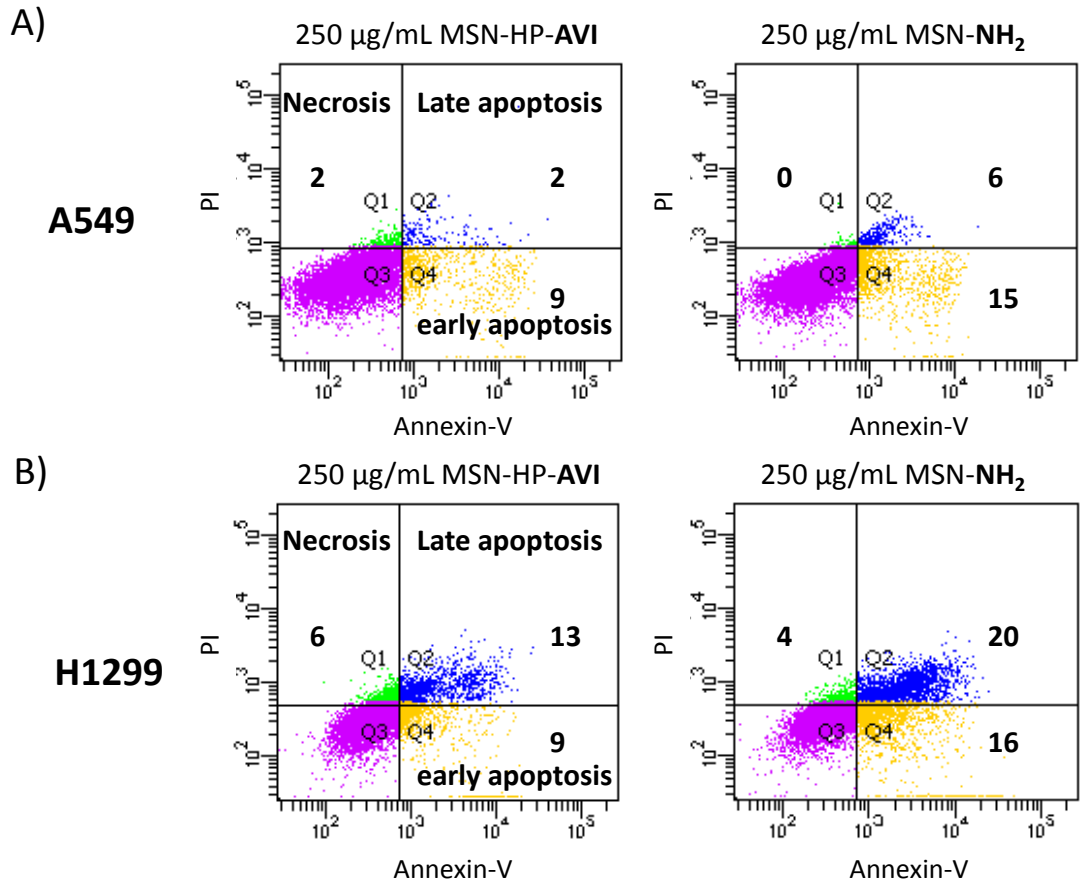

Figure 6.13. Toxicity of 250 µg/mL of MSNs containing the MMP-9 responsive release system (MSN-HP-AVI) and of non-coated particles (MSN-NH_2) after 24 h of exposure in A) A549 and B) H1299 lung cancer cell lines by Annexin-V/PI staining and FACS analysis, numbers represent percentage of cells that are counted in marked boxes.

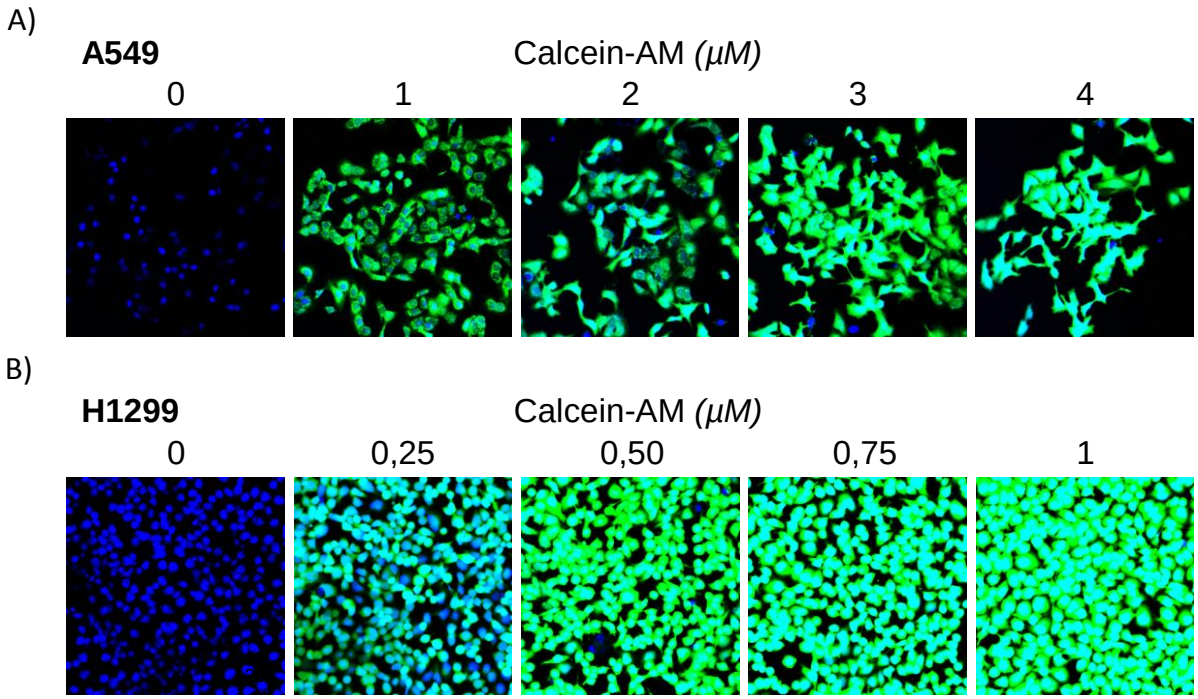

Figure 6.14. Confocal images showing increasing concentrations of calcein-AM (calcein, green) directly given to A) A549 and B) H1299 cells. Hoechst was used as counterstain (nuclei, blue).

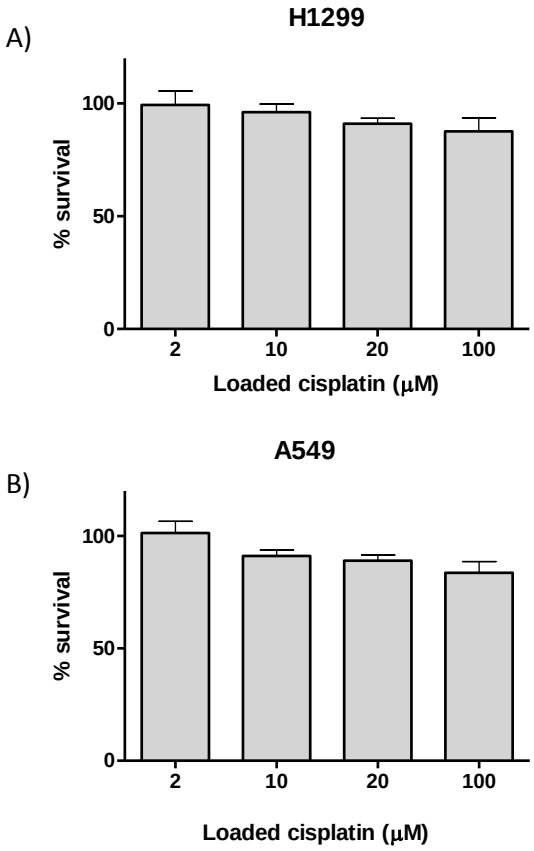

Figure 6.15. MSN-NHP-AVI particles encapsulated with 2, 10, 20 or 100 µM solution of cisplatin and incubated with 1 µg/mL MMP-9 for 24 h did not result in signifcant toxicity in a) H1299 cells and b)A549 cells (non-exposed cells were set to 100 % survival).

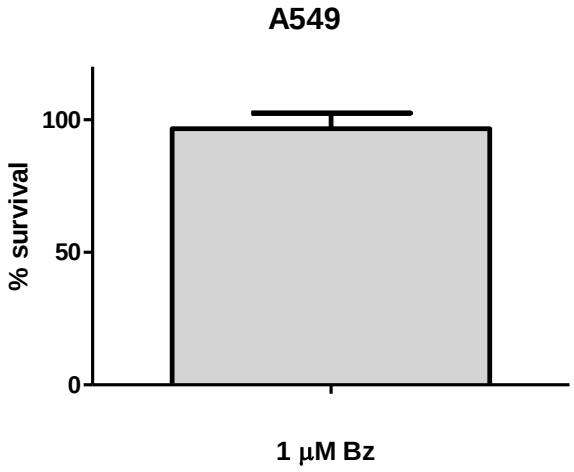

Figure 6.16. MSN-HP-AVI particles encapsulated with 1 µM solution of Bz and incubated with 1 µg/mL MMP-9 for 24 h did not result in any toxicity in A549 cells (non-exposed cells were set to 100 % survival).

6.6 References

[1] R. A. Petros, J. M. DeSimone, *Nat. Rev. Drug Discovery* **2010**, *9*, 615.

[2] Y. Malam, E. J. Lim, A. M. Seifalian, *Curr. Med. Chem.* **2011**, *18*, 1067.

[3] B. G. Trewyn, S. Giri, Slowing, II, V. S. Y. Lin, *Chem. Commun.* **2007**, 3236.

[4] L. Pasqua, S. Cundari, C. Ceresa, G. Cavaletti, *Curr. Med. Chem.* **2009**, *16*, 3054.

[5] Z. X. Li, J. C. Barnes, A. Bosoy, J. F. Stoddart, J. I. Zink, *Chem. Soc. Rev.* **2012**, *41*, 2590.

[6] C. Argyo, V. Weiss, C. Bräuchle, T. Bein, *Chem. Mater.* **2014**, *26*, 435.

[7] F. Q. Tang, L. L. Li, D. Chen, *Adv. Mater.* **2012**, *24*, 1504.

[8] V. Cauda, A. Schlossbauer, J. Kecht, A. Zürner, T. Bein, *J. Am. Chem. Soc.* **2009**, *131*, 11361.

[9] A. M. Sauer, A. Schlossbauer, N. Ruthardt, V. Cauda, T. Bein, C. Bräuchle, *Nano Lett.* **2010**, *10*, 3684.

[10] V. Mamaeva, J. M. Rosenholm, L. T. Bate-Eya, L. Bergman, E. Peuhu, A. Duchanoy, L. E. Fortelius, S. Landor, D. M. Toivola, M. Linden, C. Sahlgren, *Mol. Ther.* **2011**, *19*, 1538.

[11] C.-H. Lee, S.-H. Cheng, Y. Wang, Y.-C. Chen, N.-T. Chen, J. Souris, C.-T. Chen, C.-Y. Mou, C.-S. Yang, L.-W. Lo, *Adv. Funct. Mater.* **2009**, *19*, 215.

[12] Y.-L. Zhao, Z. Li, S. Kabehie, Y. Y. Botros, J. F. Stoddart, J. I. Zink, *J. Am. Chem. Soc.* **2010**, *132*, 13016.

[13] S. Giri, B. G. Trewyn, M. P. Stellmaker, V. S. Y. Lin, *Angew. Chem. Int. Ed.* **2005**, *44*, 5038.

[14] E. Aznar, L. Mondragon, J. V. Ros-Lis, F. Sancenon, M. Dolores Marcos, R. Martinez-Manez, J. Soto, E. Perez-Paya, P. Amoros, *Angew. Chem. Int. Ed.* **2011**, *50*, 11172.

[15] A. Schlossbauer, S. Warncke, P. M. E. Gramlich, J. Kecht, A. Manetto, T. Carell, T. Bein, *Angew. Chem. Int. Ed.* **2010**, *49*, 4734.

[16] A. Schlossbauer, J. Kecht, T. Bein, *Angew. Chem. Int. Ed.* **2009**, *48*, 3092.

[17] S. Dubey, C. A. Powell, *Am. J. Respir. Crit. Care Med.* **2008**, *177*, 941.

[18] D. J. Adelstein, C. P. Rodriguez, *Seminars in Oncology* **2008**, *35*, 211.

[19] A. M. Davies, P. N. Lara, P. C. Mack, D. R. Gandara, *Clin. Cancer Res.* **2007**, *13*, 4647S.

[20] D. Schveigert, S. Cicenas, S. Bruzas, N. E. Samalavicius, Z. Gudleviciene, J. Didziapetriene, *Adv. Med. Sci.* **2013**, *58*, 73.

[21] C. Gialeli, A. D. Theocharis, N. K. Karamanos, *FEBS J.* **2011**, *278*, 16.

[22] B. E. Turk, L. L. Huang, E. T. Piro, L. C. Cantley, *Nat. Biotechnol.* **2001**, *19*, 661.

[23] S. A. Mackowiak, A. Schmidt, V. Weiss, C. Argyo, C. von Schirnding, T. Bein, C. Bräuchle, *Nano Lett.* **2013**, *13*, 2576.

[24] J. Kobler, K. Möller, T. Bein, *ACS Nano* **2008**, *2*, 791.

[25] V. Mamaeva, C. Sahlgren, M. Linden, *Adv. Drug Delivery Rev.* **2013**, *65*, 689.

[26] X. L. Huang, X. Teng, D. Chen, F. Q. Tang, J. Q. He, *Biomaterials* **2010**, *31*, 438.

[27] Q. He, Z. Zhang, F. Gao, Y. Li, J. Shi, *Small* **2011**, *7*, 271.

[28] R. Yamada, M. B. Kostova, R. K. Anchoori, S. L. Xu, N. Neamati, S. R. Khan, *Cancer Biol. Ther.* **2010**, *9*, 192.

[29] R. T. Li, W. Wu, Q. Liu, P. Y. Wu, L. Xie, Z. S. Zhu, M. Yang, X. P. Qian, Y. Ding, L. X. Yu, X. Q. Jiang, W. X. Guan, B. R. Liu, *Plos One* **2013**, *8*.

[30] L. Zhu, P. Kate, V. P. Torchilin, *ACS Nano* **2012**, *6*, 3491.

[31] J. Zhang, Z.-F. Yuan, Y. Wang, W.-H. Chen, G.-F. Luo, S.-X. Cheng, R.-X. Zhuo, X.-Z. Zhang, *J. Am. Chem. Soc.* **2013**, *135*, 5068.

[32] J. H. Xu, F. P. Gao, L. L. Li, H. L. Ma, Y. S. Fan, W. Liu, S. S. Guo, X. Z. Zhao, H. Wang, *Microporous and Mesoporous Mater.* **2013**, *182*, 165.

[33] C. Naujokat, S. Hoffmann, *Lab. Invest.* **2002**, *82*, 965.

[34] J. Voortman, G. Giaccone, *BMC Cancer* **2006**, *6*.

[35] M. K. Yunmbam, Q. D. Q. Li, E. G. Mimnaugh, G. L. Kayastha, J. J. Yu, L. N. Jones, L. Neckers, E. Reed, *Int. J. Oncol.* **2001**, *19*, 741.

[36] A. M. Davies, C. Ho, A. S. Metzger, L. A. Beckett, S. Christensen, M. Tanaka, P. N. Lara, D. H. Lau, D. R. Gandara, *J. Thorac. Oncol.* **2007**, *2*, 1112.

[37] B. Y. Cao, J. Li, X. L. Mao, *Curr. Pharm. Des.* **2013**, *19*, 3190.

[38] A. M. Davies, P. N. Lara, D. H. Lau, P. C. Mack, P. H. Gumerlock, D. R. Gandara, D. Schenkein, J. H. Doroshow, *J. Clin. Oncol.* **2004**, *22*, 642S.

7 Carbonic Anhydrase-Based pH-Responsive Cap System for Mesoporous Silica Nanoparticles

This chapter is based on work in cooperation with:

Michael Gattner, Stefan Datz, Veronika Weiss, Christoph Bräuchle, Thomas Carell, and Thomas Bein

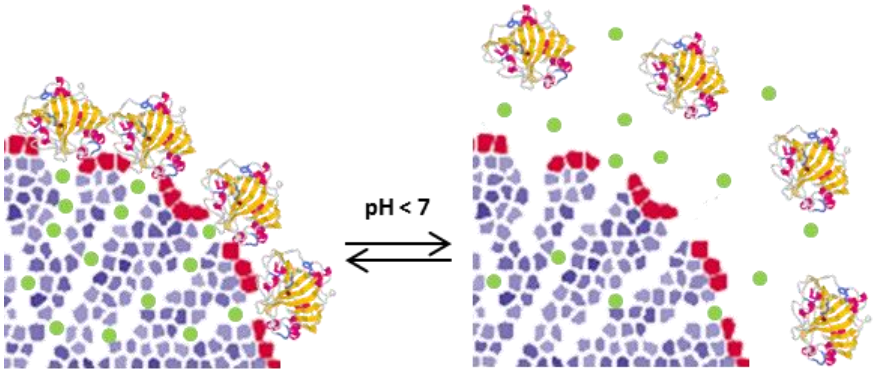

7.1 Introduction

The development of effective systems for targeted drug delivery with release on-demand properties is a challenging field in nanoscience. In particular, porous nanocarriers with high drug loading capacity and tunable surface properties are viewed as promising candidates for biomedical applications such as cancer therapy and bioimaging.[1-3] Multifunctional mesoporous silica nanoparticles (MSNs) have recently achieved advantageous performance in drug delivery applications due to their excellent porous features and the possibility to attach targeting ligands and adjustable release mechanisms for a variety of cargos.[4-6] In the last decade, remarkable efforts were made to establish various capping systems to efficiently seal the porous system of MSNs, including CdS or gold nanoparticles,[7-8] iron oxide nanocrystals,[9] bio-macromolecules,[10-11] enzymes,[12] and polymers.[13] Control over a stimuli-responsive cargo release can be achieved via different triggers such as redox reactions,[14] pH changes,[15] light-activation,[5] or change in temperature.[6] Among these techniques, drug delivery vehicles equipped with acid-sensitive capping mechanisms are highly desirable in acidified targets, such as tumors and inflammatory tissues. In particular,

nanoparticles taken up by cells through endocytosis are exposed to a natural pH change from the early endosome (pH 7.4) to late endosome or endolysosome (pH 5.5).[16]

Here, we present pH-responsive MSNs consisting of a cleavable capping structure based on carbonic anhydrase (CA) gatekeepers which are attached to the silica nanoparticle surface via benzene sulfonamide groups. The sulfonamide derivatives have been commonly used as enzyme inhibitors, efficiently blocking the active site of the carbonic anhydrase.[17] This inhibition is reversible depending on pH. The CA gatekeepers were used to exploit the endosomal pH change as an internal trigger and gain control over the release of cargo molecules from the mesoporous system. Specifically, our pH-responsive capping system consists of two essential components. First, the bulky gatekeeper CA is crucial to efficiently block the pore entrances of the porous host system. Due to its capable size (hydrodynamic diameter of 5.4 nm), the CA can block the entrances of the mesopores with diameters of about 4 nm, thus showing high potential to serve as a bulky gatekeeper for MSNs.[4, 18] The second component is the surface-bound benzene sulfonamide linker, which efficiently binds to the active site of the enzyme. Upon changing the pH, the connection is cleaved, which leads to a removal of the gatekeepers, providing access to the porous system. CA has been widely studied as a model enzyme in different research fields such as biophysics, bioanalysis and medical chemistry.[17] This broad range of applications is mainly based on its well-known catalytic mechanism and its excellent stability under standard laboratory conditions. The enzyme is abundant in various human tissues such as kidney, stomach, eye, bones, and in the blood stream. Since CA has been found to be involved in different disease processes such as glaucoma and diabetes, several inhibitors have been examined, often consisting of sulfonamide derivatives.[19] In particular, aryl sulfonamides coordinate to the Zn^{2+}-ion of the catalytic center. This inhibition is reversible upon acidification, causing a cleavage of the coordination bond.[20] Benzene sulfonamide derivatives can be attached to the surface of MSNs to bind CA in the active site at physiological pH values of 7.4. A detachment is caused by mildly acidic pH conditions of 5.5 prevailing in endolysosomes. In the following, we present a novel pH-sensitive CA-based capping system on MSNs. The MSN nanocarriers containing biomolecular valves based on carbonic anhydrase are anticipated to offer promising potential for controlled drug delivery applications, for instance in cancer therapy.

7.2 Results and Discussion

pH-responsive MSNs consisting of biomolecular valves based on the enzyme carbonic anhydrase (CA) were synthesized in a two-step approach. First, MSNs containing thiol-functionality exclusively at the external particle surface were established following our previously described delayed co-condensation approach.[4] In brief, the silica source tetraethyl orthosilicate (TEOS) and the template cetyltrimethylammonium chloride (CTAC) were mixed at elevated temperatures in an aqueous solution including the base triethanolamine (TEA), which additionally serves as a structure-directing agent to form colloidal nanoparticles. A mixture of TEOS and mercaptopropyl triethoxysilane (MPTES) was added at the very last step of the silica framework formation to create a very thin external functional shell consisting of thiol groups (sample MSN-SH). This organic moiety offers the possibility to attach further functionality exclusively on the outer surface of the MSNs, while not affecting the porous system. In a second step, benzene sulfonamide (phSA) groups were covalently attached to the silica nanoparticles *via* a short bifunctional crosslinker (maleimide-C_6-NHS) at mild reaction conditions (sample MSN-phSA). The particle sizes of functionalized MSNs were determined with dynamic light scattering (DLS) measurements (Figure 7.1a). All samples featured narrow particle size distribution implying a good colloidal stability. No agglomeration occurred due to the additional attachment of organic moieties to the particle surface. Samples MSN-SH and MSN-phSA show a maximum for particles sizes at 122 and 142 nm, respectively. For enzyme-coated particles MSN-phSA-CA a slight shift to higher values can be observed (190 nm).

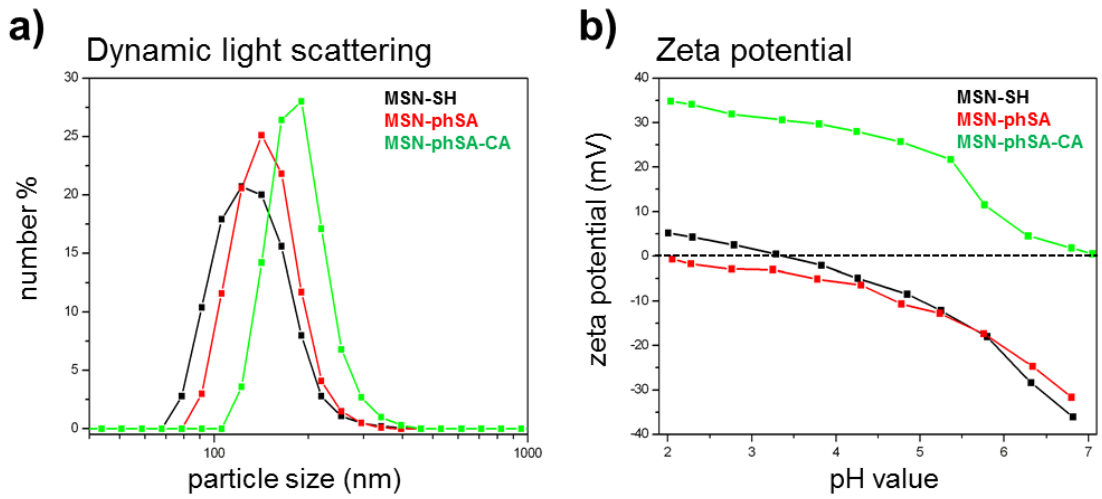

Figure 7.1: a) Dynamic light scattering (DLS) and b) zeta potential measurements of functionalized MSNs. MSN-SH (black), MSN-phSA (red), and MSN-phSA-CA (green).

DLS data provide increased values for particle sizes compared to transmission electron microscopy (TEM) images, since the hydrodynamic radius of the particles is taken into account. Random weak particle agglomeration during the DLS measurements may also further increase the measured values.[21] TEM analysis provides additional insights regarding the morphology and porosity of MSNs. Thiol-functionalized MSNs are depicted in Figure 7.2, showing mostly spherically shaped particles with a worm-like structure of the mesopores. The average diameter of the MSNs was about 70 nm.

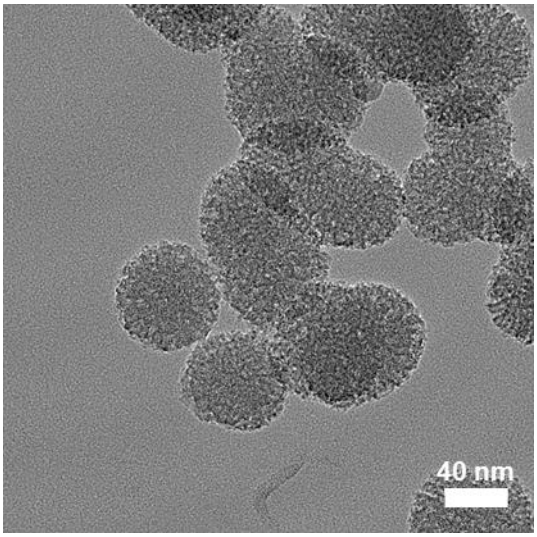

Figure 7.2: Transmission electron micrograph of thiol-functionalized MSNs (MSN-SH).

Furthermore, the first-order reflection of the mesoporous material observed with small-angle X-ray diffraction (XRD) suggests the formation of a mesoporous structure with regular but not periodic channel structure (cf. Appendix 7.5). The surface charge of silica nanoparticles, measured as the zeta potential, changed due to stepwise attachment of organic moieties (Figure 7.1b). The isoelectric point (IEP) of MSN-SH (pH 3.6) was shifted to a more acidic pH value (< 2) for MSNs containing the benzene sulfonamide groups on the outer surface. The tendency for sulfonamide groups to be protonated is relatively low due to the stabilizing resonance effect, consequently causing an increase of negative surface charge. After attachment of the carbonic anhydrase a drastic change can be observed. This enzyme consists of various amino acid residues which can be easily protonated, including arginine, histidine and lysine. Therefore, a highly positive surface charge occurs over the whole acidic pH range. MSN-phSA-CA features an IEP at neutral pH values (pH ~7). Vibrational spectroscopy including infrared (IR) and Raman spectroscopy, were performed to investigate specific vibrational bands originating from organic groups. IR data for all samples show typical vibration bands of the silica framework (Figure 7.3a). A broad peak in the range between 1300 and 1000 cm^{-1} can be assigned to Si-O-Si stretching vibration modes. Two additional bands at 900 and 780 cm^{-1} are related to asymmetric stretching and bending vibrations of Si-OH groups, respectively. Furthermore, a group of bands in the range between 3000 and 2800 cm^{-1} can be observed, which indicates C-H stretching vibrations of methylene and methyl groups from the propyl chain of organosilane moieties and residual ethoxy silane groups. Sample MSN-SH features a band at 1633 cm^{-1} which can be assigned to the bending modes of physisorbed water. This band is present in all spectra but partially overlapped by other more intensive bands for the coated particles. MSNs containing the benzene sulfonamide groups show additional C=O stretching vibration bands at 1700 and 1627 cm^{-1} which can be referred to the carbonyl groups of the short maleimide-C_6-NHS linker (maleimide and amide, respectively). Furthermore, a peak of weak intensity at 1340 cm^{-1} is present in the spectrum of sample MSN-phSA, which belongs to the typical asymmetric SO_2 stretching vibration modes of the sulfonamide groups. For the sample MSN-phSA-CA, amide vibrations (Amide I: 1639 cm^{-1}, C=O stretching vibration; Amide II: 1535 cm^{-1}, N-H deformation and C-N stretching vibration) of high intensity are observed in the range between 1700 and 1500 cm^{-1}; these are typical for enzymes.

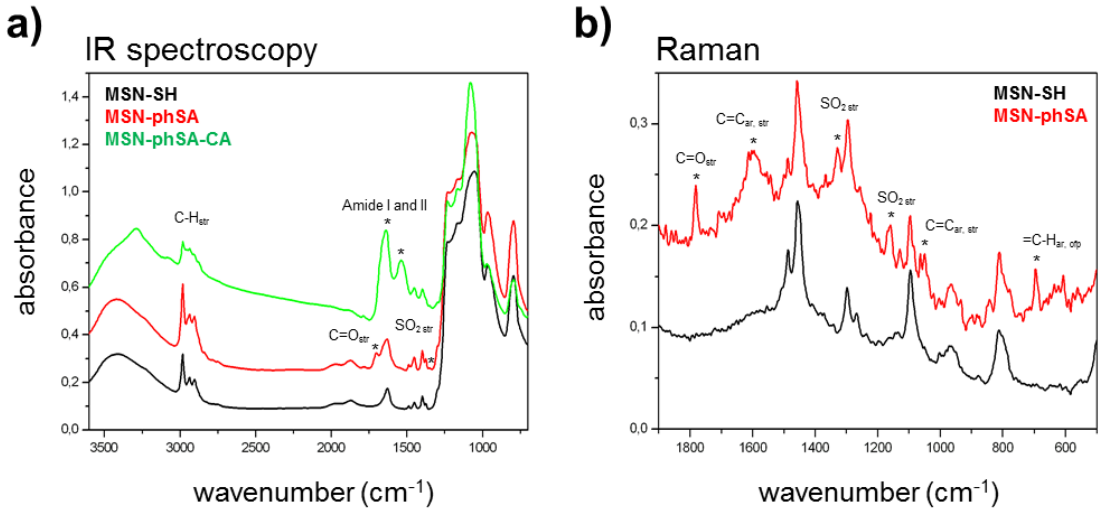

Figure 7.3: a) Infrared (IR) and b) Raman spectroscopy data of functionalized MSNs. MSN-SH (black), MSN-phSA (red), and MSN-phSA-CA (green). For better clarity, the spectra are shifted along the y-axis by 0.2 units and for Raman spectroscopy by 0.1 units.

Raman spectroscopy provides data complementary to IR spectroscopy. In Figure 7.3b a more detailed view of the spectra for MSN-SH and MSN-phSA in the range between 1900 and 600 cm^{-1} is depicted (data for MSN-phSA-CA not shown, full range of Raman spectra refer to Appendix 7.5). Various additional bands (*) can be observed for the benzene sulfonamide-functionalized particles. A sharp band at 1780 cm^{-1} can be assigned to the carbonyl stretching vibration of the diacylamine group of the maleimide residue that is covalently attached to the thiol groups of the MSN surface. The presence of phenyl groups is confirmed by characteristic bands of aromatic C=C stretching vibrations (1600 cm^{-1} and 1055 cm^{-1}) and aromatic =C-H out-of-plane deformation vibrations (693 cm^{-1}). The broadening of the signal at 1600 cm^{-1} can be assigned to the partial overlap by amide II vibration modes. The bands at 1326 and 1156 cm^{-1} are related to the characteristic asymmetric and symmetric stretching vibrations of the sulfonamide group, respectively. The amount of attached organic moieties on the MSNs was investigated by thermogravimetric analysis (TGA). MSN-phSA particles show an additional weight loss of 3 % in the range between 130 and 900 °C due to the attachment of the benzene sulfonamide linker (Figure 7.4). This is in good accordance with expected values since only 1 mol% MPTES (of total Si content) was used for the functionalization of the external silica particle surface. Enzyme-coated MSNs (MSN-phSA-CA) feature a relatively high additional weight loss compared to sample MSN-SH (+14 % at 900 °C). Apparently, degradation of the carbonized enzymes occurs only at very high temperatures,

and is not even finished at 900 °C. This was already observed before for thermogravimetric analysis of enzyme-coated MSNs.[22]

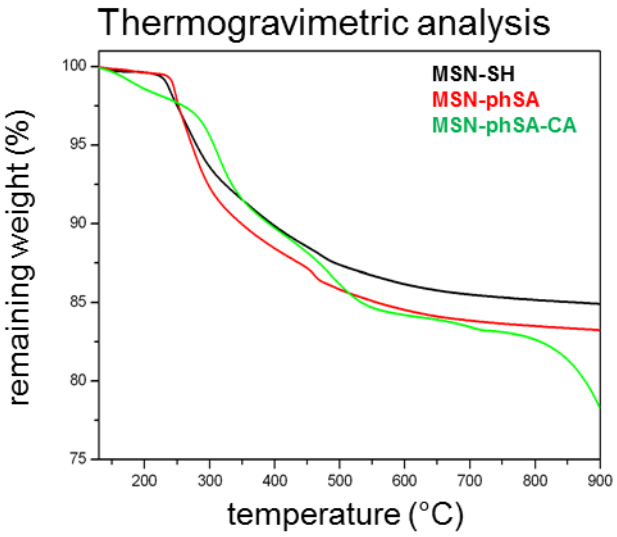

Figure 7.4: Thermogravimetric analysis of MSN-SH (black), MSN-phSA (red), and MSN-phSA-CA (green).

Nitrogen sorption measurements show type IV isotherms for MSN-SH and MSN-phSA, confirming mesoporosity of the silica nanoparticles. The corresponding nitrogen sorption isotherms are depicted in Figure 7.5a showing inflection points at $p/p_0 = 0.3$. Another hysteresis loop at about 0.9 p/p_0 is present for all samples, and can be attributed to interparticle textural porosity. Relatively high surface areas (up to 1200 m^2/g) and pore volumes (0.8 cm^3/g) can be observed for MSN-SH and MSN-phSA (Table 7.1).

Table 7.1. Porosity parameters of functionalized MSNs.

Sample	BET surface area (m^2/g)	Pore volume[a] (m^3/g)	Pore size[b] (nm)
MSN-SH	1170	0.83	3.8
MSN-pSA	1004	0.72	3.7
MSN-pSA-CA	99	0.07	–

[a]Pore volume is calculated up to a pore size of 8 nm to remove the contribution of interparticle porosity.
[b]DFT pore size refers to the peak value of the pore size distribution.

The slight reduction in these porosity parameters for benzene sulfonamide-functionalized MSNs can be assigned to the increase of sample weight by additional non-porous organic moieties. Furthermore, the DFT pore size distribution (Figure 7.5b) still shows accessible

pores. Importantly, the porous system is not affected by the attachment of the benzene sulfonamide linkers and no incorporation of organic groups inside the mesopores can be observed, which is confirmed by a constant pore size distribution. The attachment of the bulky enzyme carbonic anhydrase results in a drastic reduction of the surface area and pore volume for sample MSN-phSA-CA. Enzyme-coated MSNs feature a type II isotherm which corresponds to non-porous materials. The carbonic anhydrase enzymes act like bulky biomolecular valves that are able to efficiently block the mesopores even towards the access of small nitrogen molecules. We observed no pore size distribution for MSN-phSA-CA in the range between 2 and 9 nm.

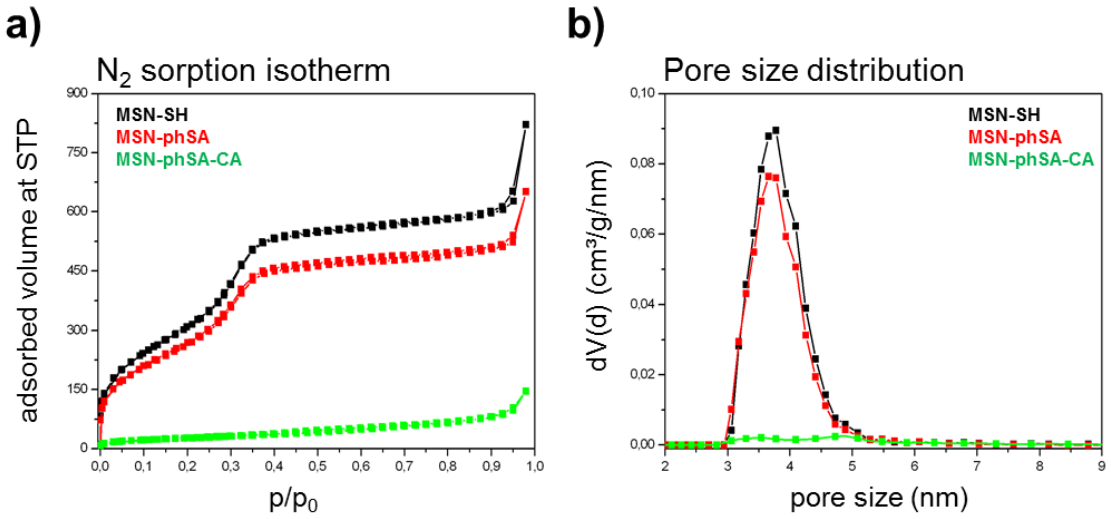

Figure 7.5: a) Nitrogen sorption isotherms and b) DFT pore size distributions of functionalized MSNs. MSN-SH (black), MSN-phSA (red), and MSN-phSA-CA (green).

All the above data confirm the successful synthesis of carbonic anhydrase coated MSNs *via* benzene sulfonamide linkers. In order to investigate the pH-responsive removal of the bulky gatekeepers from the particles, *in vial* cargo release experiments were performed. We used a custom-made two-compartment system to analyze the time-based release of the fluorescent model drug fluorescein.[11] After incorporation of fluorescein molecules into the mesoporous system, carbonic anhydrase was added to block the pore entrances. An efficient sealing of the pores and no premature release of the cargo can be observed for the sample MSN-phSA-CA dispersed in HBSS buffer (pH 7.4) at 37 °C (Figure 7.6a, closed state, black curve). After 3 h the solution was exchanged and the particles were dispersed in citric-acid phosphate buffer (CAP buffer, pH 5.5). The change to acidic milieu, which simulates the acidification of

endosomes, causes a significant increase in fluorescence intensity over time reaching its maximum after 18 hours (open state, red curve). Furthermore, we could show a long-term stability of the capping system for more than 16 hours in HBSS buffer and cell medium at pH 7.4 (Figure 7.6b). These *in vial* release experiments demonstrate an efficient sealing of the pores with the carbonic anhydrase as bulky gatekeepers, preventing premature cargo release and a stimuli-responsive release behavior upon acid-sensitive detachment of the capping system.

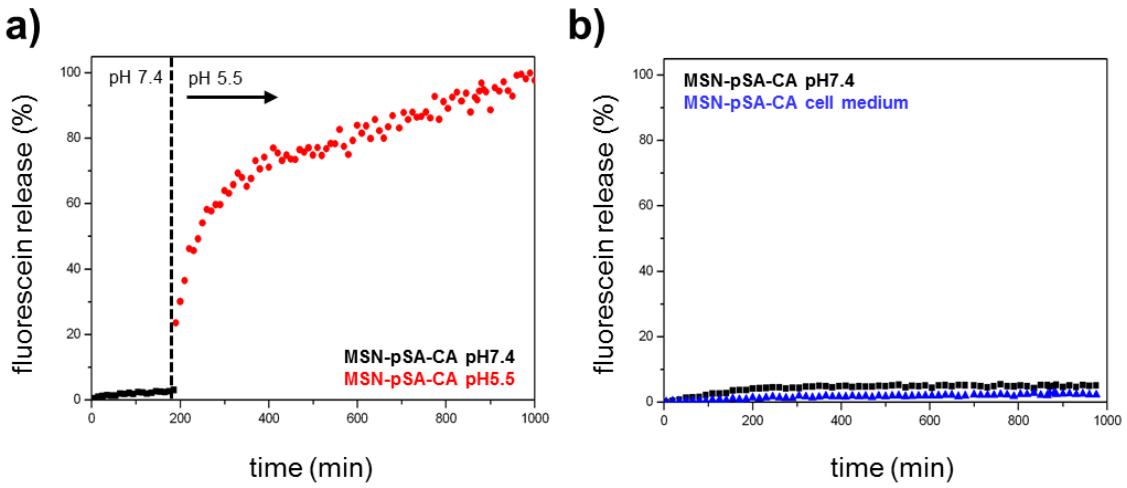

Figure 7.6: *In vial* release kinetics of fluorescein molecules from the enzyme-coated MSNs at different pH values. (a) Sample MSN-pSA-CA features no premature release of the fluorescent cargo molecules in HBSS buffer solution at pH 7.4 (closed state, black curve). After 3 h the medium was changed to slightly acidic milieu (CAP buffer, pH 5.5, red curve) resulting in a significant increase in fluorescence intensity. The gatekeepers are detached from the particle surface upon acidic pH values causing an efficient and precisely controllable release of the fluorescein from the mesoporous system. (b) Long-term stability of the capping system was investigated in HBSS buffer (pH 7.4, black curve) and cell medium (blue curve). No unintended cargo release was observed within about 16 h.

Enzyme activity assays provide information about the binding affinity of carbonic anhydrase on the surface of sulfonamide-functionalized MSNs (Figure 7.7). The enzyme activity assay investigates the hydrolysis in TRIS-buffered solution of a chromogenic substrate (*p*-nitrophenyl acetate, NPA) in the presence of the enzyme, generating nitrophenol. UV-Vis spectroscopy is used to measure the resulting absorption maximum at 400 nm. Figure 7.7 shows the resulting curve for the non-catalyzed (no carbonic anhydrase) reaction, which can be taken as baseline. The slight slope for this curve is due to the hydrolysis rate of the pure substrate in aqueous solution in the absence of catalytic enzymes. In the presence of 100 nM enzyme (non-inhibited) the maximum conversion of the substrate can be obtained. A slight decrease in conversion efficiency can be observed upon addition of 50 µg of MSN-SH particles due to marginal reduction of enzyme activity in the presence of silica nanoparticles.

We assume that this effect corresponds to minor unspecific attachment of the carbonic anhydrase to the silica nanoparticles causing blocking of the active sites to some extent. In comparison, the addition of inhibitor-containing particles (MSN-phSA) causes a significant decrease of the slope of the resulting curve. Thus we have shown conclusively that the sulfonamide-functionalized MSNs are able to inhibit/bind the enzyme carbonic anhydrase. At neutral pH values, the enzyme is specifically attached to the sulfonamide-functionalized particle surface resulting in an inhibition of the enzyme's active site. This leads to a drastic decrease in enzyme activity.

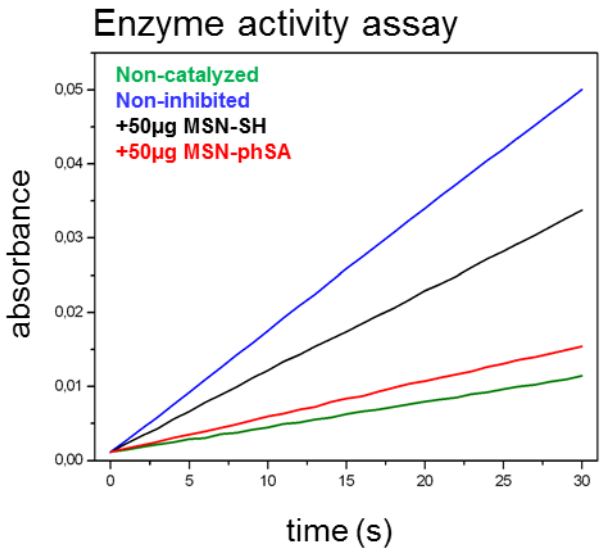

Figure 7.7: Enzyme activity assay of CA catalyzing the hydrolysis of the chromogenic substrate *p*-nitrophenyl acetate measured by UV-Vis spectroscopy (absorbance at 400 nm). Non-catalyzed (green) and non-inhibited (blue) reaction and after addition of MSN-SH (black) or MSN-phSA (red).

Employing fluorescent live-cell imaging, we investigated the *in vitro* release behavior of the host MSN-phSA-CA, loaded in the channel system with 4',6-diamidino-2-phenylindole (DAPI), on HeLa cancer cells. The size of DAPI is similar to fluorescein molecules and therefore may be efficiently encapsulated in the mesoporous system of our CA-capped silica nanoparticles. DAPI is commonly used as a nuclei counterstain in cell imaging due to its effective turn-on fluorescence upon intercalation with DNA double strands (about 20 fold enhancement in fluorescence intensity).[23] Since DAPI is cell membrane permeable, free fluorescent dye molecules are able to stain the nucleus within very short time periods (1-5 min), as suggested by several staining protocols.[24] After incorporation of DAPI into the mesoporous system of the silica nanocarriers, the pores were sealed by addition of carbonic

anhydrase enzymes. The HeLa cells were incubated for a total time period of 24 h with the loaded particles, which were additionally labeled with Atto 633 dye (red), as depicted in Figure 7.8. After 7 h of incubation, MSNs were efficiently uptaken by the cells and were found to be located in endosomes. Importantly, almost no staining of the nuclei with DAPI (blue) could be observed at this time point. Only after 15 h, blue fluorescent color (even more intensive after 24 h) provides evidence about an efficient release of DAPI from the MSNs. Reference experiments with the sample supernatant after particle separation (centrifugation) showed no significant nuclei staining even after 24 h (Figure 7.8d). This proves a substantial release from the mesopores of our nanocarrier system, and also shows that no free dye molecules were present in the solution. These cell experiments illustrate the time-dependent release behavior of DAPI to HeLa cells. We suggest that this delayed nuclei staining results from a cascaded release mechanism. First, acidification throughout the endosomal pathway to late endosomes or endolysosomes is of key importance. The pH change to mildly acidic values (about 5.5) is essential for the detachment of the bulky gatekeepers from the MSN hosts, and subsequently the opening of the pores leads to an efficient cargo release.

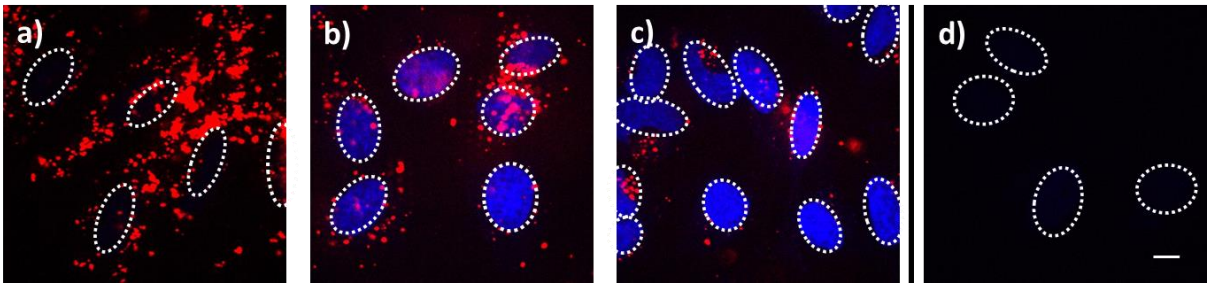

Figure 7.8: Fluorescence microscopy of HeLa cells incubated with MSN-phSA-CA nanoparticles loaded with DAPI and labeled with Atto 633 (red) after a) 7 h, b) 12 h and c) 24 h of incubation with the cells. The delayed nuclei staining with DAPI (blue) is caused by a time-dependent release of DAPI based on the need for an acidic environment. d) In a reference experiment, the incubation with the supernatant solution (without MSNs) showed no staining of the nuclei with DAPI after 24 h, suggesting that no free DAPI molecules are present in the particle solution. The nuclei are indicated with dashed circles. The scale bar represents 10 µm.

In order to verify the fate of our drug delivery vehicles ending up in acidic cell compartments, co-localization experiments with labeled MSNs and endosomes or lysosomes were performed. Simultaneous with particle incubation, the HeLa cells were treated with different fusion-constructs of green fluorescent protein (GFP) and early/late endosome or lysosome markers, respectively. After 24 h of incubation with fluorescently labeled nanoparticles, almost no co-localization (yellow) between early endosomes and MSNs could be observed, as can be seen in Figure 7.9a. In contrast, multiple yellow spots indicating co-localization between GFP

(green) and MSNs (red) were clearly visible in the case of late endosomal and lysosomal staining after 21 h (Figure 7.9b/c, denoted by arrows). This shows that the localization of our nanocarriers in an acidic compartment is crucial to initiate cargo release.

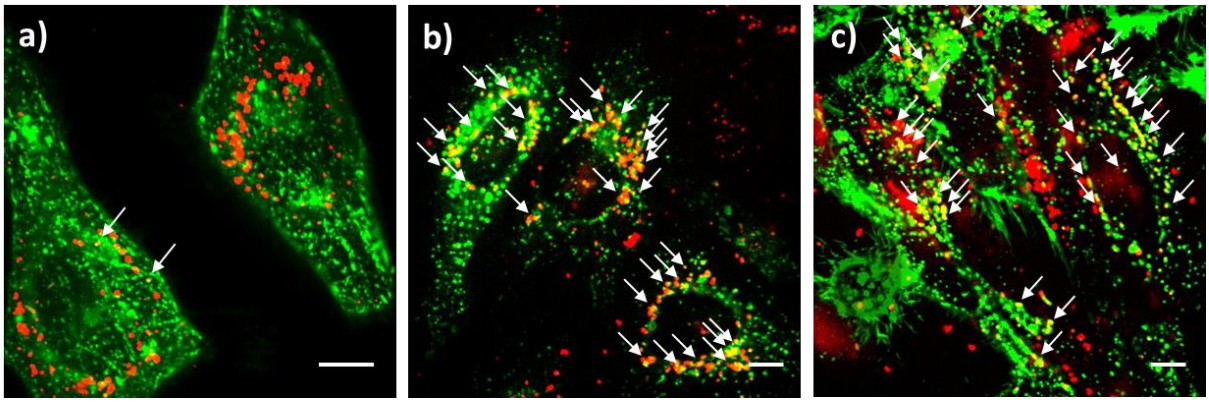

Figure 7.9: Fluorescence microscopy of HeLa cells incubated with Atto 633-labeled MSN-phSA-CA (red) after a) 24 h on GFP-early endosome (green) tagged cells, b) 21 h incubation on GFP-late endosome (green) tagged cells, and c) 21 h on GFP-lysosome (green) tagged cells. Co-localization (yellow) could be primarily observed for late endosomes and lysosomes (indicated with arrows) suggesting that the multifunctional MSNs are located in acidic compartments after endocytosis. The scale bar represents 10 µm.

As depicted in Figure 7.10, a detailed view on GFP-lysosome tagged cells revealed that the MSNs loaded with DAPI were co-localized (white) with lysosomes (cf. Figure 7.9c, for clarity reasons the blue DAPI channel was not shown before). Additionally, a successful DAPI release could be observed by efficient nuclei staining (blue) after 21 h of incubation on HeLa cells. For the present pH-responsive drug nanocarrier system, it is crucial to gain access to an acidic cell compartment such as late endosome or lysosome. Subsequently, the on-demand release can be triggered by the low pH. The above co-localization studies provide good evidence for the delayed release kinetics observed after several hours of particle incubation.

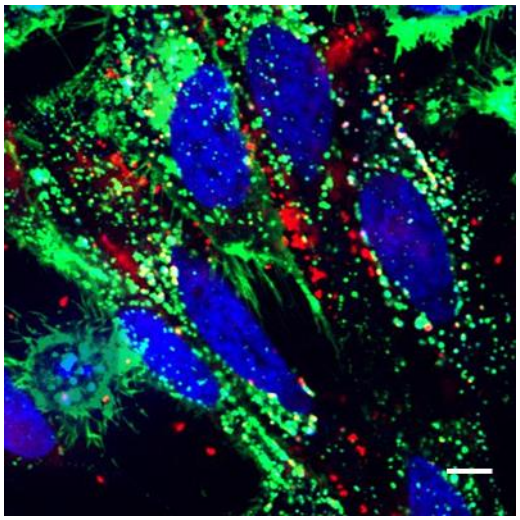

Figure 7.10: Fluorescence microscopy of HeLa cells incubated with MSN-phSA-CA nanoparticles loaded with DAPI (blue) and labeled with Atto 633 (red) after 21 h on GFP-lysosome (green) tagged cells. The white spots indicate co-localization between MSNs and lysosomes. A successful DAPI delivery is clearly visible by efficient nuclei staining (blue). The scale bars represent 10 µm.

7.3 Conclusions

In summary, we conclude that the novel capping system concept based on pH-responsive detachment of carbonic anhydrase is a suitable candidate for a highly controllable drug release from porous nanocarriers. Our drug delivery system provides an on-demand release mechanism shown by *in vial* and *in vitro* cargo release experiments. The multifunctional MSNs were capable of efficient endocytosis by cancer cells and were subsequently located in acidic cell compartments including late endosomes and lysosomes. The acidic milieu caused cleavage of the coordination bond between the sulfonamide linkers and the bulky gatekeepers and successful cargo release occurred. This was proven by the appearance of strong fluorescent nuclei staining with DAPI. We note that our pH-responsive gatekeeper system might show potential for reversible pore blocking behavior. Once the nanocarriers are exocytosed, they will be exposed to neutral pH values agian. Since carbonic anhydrase is abundant in the blood stream it is anticipated that a re-capping of the MSNs is feasible and that it could prevent subsequent leakage of not yet released cargo molecules, provided that the sulfonamide linker survives the lysosome. Consequently, spreading of chemotherapeutics in the organism would be limited and systemic side-effects could be further reduced. A detailed investigation of this intriguing aspect is subject of future work. Our newly developed concept for pH-responsive gatekeepers provides a promising basis for future work on mesoporous silica particles serving as powerful and versatile drug delivery platform.

7.4 Experimental

Materials. Tetraethyl orthosilicate (TEOS, Fluka, > 99 %), triethanolamine (TEA, Aldrich, 98 %), cetyltrimethylammonium chloride (CTAC, Fluka, 25 % in H_2O), (3-mercaptopropyl)-triethoxysilane (MPTES, Sigma Aldrich, > 80 %), 6-maleimidohexanoic acid *N*-hydroxysuccinimide ester (Fluka, > 98 %), bovine carbonic anhydrase (bCA, Sigma, > 95 %), 4-(2-aminoethyl)benzenesulfonic acid (Aldrich, 98 %), ammonium nitrate (NH_4NO_3, Aldrich), ammonium fluoride (NH_4F, Aldrich), hydrochloric acid (37 %), fluorescein disodium salt dihydrate (Aldrich, 90 %), and Hank´s balanced salt solution (HBSS-buffer, Sigma Aldrich) were used as received. Ethanol (EtOH, absolute, Aldrich) and dimethylformamide (DMF, dry, Aldrich) were used as solvent without further purification. Bidistilled water was obtained from a millipore system (Milli-Q Academic A10). Citric-acid phosphate buffer (CAP-buffer, pH 5.5) was freshly prepared by carefully mixing a certain amount of disodium hydrogen phosphate (Na_2HPO_4, 0.2 M in H_2O) and citric acid (0.2 M in H_2O) to adjust a pH value of 5.5. Subsequently, the solution was diluted with bidistilled H_2O to a total volume of 500 mL.

Synthesis of thiol-functionalized MSNs (MSN-SH). A mixture of TEOS (1.92 g, 9.22 mol) and TEA (14.3 g, 95.6 mmol) was heated to 90 °C for 20 min under static conditions in a polypropylene reactor. Then, a preheated (60 °C) mixture of CTAC (2.41 mL, 1.83 mmol, 25 % in H_2O) and NH_4F (100 mg, 0.37 mmol) in bidistilled H_2O (21.7 g, 1.21 mol) was added and the resulting reaction mixture was stirred vigorously (700 rpm) for 30 min while cooling down to room temperature. Afterwards, TEOS (18.2 mg, 92 µmol) and MPTES (18.1 mg, 92 µmol) were premixed briefly before addition to the reaction mixture. The final reaction mixture was stirred over night at room temperature. After dilution with absolute ethanol (100 mL), the nanoparticles were collected by centrifugation (19,000 rpm, 43,146 rcf, 20 min) and redispersed in absolute ethanol. Template extraction was performed in an ethanolic solution of MSNs (100 mL) containing NH_4NO_3 (2 g) which was heated at reflux conditions (90 °C oil bath) for 45 min. This was followed by a second extraction step (90 mL absolute ethanol and 10 mL hydrochloric acid (37 %)) under reflux conditions for 45 min (the material was washed with absolute ethanol after each extraction step and collected by centrifugation); finally the particles were redispersed in absolute ethanol and stored as colloidal suspension.

Synthesis of sulfonamide-functionalized MSNs (MSN-phSA). For the covalent attachment of a sulfonamide derivative to the external particle surface, a thiol-reactive linker was synthesized. 6-maleimidohexanoic acid *N*-hydroxysuccinimide ester (mal-C_6-NHS, 10 mg, 33 µmol) was dissolved in DMF (500 µL, dry) and was added to an ethanolic solution (15 mL) containing 4-(2-aminoethyl)benzene sulfonamide (6.7 mg, 33 µmol). The resulting reaction mixture was stirred for 1 h at room temperature. Afterwards, thiol-functionalized silica nanoparticles (MSN-SH, 100 mg) in absolute ethanol (10 mL) were added and the mixture was stirred over night at room temperature. Subsequently, the particles were collected by centrifugation (19,000 rpm, 41,146 rcf, 20 min), washed twice with absolute ethanol and were finally redispersed in ethanol (15 mL) to obtain a colloidal suspension.

Cargo loading and particle capping. MSNs (MSN-phSA, 1 mg) were immersed in an aqueous solution of fluorescein (1 mL, 1 mM) or DAPI (500 µL, 14.3 mM) and stirred over night or for 1 h, respectively. After collection by centrifugation (14,000 rpm, 16,837 rcf, 4 min), the loaded particles were redispersed in a HBSS buffer solution (1 mL) containing carbonic anhydrase (1 mg) and the resulting mixture was allowed to react for 1 h at room temperature under static conditions. The particles were thoroughly washed with HBSS buffer (4 times), collected by centrifugation (5,000 rpm, 2,200 rcf, 4 min, 15 °C), and finally redispersed in HBSS buffered solution.

Characterization. DLS and zeta potential measurements were performed on a Malvern Zetasizer Nano instrument equipped with a 4 mW He-Ne-Laser (633 nm) and an avalanche photodiode detector. DLS measurements were directly recorded in diluted colloidal suspensions of the particles at a concentration of 1 mg/mL. Zeta potential measurements were performed using the add-on Zetasizer titration system (MPT-2) based on diluted NaOH and HCl as titrants. For this purpose, 1 mg of the particles was diluted in 10 mL bi-distilled water. Thermogravimetric analyses (TGA) of the bulk extracted samples (approximately 10 mg) were recorded on a Netzsch STA 440 C TG/DSC. The measurements proceeded at a heating rate of 10 °C/min up to 900 °C in a stream of synthetic air of about 25 mL/min. Nitrogen sorption measurements were performed on a Quantachrome Instrument NOVA 4000e at -196 °C. Sample outgassing was performed for 12 hours at a vacuum of 10 mTorr at 60 °C. Pore size and pore volume were calculated by a NLDFT equilibrium model of N_2 on silica, based on the desorption branch of the isotherms. In order to remove the contribution of the interparticle textural porosity, pore volumes were calculated only up to a pore size of 8 nm. A BET model was applied in the range of 0.05 – 0.20 p/p_0 to evaluate the specific surface area.

Infrared spectra of dried sample powder were recorded on a ThermoScientific Nicolet iN10 IR-microscope in reflexion-absorption mode with a liquid-N_2 cooled MCT-A detector. Raman spectroscopy measurements were performed on a confocal LabRAM HR UV/VIS (HORIBA Jobin Yvon) Raman microscope (Olympus BX 41) with a SYMPHONY CCD detection system. Measurements were performed with a laser power of 10 mW at a wavelength of 633 nm (HeNe laser). Dried sample powder was directly measured on a coverslip. UV/VIS measurements were performed on a Perkin Elmer Lambda 1050 spectrophotometer equipped with a deuterium arc lamp (UV region) and a tungsten filament (visible range). The detector was an InGaAs integrating sphere. Fluorescence spectra were recorded on a PTI spectrofluorometer equipped with a xenon short arc lamp (UXL-75XE USHIO) and a photomultiplier detection system (model 810/814). The measurements were performed in HBSS buffer solution at 37 °C to simulate human body temperature. For time-based release experiments of fluorescein a custom made container consisting of a Teflon tube, a dialysis membrane (ROTH Visking type 8/32, MWCO 14,000 g/mol) and a fluorescence cuvette was used. The excitation wavelength was set to $\lambda = 495$ nm for fluorescein-loaded MSNs. Emission scans (505 – 650 nm) were performed every 5 min. All slits were adjusted to 1.0 mm, bandwidth 8 nm).

Cell Culture. HeLa cells were grown in Dulbecco's modified Eagle's medium (DMEM):F12 (1:1) (Invitrogen) with Glutamax I medium supplemented with 10 % fetal bovine serum (FBS) at 37 °C in a 5 % CO_2 humidified atmosphere. The cells were seeded on collagen A-coated LabTek chambered cover glass (Nunc). For live cell imaging the cells were seeded 24 or 48 h before measuring, at a cell density of $2x10^4$ or $1x10^4$ cells/cm^2.

***In vitro* Cargo Release.** Cells were incubated 7 – 24 h prior to the measurements at 37 °C under a 5% CO_2 humidified atmosphere. Shortly before imaging, the medium was replaced by CO_2-independent medium (Invitrogen). During the measurements all cells were kept on a heated microscope stage at 37 °C. The subsequent imaging was performed as described in the spinning disk confocal microscopy section.

Endosomal compartment staining. To stain the early/late endosome or the lysosome with GFP, commercially available CellLight© staining from Invitrogen was used (CellLight© Early Endosome-GFP, Late Endosome-GFP, and Lysosome-GFP, BacMam 2.0). The cells were simultaneously incubated with MSNs and the BacMam 2.0 reagent. The concentration of the labeling reagent was chosen with 25 particles per cell (PCP) of the BacMam 2.0 reagent

(cf. staining protocol[25]). For incubation, the cells stayed at 37 °C under 5% CO_2 humidified atmosphere for 21 – 24 h till the measurement.

Spinning disc confocal microscopy. Confocal microscopy for live-cell imaging was performed on a setup based on the Zeiss Cell Observer SD utilizing a Yokogawa spinning disk unit CSU-X1. The system was equipped with a 1.40 NA 100x Plan apochromat oil immersion objective from Zeiss. For all experiments the exposure time was 0.1 s and z-stacks were recorded. GFP was imaged with approximately 0.48 W/mm^2 of 488 nm excitation light. Atto 633 was excited with 11 mW/mm^2 of 639 nm and DAPI with 0.16 W/mm^2 of 405 nm. In the excitation path a quad-edge dichroic beamsplitter (FF410/504/582/669-Di01-25x36, Semrock) was used. For two color detection of GFP or DAPI and Atto 633, a dichroic mirror (560 nm, Semrock) and band-pass filters 525/50 and 690/60 (both Semrock) were used in the detection path. Separate images for each fluorescence channel were acquired using two separate electron multiplier charge coupled device (EMCCD) cameras (PhotometricsEvolve™).

7.5 Appendix

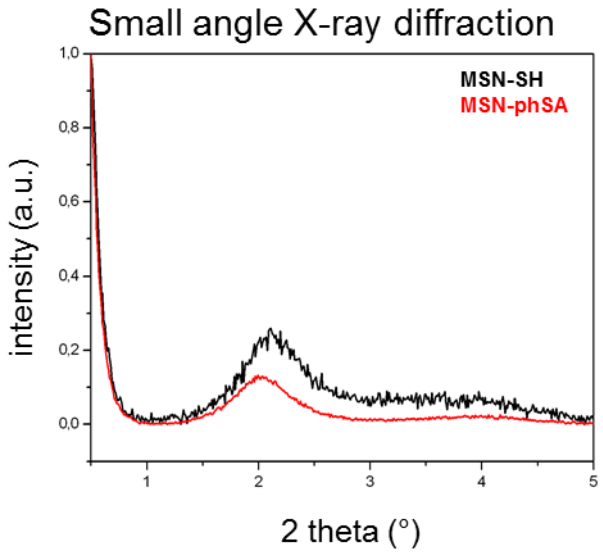

Figure 7.11: Small-angle X-ray diffraction pattern of MSN-SH (black) and MSN-phSA (red).

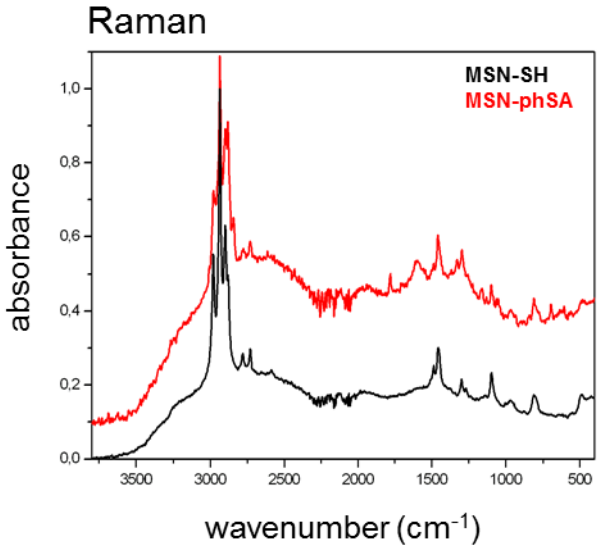

Figure 7.12: Raman spectroscopy data of functionalized MSNs. MSN-SH (black) and MSN-phSA (red). For clarity reasons, the spectra are shifted along the y-axis by 0.1 units. Measurements were performed at an excitation wavelength of 633 nm.

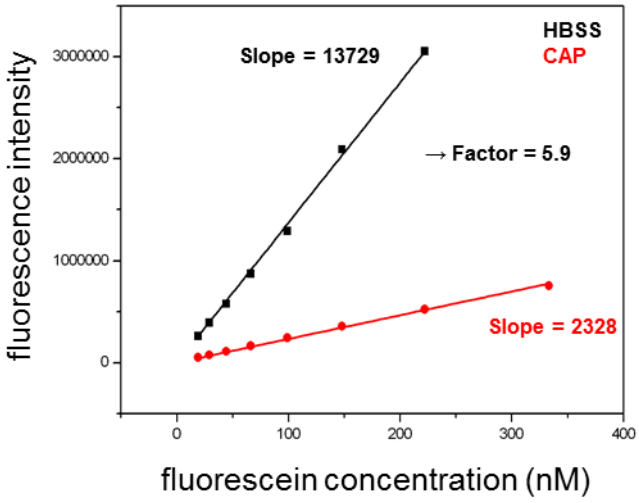

Figure 7.13: Calibration curves of fluorescein at pH 7.4 (HBSS buffer, black curve) and pH 5.5 (CAP buffer, red curve)

7.6 References

[1] Z. X. Li, J. C. Barnes, A. Bosoy, J. F. Stoddart, J. I. Zink, *Chem. Soc. Rev.* **2012**, *41*, 2590.

[2] J. L. Vivero-Escoto, I. I. Slowing, B. G. Trewyn, V. S. Y. Lin, *Small* **2010**, *6*, 1952.

[3] J. M. Rosenholm, V. Mamaeva, C. Sahlgren, M. Linden, *Nanomedicine* **2012**, *7*, 111.

[4] V. Cauda, A. Schlossbauer, J. Kecht, A. Zürner, T. Bein, *J. Am. Chem. Soc.* **2009**, *131*, 11361.

[5] S. A. Mackowiak, A. Schmidt, V. Weiss, C. Argyo, C. von Schirnding, T. Bein, C. Bräuchle, *Nano Lett.* **2013**, *13*, 2576.

[6] A. Schlossbauer, S. Warncke, P. M. E. Gramlich, J. Kecht, A. Manetto, T. Carell, T. Bein, *Angew. Chem. Int. Ed.* **2010**, *49*, 4734.

[7] E. Aznar, L. Mondragon, J. V. Ros-Lis, F. Sancenon, M. Dolores Marcos, R. Martinez-Manez, J. Soto, E. Perez-Paya, P. Amoros, *Angew. Chem. Int. Ed.* **2011**, *50*, 11172.

[8] C.-Y. Lai, B. G. Trewyn, D. M. Jeftinija, K. Jeftinija, S. Xu, S. Jeftinija, V. S. Y. Lin, *J. Am. Chem. Soc.* **2003**, *125*, 4451.

[9] S. Giri, B. G. Trewyn, M. P. Stellmaker, V. S. Y. Lin, *Angew. Chem. Int. Ed.* **2005**, *44*, 5038.

[10] Z. Luo, K. Cai, Y. Hu, L. Zhao, P. Liu, L. Duan, W. Yang, *Angew. Chem. Int. Ed.* **2011**, *50*, 640.

[11] A. Schlossbauer, J. Kecht, T. Bein, *Angew. Chem. Int. Ed.* **2009**, *48*, 3092.

[12] W. Zhao, H. Zhang, Q. He, Y. Li, J. Gu, L. Li, H. Li, J. Shi, *Chem. Commun.* **2011**, *47*, 9459.

[13] R. Liu, X. Zhao, T. Wu, P. Feng, *J. Am. Chem. Soc.* **2008**, *130*, 14418.

[14] C. Wang, Z. Li, D. Cao, Y.-L. Zhao, J. W. Gaines, O. A. Bozdemir, M. W. Ambrogio, M. Frasconi, Y. Y. Botros, J. I. Zink, J. F. Stoddart, *Angew. Chem. Int. Ed.* **2012**, *51*, 5460.

[15] Q. Gan, X. Lu, Y. Yuan, J. Qian, H. Zhou, X. Lu, J. Shi, C. Liu, *Biomaterials* **2011**, *32*, 1932.

[16] M. Lakadamyali, M. J. Rust, H. P. Babcock, X. W. Zhuang, *Proc. Natl. Acad. Sci. U.S.A.* **2003**, *100*, 9280.

[17] V. M. Krishnamurthy, G. K. Kaufman, A. R. Urbach, I. Gitlin, K. L. Gudiksen, D. B. Weibel, G. M. Whitesides, *Chemical Reviews* **2008**, *108*, 946.

[18] K. Möller, J. Kobler, T. Bein, *Adv. Funct. Mater.* **2007**, *17*, 605.

[19] D. K. Srivastava, K. M. Jude, A. L. Banerjee, M. Haldar, S. Manokaran, J. Kooren, S. Mallik, D. W. Christianson, *J. Am. Chem. Soc.* **2007**, *129*, 5528.

[20] P. W. Taylor, R. W. King, A. S. V. Burgen, *Biochemistry* **1970**, *9*, 3894.

[21] J. Kobler, K. Möller, T. Bein, *ACS Nano* **2008**, *2*, 791.

[22] A. Schlossbauer, D. Schaffert, J. Kecht, E. Wagner, T. Bein, *J. Am. Chem. Soc.* **2008**, *130*, 12558.

[23] M. L. Barcellona, G. Cardiel, E. Gratton, *Biochem. Biophys. Res. Commun.* **1990**, *170*, 270.

[24] http://tools.lifetechnologies.com/content/sfs/manuals/mp01306.pdf.

[25] http://tools.lifetechnologies.com/content/sfs/manuals/mp10582.pdf.

8 Targeted Drug Delivery in Cancer Cells with Red-Light Photoactivated Mesoporous Silica Nanoparticles

This chapter is based on the following publication:

Stephan Mackowiak, Alexandra Schmidt, Veronika Weiss, Christian Argyo, Constantin von Schirnding, Thomas Bein, and Christoph Bräuchle, *Nano Letters*, **2013,** 13, 2576 – 2583.

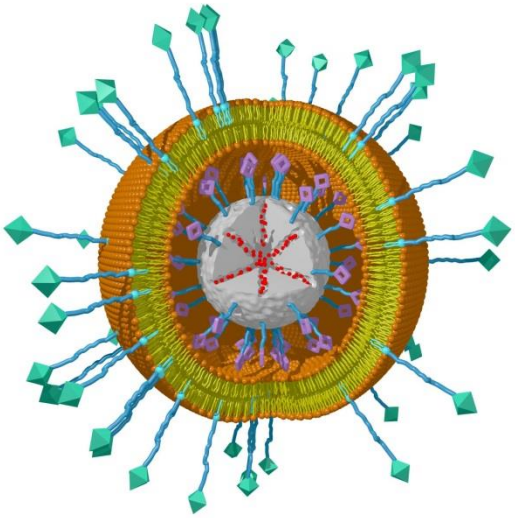

8.1 Introduction

The delivery of large amounts of cancer therapeutics specifically into the cytosol of cancer cells still faces significant challenges. Promising approaches in the field of drug delivery encompass the utilization of various types of nanoparticles such as polyplexes,[1-3] dendrimers,[4-6] gold nanoparticles,[7] and colloidal mesoporous silica nanoparticles (MSNs).[8-10] Each of these systems has its inherent advantages and disadvantages. Usually, they are either optimized for specific uptake by cancer cells, amount of cargo delivered, release of cargo into the cytosol, or ease of synthesis of the system itself. However, often they do not perform well in all of these required areas. Notably, release of the drug from the endosome poses a significant hurdle on the way toward drug delivery with high efficacy. Here, we will present a system that provides solutions for all of these aspects. In particular, a photoactivatable drug delivery system based on core−shell colloidal MSNs will be employed, which allows exact spatial and temporal control of the release of the cargo from both the

MSNs and the endosome.[11-12] Core−shell MSNs are more suitable than regular MSNs for this task because they can have different functionalizations in the core and the shell. This allows us to optimize the core functionalization, for example, for cargo uptake or covalent binding of the cargo to the core by disulfide bridges.[13] Moreover, the surface functionalization can be chosen to implement various gating mechanisms, such as surrounding the MSNs with a lipid bilayer to enclose the cargo in it.[11, 14] Previously, our groups published a photoactivatable drug delivery system performing some of the above-mentioned tasks.[14] The current system is improved in three key areas. The used photosensitizer (PS) will be activated by red light instead of blue light; the synthesis is significantly simplified, and targeting ligands have now been added to the system. The function of the photosensitizer is to solve the problem of endosomal entrapment. Other approaches addressing this issue such as taking advantage of the proton sponge effect,[15-16] employing fusogenic or endosomolytic peptides,[17-20] and others have been used.[21-22] There, the endosomal escape occurs at a less defined time point and for all particles regardless of their location in healthy or cancerous cells. In contrast, the photoactivation approach offers a solution for both of these shortcomings by initiating the cargo release through an external stimulus in the form of a laser beam. The laser beam can be directed into the cancer tissue and activated at the right time point. The activation of the photosensitizer with red light instead of blue light reduces the phototoxicity and significantly increases the depth of tissue penetration,[23] which will be crucial when activation *in vivo* is required as shown by the Kataoka group.[24] In comparison to regular photochemical internalization and other photoactivatable systems our system exhibits specific uptake by cancer cells due to the presence of targeting ligands. Schlossbauer *et al*.[14] presented MSNs with photosensitizers that allowed free choice and controlled release of the cargo. However, the issue of the targeting capability of the system was not addressed. In the current approach, we covalently link the photosensitizer molecule (PS) to the MSN surface and encapsulate the MSNs with a supported lipid bilayer (SLB) to retain the drug. This allows for choosing a drug different from the PS and implementing a gating mechanism as well. Most cancer cells have specific receptors overexpressed on their surface. These receptors are only present in small concentrations or not at all on the surface of healthy cells. Ideally, a drug delivery system can be easily modified to make it specific for multiple cancer cell types. Here we introduce the choice between two targeting ligands to our MSNs, namely, folic acid (FA) as an example of

a small molecule ligand and epidermal growth factor (EGF) as an example for a protein ligand. Both ligands are relevant for cancer cell targeting. For this purpose, targeting ligands (TL) are inserted into the SLB by diffusion to achieve specific uptake of the drug delivery vehicle by cancer cells. In the following, we will first discuss the synthesis and characteristics of our drug delivery system. Subsequently, live cell microscopy studies will be presented to evaluate the functionality of the employed targeting ligands and the release of the cargo from the MSNs by photoactivation.

8.2 Results and Discussion

Synthesis and Characterization. The core−shell MSNs were synthesized via a sol−gel method using tetraethyl orthosilicate (TEOS) as a silica source and CTAC as a pore template.[12] The MSN core was functionalized with thiol groups and the surface with cyano groups. The cyano groups were hydrolyzed at elevated temperatures under acidic medium to result in carboxy groups exclusively at the external silica particle surface. A next step was the covalent binding of the PS to the MSNs. We note that a direct attachment of the $AlPcS_{2a}$ resulted in a significantly reduced pore accessibility and particle aggregation (data not shown). Introduction of a spacer helped to retain pore access and colloidal stability. Here, bifunctional PEG linkers were attached to the outer surface of MSNs via the EDC amidation synthesis route; they additionally offer a site for further functionalization. This strategy can be further utilized for covalent binding of PS molecules, targeting ligands or other biocompatible moieties. Previous studies have shown that coating of MSNs with hydrophilic polymers, including PEG, improves biocompatibility and colloidal stability of the drug delivery vehicles in aqueous media.[25] However, the length of the integrated PEG linker should not be too long because otherwise the formation of the SLB around the nanoparticle can be difficult. Scheme 8.1 depicts the complete synthesis strategy resulting in multifunctional mesoporous silica nanocarriers for a red-light photoactivated targeted drug release into cancer cells.

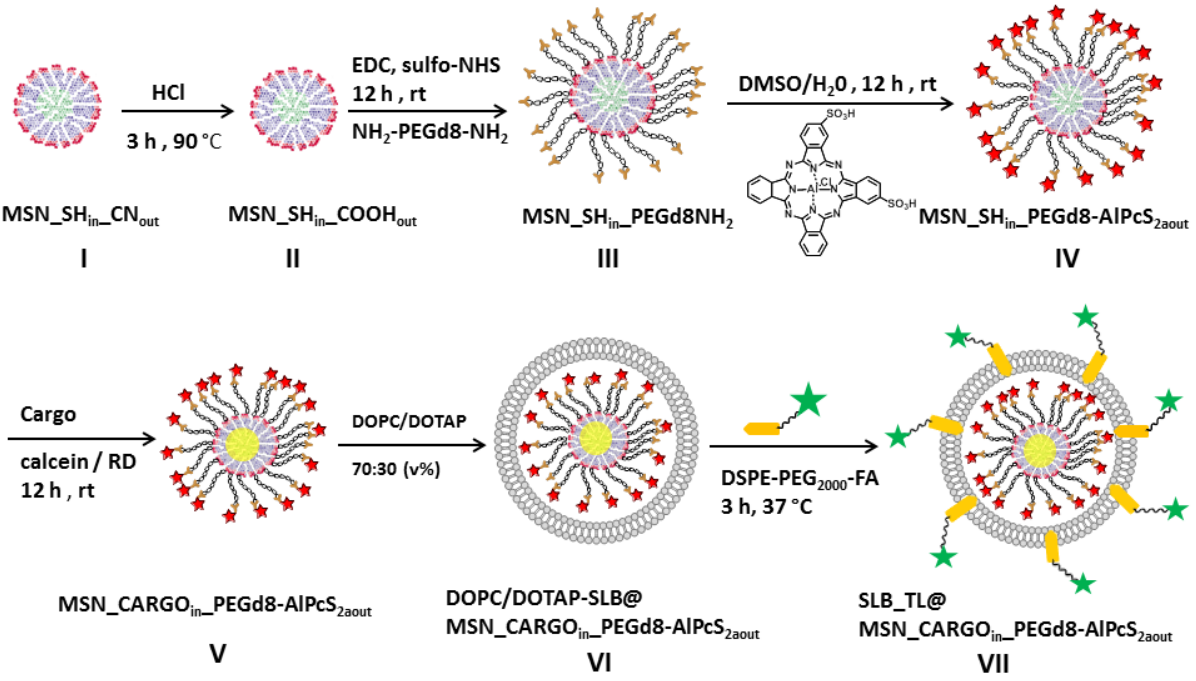

Scheme 8.1. Synthesis pathway of core (Green) shell (Red) MSNs with covalently linked $AlPcS_{2a}$ (red star) via PEG linker (black chain) and surrounded by DOPC/DOTAP supported lipid bilayer with targeting ligand (green star, TL). Before the formation of the SLB, the MSN core is loaded with a cargo (yellow), in our case calcein or a rhodamine derivative. Drawing is not to scale.

The transmission electron microscope (TEM) image of the MSNs (species I in Scheme 8.1) shows spherical particles with a mean diameter of 70 nm (Figure 8.1a). The mesoporous channel structure radiating from the particle center is apparent in the image. From dynamic light scattering (DLS) and nitrogen sorption experiments a mean particle size of 69 nm and a mean pore size of 5.2 nm was determined (black squares in Figure 8.1b and c).

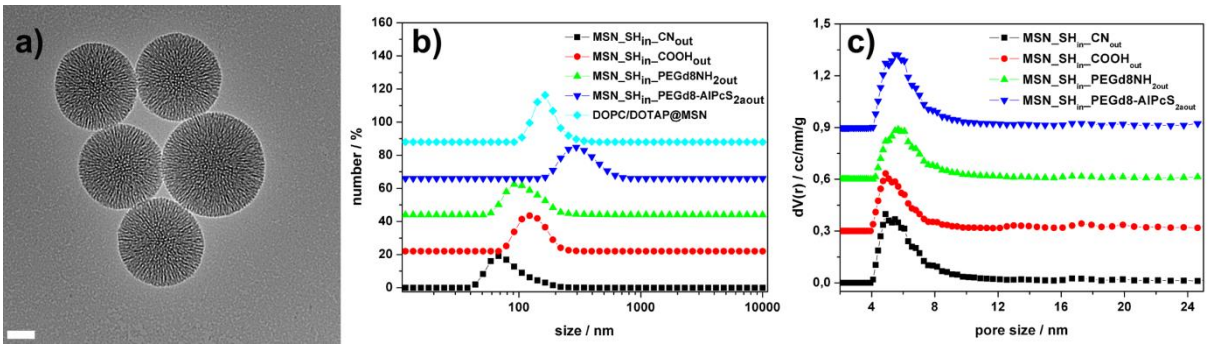

Figure 8.1: (a) TEM image showing bare MSNs (I). The scale bar is 20 nm. (b) Particle sizes of species I−VI in Scheme 1 obtained by DLS measurements. All curves, except of species I (black curve, MSN_SH$_{in}$_CN$_{out}$), are shifted by a value of 30 along the y-axis for clarity. (c) Pore size distributions of species I−IV. The exact values of the maxima are given in Table 1. Data are shifted by a value of 0.3 along the y-axis for clarity. Species I (black curve) represent MSN_SH$_{in}$_CN$_{out}$, species II (red curve) are MSN_SH$_{in}$_COOH$_{out}$, species III (green curve) are MSN_SH$_{in}$_PEGd8NH$_2$, species IV (blue curve) are MSN_SH$_{in}$_PEGd8-AlPcS$_{2aout}$, species VI (cyan curve) are DOPC/DOTAP-SLB@MSN_CARGO$_{in}$_PEGd8-AlPcS$_{2aout}$.

The nitrogen sorption isotherms of the samples MSN_SH$_{in}$_CN$_{out}$ (I, black squares), MSN_SH$_{in}$_COOH$_{out}$ (II, red circles), MSN_SH$_{in}$_PEGd8NH$_{2out}$ (III, green up triangles), and MSN_SH$_{in}$_PEGd8-AlPcS$_{2aout}$ (IV, blue inverted triangles) can be seen in Figure 8.2, exhibiting a typical type IV isotherms for mesoporous materials.

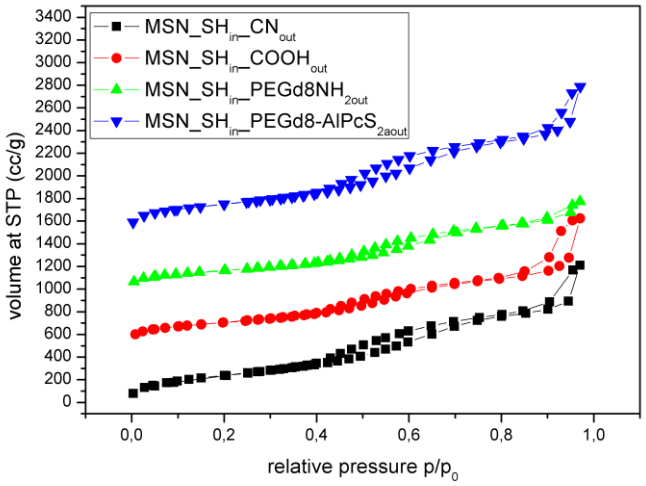

Figure 8.2: Nitrogen sorption isotherms for the samples MSN_SH$_{in}$_CN$_{out}$ (black squares), MSN_SH$_{in}$_COOH$_{out}$ (red circles), MSN_SH$_{in}$_PEGd8NH$_{2out}$(green up triangles) and MSN_SH$_{in}$_PEGd8-AlPcS$_{2a}$ (blue down triangles). For clarity reasons curves for MSN_SH$_{in}$_COOH$_{out}$, MSN_SH$_{in}$_PEGd8NH$_{2out}$, and MSN_SH$_{in}$_PEGd8-AlPcS$_{2aout}$ are shifted along the y-axis by a value of 500 each.

The Brunauer-Emmett-Teller (BET) surface areas for each sample are calculated from the corresponding nitrogen sorption isotherm in the range $p/p_0 = 0.05 – 0.2$ and are summarized in Table 8.1. All samples feature a high specific surface area typical for our MSNs. We assume that the reduced BET surface area in the sample MSN_SH_{in}_$COOH_{out}$ (II) in comparison with MSN_SH_{in}_CN_{out}(I) comes from the more condensed silica network and pore shrinkage resulting from the hydrolysis of the cyano-moiety in hydrochloric acid. The decrease of the specific surface area in the sample MSN_SH_{in}_$PEGd8NH_{2out}$ (III) can be explained by the addition of non-porous PEG and the blocking of some pores by frozen PEG-linker in the surface layer of the MSNs.

Table 8.1: Particle size, specific BET surface area, pore size and relative mass loss derived from Figure. 8.1b, Figure. 8.2 and Figure 8.4.

Sample	Particle size [nm]	BET surface area [m^2/g]	Pore size [nm]	Relative mass loss [%]
MSN_SH_{in}_CN_{out}	69	934	5.2	17
MSN_SH_{in}_$COOH_{out}$	125	746	5.1	12
MSN_SH_{in}_$PEGd8NH_{2out}$	98	615	5.6	18
MSN_SH_{in}_PEGd8-$AlPcS_{2aout}$	294	918	5.5	31
DOPC/DOTAP_SLB@MSN	160	n.a.	n.a	n.a

This effect is relatively small due to the short length of the flexible spacer. In contrast, the BET surface area of the sample MSN_SH_{in}_PEGd8-$AlPcS_{2aout}$ is with 918 m^2/g significantly higher than the BET surface area for MSN_SH_{in}_$COOH_{out}$(II) and MSN_SH_{in}_$PEGd8NH_{2out}$ (III). We suppose that this effect comes from interstitial pore volume occurring upon attachment of $AlPcS_{2a}$ onto the particle shell. Considering that phthalocyanines are large, sterically hindered molecules that lack the flexibility of a PEG-linker, a covalent attachment of them to the MSN surface will result in voids at liquid nitrogen temperatures. The pore size distributions derived from NLDFT calculations are given in Figure 4c and are summarized in Table 8.1. The pore size changes little upon PEGylation and photosensitizer attachment, indicating that the mesopores are still accessible for guest molecules. Furthermore, it proves the selective functionalization of the particle shell.

To promote endosomal escape and subsequent delivery of the cargo into the cytosol, we employ a photoactivation approach. Herefore, a red-light sensitive photosensitizer, aluminum

phthalocyanine disulfonate ($AlPcS_{2a}$), is covalently linked to the surface of the MSNs via an octamer PEG linker. The PEG linker is functionalized with amino groups on both ends. In the first reaction step, the surface cyano groups of the MSNs (I) are hydrolyzed to carboxyl groups (II), and subsequently the PEG linker is attached to the MSN surface via EDC amidation (III). The ^{13}C solid state NMR (ssNMR) shows the successful implementation of these three steps (Figure 8.4a). The resonance of the carboxyl group appears at 180 ppm upon hydrolysis of the cyano groups (red trace in Figure 8.4a). Following EDC amidation, the carboxyl group disappears, and the C−O and CH_2 resonances, both from the PEG linker, appear at 70 and 42 ppm, respectively (green trace in Figure 8.4a). The other resonances originate from the functionalized silanes of the MSNs. The different surface functionalizations, including the attachment of the PEG linker, are apparent in the final relative mass levels of the thermogravimetric analysis (TGA) curves as well (Figure 8.4b and Table 8.1). Species III with the PEG linker has a significantly greater mass loss than species I and II. The slightly lower mass loss of species II in comparison to species I originates from a more stable silica network that is formed during the 3 h heating in HCl, where the cyano is converted to carboxylic acid groups. The more stable silica network is apparent from the reduced BET surface area, as measured by N_2 sorption experiments, as well. Subsequently, $AlPcS_{2a}$ is attached to the free remaining amino group of the PEG linker by linking the PEG-NH_2 group with one of the two sulfonate groups of $AlPcS_{2a}$ (IV). The successful attachment of $AlPcS_{2a}$ is inferred from the IR spectrum. The CH_2 stretching vibrations from the organic functionality (mercaptopropyl- and cyanopropyl) are visible between 2800 cm^{-1} and 2850 cm^{-1}. Furthermore, several peaks at 2900 cm^{-1} (C-H stretching vibrations) and at 1400 cm^{-1} (C-H bending vibrations) are visible. The intensity of these vibrations decreases after the carboxylation of the cyanide groups. Further condensation of the silica framework was achieved through the hydrolysis of the cyano-moiety and therefore the content of ethoxy groups was reduced. The cyanide vibration at 2253 cm^{-1} for the species I disappears completely after hydrolysis while the new -COOH vibration at 1707 cm^{-1} ($MSN\_SH_{in}\_COOH_{out}$) arises. After PEGylation by EDC amidation the C=O stretching vibration mode is moved to higher vibrational energies (1616 cm^{-1}) resulting from the newly formed amide bond. Also the N-H bending vibrations appear at 1530 cm^{-1}. The band between 1300 cm^{-1} and 900 cm^{-1} can be attributed to silica framework vibrations and is visible in all spectra. The peak at 1332 cm^{-1} represents the asymmetric stretching of the -SO_2 group in $AlPcS_{2a}$. The peak arising at 904 cm^{-1} in the spectra of $MSN\_SH_{in}\_PEGd8\text{-}AlPcS_{2aout}$ can be assigned to the stretching vibration of the newly formed N-S bond between the terminal

amino-group of the PEG-linker and $AlPcS_{2a}$. The two peaks at 743 cm^{-1} and 720 cm^{-1} correspond to the non-planar deformation vibrations of the C–H bonds of benzene rings.

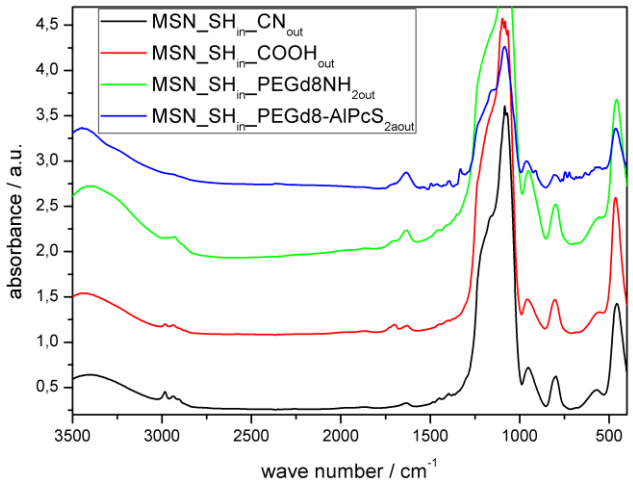

Figure 8.3: IR spectra of MSN_SH$_{in}$_CN$_{out}$ (black), MSN_SH$_{in}$_COOH$_{out}$ (red),MSN_SH$_{in}$_PEGd8NH$_{2out}$ (green) and MSN_SH$_{in}$_PEGd8-AlPcS$_{2aout}$ (blue). For clarity reasons curves were shifted along the y-axis by a value of 0.8 each.

Thermogravimetric analysis shows a high mass loss for species IV which is comparably large due to the high molecular mass of $AlPcS_{2a}$. In particular, the ratio of the mass loss going from species III to IV and from species II to III is 2. This can be related to the molecular mass ratio of the PS and the PEG, which is 2 as well.

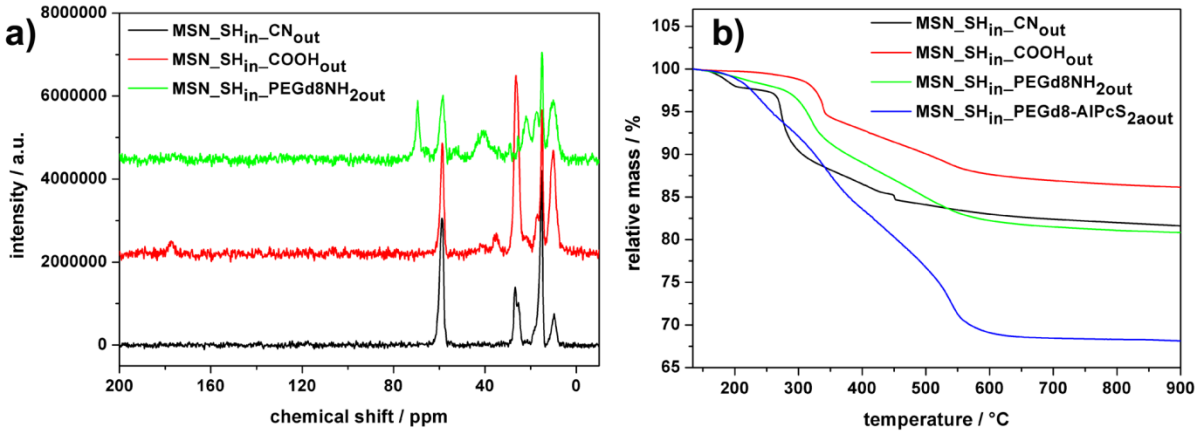

Figure 8.4: (a) Solid state ^{13}C NMR spectra of species I−III. It shows the successful conversion of the surface cyano groups to carboxyl groups and the subsequent linkage of the PEG8 linker to the MSN shell. Spectra for MSN_SH$_{in}$_COOH$_{out}$ (red) and MSN_SH$_{in}$_PEGd8NH$_{2out}$ (green) are shifted by a value of 2 × 106 each for clarity reasons. (b) Thermogravimetric analysis of species I−IV. The relative mass losses are given in Table 1.

The cyanopropyl groups of the sample MSN_SH_{in}_CN_{out} (I, black squares) are uncharged at high or low pH values, resulting in a zeta potential curve that is similar to the one of unfunctionalized MSNs. The successful attachment of NH_2-PEGd8-NH_2 to the sample MSN_SH_{in}_$COOH_{out}$ results in a higher zeta potential value due to protonation of the amino groups at low pH values (green). The sample MSN_SH_{in}_PEGd8_$AlPcS_{2aout}$ (IV) couldn't be measured because the laser wavelength of 633 nm leads to an excitation of the photosensitizer, resulting in oxygen production with bubble formation on the electrode. Shorter measurement times did not lead to sufficient results.

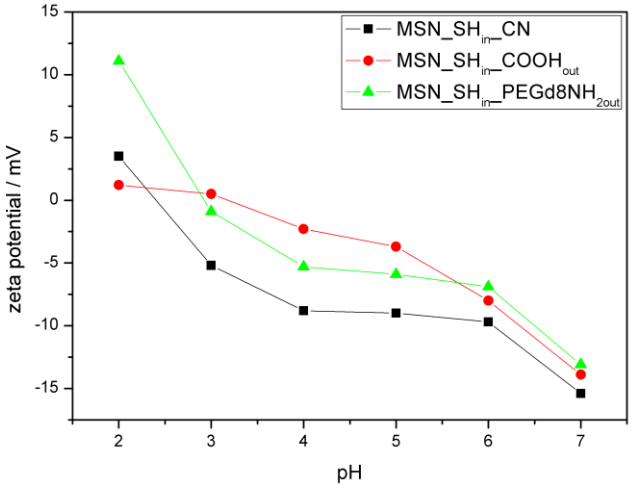

Figure 8.5: Zeta potential measurements of the samples MSN_SH_{in}_CN_{out} (black squares), MSN_SH_{in}_$COOH_{out}$ (red circles), MSN_SH_{in}_PEGd8NH_{2out} (green up triangles).

Cargo loading and release. To utilize the above multifunctional nanoparticles as drug delivery vehicles, a cargo was loaded into the MSN pores, and the entire nanoparticle was enclosed by a supported lipid bilayer to prevent premature release of the cargo from the MSN core. The cargo was loaded into the MSNs by incubating them in a concentrated solution of the cargo overnight. In our system different types of cargo can be loaded. Here we show two examples, calcein and a rhodamine derivative. After the loading of the cargo the SLB is formed around the nanoparticle via the solvent exchange method as published by Cauda *et al.*[11] The SLB consists of a lipid mixture of 70 vol% of 1,2-dioleoyl-snglycero-3-phosphocholine (DOPC) and 30 vol% of 1,2- dioleoyl-3-trimethylammonium-propane (DOTAP). The DLS data (Figure 8.1b) show that the modifications of the MSN surface, the attachment of the PEG linker, the linking of the photosensitizer, and the formation of the 70 vol% DOPC/30 vol% DOTAP shell (SLB) result in colloidal systems with slightly varying

hydrodynamic particle sizes (Figure 8.1b and Table 8.1, respectively). In particular, it appears that the presence of carboxyl- or sulfonyl groups, either directly on the MSN surface or on the $AlPcS_{2a}$, results in an increase of the effective particle size. In contrast, the presence of PEG molecules on the MSN surface as well as the presence of the SLB results in a decrease of the effective particle size. In both cases, the origin of the size decrease can be attributed to the weaker interactions between the particles caused by steric or electrostatic stabilization. The accessible pore size as obtained by nitrogen sorption measurements is barely affected by the various surface modifications, as expected for particles that feature true core−shell spatially distributed functionalities (Figure 8.1c). The permeability of the SLB and the opening of the SLB by photoactivation were examined in situ with a cuvette, containing a semipermeable membrane.[26] Figure 8.6 shows the release of cargo, either calcein (blue triangles) or a rhodamine derivative (RD) (black squares), from the MSN−PS−SLB (VI).

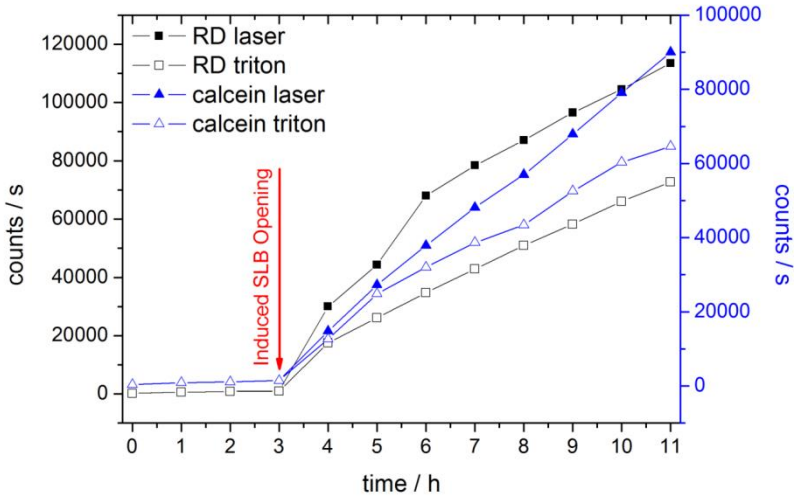

Figure 8.6: Release kinetics of calcein (solid blue triangle) and a rhodamine derivative (RD, solid black squares) before and after photoactivation at 3 h with light of λ = 639 nm and 0.55 mW/mm^2 for 1 min of MSN-PS-SLB measured in situ. Only after photoactivation a significant amount of cargo is released, demonstrating the impermeability of the SLB before. Analogously, the SLB can be opened by addition of triton to the MSN solution after a 3 h time period. For both calcein (open blue triangles) and the RD (open black squares) the release by triton is slower as compared to the opening of the SLB by photoactivation.

The amount of released cargo over a 3 h time period before opening the SLB is minimal, demonstrating the integrity of the SLB. After 3 h in the cuvette the SLB was opened either by photoactivation or triton addition. To open the SLB through photoactivation the MSN-PS-SLB particles were exposed to 639 nm light with a power density of 0.55 mW/mm^2 for 1 min,

resulting in an activation of the photosensitizer and singlet oxygen production. The singlet oxygen reacts with the double bonds of the DOPC and opens the SLB. This is apparent from the strong increase of fluorescence starting after 3 h, originating from the release of the cargo from the MSN core. Alternatively, the SLB can be opened by triton addition. A strong increase of fluorescence for calcein (open blue triangles) and RD (open black squares) is apparent. However, the SLB opening via photoactivation seems to be more efficient, judging from the release rate of the cargos after induced SLB opening.

Targeting. Besides the prevention of premature release of the cargo from the MSN core, the SLB offers the opportunity to add various targeting ligands to our nanoparticle system. In the following section, we will discuss how our MSN-PS-SLB system can be modified with two different targeting ligands, namely, folic acid (FA) and epidermal growth factor (EGF). The efficient modification of our drug delivery system with various targeting ligands as the final step in the synthesis allows for tuning of our multifunctional nanoparticles for a wide range of cell types without constructing a completely new system for each cell type.The system presented above offers this opportunity because the MSN-PS-SLB (VI) is only modified at the very end of the synthesis for a specific targeting ligand (TL). The basic building block for adding the targeting ligand to the MSN-PS-SLB (VI) is a DSPE-PEG_{2000}-TL conjugate molecule. This building block is inserted into the SLB by incubating the MSN-PS-SLB (VI) with DSPE-PEG_{2000}-TL at 37 °C for 3 h (FA) and 12 h (EGF), respectively. In the studies presented here, we chose FA and EGF as targeting ligands because their receptors are commonly overexpressed on a wide range of cancer cells.[27-28] FA receptors are overexpressed on various cell lines such as HeLa cells and KB cells,[27] and the EGF receptor is abundant on HuH7 cells, for example.[29] The functionality of the targeting ligands on our nanoparticle system was evaluated by performing competition experiments and by evaluating the MSN-PS-SLB-TL (VII) uptake with live cell confocal fluorescence microscopy.

In a competition experiment the MSN-PS-SLB-TL (VII) are incubated with cells that were either previously incubated with free targeting ligand or not. Preincubation of cells with free targeting ligand will block the specific receptors on the cell surface. Consequently, uptake of the MSN-PS-SLB-TL (VII) should only happen unspecific and therefore is expected to take much longer than receptor-mediated endocytosis. To evaluate the functionality of the FA ligand, KB cells were used. In the experiments shown in Figure 8.7a the cells were preincubated with FA for 2 h at 37 °C before the MSN-PS-SLB-FA (VII) particles were added to the cells and incubated for 3 h at 37 °C. Recording z-stacks of the cells with a

spinning disk confocal fluorescence microscope allows us to indicate MSNs inside or outside the cell. A typical cut through the cell is shown in Figure 8.7.

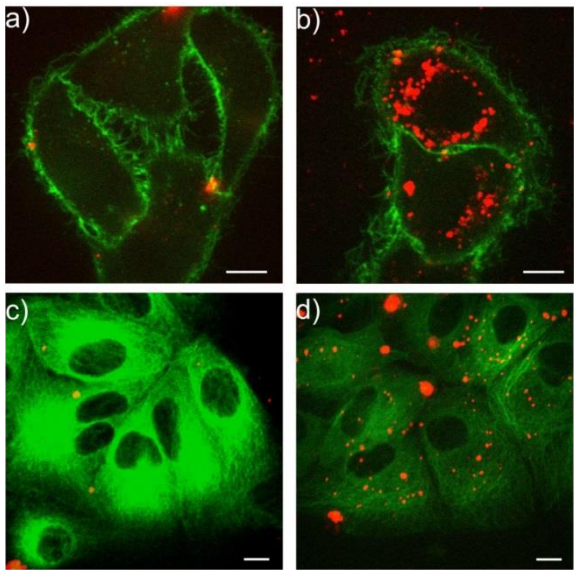

Figure 8.7: Unspecific and receptor-mediated endocytosis of MSN-PS-SLB particles with folic acid ligand (MSN-PS-SLB-FA) by KB cells and MSN-PS-SLB particles with EGF ligand (MSN-PS-SLB-EGF) by HuH7 cells with GFP tagged tubulins (HuH7tub), respectively. (a) Incubation of MSN-PS-SLB-FA particles with FA preincubated KB cells for 3 h at 37 °C. (b) Incubation of MSN-PS-SLB-FA particles with KB cells, not FA preincubated, for 3 h at 37 °C. (c) Internalization of MSN-PS-SLB-EGF particles by HuH7tub with EGF preincubated and (d) non pre-incubated HuH7tub cells. The KB cell membrane is shown in green and the particles in red. For HuH7tub the GFP tagged tubulins are shown in green and the particles in red. Images were taken with live KB cells and HuH7tub cells. The scale bar is 10 µm.

It shows that in KB cells only a few individual particles are present inside the cell (Figure 8.7a), whereas full stacks emphasize the quasi absence of nanoparticles inside the cell, independent of the chosen focal plane. In contrast, incubation of MSN-PS-SLB-FA (VII) with KB cells that were not preincubated with FA before resulted in significant uptake of particles (Figure 8.7b). The nanoparticles appear in the single representative z-slice as well as in the full stack, through the entire height of the cell. This clearly demonstrates that the particles are taken up by receptor-mediated endocytosis and that unspecific uptake of the particles by KB cells is small after 3 h incubation time. To utilize EGF as another targeting ligand beside folic acid, we synthesized a lipid-EGF construct, where the EGF (50 µg) is covalently attached to the lipid DSPE-PEG_{2000}-maleimide (Scheme 8.2). In a first step, the N-terminus of the targeting peptide was modified via the Traut's reagent (2-Iminothiolane, 2 equiv., 16 nmol) in an aqueous solution by stirring for 1 h at room temperature. This resulted in a terminal thiol group which can be used for further functionalization. Subsequently, the modified EGF was

covalently attached to the lipid DSPE-PEG_{2000}-maleimide (3.5 µL of a 10 mg/mL 60/40 H_2O/EtOH v%). The final DSPE-PEG_{2000}-EGF construct can be further utilized to use as targeting ligand on the nanoparticle as described below.

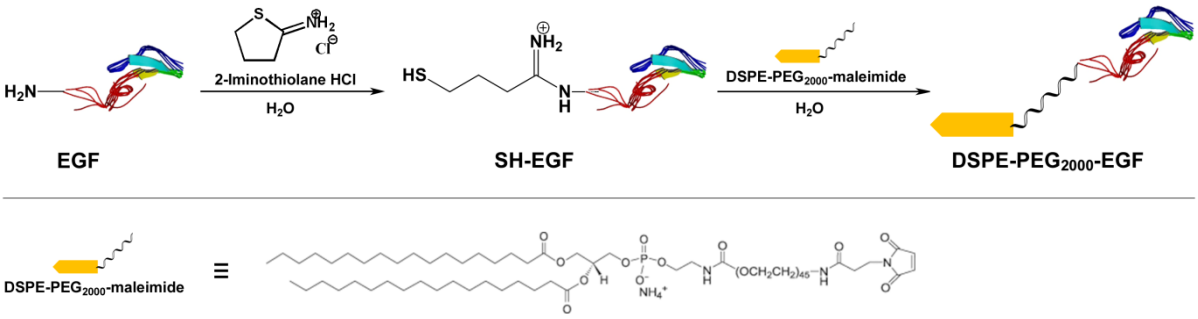

Scheme 8.2: Chemical modification of the EGF targeting ligand via the Traut's reagent (2-iminothiolane) to achieve thiolation of the N-termius of EGF. In a second step the lipid DSPEPEG_{2000}-maleimide covalently binds to the modified EGF.

Similar to the FA experiments, we performed competition experiments with the EGF ligand. Experiments were performed with HuH7 cells, which are known to overexpress the EGF receptor.[29] Figure 8.7c shows that in the case of preincubation of HuH7 cells with EGF almost no MSN-PS-SLB-EGF (VII) particles are endocytosed by the HuH7 cells after 3 h. In contrast, a significant number of the particles is present inside the cells when the cells were not preincubated with EGF (Figure 8.7d). Again typical slices of the z-stacks are shown in Figure 8.7c,d. The above results demonstrate that our MSN-PS-SLB nanoparticles can be modified efficiently to meet the specific requirements of various cancer types and to ensure a specific receptor-mediated uptake. In addition, in the two cell types discussed here the unspecific uptake of the MSNs is very small after 3 h. Both are important factors for successful drug delivery vehicles in order to prevent damage of healthy cells by cancer therapeutics. Furthermore, the targeting ligand is introduced after the completion of the synthesis of the actual nanoparticle system. This offers more flexibility to separately synthesize both the nanoparticle system and the DSPE-PEG_{2000}-TL because possible incompatible reaction conditions can be avoided. This allows for selecting the synthesis strategies for both components more freely, which is considered a significant advantage for the incorporation of fragile peptides into these systems. Besides the specific uptake of the drug delivery vehicle by cancer cells, it is of key importance for efficient drug delivery to release the drug into the cytosol, and ideally to do so with spatial and temporal control. In the following, we will show that our system provides the means to achieve this.

***In vitro* cargo release by photoactivation.** One of the main challenges for drug delivery with high efficacy is to overcome the endosomal entrapment in order to release the drug into the cytosol. A photoactivation approach provides both of these capabilities. In the studies where MSNs and photosensitizers were used, the photosensitizer was either loaded as a cargo into MSNs[30] or covalently attached to them.[14] The covalent attachment of the photosensitizer is advantageous compared to loading it into the MSN pores. The ratio of MSNs to photosensitizer is more easily controlled, the loading capacity of the MSNs can be completely used for the drug, and a spatial separation between drug and photosensitizer exists. This could be important considering that the singlet oxygen, produced by photoactivation of the photosensitizer, will most likely damage the drug when not spatially separated from it. In previous work from our group,[14] the photosensitizer had to be excited by blue light, which cannot penetrate the tissue very deeply.[23] Here we have improved this system by using a different photosensitizer, namely, $AlPcS_{2a}$. First, it is photoactivatable with red light, and thereby the phototoxicity caused by light activation with blue light is reduced. Additionally, the potential depth of tissue penetration of the activation laser is increased by a factor of about 5. The latter feature will become important if this drug delivery system is tested *in vivo*. Nishiyama *et al*. demonstrated this by using $AlPcS_{2a}$ for a transfection of the conjunctival tissue in rat eyes.[24] Finally, AlPcS2a can be more easily attached to the MSN surface than the previously used photosensitizer because a sulfonate group can be directly linked to an amino group. To verify that the drug delivery mechanism works *in vitro*, we incubated MSN-Calcein-PS-SLB-FA nanoparticles for 3 h with HeLa cells. In comparison to the incubation with free calcein, the incubation of the nanoparticles containing calcein as a cargo produces a significantly higher calcein concentration inside the cell (Figure 8.8a).

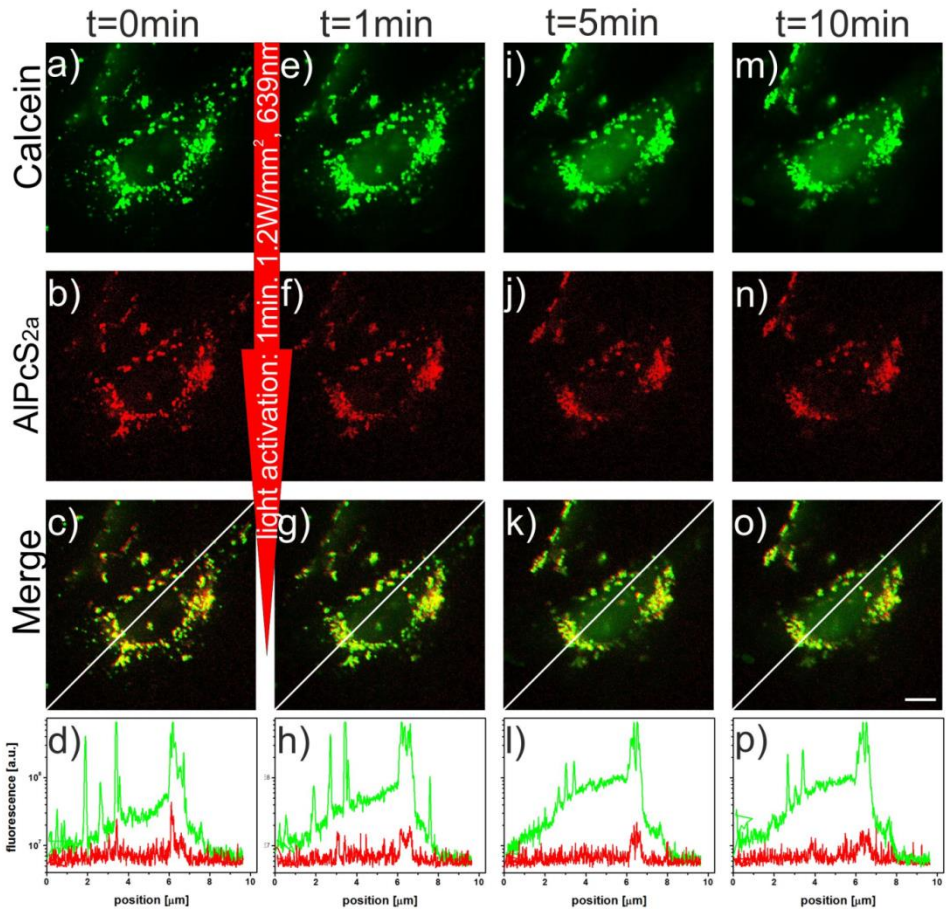

Figure 8.8: Fluorescence microscopy of MSN-PS-SLB-FA nanoparticles loaded with calcein inside HeLa cells, after an incubation time of 16 h. (a−c) Calcein (green) and $AlPcS_{2a}$ (red) are colocalized (yellow) prior to photoactivation. (d) Intensity profile along the white line in the merged image for both. (e−h) 1 min, (i−l) 5 min, and (m−p) 10 min after photoactivation. The scale bar is 10 µm.

The uptake of free calcein by KB cells is negligible. This demonstrates that our drug delivery system can be used to efficiently transport membrane impermeable cargos into the cell. Before photoactivation, calcein and the photosensitizer are colocalized (yellow color in Figure 8.8c) and exhibit a dot-like pattern, indicating that calcein and the MSN-PS-SLB-FA particles are still inside the endosomes (Figure 8.8a−c). This demonstrates that the escape from the endosome does not happen automatically and that a mechanism is required to overcome this key challenge in the field of drug delivery. To induce the opening of the SLB coat around the MSNs and the following endosomal escape in a cascaded manner, we activated the integrated photosensitizer $AlPcS_{2a}$ with 1.2 W/mm^2 of 639 nm light for 1 min, at similar conditions as those used for the in situ experiment in Figure 8.6. As a result, 1 min after activation an increase of the green fluorescence caused by calcein through the entire cell and in particular in the nucleus can be observed (Figure 8.8e and h). In contrast, no change of the red fluorescence pattern originating from the photosensitizer is observed; only a small decrease in

fluorescence can be seen due to photobleaching during the photoactivation step. This trend continues over time as is apparent from the images taken at 5 min (Figure 8.8i−k) and at 10 min (Figure 8.8m−o) after photoactivation. In the merged image after 1, 5, and 10 min (Figure 8.8g, k, and o), the presence of the green signal becomes dominant, indicative of a lower colocalization between calcein and photosensitizer due to the spreading of calcein in the cell. The green fluorescence is observed in particular inside the cell nucleus. This time-series of images shows that photoactivation can open the SLB and the endosome via an activation cascade, resulting in the release of calcein into the cytosol. While the green fluorescence from calcein is present through the entire cytosol after photoactivation (Figure 8.8e, i, and m), the dot-like pattern of the red fluorescence, caused by the PS on the MSNs, does not change (Figure 8.8f, j, and h). This shows that, in contrast to calcein, the MSNs do not escape from the endosomes. The reason for this behavior is unknown but has been observed before.[30] However, we note that free PS in endosomes does spread after photoactivation, and it is therefore not believed to cause much damage to the cell. The destruction of cells through photosensitizers is also discussed in the literature, and if the photosensitizer is not located close to the cell membrane it cannot cause necrosis.[31] The induction of apoptosis is dependent on the cell line, the overall light dose, the localization, the type of photosensitizer, concentration of the photosensitizer, and many more parameters, and therefore it should be subject of continuing intensive studies. However, for the intensities in the range of 0.12−1.2 W/mm^2, which were used in this work, the system works without observable damage. Furthermore, the lifetime of singlet oxygen is relatively short (around 2×10^{-7} s[32]). We emphasize that the cargo is located in the channels of the MSNs, whereas the photosensitizer is clearly separated from the pores via a PEG linker and located at the outside of the MSNs. Consequently the singlet oxygen cannot destroy much of the cargo or of the cell membrane during the activation, as it cannot diffuse inside the pores or too close toward the cell environment in this short time. In addition to calcein, our multifunctional system can be loaded with various cargos (not shown here). As a result, our system provides a means to spatially control the release of cargo by applying laser light at specific areas, in particular the cancer tissue. This spatial control is available in addition to the ligand based targeting ability of our particles and should further reduce unintentional exposure of healthy cells to cancer therapeutics. Therefore, the selectivity of drug release should be enhanced in comparison to the cases where only the proton sponge effect or fusogenic/endosomolytic peptides are used.

8.3 Conclusions

In summary, we have developed a drug delivery system based on mesoporous silica nanoparticles that addresses some of the key issues in the field of drug delivery. These involve high selectivity and drug delivery with high efficacy. Furthermore, a combination of the high loading capacity of MSNs, the supported lipid bilayer for controlled release, the addition of targeting ligands, and overcoming of endosomal entrapment by photoactivation makes this system a potent drug delivery vehicle. Employing fluorescence microscopy, we were able to demonstrate the selective uptake of our nanoparticles by various cancer cell lines and the release of different cargos *in vitro*. Furthermore, we have demonstrated that the red-light-based photoactivation approach has many advantages compared to other approaches used in the field. In particular, by covalently linking the PS to the MSN surface and using a PS that can be excited by red light, negative side effects of the PS can be minimized, and activation of the PS *in vivo* is feasible. Moreover, photoactivation for cargo release enhances the spatial selectivity of where the drug is released as compared to using targeting ligands only. With this new system we have created a platform for drug delivery based on MSNs that is flexible regarding the loaded type of drug as well as regarding the employed targeting ligand (implying the desired cell type for drug delivery). We anticipate that the integration of all these strategies into one multifunctional drug delivery vehicle as well as the efficient synthesis and modification of the nanoparticles for multiple cell types will hold promise for wide-ranging applications, especially in cancer therapy.

8.4 Experimental

Chemicals. Tetraethyl orthosilicate (TEOS, Fluka, >99%), (3-mercaptopropyl)-triethoxysilane (MPTES, Gelest, 95%), (3-cyanopropyl)-triethoxysilane (CN-TES, ABCR, 98%), cetyltrimethylammonium chloride (CTAC, Fluka, 25 wt% in H_2O), triethanolamine (TEA, Aldrich, 98%), ammonium fluoride (NH_4F, Sigma, >98%), α,ω-bis-amino octa (ethylene glycol) (NH_2-PEGd8-NH_2, Iris Biotech), Al(III) phthalocyanine chloride disulfonic acid ($AlPcS_{2a}$, Frontier Scientific), ammonium nitrate (Sigma, 99%), conc. hydrochloric acid (Aldrich, >95%, 37 wt%), 1,3,5-triisopropylbenzene (TiPB, Fluka, 96%), sulfo-*N*-hydroxysuccinimide (sulfo-NHS, Aldrich, 98%), *N*-(3-dimethylaminopropyl)-*N*′-ethylcarbodiimide (EDC, Sigma, 97%), calcein (CAL, Sigma), dimethyl sulfoxide (DMSO, Sigma, >99.5%), ethanol (EtOH, Aldrich, >99.5%), 1,2-dioleoyl-sn-glycero-3-phosphocholine (DOPC, Avanti Polar Lipids), 1,2-distearoyl-sn-glycero-3-

phosphoethanolamine-*N*-[folate(polyethylene glycol)-2000] (ammonium salt) (DSPE-PEG_{2000}-FA, Avanti Polar Lipids), 1,2-distearoyl-sn-glycero-3-phosphoethanolamine-*N*-[maleimide(polyethylene glycol)-2000] (ammonium salt) (DSPE-PEG_{2000}-maleimide, Avanti Polar Lipids), 2-Iminothiolane hydrochloride (Traut's reagent, Sigma-Aldrich), 5(6)-Carboxy-X-rhodamine (RD, Sigma), Wheat germ agglutinin (WGA) Alexa Fluor 488 conjugate (Invitrogen), epidermal growth factor (EGF, PeproTech, >98%), Folic acid (FA, Sigma, >97%). All chemicals were used as received without further purification. Doubly distilled water from a Millipore system (Milli-Q Academic A10) was used for all synthesis and purification steps.

Synthesis of core-shell MSNs. Bi-functional core-shell colloidal mesoporous silica nanoparticles were synthesized according to a slightly modified published method.[12, 33] A mixture of TEOS (1.63 g, 9.22 mmol), MPTES (112 mg, 0.48 mmol) and TEA (14.3 g, 95.6 mmol) was heated under static conditions at 90 °C for 20 min in a polypropylene reactor. Then a solution of CTAC (25 wt% in water, 2.41 mL, 1.83 mmol), NH_4F (100 mg, 2.70 mmol) and TiPB (2.54 g, 12.4 mmol) in water (21.7 g, 1.21 mol) was preheated to 60 °C and added quickly. The reaction mixture was stirred vigorously (1000 rpm) at room temperature for 20 minutes. Subsequently TEOS (138.2 mg, 0.922 mmol) was added in four equal increments every three minutes. This step was followed by 30 minutes of stirring at room temperature. For the shell functionalization a mixture of TEOS (19.3 mg, 92.5 μmol) and CN-TES (21.4 mg, 92.5 μmol) was added to the reaction. The resulting mixture was then allowed to stir at room temperature for 12 h. After the addition of 100 mL ethanol, the MSNs were collected by centrifugation, redispersed in 100 mL of ethanol and extracted according to the procedure described below.

Extraction of MSNs. Extraction of the surfactant was performed by heating 250 mg of MSN for 45 minutes under reflux at 90 °C in a solution containing 2 g ammonium nitrate in 100 mL ethanol. This extraction step was performed twice. The template-free MSNs were separated by centrifugation and washed with ethanol after each extraction step. $MSN\_SH_{in}\_CN_{out}$ were obtained as colloidal suspension in EtOH.

Hydrolysis of MSNs containing cyano groups. 250 mg of $MSN\_SH_{in}\_CN_{out}$ in EtOH were collected by centrifugation and washed with H_2O once. The particles were re-dispersed in 10 mL H_2O and 30 mL hydrochloric acid (37 wt%) was added carefully. The reaction mixture was heated to reflux for 3 h. After cooling down, 20 mL H_2O were added and the synthesis

was stirred at room temperature overnight. The resulting colloidal suspension of $MSN\_SH_{in}\_COOH_{out}$ was diluted further with 100 mL H_2O, collected by centrifugation, and redispersed in 100 mL of water. This washing step was repeated twice with both water and ethanol. $MSN\_SH_{in}\_COOH_{out}$ were obtained as an ethanolic suspension.

PEGylation of MSNs. An ethanolic suspension containing 20 mg of $MSN\_SH_{in}\_COOH_{out}$ was centrifuged and redispersed in 60 mL of water. This washing step was repeated twice. EDC (0.85 µl, 4.6 µmol, 1.2 eq) was added at room temperature to a diluted suspension of $MSN\_SH_{in}\_COOH_{out}$ in 40 mL of water. The reaction mixture was stirred for 5 min before sulfo-NHS (1 mg, 4.6 µmol, 1.2 eq) was added. A second solution, containing bi-functional NH_2-PEGd8-NH_2 (7.05 mg, 19.2 µmol, 5 eq.) dissolved in 2 mL water was prepared. The EDC-activated $MSN\_SH_{in}\_COOH_{out}$ were added dropwise to the PEG containing solution. Afterwards, the pH was adjusted with two drops of hydrochloric acid (37 wt%) to a value pH < 7 and the reaction mixture was stirred for 12 h at ambient temperature. In order to remove the excess of the PEG-linker, the reaction mixture was washed five times with 30 mL of water to remove unbound PEG. All washing steps were followed by centrifugation. Finally, the sample $MSN\_SH_{in}\_PEGd8NH_{2out}$ was re-dispersed in 10 mL ethanol.

Attachment of PS. 1 mg of $MSN\_SH_{in}\_PEGd8NH_{2out}$ in ethanolic solution was centrifuged and resuspended in a 500 µL water/DMSO mixture (2:1). Subsequently, 40 µL of an $AlPCS_{2a}$ stock solution (2 mg in 1 mL DMSO) were added to the MSNs. The reaction mixture was stirred in the dark at room temperature for 72 h. The resulting $MSN\_SH_{in}\_PEGd8\text{-}AlPcS_{2aout}$ were extensively washed by centrifugation with water/DMSO (1:1) in order to remove excess photosensitizer. In order to remove DMSO from the mesopores the sample was washed three times with water after no free PS could be detected. The colloidal solution of sample $MSN\_SH_{in}\_PEGd8\text{-}AlPcS_{2aout}$ was used for further experiments immediately.

Cargo loading. 0.5 mg of the sample $MSN\_SH_{in}\_PEGd8\text{-}AlPcS_{2aout}$ in ethanol were centrifuged and redispersed in 1 mL water. This washing step was repeated twice. Then, the suspension was centrifuged again and redispersed in 500 µL calcein in water (1 mM stock solution in water) or RD (1 mM stock solution in water), respectively. The mixture was stirred over night in the dark yielding the sample $MSN\_CARGO_{in}\_PEGd8\text{-}AlPcS_{2aout}$.

SLB formation. 0.5 mg of $MSN\_CARGO_{in}\_PEGd8\text{-}AlPcS_{2aout}$ in 1 mL dye solution were centrifuged (14000 rpm, 4 min) and the supernatant discarded. Afterwards, a mixture of 70 µL DOPC and 30 µL DOTAP (each 2.5 mg/mL in 60:40 H_2O:EtOH) were added to the resulting pellet, mixed extensively, and sonicated for 10 s. To form the supported lipid bilayer

around the MSNs via solvent exchange method, 700 µL of water were added. The resulting suspension was mixed and sonicated for 10 s, yielding DOPC/DOTAP@MSN_CARGO$_{in}$_PEGd8-AlPcS$_{2aout}$.

TL incorporation. 0.5 mg of DOPC/DOTAP@MSN_CARGO$_{in}$_PEGd8-AlPcS$_{2aout}$ in 800 µl water were incubated with 6 µL of DSPE-PEG$_{2000}$-TL for 3 h (for DSPE-PEG$_{2000}$-Folate) and 12 h respectively (for DSPEPEG$_{2000}$-EGF) at 37 °C. The resulting sample DOPC/DOTAP@MSN_CARGO$_{in}$_PEGd8-AlPcS$_{2aout}$-TL was used without further purification for confocal microscopy studies.

Cargo release experiments. Fluorescence time-based release experiments were recorded on a PTI fluorescence system featuring a PTI 814 photomultiplier detector and a PTI A1010B Xenon arclamp driven by a PTI LPS-220B lamp power supply. For temperature settings, a Quantum Northwest TC 125 sample holder was used. Our previously described custom-made release cuvette system was used for all experiments.[26] All samples were measured at a temperature of 37 °C with slits of 2/2/2/2. For RD an excitation wavelength of 575 nm was used (emission maximum at 597 nm), whereas calcein was excited with 495 nm and with an emission maximum at 516 nm. Results are given in Figure 6. For all experiments, 0.5 mg of DOPC/DOTAP@MSN_CARGO$_{in}$_PEGd8-AlPcS$_{2aout}$ was used. 200 µL of the particle suspension was filled into the reservoir cap sealed with a dialysis membrane (Molecular weight cut-off 14000 g/mol) allowing released dye molecules to pass into the fluorescence cuvette. In order to monitor the release of adsorbed dyes upon membrane rupture with singlet oxygen, the sample was excited with 0,56 W/mm^2 of 633 nm light for 1 minute prior the measurement. For triton mediated release, 5 µL of a 1 mM stock solution of TritonX100 was added to the particle solution.

Characterization. All samples were investigated with a FEI Titan 80-300 operating at 300 kV with a high-angle annular dark field detector. A droplet of the diluted MSN solution in ethanol absolute was dried on a carbon-coated copper grid. Nitrogen sorption measurements were performed on a Quantachrome Instruments NOVA 4000e. All four samples (15 mg each) were heated to 393 K for 12 h in vacuum (10 mTorr) to outgas the samples before nitrogen sorption was measured at 77 K. For calculations of pore sizes and volumes a non-local density functional theory (NLDFT) equilibrium model of nitrogen on silica was used. Dynamic light scattering (DLS) measurements were performed on a Malvern Zetasizer-Nano instrument equipped with a 4 mW He-Ne laser (633 nm) and an avalanche

photodiode. The hydrodynamic radius of the particles was determined by dynamic light scattering in ethanolic suspension. For this purpose, 100 µL of an ethanolic suspension of MSN particles (ca. 10 mg/mL) was diluted with 3 mL of ethanol prior to the measurement. Zeta potential measurements of the samples were performed on a Malvern Zetasizer-Nano instrument equipped with a 4 mW He-Ne laser (633 nm) and an avalanche photodiode. For determination of the zeta potential curves, two drops of the ethanolic MSN suspension (~ 3 %wt.) was mixed with 1 mL commercial Hydrion Buffer solution of the appropriate pH prior to measurement. IR measurements were performed on a Bruker Equinox 55 FTIR/FTNIR Spectrometer in absorbance mode (spectra were background substracted). Thermogravimetric analysis of the bulk samples MSN_SH_{in}_CN_{out}, MSN_SH_{in}_$COOH_{out}$, MSN_SH_{in}_PEGd8NH_{2out} and MSN_SH_{in}_PEGd8-$AlPcS_{2aout}$ was performed on a Netzsch STA 440 C TG/DSC with a heating rate of 10 K/min in a stream of synthetic air of about 25 mL/min. The mass was normalized to 100% at 133.8 °C for all samples. Cross-polarized ^{13}C solid-state NMR (ssNMR) measurements were performed on a Bruker DSX Avance500 FT spectrometer in a 4 mm ZrO_2 rotor. The spinning rate was 10 kHz and a total number of up to 8000 scans were recorded.

Cell culture. KB cells were grown in folic acid deficient Roswell Park Memorial Institute 1640 medium (RPMI 1640, Invitrogen) supplemented with 10% FCS at 37 °C in a 5% CO_2 humidified atmosphere. The cells were seeded on ibidiTreat µ-Slide (IBIDI). HuH7 cells were grown in Dulbecco's modified Eagle's medium (DMEM):F12 (1:1) (Invitrogen) medium supplemented with 10% fetal bovineserum (FBS) at 37 °C in a 5% CO_2 humidified atmosphere. To reduce autofluorescence of the cells, the medium was changed to DMEM:F12(Invitrogen) supplemented with 10% B-27 two days before seeding. The cells were seeded on collagen A-coated LabTek chambered cover glass (Nunc). HeLa cells were grown in Dulbecco's modified Eagle's medium (DMEM):F12 (1:1) (Invitrogen) with Glutamax I medium supplemented with 10% fetal bovineserum (FBS) at 37 °C in a 5% CO_2 humidified atmosphere. The cells were seeded on collagen A-coated LabTek chambered cover glass (Nunc). For live cell imaging the cells were seeded 24 or 48 h before measuring, at a cell density of 2x104 or 1x104 cells/cm^2.

Uptake studies. To evaluate the functionality of the folic acid ligand, KB cells were incubated with nanoparticles for 3 h at 37 °C under a 5% CO_2 humidified atmosphere. In the case of live cell imaging the cell membrane was stained afterwards by adding 4 µL of 1 mg/mL wheat germ agglutinin Alexa Fluor 488 or 633 conjugate (WGA488, WGA633,

Invitrogen) to 400 µL of cell medium. After 1 min, the cell medium was removed, the cells were washed twice with cell medium, and imaged immediately. In the case of fixed cells the cells were washed three times after the 3 h incubation time with PBS (Invitrogen). Afterwards 200 µL of 4% paraformaldehyde (PFA, Science Service) were added for 15 minutes. After removing PFA the cells were washed three times with PBS and stained by adding 4 µL of 1 mg/mL WGA 488 to 400 µL of PBS. After 1 min the cell medium was removed, the cells were washed twice with PBS and imaged. In control experiments, the FA receptors on the KB surface were blocked by pre-incubation of the cells with 3 mM folic acid (Sigma) for 2 h at 37 °C under a 5% CO_2 humidified atmosphere, before particle were added. In the case of EGF, HuH7 cells with GFP tagged tubulin were used in addition to staining the cell membrane. In the case of HuH7 tubulin the cell medium was exchanged with CO_2-independent medium (Invitrogen) and imaged immediately after incubation with cells. After incubation with nanoparticles, the cell medium was exchanged with CO_2-independent medium (Invitrogen) and imaged immediately. The wildtype HuH7 cells were treated equivalent to the live cell imaging of the KB cells. For the control experiments, EGF receptors on the HuH7 surface were saturated by pre-incubating the cells with 0.2 µM EGF (PeproTech, >98%) for 2 h at 37 °C under a 5% CO_2 humidified atmosphere, before particle addition.

Cargo release experiments. Cells were incubated 16 – 22 h prior to the measurements at 37 °C under a 5% CO_2 humidified atmosphere. Shortly before imaging, the medium was replaced by CO_2-independent medium (Invitrogen). During the measurements all cells were kept on a heated microscope stage at 37 °C. The photosensitizer $AlPcS_{2a}$ was activated by 1.2 W/mm^2 of 639 nm light for 1 min. The subsequent imaging was performed as described in the Spinning disk confocal microscopy section.

Spinning disc confocal microscopy. Confocal microscopy for live-cell imaging was performed on a setup based on the Zeiss Cell Observer SD utilizing a Yokogawa spinning disk unit CSU-X1. The system was equipped with a 1.40 NA 100x Plan apochromat oil immersion objective from Zeiss. For all experiments the exposure time was 0.1 s and the frame rate varied between 3 frames/s and 1 frame/30s, depending on the specific requirements of the experiment. Calcein and WGA488 were imaged with approximately 0.4 W/mm^2 of 488 nm excitation light. The rhodamine derivative (RD) was excited with 1.2 W/mm^2 of 561 nm light. $AlPcS_{2a}$ was excited with 0.12 W/mm^2 of 639 nm for imaging and for photoactivation with 1.2 W/mm^2. In the excitation path a quad-edge dichroic beamsplitter

(FF410/504/582/669-Di01-25x36, Semrock) was used. For two color detection of calcein and $AlPcS_{2a}$ and accordingly WGA 488 and $AlPcS_{2a}$, a dichroic mirror (660 nm, Semrock) and band-pass filters 525/50 and 690/60 (both Semrock) were used in the detection path. In case of RD a band-pass filter 629/60 (Semrock) was used. Separate images for each fluorescence channel were acquired using two separate electron multiplier charge coupled devices (EMCCD) cameras (PhotometricsEvolveTM).

8.5 References

[1] D. W. Pack, A. S. Hoffman, S. Pun, P. S. Stayton, *Nat. Rev. Drug. Discovery* **2005**, *4*, 581.

[2] T. Fröhlich, E. Wagner, *Soft Matter* **2010**, *6*, 226.

[3] K. Miyata, N. Nishiyama, K. Kataoka, *Chem. Soc. Rev.* **2012**, *41*, 2562.

[4] E. R. Gillies, J. M. J. Frechet, *Drug Discovery Today* **2005**, *10*, 35.

[5] S. Svenson, D. A. Tomalia, *Adv. Drug Delivery Rev.* **2005**, *57*, 2106.

[6] C. C. Lee, J. A. MacKay, J. M. J. Frechet, F. C. Szoka, *Nat. Biotechnol.* **2005**, *23*, 1517.

[7] P. Ghosh, G. Han, M. De, C. K. Kim, V. M. Rotello, *Adv. Drug Delivery Rev.* **2008**, *60*, 1307.

[8] J. L. Vivero-Escoto, I. I. Slowing, B. G. Trewyn, V. S. Y. Lin, *Small* **2010**, *6*, 1952.

[9] J. M. Rosenholm, A. Meinander, E. Peuhu, R. Niemi, J. E. Eriksson, C. Sahlgren, M. Linden, *ACS Nano* **2009**, *3*, 197.

[10] M. Liong, J. Lu, M. Kovochich, T. Xia, S. G. Ruehm, A. E. Nel, F. Tamanoi, J. I. Zink, *ACS Nano* **2008**, *2*, 889.

[11] V. Cauda, H. Engelke, A. Sauer, D. Arcizet, C. Bräuchle, J. Rädler, T. Bein, *Nano Lett.* **2010**, *10*, 2484.

[12] J. Kecht, A. Schlossbauer, T. Bein, *Chem. Mater.* **2008**, *20*, 7207.

[13] A. M. Sauer, A. Schlossbauer, N. Ruthardt, V. Cauda, T. Bein, C. Bräuchle, *Nano Lett.* **2010**, *10*, 3684.

[14] A. Schlossbauer, A. M. Sauer, V. Cauda, A. Schmidt, H. Engelke, U. Rothbauer, K. Zolghadr, H. Leonhardt, C. Bräuchle, T. Bein, *Adv. Healthcare Mater.* **2012**, *1*, 316.

[15] J. P. Behr, *Chimia* **1997**, *51*, 34.

[16] N. D. Sonawane, F. C. Szoka, A. S. Verkman, *J. Biol. Chem.* **2003**, *278*, 44826.

[17] H. R. Marsden, N. A. Elbers, P. H. H. Bomans, N. Sommerdijk, A. Kros, *Angew. Chem. Int. Ed.* **2009**, *48*, 2330.

[18] C. E. Ashley, E. C. Carnes, G. K. Phillips, D. Padilla, P. N. Durfee, P. A. Brown, T. N. Hanna, J. W. Liu, B. Phillips, M. B. Carter, N. J. Carroll, X. M. Jiang, D. R. Dunphy, C. L. Willman, D. N. Petsev, D. G. Evans, A. N. Parikh, B. Chackerian, W. Wharton, D. S. Peabody, C. J. Brinker, *Nat. Mater.* **2011**, *10*, 389.

[19] C. E. Ashley, E. C. Carnes, K. E. Epler, D. P. Padilla, G. K. Phillips, R. E. Castillo, D. C. Wilkinson, B. S. Wilkinson, C. A. Burgard, R. M. Kalinich, J. L. Townson, B. Chackerian, C. L. Willman, D. S. Peabody, W. Wharton, C. J. Brinker, *ACS Nano* **2012**, *6*, 2174.

[20] M. Meyer, C. Dohmen, A. Philipp, D. Kiener, G. Maiwald, C. Scheu, M. Ogris, E. Wagner, *Mol. Pharmaceutics* **2009**, *6*, 752.

[21] A. Schlossbauer, C. Dohmen, D. Schaffert, E. Wagner, T. Bein, *Angew. Chem. Int. Ed.* **2011**, *50*, 6828.

[22] A. K. Varkouhi, M. Scholte, G. Storm, H. J. Haisma, *J. Control. Rel.* **2011**, *151*, 220.

[23] R. R. Anderson, J. A. Parrish, *J. Investig. Dermatol.* **1981**, *77*, 13.

[24] N. Nishiyama, A. Iriyama, W. D. Jang, K. Miyata, K. Itaka, Y. Inoue, H. Takahashi, Y. Yanagi, Y. Tamaki, H. Koyama, K. Kataoka, *Nat. Mater.* **2005**, *4*, 934.

[25] V. Cauda, C. Argyo, T. Bein, *J. Mater. Chem.* **2010**, *20*, 8693.

[26] A. Schlossbauer, J. Kecht, T. Bein, *Angew. Chem. Int. Ed.* **2009**, *48*, 3092.

[27] C. A. Ladino, R. V. J. Chari, L. A. Bourret, N. L. Kedersha, V. S. Goldmacher, *Int. J. Cancer* **1997**, *73*, 859.

[28] Y. H. Xu, N. Richert, S. Ito, G. T. Merlino, I. Pastan, *Proc. Natl. Acad. Sci. U.S.A.* **1984**, *81*, 7308.

[29] F. M. Mickler, L. Möckl, N. Ruthardt, M. Ogris, E. Wagner, C. Bräuchle, *Nano Lett.* **2012**, *12*, 3417.

[30] S. Febvay, D. M. Marini, A. M. Belcher, D. E. Clapham, *Nano Lett.* **2010**, *10*, 2211.

[31] H. Mojzisova, S. Bonneau, D. Brault, *Eur. Biophys. J.* **2007**, *36*, 943.

[32] K. I. Salokhiddinov, I. M. Byteva, G. P. Gurinovich, *J. Appl. Spectrosc.* **1981**, *34*, 561.

[33] L. Cao, M. Kruk, *Colloids Surf., A* **2010**, *357*, 91.

9 Investigation of the Endosomal Escape via the Proton Sponge Effect with Dendron-Functionalized Mesoporous Silica Nanoparticles

This chapter is based on work in cooperation with:

Veronika Weiss, Stephan Mackowiak, Tim Gatzenmeier, Christoph Bräuchle, and Thomas Bein.

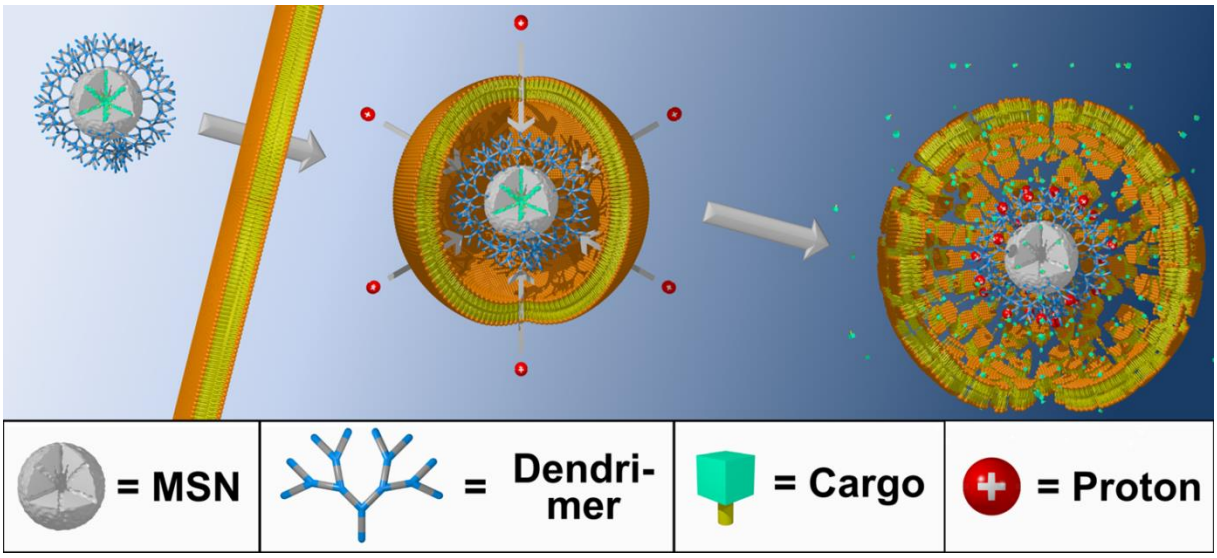

9.1 Introduction

Nano-sized drug delivery systems such as multifunctional mesoporous silica nanoparticles (MSNs) encounter many challenges on their way towards selectively reaching their desired target and efficiently release their cargos at the desired location. In particular, endosomal entrapment is a major obstacle for efficient drug and cargo delivery, faced by MSNs and other nanocarrier systems that are internalized by cells via endocytosis.[1-3] Especially for non-membrane permeable or immobilized cargo molecules, the nanocarriers need to enter the cytosol for an efficient delivery to the targeted cell compartments, such as nucleus, mitochondria or the microtubule network. Several strategies have already been described to address the demanding task of endosomal escape, including pore formation, membrane fusion, photoactivated endosomal membrane rupture, and the proton sponge effect.[4-7] Recently, the issue of endosomal entrapment has been addressed in a joint project of the groups of Bräuchle, Bein and coworkers showing no efficient cytosolic delivery of the cargo

cysteine after endocytosis from multifunctional MSNs designed for a redox-driven disulfide cleavage-based drug release system.[1] In order to overcome this barrier, photo-induced endosomal release via excitation of co-incubated photosensitizer molecules was employed, causing rupture of the endosomal membrane upon singlet oxygen generation. Compared to the photoactivation pathway needing an external stimulus to cause endosomal escape, the proton sponge effect could be an alternative promising "automatic" strategy for endosomal release of the nanocarriers. The mechanism of the proton sponge effect follows an intrinsic osmotic swelling caused by the buffering capacity of modified nanocarriers and finally results in rupture of the endosomal membrane.[8] The intracellular trafficking of endosomal vesicles to become late endosomes or endolysosomes leads to an acidification of the endosomal compartment by proton pumps (H^+-ATPase) causing a decrease of the internal pH value from 7.4 to 5.5.[9] Investigation of diverse cationic lipids and polymers such as poly (ethyleneimine) (PEI) showed their substantial buffering capacity below the physiological pH.[10-11] After endocytosis, such polymers or particles act like a proton trap preventing a drop in pH.[12] The buffering capacity of these species leads to a continuous inflow of protons driven by the proton pumps, coupled with a passive influx of chloride anions to maintain electrical neutrality within the compartment. Subsequently, osmotic swelling and ultimately rupture of the endosomal membrane is caused by the substantial increase of the ionic concentration within the endosome. Several cationic polymers with high buffering capacities have been examined as potential proton sponges, whereupon poly(amidoamine) (PAMAM) dendron structures have attracted great interest due to their high amino group content, simple and variable synthesis as well as biomimetic structure.[13-16] Dendrons represent a structural component of a parent dendrimer structure that are highly ordered, monodisperse, three-dimensional, tree-like polymers comprising specific size and shape characteristics.[17] Due to their high positive surface charge at physiological pH, PAMAM dendrimers also form stable complexes with DNA. *In vivo* experiments demonstrated that the use of high PAMAM dendrimer generations (G7-10) as transfection agent for DNA is highly efficient.[18-19] The resulting transfection was explicitly attributed to an activated proton sponge mechanism. Experiments on PAMAM-coating of carbon nanotubes further indicate that PAMAM structures are beneficial for cellular uptake and provide a reduction of cytotoxicity of carbon nanotubes.[20] Lin and co-workers investigated a gene transfection nanocarrier system based on MCM-41-type mesoporous silica nanospheres containing covalently attached second

generation (G2) PAMAM dendrimers.[21] An intracellular delivery of plasmid-DNA complexed by the PAMAM dendrimers could be observed. In recent years, MSNs have been intensively utilized as drug delivery vehicles, due to their excellent material features such as good biocompatibility, large capacity of its mesoporous system and efficient attachment of organic surface functionalization or targeting ligands.[22-27]

In the present work, we have established newly designed multifunctional core-shell MSNs coated with poly(amidoamine) (PAMAM) dendron structures on the outer surface which feature a high buffering capacity, acting as a pH-dependent intrinsic endosomal escape mechanism *via* the proton sponge effect. Covalent binding sites (mercapto groups) located exclusively inside the mesopores can form disulfide bridges for immobilization for cargo molecules. Subsequently, this nanocarrier system offers controlled cargo release upon redox-driven cleavage of disulfide bridges when entering the reductive milieu of the cytosol. Further attachment of the targeting ligand folate at the outer dendron periphery of the nanocarriers provide specific receptor-mediated cellular uptake. The targeting efficiency of folate molecules has been extensively investigated by many research groups.[28-30] Folate specifically binds to the folate receptor FR-α, which is overexpressed on many cancer cell lines, including HeLa and KB cells, while only minimally present in healthy tissue.[5, 31-32] Our nanocarrier system can be modified at the very last synthesis stage with various ligands for specific targeting of cancer cells. It is anticipated that the combination of all these important requirements for an efficient drug delivery makes the mesoporous silica nanocarriers a promising platform for specific cancer therapy.

9.2 Results and Discussion

The synthesis of PAMAM dendron-coated MSNs was carried out in three steps. First, propargyl-PAMAM dendrons were obtained in three different generations (D1, D2, and D3) by iterative steps of Michael additions and amidations following a previously described procedure.[33] The synthetic route comprising alternating use of the reagents methyl acrylate and 1,2-ethylenediamine for a stepwise creation of increasing PAMAM dendron generations is shown in Figure 9.1.

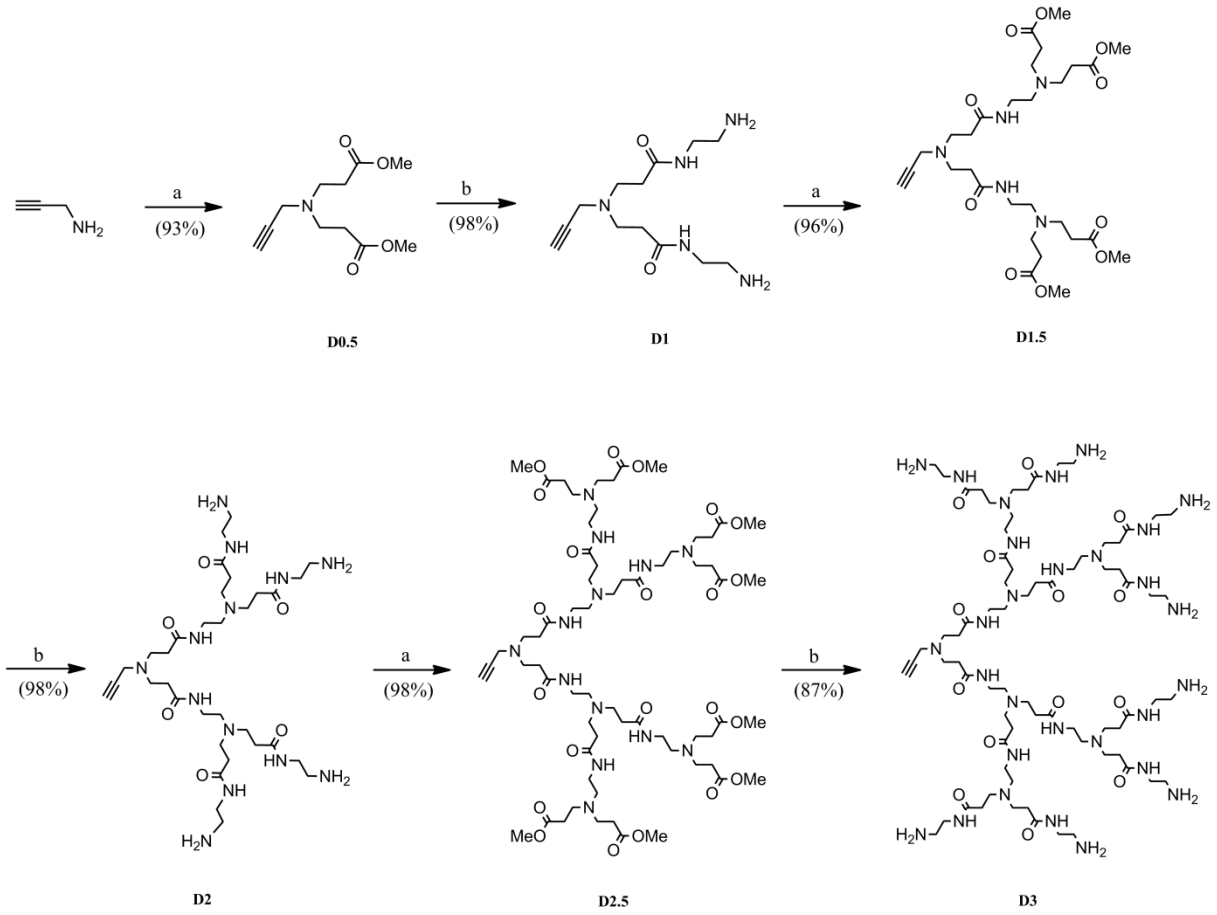

Figure 9.1: Synthesis of propargyl-PAMAM dendrons (D0.5 – D3). Reagents and reaction conditions: a) methyl acrylate (large excess), MeOH, 0 → 25 °C, 48 h and b) 1,2-ethylenediamine (large excess), MeOH, 0 → 25 °C, 48 h.

For a convergent synthesis route to covalently attach the PAMAM dendrons at the external MSN surface, a PAMAM dendron silane precursor was synthesized in a second step. Three PAMAM dendron silanes were synthesized by performing a Huisgen click reaction to attach azidopropyl trimethoxysilane to the propargyl-PAMAM dendrons. According to a previous report,[34] the azidopropyl trimethoxysilane was synthesized and subsequently reacted with alkyne-PAMAM dendrons to gain triazole-linked PAMAM moieties by using azide-alkyne click chemistry. Successful conversion was observed by IR spectroscopy (cf. Appendix 9.5). In a last step, this silane linker was used in a delayed co-condensation approach to create core-shell functionalized MSNs via a sol-gel process, as described previously.[23, 25] In brief, tetraethyl orthosilicate (TEOS) was used as a silica source and cetyltrimethylammonium chloride (CTAC) as template. The silica framework formation was catalyzed by the base triethanolamine (TEA), which also served as a structure directing agent to result in colloidal

silica nanoparticles. Specifically, three different bifunctional MSNs (MSN-SH_{IN}-Dn_{OUT}, n = 1-3) equipped with different dendron generations (D1, D2 and D3) on the external surface were prepared via a delayed co-condensation approach. The MSNs consisted of a thiol-functionalized particle core, and additionally PAMAM dendrons were exclusively present on the outer particle surface. For all resulting MSN samples, the nitrogen sorption measurements showed type IV isotherms indicating a mesoporous structure of the nanoparticles with typical inflection points at about 0.3 p/p_0 (Figure 9.2a).

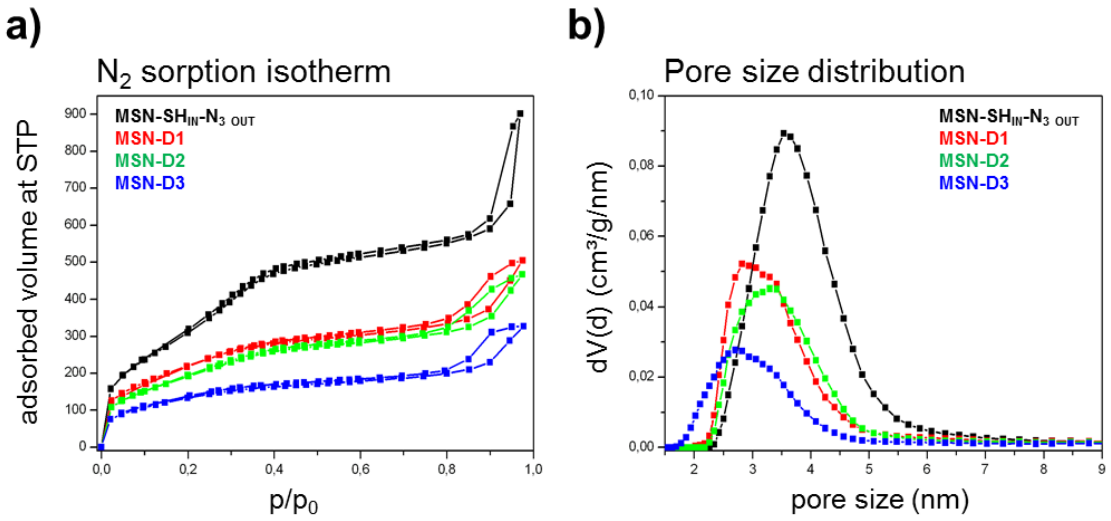

Figure 9.2: a) Nitrogen sorption isotherms and b) DFT pore size distributions of functionalized MSNs. MSN-SH_{IN}-$N_{3\ OUT}$ (black), MSN-D1 (red), MSN-D2 (green), and MSN-D3 (blue).

At higher partial pressures (about 0.9 p/p_0) a second hysteresis loop arose for all samples, which we attribute to interparticle textural porosity. For the reference sample MSN-SH_{IN}-$N_{3\ OUT}$ a relatively high BET surface area and pore volume was observed (data summarized in Table 9.1). For all PAMAM dendron-coated MSNs these structural parameters decreased depending on the size of the dendrons. This effect was partially due to the increasing sample mass by addition of the non-porous organic polymer. Furthermore, large PAMAM dendron generations might have caused clogging of some pore entrances towards to access of nitrogen molecules at the low measurement temperatures (-196 °C). A slight average pore constriction could also be observed, which correlates with the size of the attached PAMAM structures. This decrease could be due to the reduction of the pore mouth diameters partially covered by frozen organic PAMAM moieties. Nevertheless, PAMAM dendron-coated MSNs still exhibited a large accessible mesoporous structure offering enough space for the incorporation of cargo molecules.

Table 9.1: Structural parameter of functionalized MSNs.

Sample	BET surface area (m^2/g)	Pore volume[a] (m^3/g)	DFT pore size[b] (nm)
MSN-SH_{IN}-$N_{3\ OUT}$	1190	0.74	2.9 – 4.4
MSN-D1	823	0.42	2.5 – 3.9
MSN-D2	718	0.39	2.6 – 4.1
MSN-D3	497	0.24	2.2 – 3.8

[a]Pore volume is calculated up to a pore size of 8 nm to remove the contribution of interparticle porosity.
[b]DFT pore size refers to FWHM of the corresponding pore size distribution.

Transmission electron microscopy shows spherically shaped nanoparticles with sizes of about 70 nm in diameter for PAMAM dendron-coated MSNs (Figure 9.3c, MSN-D3). A worm-like porous structure consisting of radially grown mesoporous channels was present for all samples. Additionally, dynamic light scattering (DLS) measurements were performed to determine particle sizes for all samples; the particle size distributions are shown in Figure 9.3a. All samples featured narrow size distributions with an average particle size of about 122 nm. The size difference between TEM and DLS data is attributed to a tendency for weak agglomeration in solution. Summarizing, the above data confirm the formation of well-defined mesoporous nanoparticles with good colloidal stability in aqueous solution.

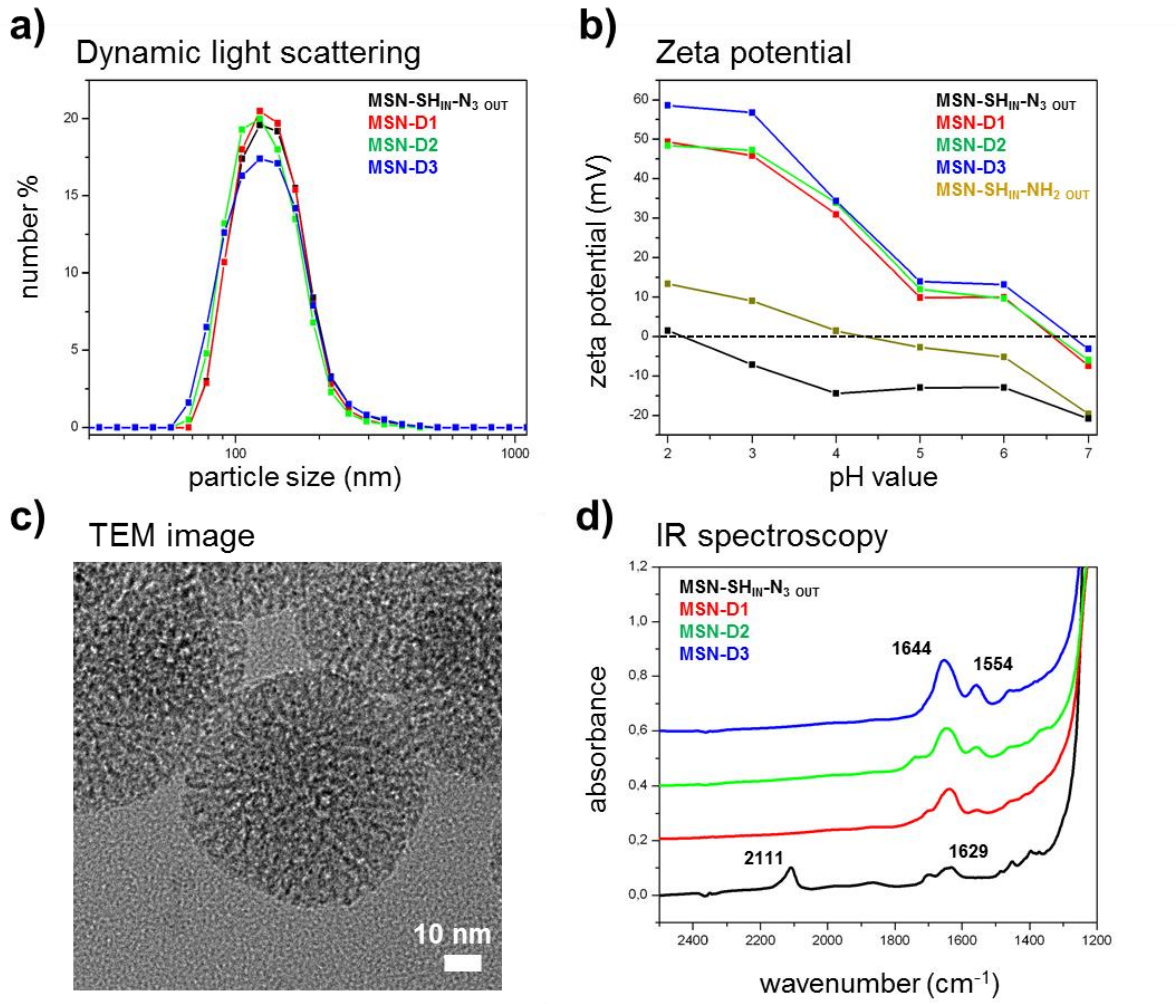

Figure 9.3: a) Dynamic light scattering (DLS) measurements, b) zeta potential measurements, c) transmission electron micrograph, and d) IR spectroscopy of functionalized MSNs. MSN-SH_{IN}-$N_{3\ OUT}$ (black), MSN-D1 (red), MSN-D2 (green), MSN-D3 (blue), and MSN-SH_{IN}-$NH_{2\ OUT}$ (brown). The TEM image shows MSN-D3. For clarity reasons, the IR spectra are shifted along the y-axis by 0.2 units.

Zeta potential measurements showed drastic changes in the surface charge of PAMAM dendron-coated MSNs (Figure 9.3b). At acidic pH values, highly positive surface charges were observed for all three samples containing PAMAM dendrons at the outer particle surface. A zeta potential of about +60 mV at pH 2 was obtained for the sample MSN-D3 consisting of the largest PAMAM generation. This sample exhibited the highest amino group content leading to a highly positively charged particle surface. The samples MSN-D1 and MSN-D2 showed slightly smaller zeta potential values (about +50 mV at pH 2). Both samples showed an almost identical zeta potential curve in acidic milieu. This suggests that the content of accessible amino groups on the periphery of both particle types was nearly identical. It is reasonable to expect a higher density of 1st generation PAMAM dendrons on the external particle surface compared to the more bulky 2nd generation due to steric hindrance of the

larger molecules. Nevertheless, the PAMAM dendron-coated MSNs showed a significant difference of the zeta potential values compared to the reference sample MSN-SH_{IN}-$N_{3\ OUT}$. Here, the isoelectric point (IEP) was close to pH 2 which resulted in a negatively charged particle surface over the pH range measured. Furthermore, MSNs functionalized with aminopropyl groups (MSN-SH_{IN}-$NH_{2\ OUT}$) featured only slightly positive surface charge with an IEP of about 4.2. The IEPs for the PAMAM-derived particles were significantly shifted to higher pH values (about 6.7). These highly positively charged particle surfaces in acidic milieu gave evidence for a high proton acceptor density of the polymer shells resulting in a high buffering capacity. For further investigation of the buffering capacity of PAMAM dendron-coated MSNs, all samples were titrated against an aqueous solution of NaOH (0.01 M). As depicted in Figure 9.4, PAMAM-derived samples featured a significant increase in the required volume of NaOH solution to be neutralized (pH 7). This suggested a high tendency for proton uptake, and a stepwise increase in buffering capacity was observed for higher PAMAM dendron generations. MSN-D3 provided great potential to act like a proton sponge showing optimal buffering effect at around pH 6 which perfectly fits the endosomal acidification range. In general, a high buffering capacity in the physiological range (pH 5 – 7) is desirable to enable endosomal release via the proton sponge mechanism. For PAMAM dendrimer or dendron structures, the buffering capacity is mainly provided by the tertiary amino groups.[13, 35]

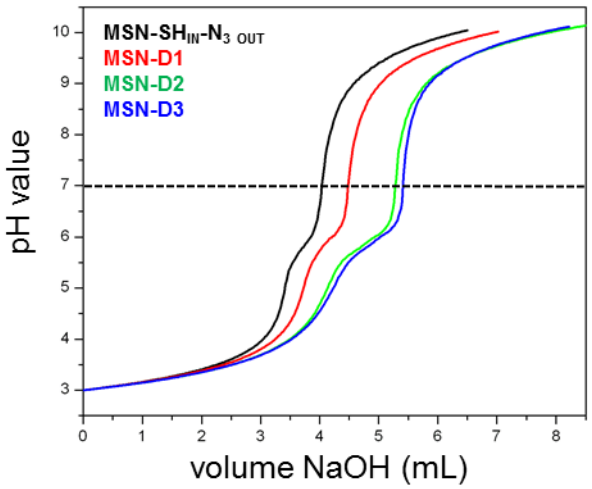

Figure 9.4: Titration data of functionalized MSNs. MSN-SH_{IN}-$N_{3\ OUT}$ (black), MSN-D1 (red), MSN-D2 (green), and MSN-D3 (blue). Quantitative data are given in the experimental part.

CHN elemental analysis provided quantitative information about the degree of organic functionalization of the modified MSNs. The data are shown in Table 9.2 (aminopropyl functionalized MSNs (MSN-SH_{IN}-$NH_{2\ OUT}$) have been used as a reference). The nitrogen content (wt% N) of the samples correlates with the amount of PAMAM functionalization A stepwise increase in nitrogen content for samples with increasing PAMAM generations was observed. Furthermore, the measured values for all PAMAM dendron coated MSNs were significantly higher compared to the reference samples MSN-SH_{IN}-$N_{3\ OUT}$ and MSN-SH_{IN}-$NH_{2\ OUT}$. These high nitrogen contents are the basis for a high protonation level in acidic milieu.

Table 9.2.: CHN elemental analysis data for functionalized MSNs.

Sample	MSN-SH_{IN}-$N_{3\ OUT}$	MSN-D1	MSN-D2	MSN-D3	MSN-SH_{IN}-$NH_{2\ OUT}$
wt% N	0.860	1.42	2.09	2.47	0.350

Organic functional groups present on the MSNs were examined with IR spectroscopy (Figure 9.3, for full range IR spectra see also Appendix 9.5). All samples featured typical bands of the silica framework appearing at 1240 – 1050 cm^{-1} (asymmetric stretching vibration of Si-O-Si), and at 964 and 796 cm^{-1} (asymmetric bending and stretching vibration of Si-OH). The reference sample MSN-SH_{IN}-$N_{3\ OUT}$ showed a characteristic signal at 2111 cm^{-1}, which was related to the azide vibration mode (asymmetric stretching vibration of $–N=N^{+}=N^{-}$). Additionally, a band at 1629 cm^{-1} indicated the bending modes of physisorbed water. This band was present in all spectra but was partially covered by other, more intensive bands for the PAMAM dendron-coated particles. The nanoparticles MSN-D1, MSN-D2 and MSN-D3 showed two additional bands at 1644 cm^{-1} (C=O stretching vibration) and 1554 cm^{-1} (N-H deformation and C-N stretching vibration) which were attributed to the amide bonds of the PAMAM dendron moieties. An increase in intensity of these signals was observed with increasing PAMAM dendron generations indicating increasing amounts of functional groups within the samples. Further characterization of the attached functional groups was performed by ^{13}C solid state NMR spectroscopy (Figure 9.5). MSN-SH_{IN}-$N_{3\ OUT}$ showed distinct signals for the propyl chains of the mercaptopropyl- and azidopropyl-moieties (which have been incorporated into the silica framework during the co-condensation approach) at 53 ppm (a, -$\underline{C}H_2$-N_3), 27 ppm (b, -$\underline{C}H_2$-SH), 22 ppm (c, CH_2-$\underline{C}H_2$-CH_2-), and 10 ppm (d, Si-$\underline{C}H_2$-).

Additional peaks of high intensity at 58 ppm (e, O-$\underline{C}H_2$-CH_3) and 15 ppm (f, O-CH_2-$\underline{C}H_3$) were present in all samples and were attributed to surface-bound ethoxy groups resulting from the extraction steps in ethanolic solution. PAMAM dendron functionalized MSNs featured characteristic peaks for the amide groups of the PAMAM dendrons at 173 ppm (g, C=O). Furthermore, weak signals at 144 ppm (h) and 125 ppm (i) were observed, these are attributed to the two carbon atoms in the triazole ring, thus providing evidence for a successful click reaction of the PAMAM dendron silane precursor. Several strong signals in the range between 60 to 10 ppm correspond to different types of methylene groups belonging to the PAMAM moieties (52 and 40 ppm (k and l, N-$\underline{C}H_2$-R), 21 and 10 ppm (m and n, R-$\underline{C}H_2$-R)).

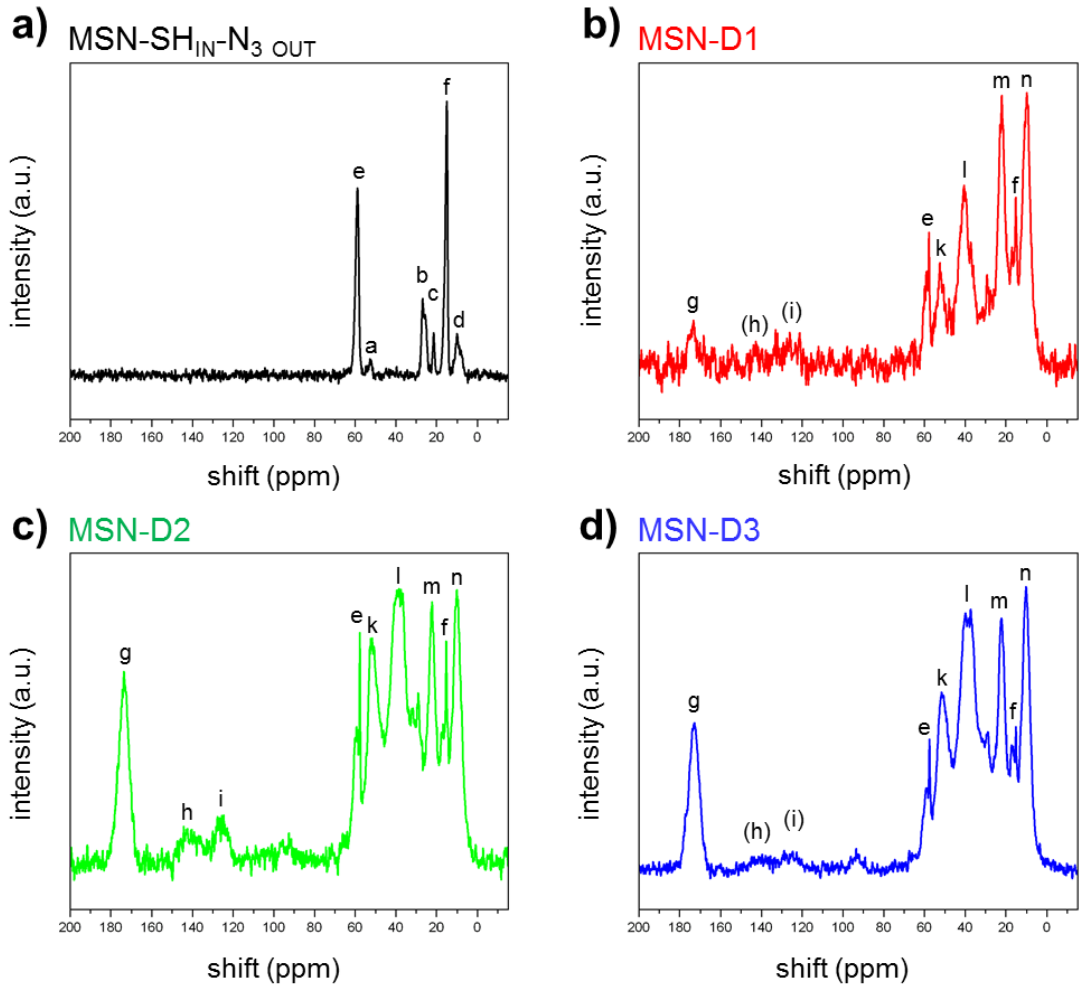

Figure 9.5: ^{13}C solid state NMR spectra of functionalized MSNs. a) MSN-SH$_{IN}$-N$_{3\ OUT}$ (black), b) MSN-D1 (red), c) MSN-D2 (green), and d) MSN-D3 (blue). a refers to -$\underline{C}H_2$-N_3 (53 ppm), b to -$\underline{C}H_2$-SH (27 ppm), c to CH_2-$\underline{C}H_2$-CH_2- (22 ppm), d to Si-$\underline{C}H_2$- (10 ppm), e to O-$\underline{C}H_2$-CH_3 (58 ppm), f to O-CH_2-$\underline{C}H_3$ (15 ppm), g to C=O (173 ppm), h and i to carbon atoms of the triazole ring (144 and 125 ppm, respectively), k and l to N-$\underline{C}H_2$-R) (52 and 40 ppm, respectively), and m and n to R-$\underline{C}H_2$-R (21 and 10 ppm, respectively).

From all the above results, we conclude a successful synthesis of core-shell functionalized MSNs with different generations of PAMAM dendrons (D1, D2 and D3) *via* the delayed co-condensation approach. The PAMAM moieties are exclusively located at the external particle surface resulting in an organic polymer coating of MSNs featuring high buffering capacity. The sample MSN-D3 showed optimal properties and is expected to have great potential for generating the proton sponge effect. Hence, in the following we exclusively investigated the MSN-D3 particles for cargo release, cell uptake and cell targeting experiments.

To prove a stimuli-responsive cargo release behavior of the PAMAM dendron-coated MSNs, we performed time-based release experiments of the fluorescent model drug 5(6)-carboxy-X-rhodamine (ROX). The thiol-functionalization of the particle core offers the possibility to covalently attach cargo molecules to the internal pore surface via disulfide bridges. In a reductive milieu (simulation of the cytosol), disulfide bridges can be cleaved causing a release of the cargo molecules from the mesopores. A derivative of the fluorescent dye ROX (containing the thiol-reactive group methanethiosulfonate, MTS) was covalently attached to the particle core in a one-step synthesis at mild conditions (1 h, room temperature, dark). The presence of non-bound dye was excluded due to extensive washing steps before the release experiments. A custom-made two-compartment release set-up was used to perform the *in vial* release experiments (Figure 9.6), as previously described.[26]

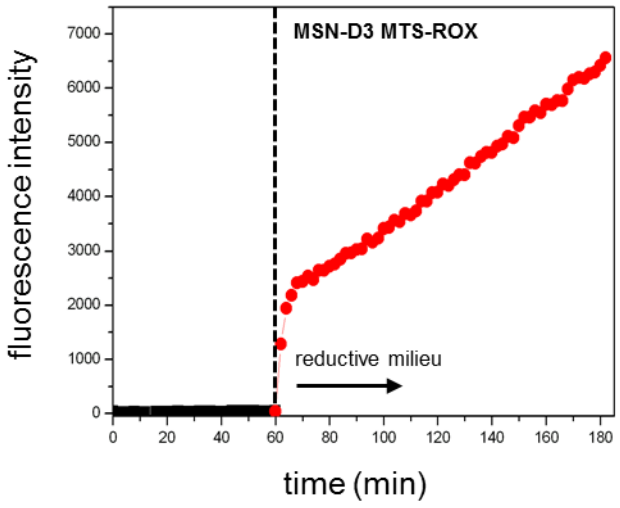

Figure 9.6: Redox-responsive release kinetics of 5(6)-carboxy-X-rhodamine (MTS-ROX) before (black) and after (red) addition of dithiothreitol (DTT) to simulate the reductive milieu of the cytosol. Before medium change, MSN-D3 shows no premature release of the fluorescent cargo molecules which are attached to the mesopores via disulfide bridges. Only in reductive milieu a significant increase in fluorescence intensity can be observed, demonstrating a redox-responsive release behavior of the MTS-ROX due to cleavage of the disulfide bridges.

The PAMAM dendron-functionalized MSNs with immobilized MTS-ROX in the mesopores showed no cargo release in (non-reducing) aqueous solution within the first hour. Only upon addition of a reducing agent (dithiothreitol, DTT), a drastic increase in fluorescence intensity was observed. This demonstrates the redox-responsive cleavage of the disulfide bridges, followed by the release of the fluorescent model drug from the pore system. The redox-responsive behavior shown here offers great potential for a specific cargo release once the mesoporous silica nanocarriers have escaped from the endosomes and entered the cytosol of the targeted cell.

We investigated the potential of PAMAM dendron-coated MSNs to achieve endosomal escape via the proton sponge effect by performing *in vitro* cell experiments. Fluorescent live-cell imaging with high-resolution spinning-disk confocal microscopy is a versatile technique to examine the cellular uptake of nanocarriers and the intracellular cargo release. In a first experiment, a derivative of the anticancer drug colchicine was covalently attached to the internal pore surface of MSNs bearing thiol groups in the particle core. Thus, colchicine molecules with the thiol-reactive group methanethiosulfonate (MTS) formed disulfide bridges. After endocytosis, the loaded nanocarriers need access to the reductive cytosol which provides the appropriate redox potential to cause cleavage of the covalent linkage and successful cargo release. The understanding of cellular redox compartmentalization is still limited and leads to a controversial discussion of the redox potential of the endosomal environment in the literature.[36] FRET experiments with disulfide-bridged folate-dye conjugates showed a time-dependent reduction of the fluorescence signal after cellular uptake to KB cells, suggesting to some extend a reductive milieu in the endosomes.[37] In contrast, Austin *et al.* showed that the pathway of endocytosis for antibody-drug conjugates containing disulfide bridges to breast carcinoma cells (SKBr3) provides a oxidizing environment and hence no significant disulfide cleavage could be observed.[38] Since the acidic milieu of lysosomes and late endosomes is not favorable for reducing agents such as glutathione (GSH), endolysosomal content could be mainly degraded by means of thiol reductases.[39] These enzymes are able to cleave disulfide bridges of free drug conjugates, but are too large to access the porous system of MSNs. Therefore, we expect that our nanocarrier system provides efficient cargo release only after endosomal rupture when the particles are freely distributed in the cytosol.

The intracellular release of the cell membrane-permeable anticancer drug colchicine causes inhibition of the microtubuli polymerization due to irreversible binding to tubulins.[40] However, the depolymerization of the microtubules, which are basic structural components of the cellular cytoskeleton, still proceeds thus ultimately leading to cell death. MTS-modified colchicine was immobilized at the inner mesoporous surface of the PAMAM dendron-coated silica nanoparticles, and subsequently these loaded drug delivery vehicles were incubated with tubulin-GFP-transfected KB cells. In Figure 9.7a, the fluorescently-labeled microtubule network (green) of untreated KB cells is depicted for comparison. Already after 2 h of particle incubation (MSNs have been additionally labeled with Atto 633, red), endocytosis occurred to a high degree (Figure 9.7b). Importantly, the microtubule network seemed to be still intact, suggesting that no release of colchicine had occurred at this time point. After 7 h of incubation, a partial destruction of the microtubule network could be observed (Figure 9.7c). After 22 h of incubation, cell death finally occurred which was indicated by the disappearance of the tubulin structure, a blurred green fluorescence signal and a rounded shape of the cells. We note that KB cell incubation with unloaded PAMAM dendron-coated MSNs showed no cytotoxic effects. The alternative uptake of free colchicine into the cells could be excluded: Reference experiments with the sample supernatant after particle separation by centrifugation showing no effect on the microtubule network for 22 h (cf. Appendix 9.5).

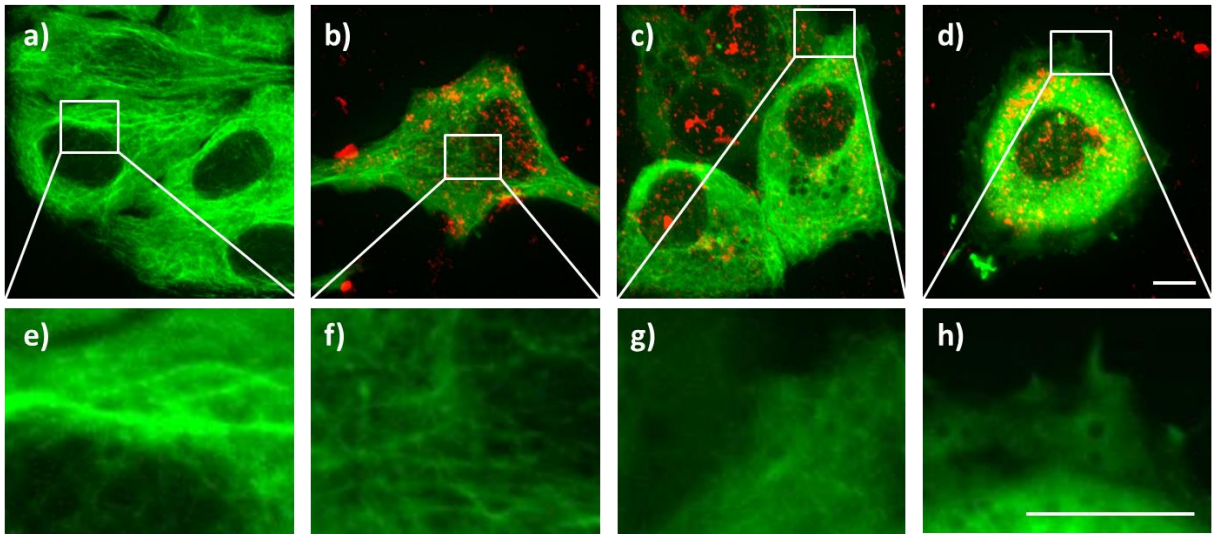

Figure 9.7: Fluorescence microscopy of a,e) KB cells with GFP tagged tubulins (green). The cells were incubated with MSN-D3 loaded with immobilized colchicine (MTS-Col) in the mesopores and labeled with Atto 633 (red) for b,f) 2 h, c,g) 7 h and g,h) 22 h. e-h) Zoom in on representative microtubule structures. A time-dependent destruction of the tubulin network can be observed, finally causing cell death. The scale bars represent 10 µm.

This destruction of the cytoskeleton due to MSN-delivered colchicine has been observed by our groups before. Cauda *et al.* could show efficient cell death triggered by colchicine after endocytosis of the drug-loaded MSN nanocarriers sealed with a supported lipid bilayer.[24] Despite the observed enhanced therapeutic effect compared to free drug molecules, concerns about premature leakage from the lipid bilayer-coated nanocarriers may arise since colchicine features membrane permeability. Thus, immobilization of the drug molecules to the internal mesoporous surface *via* stimuli-responsive cleavable linkers (e.g. disulfide bridges) as shown in the present work promises further improvement of spatially-controlled cargo release. The cell experiments discussed above demonstrate time-dependent intracellular release of immobilized colchicine from the mesoporous drug delivery vehicles. We anticipate that the natural acidification of the endosomal compartment initiated the proton sponge effect with our particles. The high buffering capacity of the PAMAM dendrons caused high internal osmotic pressure subsequently leading to rupture of the endosomal membrane and access to the cytosol. Reducing agents present in the cytosol were able to cleave the disulfide bridges and colchicine was efficiently released.

We further investigated the *in vitro* release of 4',6-diamidino-2-phenylindole (DAPI) on HeLa cancer cells. DAPI preferentially stains the nuclei of cells. The intercalation to dsDNA leads to a significantly enhanced fluorescent signal that can be detected by fluorescence live-cell imaging microscopy (20-fold increase).[41-42] PAMAM dendron-coated MSNs were immersed in a solution containing an *in situ* synthesized DAPI derivative with thiol-reactive methanethiosulfonate groups, which was subsequently covalently attached to the mercapto-functionalized mesopores of the silica nanoparticles (sample MSN-D3-MTS-DAPI). These covalent disulfide bridges should be cleaved only once the expected proton sponge effect has achieved endosomal escape and the nanocarriers have reached the reductive milieu of the cytosol. HeLa cells were incubated with MSN-D3-MTS-DAPI for 5, 10 and 22 h. Figure 9.8 shows an efficient cellular uptake behavior of the nanoparticles labeled with Atto 633 (red) already after 5 h. Moreover, only weak staining of the nuclei (blue) was observed at this time point. In contrast, free DAPI molecules are able to permeate through the cell membrane causing efficient nuclei staining already within a few minutes (1-5 min), as described by standard nucleus staining protocols.[43] Reference experiments with the sample supernatant after particle separation by centrifugation showed only a marginal staining of the nuclei, which proves that only a small amount of free dye molecules was present in the particle

solution. Therefore, we conclude that the DAPI was released from the intracellular MSNs upon cleavage of the disulfide anchors. Over the entire time range a successive increase in fluorescence intensity of the DAPI-stained nuclei could be observed. We attribute this time-dependent release behavior of DAPI to the relatively slow process of the proton sponge effect which was caused by the PAMAM dendron content of our nanocarriers. Consequently, endosomal escape was provided for an efficient cytosolic delivery of the cargo molecules. Similar observations for a delayed cargo release were made in our group for pH-responsive capping systems (cf. chapter 7 and PhD thesis of Stefan Niedermayer).[44] Acidification of the endosomal compartment is realized while trafficking along the tubulin network towards the nucleus. This process takes several hours, which can explain the fairly slow release of the DAPI cargo from the PAMAM dendron-containing multifunctional nanocarriers.

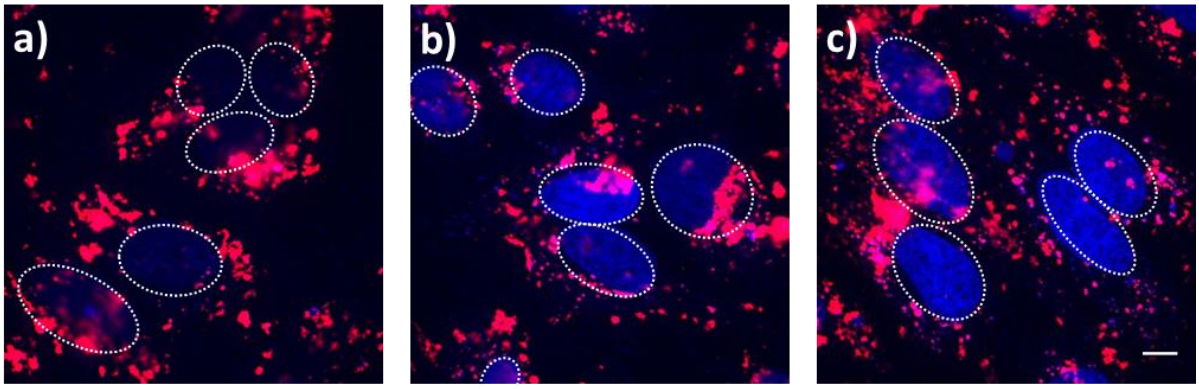

Figure 9.8: Fluorescence microscopy of HeLa cells incubated with MSN-D3 nanoparticles loaded with immobilized DAPI (MTS-DAPI, blue) inside the mesopores and labeled with Atto 633 (red) after a) 5 h, b) 10 h and c) 22 h incubation with the cells. The nuclei are indicated with dashed circles. Time-dependent nuclei staining can be observed suggesting triggered release of the cargo molecules from the nanocarriers after endosomal escape via the proton sponge effect and access to the cytosol. The scale bar represents 10 µm.

For further monitoring of the proton-sponge induced cargo delivery, bare MSNs without dendron functionalization on the external surface were loaded with DAPI (MSN-NH_2-MTS-DAPI) for reference experiments. These nanoparticles only present amino groups at the external surface. We monitored their release behavior in comparison to the sample MSN-D3-MTS-DAPI and its solution after particle separation (by centrifugation), denoted as supernatant (for fluorescence microscopy images refer to Appendix 9.5). HeLa cells were incubated with the samples for a total time period of 61 h.

The fluorescence intensity of DAPI-stained nuclei as a function of the incubation time has been investigated for all three samples (MSN-D3-MTS-DAPI, MSN-NH_2-MTS-DAPI, and supernatant of MSN-D3-MTS-DAPI). The experimental findings are summarized in

Figure 9.9. The nuclei areas were selected as distinct regions of interest (ROI) and the fluorescence intensity was evaluated at different time points for all samples. Sample MSN-D3-MTS-DAPI revealed a significant increase in fluorescence intensity over time, as discussed above (cf. Figure 9.8). This proves an efficient DAPI delivery into the cells shown by fluorescent nuclei staining. The supernatant of sample MSN-D3-MTS-DAPI exhibited no temporal increase of fluorescence intensity proving that only a very small amount of free dye was present in the solution, which was already completely incorporated into the nuclei after 5 h (first data point). As a result, DAPI needs to be released from the mesopores of the dendron-coated silica nanoparticles in order to achieve efficient nuclei staining.

Strikingly, the fluorescence intensity for the reference sample MSN-NH_2-MTS-DAPI also remained constant at a marginal level comparable to the supernatant of sample MSN-D3-MTS-DAPI. Almost no nuclei staining could be observed for sample MSN-NH_2-MTS-DAPI, indicating that negligible amounts of DAPI were released from these nanocarriers. This comparison demonstrates that the PAMAM dendron functionality of our drug delivery vehicles is of key importance to achieve successful cargo delivery to cancer cells.

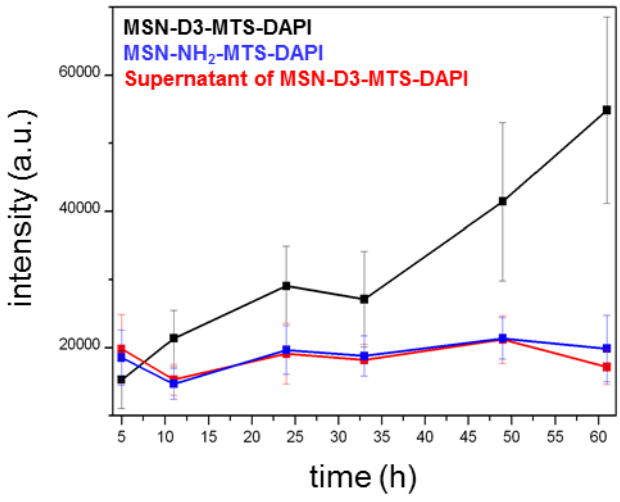

Figure 9.9: Nuclei staining kinetics of the DAPI delivery to HeLa cells from MSN-D3-MTS-DAPI (black), MSN-NH_2-MTS-DAPI (blue), and the supernatant (red) of the MSN-D3-MTS-DAPI solution (after particle separation). The fluorescence intensity of distinct regions of interest (stained nuclei) was evaluated after different time points of sample incubation. Data represent average fluorescence intensity ± standard deviation (the fluorescence intensities of 44 – 104 nuclei were determined for one data point). A time-dependent increase of fluorescence intensity can be observed for MSN-D3-MTS-DAPI, demonstrating an efficient DAPI release from the nanocarriers. In contrast, the fluorescence intensity remains constant at a marginal level for the reference samples. This shows that negligible DAPI release occurred for MSN-NH_2-MTS-DAPI and that almost no free DAPI molecules had been present in the particle solution (supernatant).

Taken together, these *in vitro* release experiments with different cell lines and different cargo molecules incorporated into the mesoporous system of PAMAM dendron-coated silica nanoparticles clearly show an efficient endosomal escape followed by intracellular delivery caused by the proton sponge effect.

Targeting. Another key feature of an effective drug delivery vehicle is specific targeting of the desired tissue, mainly cancer cells. Many cancer cell lines were found to overexpress diverse cell membrane receptors due to increased metabolic activity. In contrast, healthy tissue features only small concentrations of such receptors on the cell membrane surface. A preferential targeting of cancer cells can be achieved by exploiting a receptor-mediated cellular uptake of the nanocarriers. Targeting ligands such as folic acid can be attached to the periphery of the PAMAM dendron-coated MSNs. The covalently bound FA moieties are intended to interact with the folic acid receptor FR-α, resulting in a fast and specific endocytosis.[5, 28] Amino-group terminated PAMAM dendrons offer the possibility to covalently attach folate *via* a short bifunctional PEG-linker. Atto 633-labeled MSNs equipped with the folate targeting ligand were incubated for 5 h with KB cells to investigate receptor-mediated endocytosis. In Figure 9.10 membrane-stained KB cells (WGA 488, green) are depicted. Two cellular uptake experiments were performed simultaneously. On the one hand, KB cells were pre-treated with free folate to achieve full saturation and blocking of the cell receptors before particle incubation. Here, unspecific cell uptake could be observed only to a small degree (Figure 9.10b); this is commonly expected to take much longer than receptor-mediated endocytosis. The particle location (inside or outside the cell) can be determined by evaluating cellular z-stacks with a spinning disk confocal fluorescence microscope.

A significantly higher efficiency of particle internalization into the cells occurred for KB cells without pretreatment with free targeting ligands (Figure 9.10a). Here, the fast cellular uptake is attributed to the receptor-mediated endocytosis of MSNs with folate (MSN-D3-FA) which can also be seen in the orthogonal views.

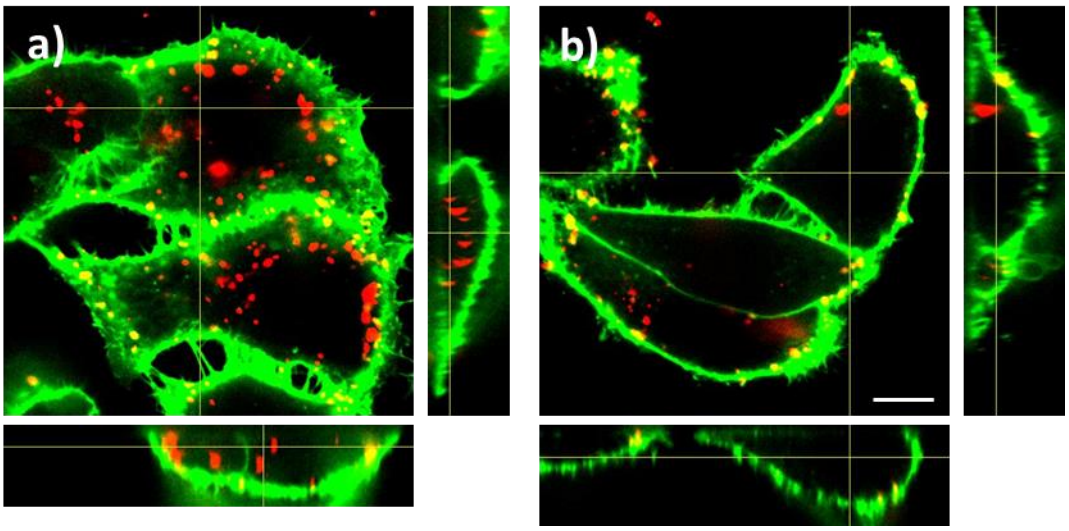

Figure 9.10: a) Receptor-mediated and b) unspecific endocytosis of MSN-D3 with targeting ligand folate (MSN-D3-FA, red) by KB cells (membrane staining, green). A specific receptor-mediated cell uptake can be observed for MSN-D3-FA with KB cells (not FA-preincubated) after 5 h incubation at 37 °C (a). Incubation of MSN-D3-FA with FA-preincubated KB cells for 5 h at 37 °C shows only unspecific cellular uptake (b). The scale bar represents 10 µm.

9.3 Conclusion

In summary, the synthesis of PAMAM dendron-coated MSNs combines advantageous structural parameters such as high loading capacity and tunable functionality with the high capacity of PAMAM dendrons for proton absorption. The novel synthesis strategy, based on creating PAMAM dendron silane precursors that were used in a delayed co-condensation approach, resulted in core-shell functionalized MSNs containing PAMAM dendron moieties exclusively at the external particle surface. We show that these multifunctional mesoporous silica nanocarriers provide triggered and efficient release of the fluorescent dye DAPI and the anticancer drug colchicine to cancer cells, which is induced by the high buffering capacity of the external PAMAM dendron shell causing the proton sponge effect. As a result, our drug delivery vehicles provide an intrinsic endosomal escape pathway for efficient intracellular release of immobilized cargo molecules. This technique prevents endosomal entrapment of the nanocarriers and can also provide access for impermeable cargos to the cytosol or to other targeted cell compartments. Furthermore, the nanoparticles offer optional attachment of various cargos inside their mesopores *via* disulfide bridges, and binding of different targeting ligands to their outer periphery. These multifunctional MSNs are viewed as a general and powerful platform for controlled drug delivery in various biomedical applications, in particular for cancer therapy.

9.4 Experimental

Materials. Propargylamine (Aldrich, 98 %), *N*,*N*-diisopropylethylamine (DIPEA, Sigma-Aldrich, ≥ 99 %), copper(I) iodide (Aldrich, 99.999 %), (3-aminopropyl) triethoxysilane (APTES, Aldrich, 99%), tetraethyl orthosilicate (TEOS, Fluka, > 98 %), triethanolamine (TEA, Aldrich, 98 %), cetyltrimethylammonium chloride (CTAC, Fluka, 25 % in H_2O), (3-mercaptopropyl) trimethoxysilane (MPTMS, Gelest, 95 %), methanethiosulfonate 5(6)-carboxy-X-rhodamine (MTS-ROX, Biotium), colchicine methanethiosulfonate (MTS-Col, Santa Cruz Biotechnology), 4,6-diamidino-2-phenylindole dihydrochloride (DAPI, Sigma Aldrich), folic acid (FA, Sigma), Atto 633 maleimide (ATTO-TEC), 1-ethyl-3-(3-dimethylaminopropyl) carbodiimide hydrochloride (EDC, Fluka, 97 %), *N*-hydroxysulfosuccinimide (sulfo-NHS, Sigma Aldrich, >98.5 %), poly (ethylene glycol) bisamine (PEG_{2000}-bisNH_2, M_W2000, Sigma Aldrich), *N*-succinimidyl oxycarbonylethyl methanethiosulfonate (NHS-3-MTS, Santa Cruz Biotechnology) and oxalic acid were used as received. Methyl acrylate (Aldrich, 99 %) and 1,2-ethylenediamine (Aldrich, 99.5 %) were freshly distilled prior to use. Ethanol (EtOH, absolute), *N*,*N*-dimethyl formamide (DMF, Sigma Aldrich, anhydrous) and methanol (MeOH, anhydrous, Sigma) were used as solvents without further purification. Bidistilled water was obtained from a Millipore system (Milli-Q Academic A10). (3-Azidopropyl)trimethoxy silane (AzTMS) was freshly prepared as previously reported.[45]

Synthesis of propargyl-PAMAM dendrons. Starting with propargylamine, the synthesis of PAMAM dendrons employs a Michael addition with methyl acrylate and amidation with 1,2-ethylendiamine in an alternating fashion. The methodology was developed by Lee *et al.*.[33]

General procedure for Michael addition**.** A solution of the amino-terminal compound in anhydrous methanol (80 mL) was added drop-wise to a stirred solution of freshly distilled methyl acrylate in methanol over a period of about 1 h at 0 °C. The resulting solution was allowed to warm up to room temperature and stirred for 48 h. The reaction progress was monitored by NMR spectroscopy and stopped when the N-H signal had disappeared. Solvent and methyl acrylate were removed *in vacuo*, traces of methyl acrylate were removed by redissolving the residue in methanol and repeated removal of the solvent. Drying under high vacuum gave the desired pure product as orange viscous oil.

General procedure for amidation. A solution of the ester-terminal compound in methanol (80 mL) was added drop-wise to a stirred solution of freshly distilled 1,2-ethylendiamine in methanol over a period of approx. 1 h at 0 °C. The resulting solution was allowed to warm up

to room temperature and stirred for 48 h. The reaction was monitored by NMR spectroscopy and stopped when no methyl ester signal could be detected anymore. Solvent was removed *in vacuo*, the excess of 1,2-ethylendiamine was removed successively by adding 100 mL of an azeotropic toluene/methanol mixture (9:1) and removal of the volatiles *in vacuo*. This procedure needed to be repeated four to six times with a final pressure after removal of < 10 mbar. Remaining toluene was removed by azeotropic distillation using methanol. Drying under high vacuum gave the desired pure product as orange viscous oil.

Dendron D0.5 Starting material: Propargylamine (1.50 g, 1.74 mL, 27.2 mmol, 1 eq.); Reagents: methyl acrylate (17.0 g, 17.9 mL, 197 mmol, 7.3 eq.) in 20 mL methanol; Yield: 5.74 g (25.3 mmol, 93 %); IR (film): 3280, 2956, 2840, 1741, 1641, 1542, 1437, 1203, 1175, 1056 cm^{-1}; ^{1}H NMR (270 MHz, $CDCl_3$) d = 3.60 (s, 6H, OMe), 3.35 (d, ^{4}J = 2.3 Hz, 2H, N-CH_2-C≡CH), 2.77 (t, J = 7.0 Hz, 4H, N-CH_2-CH_2), 2.39 (t, J = 7.1 Hz, 4H, N-CH_2-CH_2-CO), 2.14 (t, J = 2.3 Hz, 1H, CH_2-C≡C-H); ^{13}C NMR (68 MHz, $CDCl_3$) d = 172.84 (C=O), 78.22 (CH_2-C≡CH), 73.47 (CH_2-C≡CH), 51.77 (NH_2-CH_2-CH_2), 49.13 (OMe), 42.10 (N-CH_2-C≡CH), 33.09 (N-CH_2-CH_2-CO) (NMR spectra are shown in Appendix 9.5); HRMS (ESI) calculated for $C_{11}H_{17}NO_4$ ($[M+H]^+$) 228.1236, found 228.1229.

Dendron D1 Starting material: D0.5 (4.90 g, 21.6 mmol, 1 eq.); Reagents: 1,2-ethylendiamine (111 g, 100 mL, 1.85 mol, 86 eq.) in 30 mL methanol; Yield: 6.23 g (21.2 mmol, 98 %); IR (film): 3281, 3062, 2933, 2826, 1639, 1543, 1456, 1356, 1250, 1195, 935 cm^{-1}; ^{1}H NMR (400 MHz, $CDCl_3$) d = 7.31 (s, 2H, NHCO), 3.37 (d, ^{4}J = 2.4 Hz, 2H, N-CH_2-C≡CH), 3.23 (dt, J = 6.0 Hz, 4.0 Hz, 4H, CONHCH_2-CH_2), 2.78 (t, J = 6.0 Hz, 4H, N-CH_2-CH_2), 2.76 (t, J = 5.6 Hz, 4H, N-CH_2-CH_2) 2.33 (t, J = 6.1 Hz, 4H, N-CH_2-CH_2-CONH), 2.19 (t, J = 2.4 Hz, 1H, CH_2-C≡C-H), 1.67 (br s, 4H, NH_2); ^{13}C NMR (68 MHz, $CDCl_3$) d = 172.51 (C=O), 77.83 (CH_2-C≡CH), 73.85 (CH_2-C≡CH), 49.72 (N-CH_2-CH_2-CO), 42.22 (CONH-CH_2-CH_2), 41.80 (N-CH_2-C≡CH), 41.61 (NH_2-CH_2-CH_2), 34.23 (N-CH_2-CH_2-CO) (NMR spectra are shown in Appendix 9.5); HRMS (ESI) calculated for $C_{13}H_{25}N_5O_2$ ($[M+H]^+$) 284.2087, found 284.2081.

Dendron D1.5 Starting material: D1 (5.78 g, 20.4 mmol, 1 eq.); Reagents: methyl acrylate (28.5 g, 30.0 mL, 331 mmol, 16 eq.) in 40 mL methanol; Yield: 12.3 g (19.6 mmol, 96 %); IR (film): 3284, 2951, 2841, 1732, 1653, 1540, 1436, 1361, 1260, 1177, 841 cm^{-1}; ^{1}H NMR (400 MHz, $CDCl_3$) d = 7.07 (s, 2H, NHCO), 3.63 (s, 12H, OMe), 3.42 (d, ^{4}J = 2.3 Hz, 2H, N-CH_2-C≡CH), 3.25 (dt, J = 6.0 Hz, 4.0 Hz, 4H, CONH-CH_2-CH_2), 2.81 (t, J = 6.6 Hz, 4H, N-

CH_2-CH_2), 2.72 (t, J = 6.7 Hz, 8H, N-CH_2-CH_2-COOMe), 2.50 (t, J = 5.0 Hz, 4H, N-CH_2-CH_2), 2.39 (t, J = 6.6 Hz, 8H, N-CH_2-CH_2-COOMe), 2.34 (t, J = 6.5 Hz, 4H, N-CH_2-CH_2-CONH), 2.16 (t, J = 2.2 Hz, 1H, CH_2-C≡C-H); ^{13}C NMR (68 MHz, $CDCl_3$) d = 172.91 (C=O), 171.81 (C=O), 77.86 (CH_2-C≡CH), 73.42 (CH_2-C≡CH), 52.82, 51.49, 49.27, 49.16, 41.00, 36.97, 33.70, 32.60 (NMR spectra are shown in Appendix 9.5); HRMS (ESI) calculated for $C_{29}H_{49}N_5O_{10}$ ($[M+H]^+$) 628.3558, found 628.3546.

Dendron D2 Starting material: D1.5 (10.5 g, 16.7 mmol, 1 eq.); Reagents: 1,2-ethylendiamine (111 g, 100 mL, 1.85 mol, 110 eq.) in 20 mL methanol; Yield: 12.1 g (16.4 mmol, 98 %); IR (film): 3280, 2930, 2819, 1637, 1545, 1362, 1249, 1126, 933 cm^{-1}; ^{1}H NMR (400 MHz, $CDCl_3$) d = 7.90 (s, 2H, NHCO), 7.68 (s, 4H, NHCO), 3.38 (d, ^{4}J = 2.3 Hz, 2H, N-CH_2, 3.25-3.15 (m, 12H), 2.78-2.73 (m, 12H), 2.67 (t, J = 6.0 Hz, 8H), 2.46 (t, J = 5.8 Hz, 4H), 2.34-2.25 (m, 12H), 2.19 (t, J = 2.0 Hz, 1H, CH_2-C≡C-H), 1.98 (br s, 8H, NH_2); ^{13}C NMR (68 MHz, $CDCl_3$) d = 172.90 (C=O), 172.24 (C=O), 77.66 (CH_2-C≡CH), 73.66 (CH_2-C≡CH), 52.71, 49.67, 49.17, 44.48, 41.93, 41.24, 37.65, 34.15, 33.63 (NMR spectra are shown in Appendix 9.5); HRMS (ESI) calculated for $C_{33}H_{65}N_{13}O_6$ ($[M+H]^+$) 740.5259, found 740.5249.

Dendron D2.5 Starting material: D2 (6.7 g, 10.4 mmol, 1 eq.); Reagents: methyl acrylate (85.5 g, 90.0 mL, 0.99 mol, 96 eq.) in 30 mL methanol; Yield: 14.5 g (10.2 mmol, 98 %); IR (film): 3295, 2953, 2822, 1731, 1646, 1539, 1436, 1358, 1259, 1174, 844 cm^{-1}; ^{1}H NMR (270 MHz, $CDCl_3$) d = 7.64 (s, 2H, NHCO), 7.01 (s, 4H, NHCO), 3.55 (s, 24H, OMe), 3.35 (d, ^{4}J = 2.0 Hz, 2H, N-CH_2-C≡CH), 3.22-3.12 (m, 12H), 2.74-2.60 (m, 28H), 2.50-2.40 (m, 12H), 2.36-2.20 (m, 28H), 2.12 (t, J = 2.0 Hz, 1H, CH_2-C≡C-H); ^{13}C NMR (68 MHz, $CDCl_3$) d = 172.99 (C=O), 172.89 (C=O), 172.30 (C=O), 78.01 (CH_2-C≡CH), 73.51 (CH_2-C≡CH), 52.90, 52.49, 51.59, 49.87, 49.71, 49.22, 40.96, 37.37, 37.14, 33.83, 32.57 (NMR spectra are shown in Appendix 9.5); HRMS (ESI) calculated for $C_{65}H_{113}N_{13}O_{22}$ ($[M+H]^+$) 1428.8201, found 1428.8189.

Dendron D3 Starting material: D2.5 (6.42 g, 4.50 mmol, 1 eq.); Reagents: 1,2-ethylendiamine (122 g, 110 mL, 2.0 mol, 452 eq.) in 10 mL methanol; Yield: 6.5 g (3.91 mmol, 87 %); IR (film): 3271, 3074, 2933, 2863, 1636, 1540, 1436, 1359, 1197, 1127, 935 cm^{-1}; ^{1}H NMR (270 MHz, $CDCl_3$) d = 7.98 (s, 2H, NHCO), 7.77 (s, 4H, NHCO), 7.57 (s, 8H, NHCO), 3.39 (d, ^{4}J = 2.0 Hz, 2H, N-CH_2-C≡CH), 3.29-3.11 (m, 32H), 2.79-2.72 (m, 24H), 2.70-2.64 (m, 12H), 2.63-2.56 (m, 12H), 2.51-2.42 (m, 8H), 2.38-2.21 (m, 24H), 2.12 (t, J = 2.0 Hz, 1H, CH_2-C≡C-H), 1.65 (br s, 16H, NH_2); ^{13}C NMR (68 MHz, $CDCl_3$) d =

173.37 (C=O), 173.15 (C=O), 172.82 (C=O), 77.43 (CH_2-C≡CH), 72.69 (CH_2-C≡CH), 53.05, 52.66, 52.17, 50.75, 50.25, 46.46, 45.01, 42.49, 42.32, 41.66, 37.86, 34.51, 34.13 (NMR spectra are shown in Appendix 9.5); HRMS (ESI) calculated for $C_{73}H_{145}N_{29}O_{14}$ ($[M+H]^+$) 1653.1604, found 1653.1595.

Synthesis of PAMAM Silanes. Huisgen azide-alkyne 1,3-dipolar cycloaddition with amino-terminated propargyl-PAMAM dendrons and AzTMS was performed based on a similar reaction of AzTMS with an alkyne compound reported by Lim *et al.*.[46]

General procedure. The amino-terminated propargyl-PAMAM dendron **D1, D2, or D3** (1 eq.) was dissolved in a suspension of molecular sieves (3 Å) in anhydrous methanol (15 mL) and DIPEA (2 eq.). The resulting suspension was degassed afterwards. Under an atmosphere of nitrogen, copper(I) iodide (10 mol%), as catalyst, and AzTMS (0.25 eq.) were added. The reaction was stirred for 24 h at room temperature and subsequently filtered using a syringe filter. After exposure to air the solution turned purple-blue very quickly. The solvent was removed *in vacuo*; drying of the crude product at high vacuum yielded a blue gum which was used without further purification.

S1 Starting material: **D1** (134 mg, 0.471 mmol); Reagents: AzTMS (24.2 mg, 24.2 mL, 0.118 mmol), DIPEA (122 mg, 164 mL, 0.942 mmol), CuI (9.50 mg, 0.050 mmol); Crude product: 204 mg containing 47.6 mg (0.106 mmol) of **S1.**

S2 Starting material: **D2** (1.48 g, 2.00 mmol); Reagents: AzTMS (103 mg, 103 mL, 0.500 mmol), DIPEA (517 mg, 697 mL, 4.00 mmol), CuI (38.1 mg, 200 mmol); Crude product: 1.38 g containing 425 mg (0.45 mmol) of **S2.**

S3 Starting material: **D3** (3.31 g, 2.00 mmol); Reagents: AzTMS (103 mg, 103 mL, 0.500 mmol), DIPEA (517 mg, 697 mL, 4.00 mmol), CuI (38.1 mg, 0.200 mmol); Crude product: 3.5 g containing 836 mg (0.45 mmol) of **S3**.

Synthesis of dendron-functionalized MSNs (MSN-SH_{IN}-$D_{n\ OUT}$, n = 1-3). Colloidal mesoporous silica nanoparticles (MSN-SH_{IN}-$D_{n\ OUT}$, n = 1-3) were prepared according to a synthesis procedure published by Cauda *et al.*.[23] The amount of functionalized silane was calculated to be 1% of total silica. A mixture of TEA (14.3 g, 95.6 mmol), TEOS (1.56 g, 7.48 mmol) and MPTMS (92.3 mg, 87.3 mL, 0.47 mmol) was heated for 20 min at 90 °C without stirring in a polypropylene reactor. Afterwards, a preheated (to 60 °C) mixture of CTAC (2.41 mL, 7.29 mmol) and H_2O (21.7 g, 1.21 mol) was added to the first solution and

stirred for 20 min at room temperature. Then, every 3 min 37.2 µL TEOS (34.6 mg) was added to the stirring suspension, four times in total. The reaction was stirred for further 30 min. After this time, a mixture of TEOS (19.2 mg, 92.2 µmol) and functionalized trialkoxysilane (RTMS: AzTMS, **S1**, **S2**, or **S3**) (92.2 µmol) was added. In the case of the PAMAM silanes **S1-3**, the amount of crude product to be used for particle functionalization was calculated from the mass fraction of the silane in the crude product (the yield of **S1**, **S2** and **S3** was estimated at 90 %; 0.106 mmol for **S1**; 0.45 mmol for **S2** and **S3**). Furthermore, the mixture of TEOS and PAMAM silane was dissolved in a solution of 2 mL methanol and 1 mL water briefly before the addition to the reaction mixture. The reaction was stirred at room temperature over night. The suspension was diluted 1:1 with absolute ethanol, the colloidal MSNs were separated by centrifugation (19,000 rpm, 43,146 rcf, 20 min) and redispersed in absolute ethanol. The subsequent template extraction was performed by heating the samples under reflux at 90 °C (oil bath) for 45 min in a solution of ammonium nitrate (2 wt% in ethanol) followed by 45 min under reflux at 90 °C in a solution of 10 mL conc. HCl (37 %) in 90 mL ethanol. The extracted MSNs were collected by centrifugation after each extraction step and finally washed with 100 mL absolute ethanol. The resulting MSNs were stored in an ethanol/water solution (2:1).

Cargo loading. MSN-D3 (1 mg) was incubated for 2 h at room temperature in the dark with MTS-ROX (5 µL, 5 mg/mL in DMF), MTS-Col (50 µL, 5 mg/mL in DMF), or MTS-DAPI for a one-step covalent attachment of the cargo molecules to the internal surface of the mesopores *via* disulfide bridges. MTS-DAPI was prepared in-situ by mixing DAPI (10 µL, 5 mg/mL in DMF) and NHS-3-MTS (100 µg) in an aqueous solution for 1 h at room temperature in the dark. This reaction mixture was subsequently added to MSN-D3. The particles were washed five times (centrifugation, 4 min, 14,000 rpm, 16,837 rcf) with water and were finally redispersed in 1 mL H_2O.

MSN labeling. MSN-D3 (0.5 mg) were mixed with Atto 633 maleimide (1 µL, 2 mg/mL in DMF). After 2 h of stirring at room temperature in the dark the labeled particles were washed three times with water by subsequent centrifugation (4 min, 14,000 rpm, 16,837 rcf) and redispersed in H_2O.

Attachment of the targeting ligand folate. Oxalic acid, EDC, and sulfoNHS (each 5 mg) were successively added to an aqueous dispersion of MSN-D3 (0.5 mg) and the resulting reaction mixture was stirred at room temperature in the dark for another 2 h. Subsequently, the particles were washed three times (centrifugation, 4 min, 14,000 rpm, 16,837 rcf) and

redispersed in 300 µL H_2O. The PEG linker was attached via EDC amidation. EDC, sulfoNHS and PEG_{2000}-bisNH_2 (each 5 mg) were consecutively added to the particle dispersion and stirred for another 2 h at room temperature in the dark. The particles were washed three times by centrifugation (4 min, 14.000 rpm) and redispersed in 100 µL water. Then 400 µL of a folate stock solution (0.75 µM in H_2O), EDC (5 mg), and sulfoNHS (5 mg) were added. The reaction mixture was stirred over night at room temperature in the dark. After washing the particle three times with water (centrifugation, 4 min, 14,000 rpm, 16,837 rcf) the MSN-D3-FA sample was finally redispersed in 1 mL H_2O.

Characterization. NMR spectra were recorded on a Jeol Eclipse 270 (^{1}H: 270 MHz,^{13}C: 67.9 MHz), a Jeol Eclipse 400 (^{1}H: 400 MHz,^{13}C: 101 MHz) NMR or a Jeol 500 Eclipse spectrometer (^{1}H: 500.16 MHz,^{13}C: 125.77 MHz). ^{13}C solid-state NMR measurements were performed on a Bruker DSX Avance500 FT spectrometer in a 4 mm ZrO_2 rotor (100 mg sample) at a frequency of 10 kHz (^{13}C{^{1}H} cross polarization, pulse sequence program *CPRAMP*). IR spectra were recorded on a Bruker Equinox 55. The dried powder of the silica nanoparticles (1.5 mg) was mixed with KBr (200 mg) to produce pressed, transparent pellets to be measured in absorbance mode. For background measurements a neat KBr pellet (200 mg) was used. IR spectra of the organic compounds were recorded in the attenuated total reflectance (ATR) mode on the same device or on a Perkin-Elmer FT-IR Spektrum BXII spectrometer with Schmith Dura SampIIR II ATR-Unit. Mass spectra were measured on a Thermo Finnigan LTQ FT with IonMax (ion source with ESI head). Elementary analysis was performed on a Vario EL or Vario micro cube CHN analyzer detecting carbon, nitrogen, hydrogen and sulfur. The dried powder of the silica nanoparticles was pyrolized at 1150 °C in an oxygen-enriched He-atmosphere. The resulting gases were detected by thermal conductivity measurements. Acid-base titrations were performed on a Metrohm 905 Titrando potentiometric titrator combined with the software tiamo. The titration method met the following parameters: monotonic equivalence point titration (MET); stirring speed 5; measurement value drift 20.0 mV/min; min. delay 0 s; max. delay 300 s; volume increment 0.025 mL; dosing speed maximal; stop value pH 10.2. The samples were prepared as follows: A volume containing 13.7 mg particles from the suspensions was added to 30.0 mL H_2O. The starting pH was set to 3.000 using HCl (0.1 M) and NaOH (0.01 M) from the dosing unit. The samples were titrated against NaOH (0.01 M). TGA measurements of the bulk extracted samples (about 10 mg of dried powder) were performed on a Netzsch STA 440 Jupiter

thermobalance (heating rate of 10 K/min in a stream of synthetic air of about 25 mL/min). XRD patterns were collected at small angles on a Bruker D8 Discover with Ni-filtered Cu-K_α radiation and a position sensitive detector (Vantec) and in the range of 10 – 45 ° on a Stoe Stadi P powder diffractometer equipped with an image plate detector system, in transmission geometry, with Cu-K_α radiation. Nitrogen sorption measurements were performed on a Quantachrome Instruments NOVA 4000e at -196 °C. Sample out-gassing was performed at 120 °C for 12 h at a pressure of 10 mTorr. Pore size and pore volume were calculated using a NLDFT equilibrium model of N_2 on silica, based on the desorption branch of the isotherm. The BET model was used in the range of 0.05 – 0.20 p/p_0 to estimate the specific surface area. DLS and zeta potential measurements were performed on a Malvern Zetasizer-Nano instrument equipped with a 4 mW He-Ne laser (633 nm) and avalanche photodiode detector. DLS measurements were directly recorded on aqueous colloidal suspension at a constant concentration for all sample solutions of 1 mg/mL. For determination of the zeta potential profiles, one to three drops of the ethanolic particle suspension (ca. 3 wt%) was mixed with 1 mL of commercial Hydrion Buffer solution of the appropriate pH prior to measurement. Hückel's approximation was used for interpretation. For TEM (using a Titan 80–300 kV microscope operating at 300 kV), samples were prepared by dispersing MSNs (1 mg) in 4 mL absolute ethanol, by means of an ultrasonic bath, and drying a drop of the resulting diluted suspension on a carbon-coated copper grid.

Cell culture. KB cells were grown in folic acid deficient Roswell Park Memorial Institute 1640 medium (RPMI 1640, Invitrogen) supplemented with 10 % fetal bovine serum (FBS) at 37 °C in a 5 % CO_2 humidified atmosphere. The cells were seeded on ibidiTreat µ-Slide (IBIDI). HeLa cells were grown in Dulbecco's modified Eagle's medium (DMEM):F12 (1:1) (Invitrogen) with Glutamax I medium supplemented with 10 % FBS at 37 °C in a 5 % CO_2 humidified atmosphere. The cells were seeded on collagen A-coated LabTek chambered cover glass (Nunc). For live cell imaging the cells were seeded 24 or 48 h before measuring, at a cell density of $2x10^4$ or $1x10^4$ cells/cm^2.

***In vitro* cargo release.** Cells were incubated 5 – 48 h prior to the measurements at 37 °C under a 5% CO_2 humidified atmosphere. Shortly before imaging, the medium was replaced by CO_2-independent medium (Invitrogen). During the measurements all cells were kept on a heated microscope stage at 37 °C. The subsequent imaging was performed as described in the Spinning disk confocal microscopy section.

Nuclei staining kinetics with DAPI. HeLa cells were measured 5, 11, 24, 33, 49, and 61 h after incubation with the samples MSN-D3-MTS-DAPI, MSN-NH_2-MTS-DAPI and the supernatant of MSN-D3-MTS-DAPI (after particle separation). Each time point was measured with an independently incubated set of cells. In order to evaluate the fluorescence of the nucleoli, the z-stack position was set exclusively in the region of the nuclei. The integrated intensity of a distinct region of interest (ROI) around the nuclei was determined (44 – 104 nuclei for each data point) and divided by the area of the ROI. Thus, the average integrated density per nuclei area (± standard deviation, represented by error bars) could be plotted dependent on incubation time. The relatively large error bars are assumed to result from a different particle uptake behavior for each cell. The number of particles internalized by the cells was not taken into account.

Cell targeting. To evaluate the functionality of the folic acid ligand, KB cells were incubated with nanoparticles for 5 h at 37 °C under a 5 % CO_2 humidified atmosphere. The cell membrane was stained shortly before the measurement by adding 4 µL of 1 mg/mL wheat germ agglutinin Alexa Fluor 488 conjugate (WGA488, Invitrogen) to 400 µL of cell medium. After 1 min, the cell medium was removed, the cells were washed twice with cell medium, and imaged immediately. In control experiments, the FA receptors on the KB surface were blocked by pre-incubation of the cells with 3 mM folic acid (Sigma) for 2 h at 37 °C under a 5% CO_2 humidified atmosphere, before particles were added.

Spinning disc confocal microscopy. Confocal microscopy for live-cell imaging was performed on a setup based on the Zeiss Cell Observer SD utilizing a Yokogawa spinning disk unit CSU-X1. The system was equipped either with a 1.40 NA 100x or a 1.40 NA 63x Plan apochromat oil immersion objective from Zeiss. For all experiments the exposure time was 0.1 s and z-stacks were recorded. WGA488 was imaged with approximately 0.14 W/mm^2 and GFP with 6.6 W/mm^2 of 488 nm excitation light. Atto 633 was excited with 11 mW/mm^2 of 639 nm and DAPI with 0.16 W/mm^2 of 405 nm excitation light. In the excitation path a quad-edge dichroic beamsplitter (FF410/504/582/669-Di01-25x36, Semrock) was used. For two color detection of WGA488, GFP, or DAPI and Atto 633, a dichroic mirror (560 nm, Semrock) and band-pass filters 525/50 and 690/60 (both Semrock) were used in the detection path. Separate images for each fluorescence channel were acquired using two separate electron multiplier charge coupled device (EMCCD) cameras (PhotometricsEvolve^{TM}).

9.5 Appendix

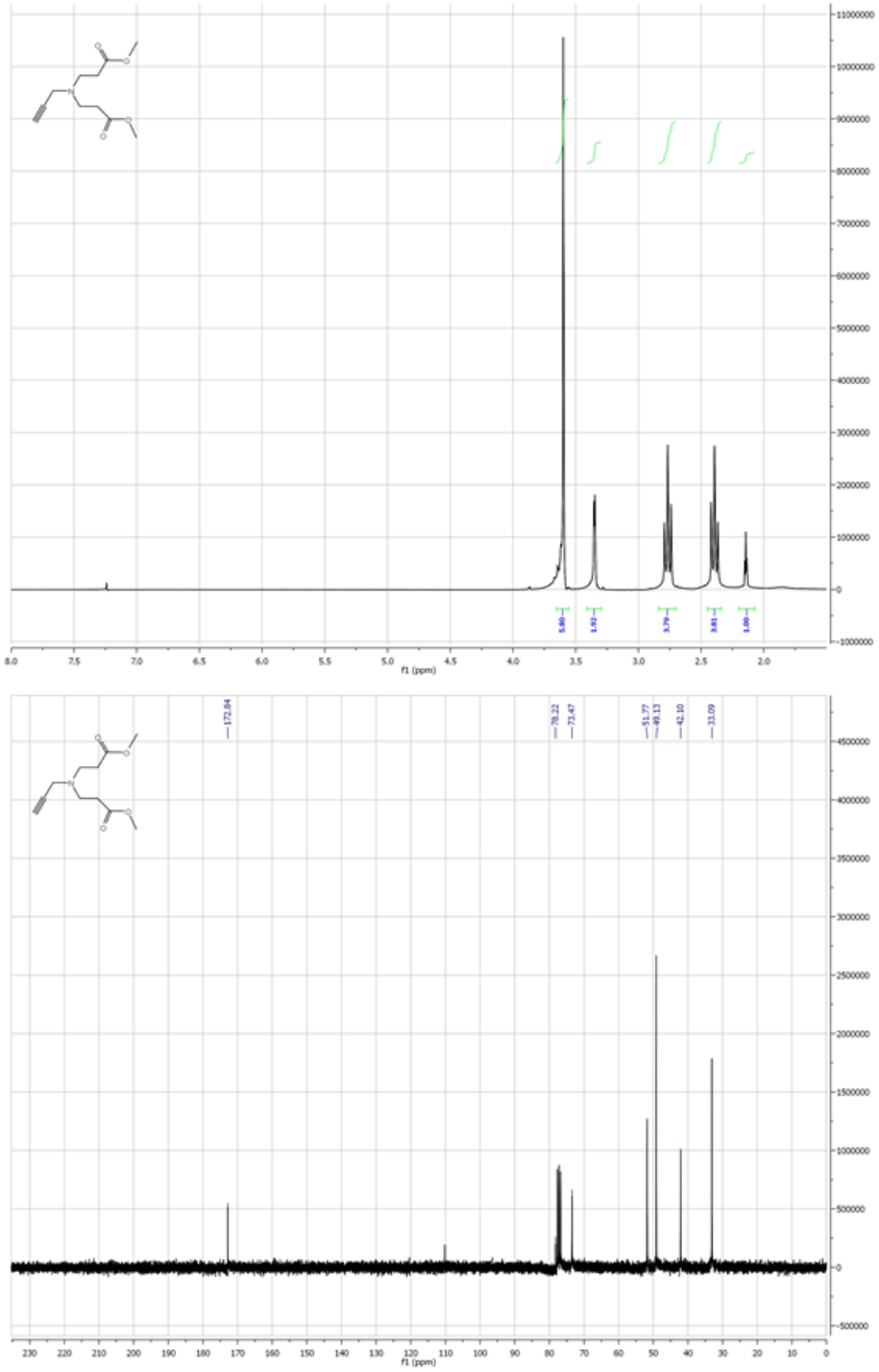

Figure 9.11: ^{1}H and ^{13}C NMR spectrum of propargyl-dendron D0.5.

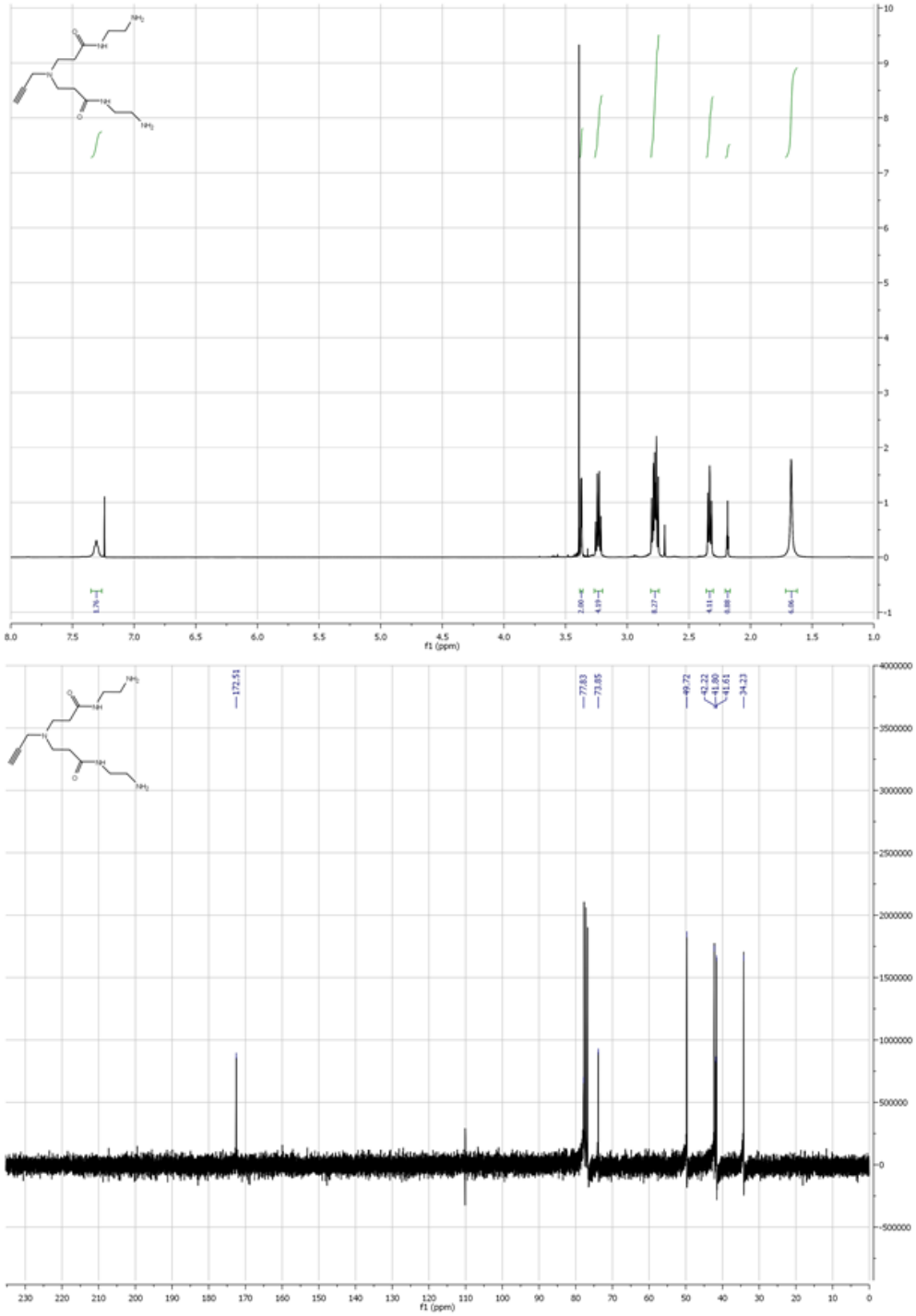

Figure 9.12: ^{1}H and ^{13}C NMR spectrum of propargyl-dendron D1.

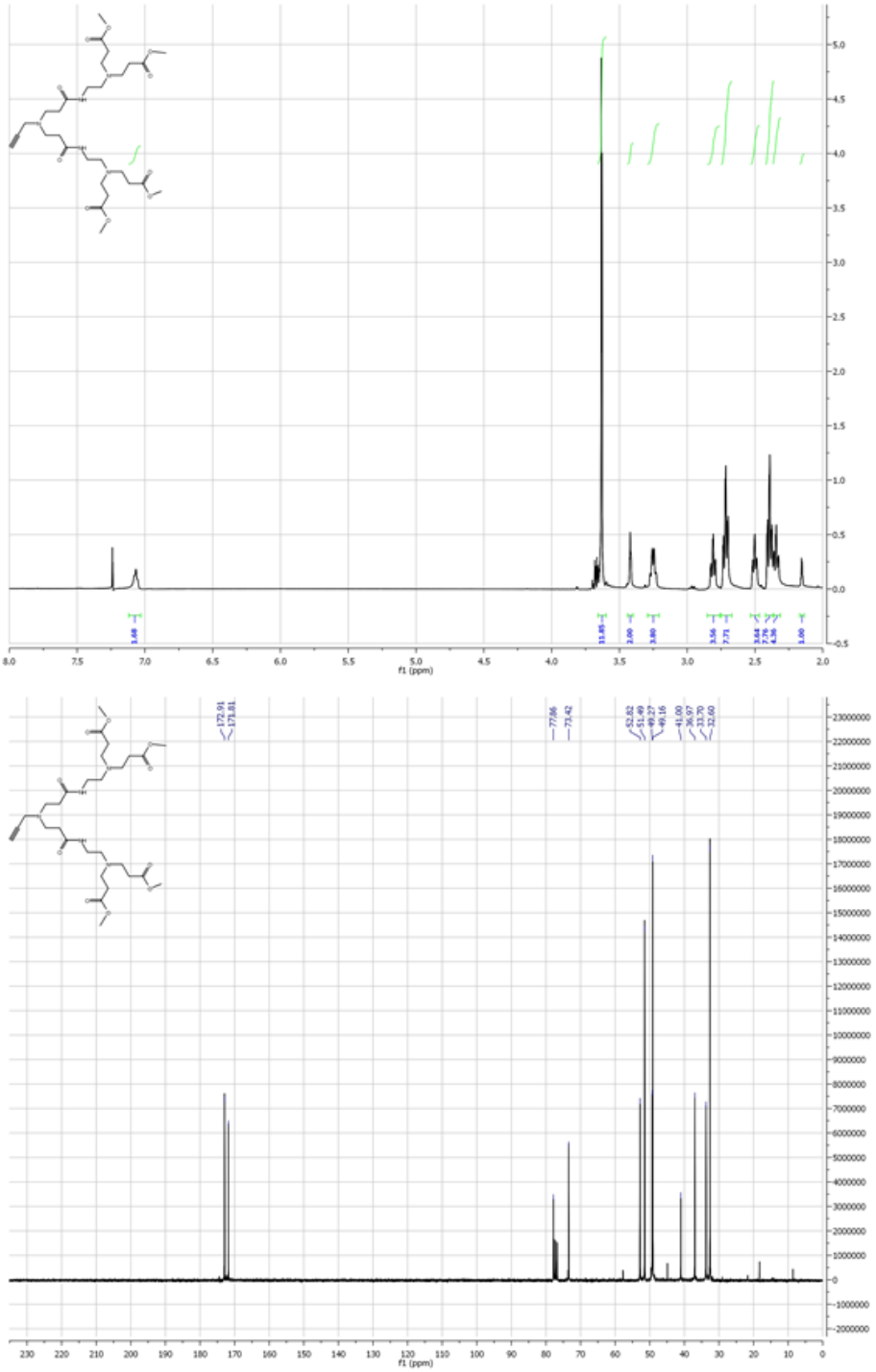

Figure 9.13: ^{1}H and ^{13}C NMR spectrum of propargyl-dendron D1.5.

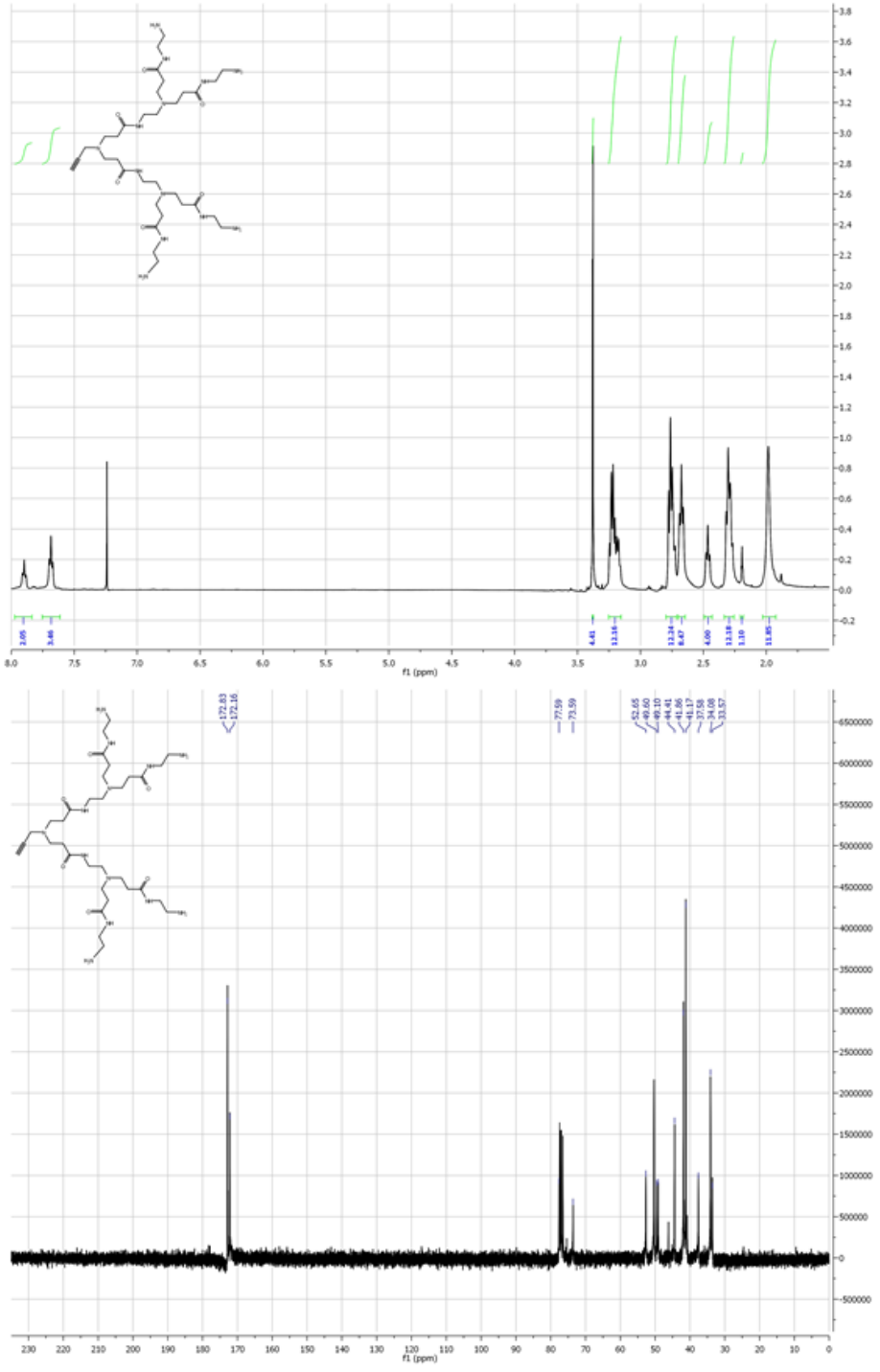

Figure 9.14: ^{1}H and ^{13}C NMR spectrum of propargyl-dendron D2.

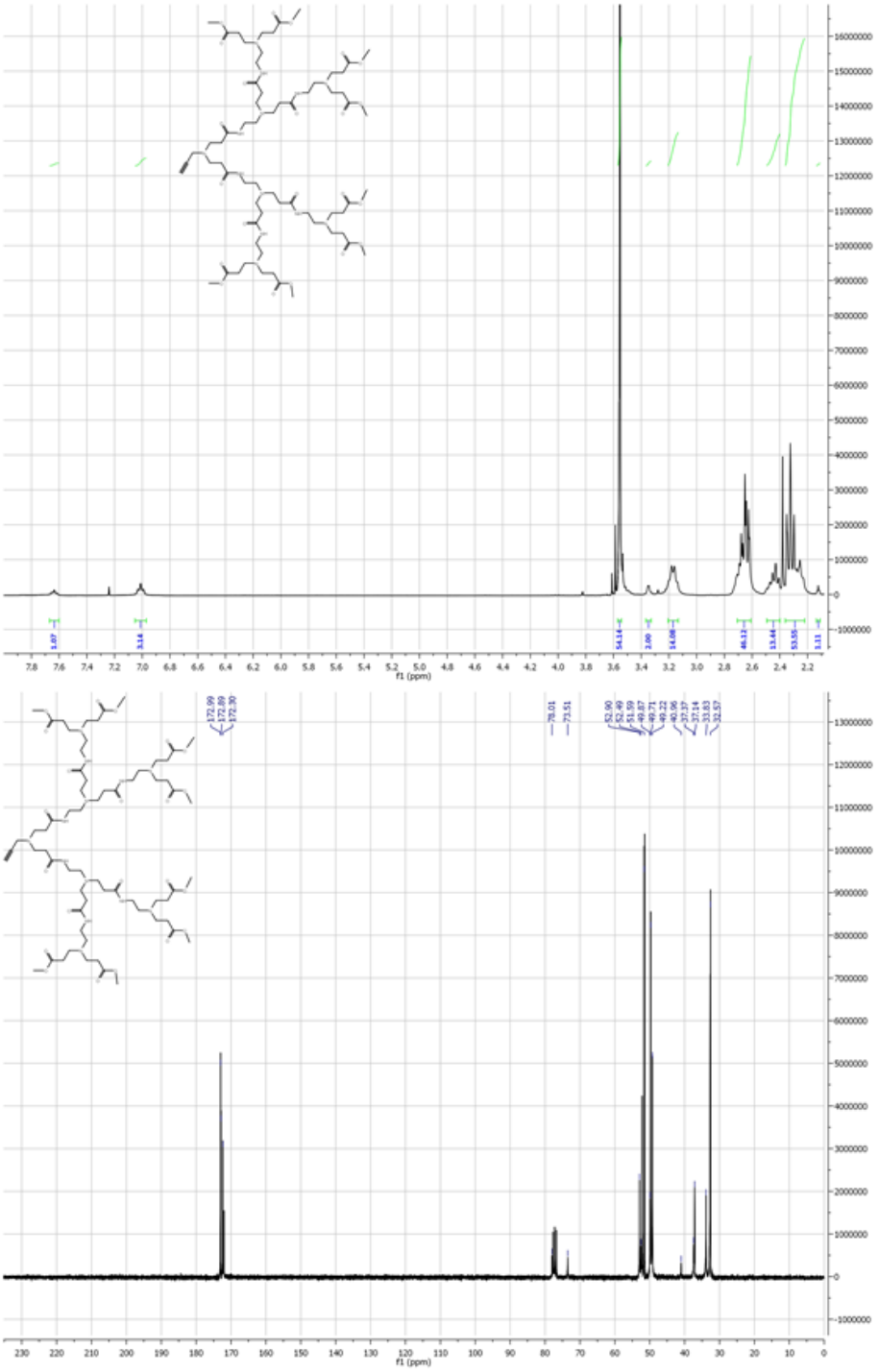

Figure 9.15: ^{1}H and ^{13}C NMR spectrum of propargyl-dendron D2.5.

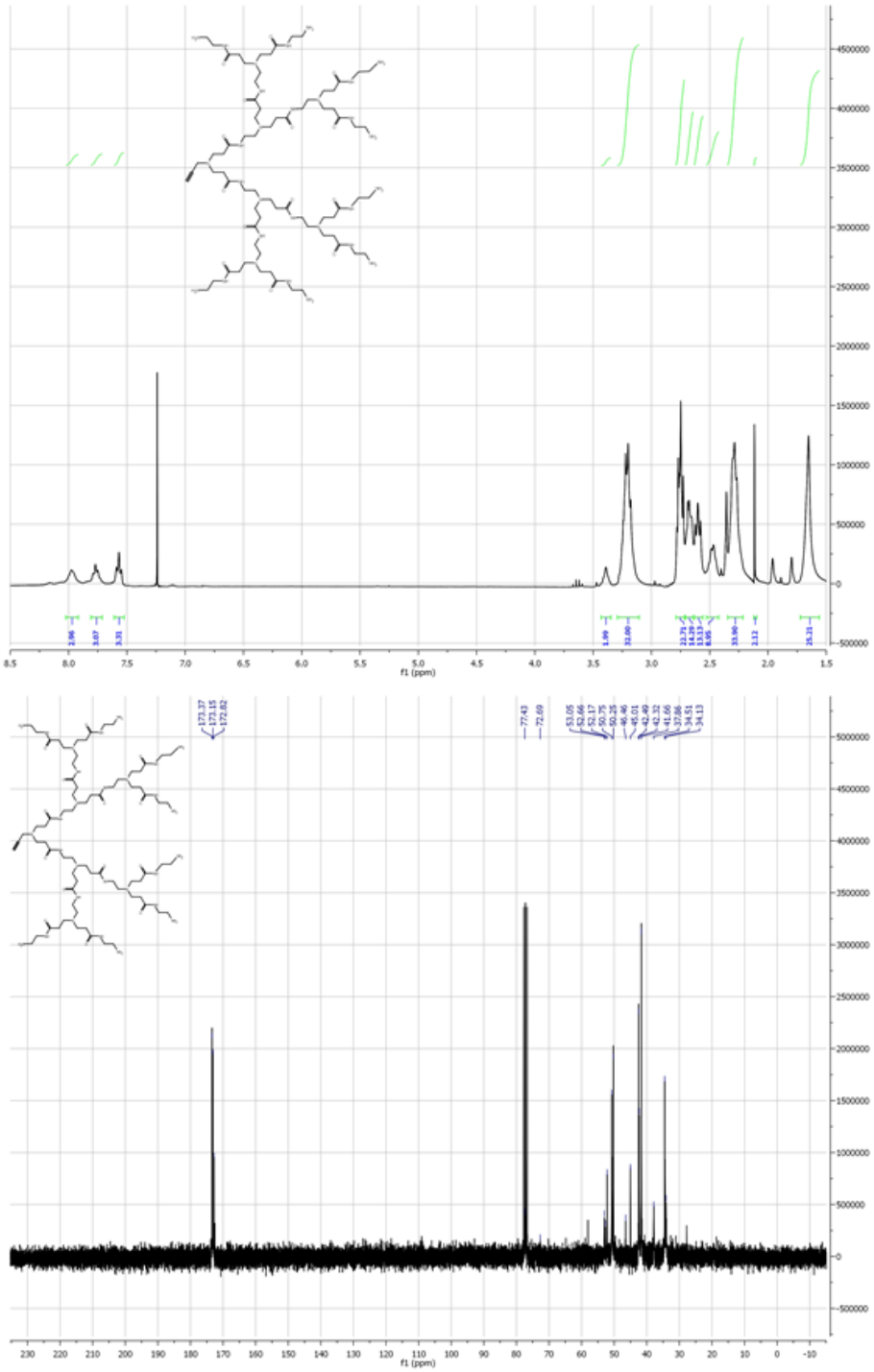

Figure 9.16: ^{1}H and ^{13}C NMR spectrum of propargyl-dendron D3.

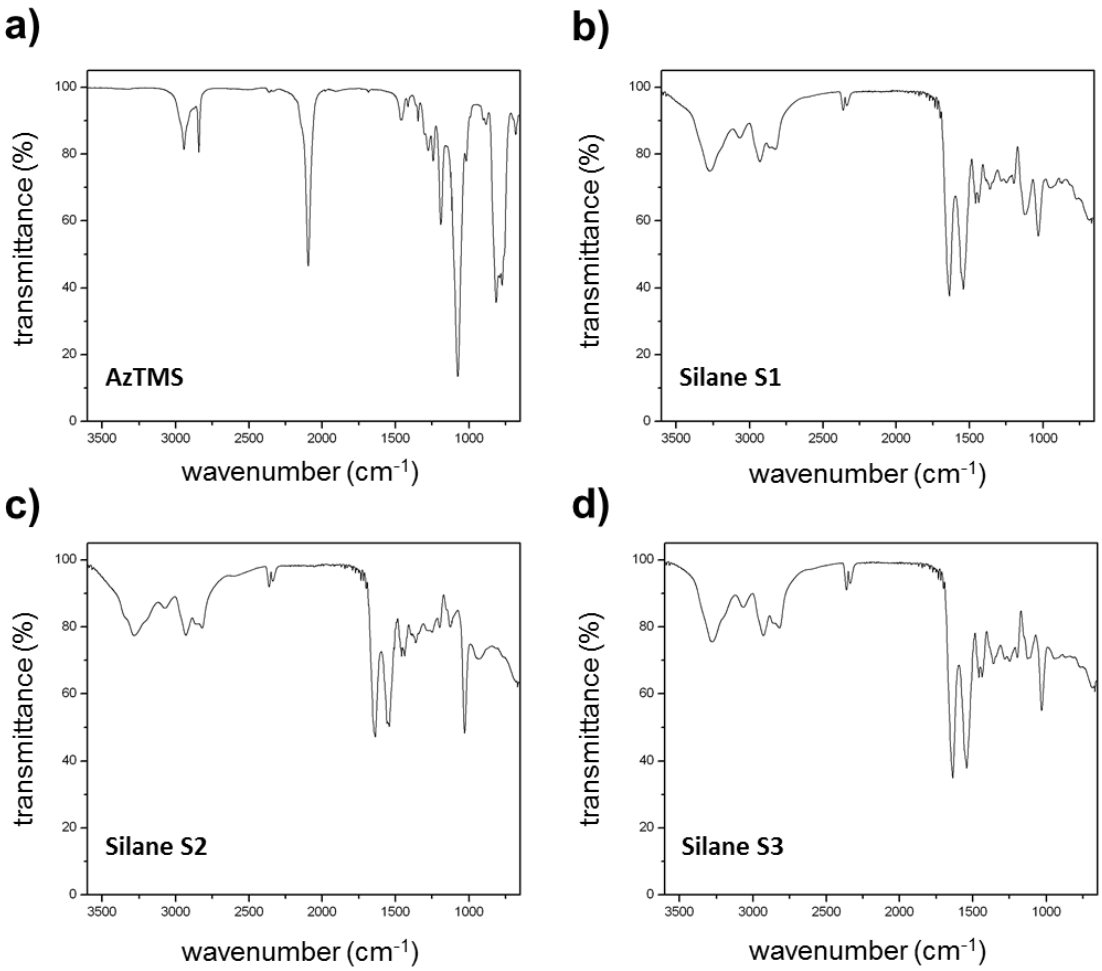

Figure 9.17: IR spectroscopy data of a) AzTMS, b) dendron-silane S1, c) dendron-silane S2, and d) dendron-silane S3.

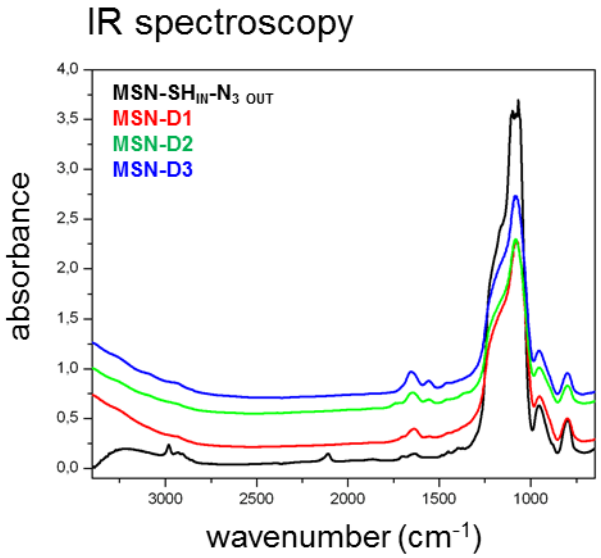

Figure 9.18: IR spectroscopy data of functionalized MSNs.

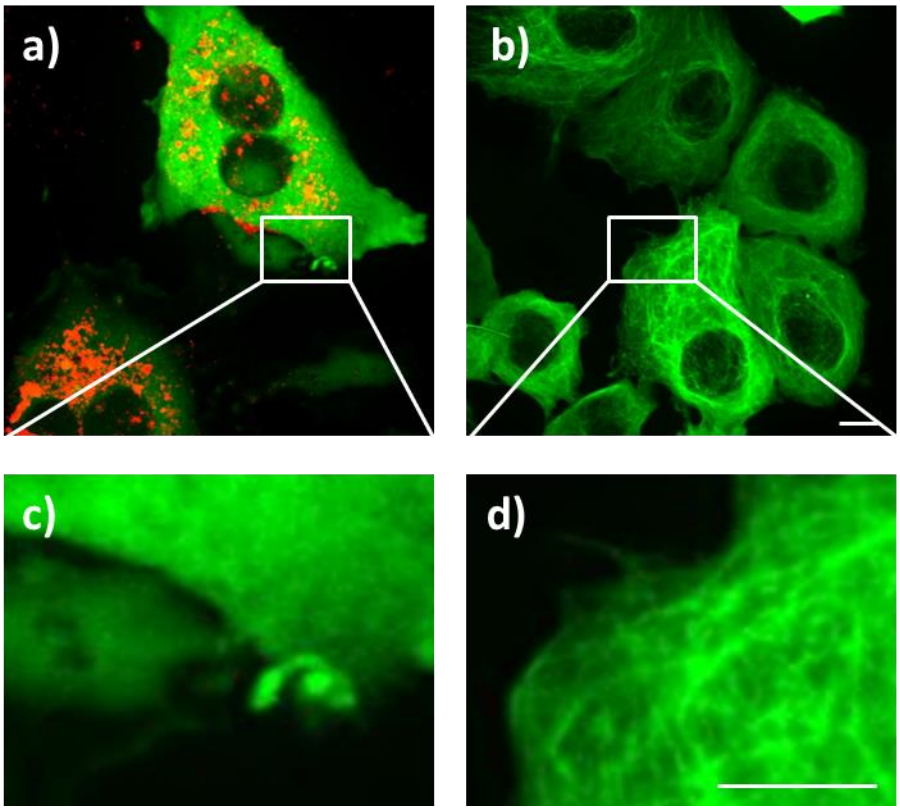

Figure 9.19: Fluorescence microscopy of KB cells with GFP tagged tubulins (green). a/c) The cells were incubated with MSN-D3 loaded with immobilized colchicine (MTS-Col) in the mesopores and labelled with Atto 633 (red) after 22 h incubation on the cells. b/d) Cells were incubated with sample supernatant (after particle separation by centrifugation) for 22 h. c/d) Zoom in on representative microtubule structures. A destruction of the tubulin network was only observed for particle-incubated cells. The scale bars represent 10 µm.

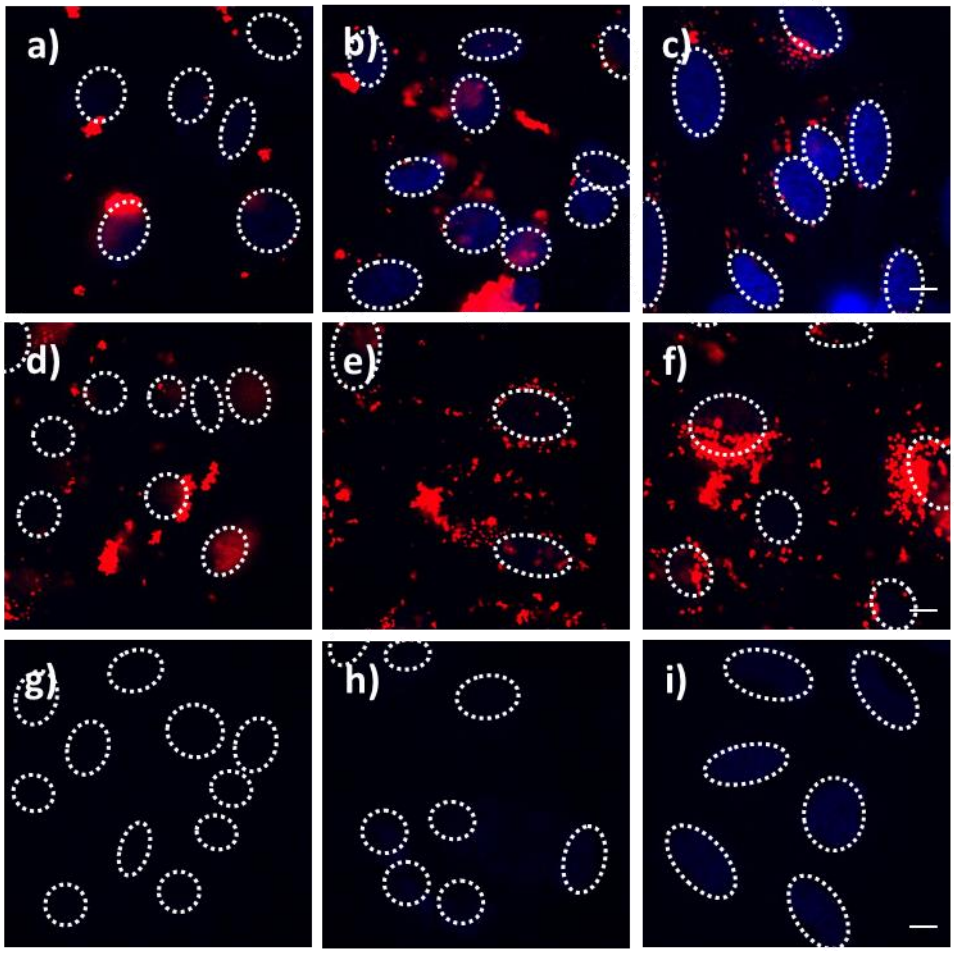

Figure 9.20: Fluorescence microscopy of HeLa cells incubated with MSN-D3-MTS-DAPI (a, b, c), MSN-NH_2-MTS-DAPI (d, e, f), and the supernatant of MSN-D3-MTS-DAPI (g, h, i). The nanoparticles were loaded with covalently attached DAPI (MTS-DAPI, blue) and labeled with Atto 633 (red). The cells were incubated with the samples for 5 h (a, d, g), 24 h (b, e, h) and 61 h (c, f, i). The nuclei are indicated with dashed circles. A time-dependent nuclei staining can be observed for MSN-D3-MTS-DAPI, suggesting triggered release of the cargo molecules from the nanocarriers after endosomal escape via the proton sponge effect and access to the cytosol. For MSN-NH_2-MTS-DAPI and the supernatant incubation almost no nucleic staining can be detected, which implies that no DAPI has been released from the particles or has been present in the solution, respectively. The scale bars represent 10 µm.

9.6 References

[1] A. M. Sauer, A. Schlossbauer, N. Ruthardt, V. Cauda, T. Bein, C. Bräuchle, *Nano Lett.* **2010**, *10*, 3684.

[2] K. de Bruin, N. Ruthardt, K. von Gersdorff, R. Bausinger, E. Wagner, M. Ogris, C. Bräuchle, *Mol. Ther.* **2007**, *15*, 1297.

[3] C. Argyo, V. Weiss, C. Bräuchle, T. Bein, *Chem. Mater.* **2014**, *26*, 435.

[4] A. K. Varkouhi, M. Scholte, G. Storm, H. J. Haisma, *J. Control. Rel.* **2011**, *151*, 220.

[5] S. A. Mackowiak, A. Schmidt, V. Weiss, C. Argyo, C. von Schirnding, T. Bein, C. Bräuchle, *Nano Lett.* **2013**, *13*, 2576.

[6] C. E. Ashley, E. C. Carnes, K. E. Epler, D. P. Padilla, G. K. Phillips, R. E. Castillo, D. C. Wilkinson, B. S. Wilkinson, C. A. Burgard, R. M. Kalinich, J. L. Townson, B. Chackerian, C. L. Willman, D. S. Peabody, W. Wharton, C. J. Brinker, *ACS Nano* **2012**, *6*, 2174.

[7] C. E. Ashley, E. C. Carnes, G. K. Phillips, D. Padilla, P. N. Durfee, P. A. Brown, T. N. Hanna, J. W. Liu, B. Phillips, M. B. Carter, N. J. Carroll, X. M. Jiang, D. R. Dunphy, C. L. Willman, D. N. Petsev, D. G. Evans, A. N. Parikh, B. Chackerian, W. Wharton, D. S. Peabody, C. J. Brinker, *Nat. Mater.* **2011**, *10*, 389.

[8] J. P. Behr, *Chimia* **1997**, *51*, 34.

[9] J. Gruenberg, F. R. Maxfield, *Curr. Opin. Cell Biol.* **1995**, *7*, 552.

[10] O. Boussif, F. Lezoualch, M. A. Zanta, M. D. Mergny, D. Scherman, B. Demeneix, J. P. Behr, *Proc. Natl. Acad. Sci. U.S.A.* **1995**, *92*, 7297.

[11] A. Akinc, M. Thomas, A. M. Klibanov, R. Langer, *J. Gene Med.* **2005**, *7*, 657.

[12] J. Suh, H. J. Paik, B. K. Hwang, *Bioorg. Chem.* **1994**, *22*, 318.

[13] D. A. Tomalia, H. Baker, J. Dewald, M. Hall, G. Kallos, S. Martin, J. Roeck, J. Ryder, P. Smith, *Polymer Journal* **1985**, *17*, 117.

[14] R. Esfand, D. A. Tomalia, *Drug Discovery Today* **2001**, *6*, 427.

[15] A. R. Menjoge, R. M. Kannan, D. A. Tomalia, *Drug Discovery Today* **2010**, *15*, 171.

[16] L. Albertazzi, F. M. Mickler, G. M. Pavan, F. Salomone, G. Bardi, M. Panniello, E. Amir, T. Kang, K. L. Killops, C. Bräuchle, R. J. Amir, C. J. Hawker, *Biomacromolecules* **2012**, *13*, 4089.

[17] A. Carlmark, C. J. Hawker, A. Hult, M. Malkoch, *Chem. Soc. Rev.* **2009**, *38*, 352.

[18] J. F. KukowskaLatallo, A. U. Bielinska, J. Johnson, R. Spindler, D. A. Tomalia, J. R. Baker, *Proc. Natl. Acad. Sci. U.S.A.* **1996**, *93*, 4897.

[19] J. Zhou, J. Wu, N. Hafdi, J.-P. Behr, P. Erbacher, L. Peng, *Chem. Commun.* **2006**, 2362.

[20] B.-F. Pan, D.-X. Cui, P. Xu, H. Chen, F.-T. Liu, Q. Li, T. Huang, X.-G. You, J. Shao, C.-C. Bao, F. Gao, R. He, M.-J. Shu, Y.-J. Ma, *Chin. J. Cancer Res.* **2007**, *19*, 1.

[21] D. R. Radu, C. Y. Lai, K. Jeftinija, E. W. Rowe, S. Jeftinija, V. S. Y. Lin, *J. Am. Chem. Soc.* **2004**, *126*, 13216.

[22] K. Möller, J. Kobler, T. Bein, *Adv. Funct. Mater.* **2007**, *17*, 605.

[23] V. Cauda, A. Schlossbauer, J. Kecht, A. Zürner, T. Bein, *J. Am. Chem. Soc.* **2009**, *131*, 11361.

[24] V. Cauda, H. Engelke, A. Sauer, D. Arcizet, C. Bräuchle, J. Rädler, T. Bein, *Nano Lett.* **2010**, *10*, 2484.

[25] V. Cauda, C. Argyo, T. Bein, *J. Mater. Chem.* **2010**, *20*, 8693.

[26] A. Schlossbauer, J. Kecht, T. Bein, *Angew. Chem. Int. Ed.* **2009**, *48*, 3092.

[27] A. Schlossbauer, S. Warncke, P. M. E. Gramlich, J. Kecht, A. Manetto, T. Carell, T. Bein, *Angew. Chem. Int. Ed.* **2010**, *49*, 4734.

[28] J. M. Rosenholm, A. Meinander, E. Peuhu, R. Niemi, J. E. Eriksson, C. Sahlgren, M. Linden, *ACS Nano* **2009**, *3*, 197.

[29] L.-S. Wang, L.-C. Wu, S.-Y. Lu, L.-L. Chang, I. T. Teng, C.-M. Yang, J.-A. A. Ho, *ACS Nano* **2010**, *4*, 4371.

[30] F. Wang, X. Chen, Z. Zhao, S. Tang, X. Huang, C. Lin, C. Cai, N. Zheng, *J. Mater. Chem.* **2011**, *21*, 11244.

[31] Q. Zhang, F. Liu, N. Kim Truc, X. Ma, X. Wang, B. Xing, Y. Zhao, *Adv. Funct. Mater.* **2012**, *22*, 5144.

[32] J. Pang, L. Zhao, L. Zhang, Z. Li, Y. Luan, *J. Colloid Interface Sci.* **2013**, *395*, 31.

[33] J. W. Lee, B. K. Kim, H. J. Kim, S. C. Han, W. S. Shin, S. H. Jin, *Macromolecules* **2006**, *39*, 2418.

[34] J. Nakazawa, T. D. P. Stack, *J. Am. Chem. Soc.* **2008**, *130*, 14360.

[35] U. Bohme, A. Klenge, B. Hanel, U. Scheler, *Polymers* **2011**, *3*, 812.

[36] Y.-M. Go, D. P. Jones, *Biochim. Biophys. Acta* **2008**, *1780*, 1273.

[37] J. Yang, H. Chen, I. R. Vlahov, J.-X. Cheng, P. S. Low, *Proc. Natl. Acad. Sci. U.S.A.* **2006**, *103*, 13872.

[38] C. D. Austin, X. H. Wen, L. Gazzard, C. Nelson, R. H. Scheller, S. J. Scales, *Proc. Natl. Acad. Sci. U.S.A.* **2005**, *102*, 17987.

[39] B. Arunachalam, U. T. Phan, H. J. Geuze, P. Cresswell, *Proc. Natl. Acad. Sci. U.S.A.* **2000**, *97*, 745.

[40] D. A. Skoufias, L. Wilson, *Biochemistry* **1992**, *31*, 738.

[41] K. Morikawa, M. Yanagida, *Journal of Biochemistry* **1981**, *89*, 693.

[42] M. L. Barcellona, G. Cardiel, E. Gratton, *Biochem. Biophys. Res. Commun.* **1990**, *170*, 270.

[43] http://tools.lifetechnologies.com/content/sfs/manuals/mp01306.pdf.

[44] S. Niedermayer, PhD thesis, University of Munich (LMU) (Munich), **2013**.

[45] J. E. Lim, C. B. Shim, J. M. Kim, B. Y. Lee, J. E. Yie, *Angew. Chem. Int. Ed.* **2004**, *43*, 3839.

[46] J. Lim, S. S. Lee, J. Y. Ying, *Chem. Commun.* **2010**, *46*, 806.

10 Conclusions and Outlook

The focus of the present work was the synthesis and characterization of tailor-made multifunctional mesoporous silica nanoparticles (MSNs) for advanced drug delivery applications. The customized, stimuli-responsive nanovehicles developed in this work meet various prerequisites for controlled cargo delivery regarding targeted cancer diagnosis and therapy.

In a first project (Chapter 3), the effects of high-boiling organic solvents such as TOPO, TOA and squalene on colloidal MSNs have been studied. A liquid-phase "calcination" of MSNs at elevated temperatures (275 and 400 °C) led to a higher degree of silica condensation and simultaneously to template extraction. The retention of the colloidal nature of the nanoparticles and the prevention of non-reversible aggregation during the calcination process are important advantageous of this newly developed method. It is anticipated that a higher degree of condensation and the resulting stability provide improved characteristics for biomedical applications such as stable drug delivery vehicles.

In Chapter 4, the integration of a superparamagnetic core to the silica host material offers the possibility of specific targeted delivery to cancer tissue by applying an external magnetic field. We created a new synthesis strategy to obtain multifunctional nanocomposites with a magnetic core and different functional mesoporous silica shells. An inner pore functionalization provides control over attachment, diffusion and release of cargo molecules such as chemotherapeutics. Integrated functional groups at the external particle surface enable the attachment of labels, protecting layers, and targeting ligands. Multifunctional magnetic MSNs provide a promising platform for spatially-controlled drug delivery and may improve *in vivo* investigations of biodistribution and accumulation via magnetic resonance imaging (MRI). Future experiments will have to demonstrate a magnetically driven targeted drug delivery in organisms.

Biocompatibility and hemocompatibility are important requirements for blood-stream injectable drug nanocarriers. The covalent attachment of heparin on the external surface of MSNs showed efficient anticoagulant properties for such multifunctional nanocarriers in blood-clotting tests (Chapter 5). The covalently bound heparin still showed significant activity serving as a cofactor for the anticoagulant serine protease inhibitor antithrombin. These results imply a long-term stability of heparin-functionalized MSNs injected into the blood

stream. Furthermore, in the future these novel nanomaterials could be used as anticoagulant coatings for stents with integrated drug release options.

A stimuli-responsive controlled cargo release can be achieved by judicious modification of the nanocarriers with bulky gatekeepers. In Chapter 6, an enzyme-responsive cargo release mechanism by linkage of avidin *via* short peptide sequences is described. These peptide linkers are selectively cleaved by the enzyme MMP-9 that is known to be overexpressed in cancer tissue. To the best of our knowledge we report for the first time on avidin-coated MSNs showing specific *in vitro* release of the anticancer drug cisplatin to lung cancer cells. Additionally, a combination treatment with cisplatin and the proteasome inhibitor bortezomib led to an improved performance of the MSNs for cancer treatment. Thus, the effective dose of the chemotherapeutic agent could be reduced, which can lead to a further reduction of side-effects. Future work will address *in vivo* biodistribution studies in lung tissue and *in vivo* therapeutic studies in mouse models, intended to prove the applicability of our system in organisms.

In a different project (Chapter 7), a novel pH-responsive capping system based on sulfonamide-linked carbonic anhydrase (CA) enzyme has been successfully developed. CA enzymes act here as bulky gatekeepers and have been found to efficiently block the mesoporous system of silica nanoparticles, thus preventing premature cargo release. A time-dependent release of the model drug DAPI was observed in *in vitro* studies on HeLa cancer cells with fluorescent live-cell imaging. These results can be attributed to the acidification of the endosomal compartment, initiating the pH-responsive release. Future experiments will allow the introduction of functional groups with bio-orthogonal reactivity by a precise genetic modification of the enzymes. Thus, the multifunctional MSNs may enable the attachment of targeting ligands for specific receptor-mediated cellular uptake and targeted drug delivery to cancer cells.

In this thesis, two different strategies for a successful endosomal escape of mesoporous silica nanocarriers have been developed. In Chapter 8, a photoinduced rupture of the endosomal membrane was achieved with immobilized photosensitizers. We describe the development of multifunctional drug delivery vehicles based on mesoporous silica nanoparticles equipped with a red-light sensitive photosensitizer, encapsulated by a supported lipid bilayer (SLB), and functionalized with different targeting ligands. We anticipate that these multifunctional drug delivery vehicles are a promising platform to achieve spatially and temporally controlled

drug release. Future work aims at the employment of near-infrared or two-photon excitation schemes for light-activated cargo release, which would be favorable for the enhancement of tissue penetration in *in vivo* applications.

In another project (Chapter 9), PAMAM dendron-coated MSNs that exhibit high buffering capacity were successfully synthesized. We were able to demonstrate endosomal escape from these nanocarriers *via* the proton sponge effect and controlled release of immobilized cargo molecules (the anticancer drug colchicine and the fluorescent dye DAPI), which had been covalently attached to the porous system *via* disulfide bridges. Additionally, a specific cell uptake was achieved by modification with targeting ligands. This newly designed multifunctional nanocarrier system based on PAMAM dendron-coated MSNs provides autonomous cargo delivery into cancer cells since it responds to internal cellular triggers, namely changes in pH and in redox-potential, respectively.

In summary, specially designed mesoporous silica nanoparticles with release-on-demand properties offer promising prospects as precisely controllable and efficient drug delivery vehicles. Our MSNs combine advantageous properties of different materials in one multifunctional device for theranostic treatment and bioimaging in biomedical applications such as cancer therapy. It is hoped that precise dosing of chemotherapeutics at the desired locations in cancer tissue could be achieved with the family of mesoporous carrier systems, thus significantly reducing side effects. In the present work, general drug delivery platforms based on multifunctional MSNs have been established, which will be investigated as promising candidates in future *in vivo* applications.

Multifunctional MSNs are not only bearers of drugs but maybe also bearers of hope.

11 Publications and Presentations

11.1 Publications

1. Large-Scale Preparation of Polyfunctional Benzylic Zinc Reagents by Direct Insertion of Zinc Dust into Benzylic Chlorides in the Presence of Lithium Chloride

   A. Metzger, C. Argyo, P. Knochel, *Synthesis* **2010**, *5*, 882 – 891.

2. Controlling the Delivery Kinetics from Colloidal Mesoporous Silica Nanoparticles with pH-Sensitive Gates

   V. Cauda, C. Argyo, A. Schlossbauer, T. Bein, *J. Mater. Chem.* **2010**, *20*, 4305 – 4311.

3. Impact of Different PEGylation Patterns on Long-Term Biostability of Colloidal Mesoporous Silica Nanoparticles

   V. Cauda, C. Argyo, T. Bein, *J. Mater. Chem.*, **2010**, *20*, 8693 – 8699.

4. "Liquid-Phase Calcination" of Colloidal Mesoporous Silica Nanoparticles in High-Boiling Solvents

   V. Cauda, C. Argyo, D. G. Piercey, T. Bein, *J. Am. Chem. Soc.* **2011**, *133*, 6484 – 6486.

5. Heparin-Coated Colloidal Mesoporous Silica Nanoparticles Efficiently Bind to Antithrombin as an Anticoagulant Drug-Delivery System

   C. Argyo, V. Cauda, H. Engelke, J. Rädler, G. Bein, T. Bein, *Chem. – Eur. J.* **2012**, *18*, 428 – 432.

6. A Fast Analysis Method to Quantifiy Nanoparticle Uptake on a Single Cell Level

   A. Torrano, J. Blechinger, C. Osseforth, C. Argyo, A. Reller, T. Bein, J. Michaelis, C. Bräuchle, *Nanomedicine* **2013**, *8*, 1815 – 1828.

7. Targeted Drug Delivery in Cancer Cells with Red-Light Photoactivated Mesoporous Silica Nanoparticles

   S. Mackowiak, A. Schmidt, V. Weiss, C. Argyo, C. von Schirnding, T. Bein, C. Bräuchle, *Nano Lett.* **2013**, *13*, 2576 – 2583.

8. Multifunctional Mesoporous Silica Nanoparticles as a Universal Platform for Drug Delivery

   C. Argyo, V. Weiss, C. Bräuchle, T. Bein, *Chem. Mater*. **2013**, *26*, 435 – 451.

9. Matrix metalloproteinase-9 responsive mesoporous silica nanoparticles for local drug delivery to tumor cells

   C. Argyo, D. A. Bölükbas, S. Meiners, O. Eickelberg, T. Bein, S. H. van Rijt, *submitted*.

10. Investigation of the Endosomal Escape via the Proton Sponge Effect with Dendron-Functionalized Mesoporous Silica Nanoparticles

    C. Argyo, V. Weiß, T. Gatzenmeier, C. Bräuchle, T. Bein, *in preparation*.

11. Carbonic Anhydrase-Based pH-Responsive Cap System for Mesoporous Silica Nanoparticles

    C. Argyo, M. Gattner, S. Datz, V. Weiß, C. Bräuchle, T. Carell, T. Bein, *in preparation*.

11.2 Oral Presentations

1. Controlling Endosomal Escape of Multifunctional Mesoporous Nanoparticles to Trigger Specific Drug Release

   Christian Argyo, Stephan A. Mackowiak, Alexandra Schmidt, Veronika Weiss, Christoph Bräuchle, Thomas Bein

   MRS Spring Meeting **2013**, San Francisco, CA, USA.

11.3 Poster Presentations

1. PEGylated Colloidal Mesoporous Silica Nanoparticles for Drug Delivery Applications.

   Christian Argyo, Valentina Cauda, and Thomas Bein

   Center for Nanosicence (CeNS) Workshop "Nanosciences – Merging Disiplines", **2010**, Venice, Italy

2. “Liquid-Phase Calcination” of Colloidal Mesoporous Silica Nanoparticles in High-Boiling Solvents.

   Valentina Cauda, Christian Argyo, Davin G. Piercey, and Thomas Bein

   23. Deutsche Zeolith-Tagung (DZT), **2011**, Erlangen, Germany.

3. Heparin-Coated Colloidal Mesoporous Silica Nanoparticles as Anticoagulant Drug Delivery System.

   Christian Argyo, Valentina Cauda, Hanna Engelke, Joachim Rädler, Gregor Bein, and Thomas Bein

   Center for NanoScience (CeNS) Workshop "Nanosciences: From molecular systems to functional materials", **2011**, Venice, Italy.

4. Nanopartikel zur lokalen Bekämpfung von Krebszellen.

   Christian Argyo, Alexandra Schmidt, Stefan Niedermayer, Bastian Rühle, and Thomas Bein

   11. Münchner Wissenschaftstage “Herausforderung Gesundheit”, **2011**, Munich, Germany.

5. Heparin-Coated Colloidal Mesoporous Silica Nanoparticles as Anticoagulant Drug Delivery System.

   Christian Argyo, Valentina Cauda, Hanna Engelke, Joachim Rädler, Gregor Bein, and Thomas Bein

   Nanohealth Symposium, **2011**, Seoul, South Korea.

6. Heparin-Coated Colloidal Mesoporous Silica Nanoparticles as Anticoagulant Drug Delivery System.

   Christian Argyo, Valentina Cauda, Hanna Engelke, Joachim Rädler, Gregor Bein, and Thomas Bein

   Nanomaterials for Biomedical Technologies, **2012**, Frankfurt a.M., Germany.

7. Heparin-Coated Colloidal Mesoporous Silica Nanoparticles as Anticoagulant Drug Delivery System.

   Christian Argyo, Valentina Cauda, Hanna Engelke, Joachim Rädler, Gregor Bein, and Thomas Bein

   13th European Symposium on Controlled Drug Delivery, **2012**, Egmond aan Zee, Netherlands.

8. Multifunctional Mesoporous Silica Nanoparticles for Triggered and Targeted Drug Delivery and For Studying Cell-Receptor Interactions.

   Alexandra Schmidt, Stefan Niedermayer, Christian Argyo, Bastian Rühle, Veronika Weiss, Stephan Mackowiak, Constantin von Schirnding, Christoph Bräuchle, and Thomas Bein

   Gemeinsame Tagung des SFB1032 und der NIM Forschungsbereiche 4 und 5, **2013**, Hohenkammer, Germany.

9. Matrix Metalloproteinase Responsive Mesoporous Silica Nanocarriers for Site-Specific Drug Release in Lung Tumors

   Christian Argyo, Deniz A. Bölükbas, Oliver Eikelberg, Silke Meiners, Sabine van Rijt, and Thomas Bein

   26. Deutsche Zeolith-Tagung (DZT), **2014**, Paderborn, Germany.